THE UNIVERSITY OF SYDNEY

MICROWAVE PHOTONIC SIGNAL PROCESSING USING ON-CHIP NONLINEAR OPTICS

MATTIA PAGANI

A thesis submitted in fulfilment of the requirements
for the degree of
Doctor of Philosophy
in the Faculty of Science at the University of Sydney.

2016

DECLARATION

I hereby declare that this submission is my own work and to the best of my knowledge contains no materials previously published or written by another person, or substantial proportions of material which have been accepted for the award of any other degree or diploma at the University of Sydney or any other educational institution, except where due acknowledgement is made in the thesis. Any contribution made to the research by others, with whom I have worked at the University of Sydney or elsewhere, is explicitly acknowledged in the thesis. I also declare that the intellectual content of this thesis is the product of my own work, except to the extent that assistance from others in the project's design and conception or in style, presentation and linguistic expression is acknowledged.

Mattia Pagani

ABSTRACT

The field of microwave photonics (MWP) emerged as a solution to the challenges faced by electronic systems when dealing with high-bandwidth RF and microwave signals. Photonic devices are capable of handling immense bandwidths thanks to the properties of light. MWP therefore employs such devices to process and distribute the information carried by RF and microwave signals, enabling significantly higher capacity compared to conventional electronics.

The photonic devices traditionally used in MWP circuits have mainly comprised bulky components, such as spools of fibre and benchtop optical amplifiers. While achieving impressive performance, these systems were not capable of competing with electronics in terms of size and portability. More recently, research has focused on the application of photonic chip technology to the field of MWP in order to reap the benefits of integration, such as reductions in size, weight, cost, and power consumption. Integrated MWP however is still in its infancy, and ongoing research efforts are exploring new ways to match integrated photonic devices to the unique requirements of MWP circuits.

This work investigates the application of on-chip nonlinear optical interactions to MWP. Nonlinear optics enables light-on-light interactions (not normally possible in a linear regime) which open a vast array of powerful functionalities. In particular, this thesis focuses on stimulated Brillouin scattering, resulting from the interaction of light with hypersonic sound waves, and four-wave mixing, where photons exchange energies. These two nonlinear effects are applied to implement MWP ultra-high suppression notch filters, wideband phase shifters, and ultra-fast instantaneous frequency measurement systems. Experimental demonstrations using integrated optical waveguides confirm record results.

PUBLICATIONS

The work presented in this thesis has been published in a number of journals and conferences.

Journal publications:

1. M. Merklein, A. Casas-Bedoya, D. Marpaung, T. Büttner, **M. Pagani**, B. Morrison, I. Kabakova, B. J. Eggleton, "Stimulated Brillouin scattering in photonic integrated circuits: novel applications and devices," *IEEE Journal of Selected Topics in Quantum Electronics*, accepted, 2016.

2. H. Jiang, D. Marpaung, **M. Pagani**, K. Vhu, D. Choi, S. Madden, L. S. Yan, and B. J. Eggleton, "Wide-range, high-precision multiple microwave frequency measurement using a chip-based photonic Brillouin filter," *Optica*, vol. 3, no. 1, 2016.

3. S. Shahnia, **M. Pagani**, B. Morrison, B. J. Eggleton, and D. Marpaung, "Independent manipulation of the phase and amplitude of optical sidebands in a highly-stable RF photonic filter," *Optics Express*, vol. 23, no. 18, 2015.

4. A. Casas-Bedoya, B. Morrison, **M. Pagani**, D. Marpaung, and B. J. Eggleton, "Tunable narrowband microwave photonic filter created by stimulated Brillouin scattering from a silicon nanowire," *Optics Letters*, vol. 40, no. 17, 2015.

5. **M. Pagani**, B. Morrison, Y. Zhang, A. Casas-Bedoya, T. Aalto, M. Harjanne, M. Kapulainen, B. J. Eggleton, and D. Marpaung, "Low-error and broadband microwave frequency measurement in a silicon chip," *Optica*, vol. 2, no. 8, 2015.

6. **M. Pagani**, K. Vu, D. Choi, S. J. Madden, B. J. Eggleton, and D. Marpaung, "Instantaneous microwave frequency measurement using four-wave mixing in a chalcogenide chip," *Optics Communications*, accepted, 2015.

7. D. Marpaung, B. Morrison, **M. Pagani**, R. Pant, D. Choi, B. Luther-Davies, S. J. Madden, and B. J. Eggleton, "Low power, chip-based stimulated Brillouin scattering microwave photonic filter with ultrahigh selectivity," *Optica*, vol. 2, no. 1, 2015.

8. **M. Pagani**, D. Marpaung, D. Choi, S. J. Madden, B. Luther-Davies, and B. J. Eggleton, "Tunable wideband microwave photonic phase shifter using on-chip stimulated Brillouin scattering," *Optics Express*, vol. 22, no. 23, 2014.

9. **M. Pagani**, D. Marpaung, and B. J. Eggleton, "Ultra-wideband microwave photonic phase shifter with configurable amplitude response," *Optics Letters*, vol. 39, no. 20, 2014.

10. D. Marpaung, **M. Pagani**, B. Morrison, and B. J. Eggleton, "Nonlinear integrated microwave photonics," *Journal of Lightwave Technology*, vol. 32, no. 20, 2014.

11. D. Marpaung, B. Morrison, **M. Pagani**, R. Pant, and B. J. Eggleton, "Ultra-high suppression microwave photonic bandstop filters," *Chinese Science Bulletin*, vol. 59, no. 22, 2014.

12. **M. Pagani**, E. H. W. Chan, and R. A. Minasian, "A study of the linearity performance of a stimulated Brillouin scattering-based microwave photonic filter," *Journal of Lightwave Technology*, vol. 32, no. 5, 2014.

Conference presentations:

1. **M. Pagani**, S. Shahnia, B. Morrison, B. J. Eggleton, and D. Marpaung, "Highly-stable RF photonic cancellation filter," to be presented at MWP 2015, Paphos, Cyprus.

2. **M. Pagani**, B. Morrison, Y. Zhang, A. Casas-Bedoya, T. Aalto, M. Harjanne, M. Kapulainen, B. J. Eggleton, and D. Marpaung, "Instantaneous frequency measurement system using four-wave mixing in an ultra-compact long silicon waveguide," to be presented at ECOC 2015, Valencia, Spain.

3. **M. Pagani**, D. Marpaung, B. Morrison, and B. J. Eggleton, "Tunable microwave photonic phase shifter using on-chip stimulated Brillouin scattering," presented at CLEO 2015, San Jose, CA, USA, STh3F.4.

4. **M. Pagani**, D. Marpaung, and B. J. Eggleton, "Ultra-wideband RF photonic phase shifter with 360° tunable phase and configurable amplitude response," presented at MWP 2014, Sapporo, Japan, WD-2.

5. **M. Pagani**, B. J. Eggleton, and D. Marpaung, "Novel high performance microwave photonic phase shifters based on stimulated Brillouin scattering," presented at PIERS 2014, Guangzhou, China, Invited paper.

6. **M. Pagani**, D. Marpaung, D. Choi, S. J. Madden, B. Luther-Davies, and B. J. Eggleton, "On-chip wideband tunable RF photonic phase shifter based on stimulated Brillouin scattering," presented at OECC/ACOFT 2014, Melbourne, Australia, TU3E-2.

7. **M. Pagani**, D. Marpaung, B. Morrison, and B. J. Eggleton, "Bandwidth tunable, high suppression RF photonic filter with improved insertion loss," presented at CLEO 2014, San Jose, CA, USA, STu2G.7.

ACKNOWLEDGEMENTS

Behind every page in this document are many late nights and early mornings; many meetings and discussions; weeks spent in front of a computer screen, and even more time spent in a cold (exactly 21°C) lab. My last three years working at CUDOS were undoubtedly challenging, but even more so, they were rewarding. This was an amazing experience, which has certainly had a major impact on my life, and which was made possible by a number of people to whom I am very grateful.

First I want to thank my supervisor, Prof. Benjamin Eggleton, for giving me the opportunity to work under his supervision. I thank him for all the work he does to make CUDOS such an amazing group to work in. His enthusiasm and ambitiousness drove me to put all my efforts in everything I did. I also thank him for his financial support, which always provided me with any equipment I needed, and allowed me to participate in many conferences.

Very special thanks goes to my associate supervisor, Dr. David Marpaung, for being by my side each single step of the way, supporting me especially in the most difficult times. I thank him for the immense kindness and patience he showed to me, and for all the late nights he spent away from his family to help me. His insight and his approach to everything, from writing to experiments, has always impressed me. He was a great teacher and mentor. I will greatly miss our daily meals together, our discussions, and his sense of humour.

Before moving on, I want to acknowledge the help from Prof. Eggleton and Dr. Marpaung in editing this thesis. I also sincerely thank them both for supporting me in my career choice, even if it takes me away from research.

I thank Prof. Robert Minasian and Dr. Erwin Chan, for introducing me to the field of microwave photonics, and for their supervision and guidance throughout the first year of my PhD in the Fibre-Optics and Photonics Laboratory.

Thank you to the CUDOS staff Dr. Eric Mägi, Shayan Shahnia, and Joseph Zheng for their essential technical support throughout my experiments. Thanks to Dr. Alvaro Casas-Bedoya for our discussions and friendship. Thanks to Dr. Mark Pelusi, for all the equipment he lent me. Thanks also to the CUDOS admin team, especially Shelley Martin, Vera Brinkel, and Silke Weiss, for all the work they put into organizing the various, very enjoyable, workshops and exhibitions.

Special thanks to my fellow SBS PhD students: Moritz Merklein, Iman Aryanfar, Atiyeh Zarifi, and Thomas Büttner. A big thank you especially to Blair Morrison, who is always right, for teaching me

how to do chip coupling, for all the experiments we did together, and his never-ending discussions. Thanks also to my office friends: Young Zhang, Neetesh Singh, Iman Jizan, Loris Marini, Stephanie Crawford, Caitlin Fisher, Jiakun He, Scott Brownless, Fernando Diaz, and Bjorn Sturmberg. They made this journey much more enjoyable.

I thank my parents who raised me to make this possible, and who have supported me all my life. Finally, I thank my grandparents, Carlo and Gabriella. This work is dedicated to them.

This thesis was written in LaTeXusing André Miede's *classicthesis* template, inspired by Robert Bringhurst's *"The Elements of Typographic Style"*. I know some people think this style looks unusual (e.g. not enough characters per line, or the page numbers not being neatly aligned to the right in the table of contents). Nevertheless, these features are not random and are in fact designed to improve legibility, hopefully providing the reader with a better reading experience. Personally, I think this style looks great and I thank André Miede for his work in making this package freely available.

CONTENTS

ACRONYMS

ACF amplitude comparison function

ADC analog-to-digital converter

ASE amplified spontaneous emission

BPF bandpass filter

ChG chalcogenide

CMOS complementary metal-oxide semiconductor

CPSS complementary phase-shifted spectra

CWDM coarse wavelength division multiplexer

CW continuous wave

DC direct current

DFB distributed feedback

DPMZM dual-parallel Mach-Zehnder modulator

DQPSK differential quadrature phase shift keying

DSB double sideband

EDFA erbium-doped fibre amplifier

EMI electromagnetic interference

EOM electro-optic modulator

EW electronic warfare

FCA free-carrier absorption

FD-OP Fourier-domain optical processor

FOM figure of merit

FSR free spectral range

FWHM full width at half maximum

FWM four-wave mixing

HNLF highly nonlinear fibre

IFM instantaneous frequency measurement

LCoS liquid crystal on silicon

MEMS micro-electro-mechanical system

MWP microwave photonic

MZM Mach-Zehnder modulator

PC polarisation controller

PD photodetector

PLC planar lightwave circuit

RF radio frequency

RIN relative intensity noise

rms root mean square

RoF radio over fibre

SBS stimulated Brillouin scattering

SFDR spurious-free dynamic range

SG signal generator

SMF single-mode fibre

SNR signal-to-noise ratio

SOA semiconductor optical amplifier

SOI silicon on insulator

SPM self-phase modulation

SSB single sideband

SVEA slowly varying amplitude approximation

TDL tunable delay line

TPA two-photon absorption

UWB ultrawideband

VNA vector network analyser

1 INTRODUCTION TO MICROWAVE PHOTONICS

1.1 RF AND MICROWAVE SIGNAL PROCESSING

Radio waves and microwaves are at the heart of the wireless technologies which are increasingly becoming an integral part of our society. The terms *radio frequency* (RF) and *microwave* refer to all electromagnetic waves whose frequencies fall within the range 300–3000 MHz and 3–300 GHz, respectively. Mobile phones, Wi-Fi, radio, and television are all examples of appliances which heavily rely on RF and microwave signals for wireless communication. Global navigation, such as GPS, uses RF waves to locate a user relative to fixed objects, such as satellites [1]. Other less ubiquitous, but no less important, microwave-dependent technologies include radar for detecting moving objects, antenna-arrays used in radio astronomy, and certain spectrometers used in electrochemistry [2].

At the heart of all of these devices are numerous electronic circuits which manipulate, or process, the various RF and microwave signals. Processing is mainly done digitally, and requires that the input analog signal first be converted into digital form. The problem is that electronic analog-to-digital converters (ADCs) suffer from a trade-off between sampling rate and resolution, and typically cannot handle microwave signal frequencies beyond a few tens of gigahertz [3]. Such wideband microwave signals are currently used in a number of applications, such as radar, and are set to become increasingly important in next generation's 5G networks [4].

A solution proposed to solve the limitations of ADCs involves processing the microwave signal directly in the analog domain, removing the need for analog-to-digital conversion [5]. Such RF and microwave circuits are implemented using various technologies; III–V compound semiconductors, silicon-based semiconductors, ferrites, ferroelectrics, and micro-electro-mechanical systems (MEMS) all offer distinct trade-offs between power consumption, power handling, packaging, large-scale integration, and cost [6–8]. There is however one common feature among all these technologies: the limited bandwidth that they can process. Analog microwave circuits are plagued by frequency-dependent losses and dispersion, so that their frequency response is very inflexible, tunable only over a range normally restricted to a few gigahertz [9–11].

In today's world, the exponentially growing bandwidth demand, and an increasingly congested electromagnetic spectrum, highlight the need for exploiting both RF and microwave spectra to their full

potential. This evolution can begin only with the realization of microwave devices and systems capable of ultra-wideband operation, over tens of gigahertz. This is an overwhelming task with current microwave technology, however, photonics provides a possible solution.

1.2 HISTORICAL BACKGROUND

Microwave photonics (MWP), also referred to as RF or analog photonics, deals with the application of optical components and techniques to RF and microwave fields [12–14]. This can be seen as a bidirectional relationship where microwaves are applied to optical devices, and where optical devices are used to process/transport/generate microwave signals. In MWP, high-bandwidth RF or microwave signals are converted to optical form, processed as optical signals, and reconverted back to microwave form. This cycle is illustrated in Fig. 1.1. For the past few decades, this has enabled the demonstrations of circuits with record functionalities; rapidly reconfigurable, wideband filters [15], wireless communication systems with ultra-high data rates [16], and generation of ultra-stable microwave signals [17] are just some of the breakthroughs achieved through the unique properties of photonics. The next section provides a brief overview of the past and current state of the field of MWP.

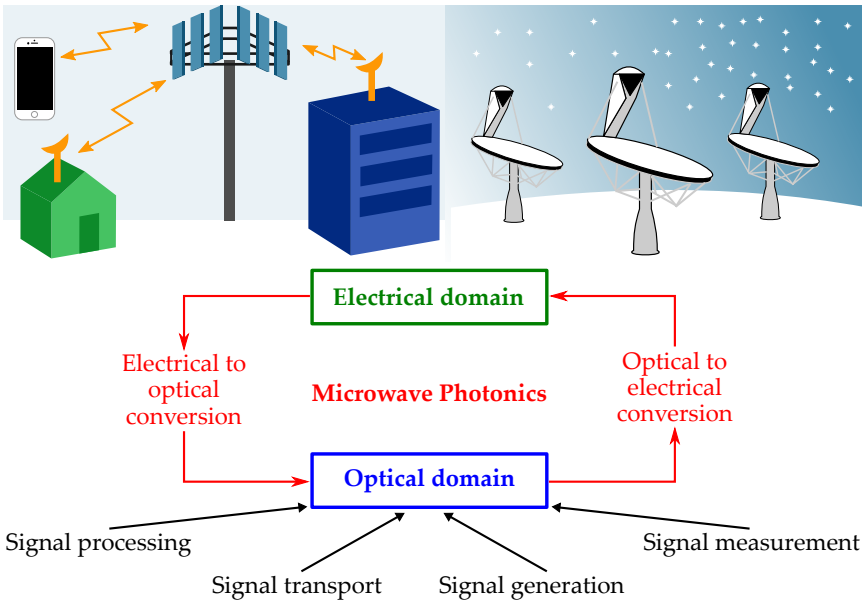

Fig. 1.1. Microwave photonics exploits the power of optics to augment the capacity of RF and microwave systems used in many applications, such as wireless communication and radio astronomy.

1.2.1 *Origins*

The 20th century saw two major advances which changed the way humans communicated. The first was brought about by the use of radio waves for wireless communication. The second progress was a resurge in optical communication, brought about by two scientific breakthroughs which have had a major impact on the world as we know it today. These were the demonstration of the first laser by Maiman in 1960 [18], and the realization of the immense potential of optical fibre for communication, by Kao and Hockham in 1966 [19]. At that time, the most transparent material under consideration as an optical waveguide was optical glass (i.e. silica, SiO_2) with a bulk loss close to 200 dB/km (at an optical wavelength of 1 μm), much too high for any long-distance transmission. It wasn't long however before improvements in fabrication processes pushed this loss to a minimum of 0.2 dB/km (at 1.55 μm wavelength), an incredible improvement over coaxial cables, whose losses varied from tens to hundreds of decibels per kilometre (e.g. 23.2 dB/100 m at 5.8 GHz [20]). These breakthroughs were quickly followed by the invention of devices which could convert electrical signals to optical signals, and vice versa, laying the foundations for the field of MWP.

Initial research activity in MWP was mainly focused towards defence applications. This is understandable since military technology strongly relied on RF technology for communication, navigation, and radar. One of the first applications of optical fibres in this regard was in 1989 in an airborne towed decoy, shown in Fig. 1.2, for protection from radar-guided missiles in military applications [21]. An antenna on the decoy would detect the threat radar (microwave) signal, amplify it, and re-transmit it with a higher power, luring the missile towards the decoy and away from the aircraft. However, size

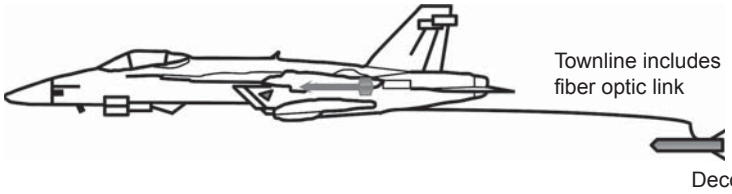

Fig. 1.2. A depiction of an RF towed decoy from an F/A 18. Figure and caption adapted from [21].

and aerodynamic constraints meant that only a limited amount of signal processing could be performed on the decoy itself. For this, a fibre-optic link connected the decoy to the aircraft, where the heavy signal processing equipment was located. In this particular scenario, an additional advantage provided by optical fibres was their considerably lower weight and bulk (31 kg/km compared to 113 kg/km for military-grade fibre-optic and coaxial cables, respectively). The

weight of a fibre-optic link is further reduced by the fact that optical fibres, being dielectrics, are immune to electromagnetic interference (EMI) and thus do not require any electromagnetic shielding, unlike coaxial cables, which are conductors.

MWP however did not remain confined to military applications, and communication providers were quick to see its superiority over coaxial cable for long distance transmission. Two of the first commercial applications of MWP were in the distribution of cable television channels [22] and wireless telephony [23]. This marked the beginning of radio over fibre (RoF) technology, where wireless (i.e. RF and microwave) signals are transmitted, as optical signals, along optical links to facilitate wireless access. The fact that signals could now be easily transferred across long distances meant that the signals received at various base stations could now all be transported to a single central station for processing. This more centralized architecture permitted the relocation of all the processing equipment to the safer, more accessible central station, cutting redundancy and greatly simplifying the base station requirements. As shown in Fig. 1.3, the base station now only had to be equipped with an antenna, and devices for optical/electrical conversion. The received signals could then be sent to a central station, to be processed, switched, and routed. A centralized control station was more desirable also because it enabled dynamic reconfiguration of network resources in accordance with a varying load, making the system more robust and efficient.

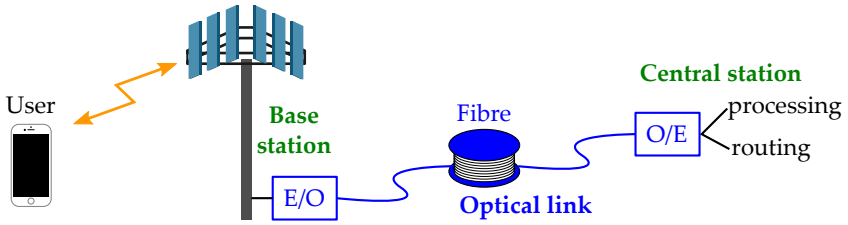

Fig. 1.3. Basic concept of RoF system, where a wireless or microwave signal is detected at the base station, converted to an optical signal and transmitted, through a length of fibre, to a central station for processing.

Soon after the introduction of RoF systems, it became evident that photonics could aid wireless communication systems in more than just signal transportation. In the 1990's wireless systems began transitioning to high-frequency, millimetre wave signals to address the increasing demands for high data-rate communications and the problem of spectral congestion at lower RF frequencies. Electronic oscillators however did not have the power and the performance for generating such high microwave frequencies. MWP research demonstrated how photonic techniques could generate such millimetre wave signals, by heterodyning either two laser sources [24], or the modes of mode-locked lasers [25], thus overcoming the limitations of traditional microwave sources.

Optical fibre was initially conceived simply as a medium for transportation; and in fact, most RoF systems were based on the structure shown in Fig. 1.4(a), where the input RF signal is converted to optical form at the transmitter, recovered at the receiver, and processed as an electrical signal. However, there was another advantage of using light to carry information, which has become increasingly important over time. That was the fact that the frequency of light is orders of magnitude higher than that of electrical signals, so that even the highest frequency, millimetre wave microwave signals used in satellite communication, represent less than 1% of the frequency of the optical carrier used to carry the information along the fibre (typically 193.6 THz). Such small fractional bandwidths mean that optical fibres can be used to transfer information independent of the bit-rate or the protocol being used. This is shown in Fig. 1.5(a) where, unlike coaxial cable, the loss displayed by optical fibres is essentially constant across entire microwave frequency bands.

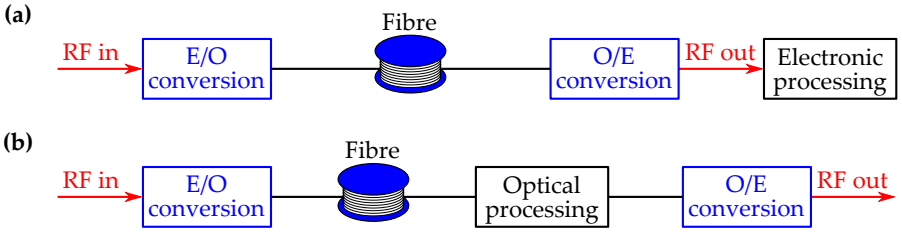

Fig. 1.4. (a) Photonic link where the input RF signal undergoes electrical-to-optical (E/O) conversion simply to take advantage of the low loss and wideband capacity of optical fibre for long-distance transmission. (b) In this photonic link, the signal is processed while in the optical domain, taking advantage of the wideband processing ability enabled by optics.

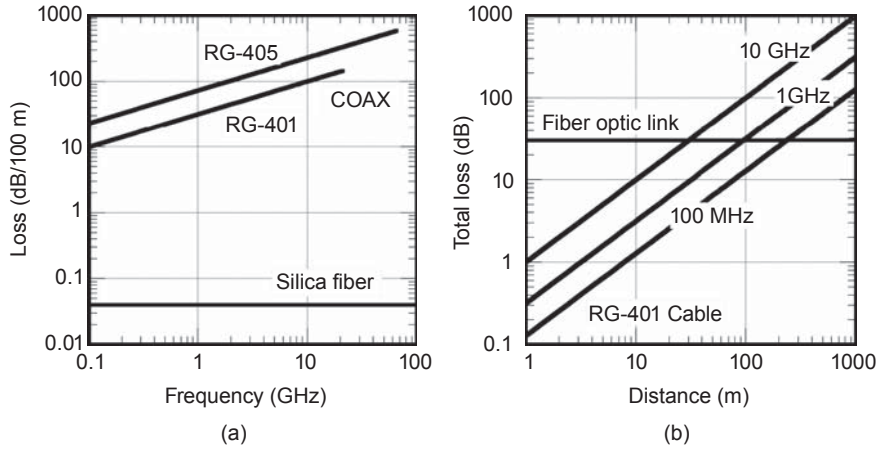

Fig. 1.5. Loss as a function of (a) frequency including only propagation loss in the cable for RG-401, RG-405, and silica fibre and (b) propagation distance for RG-401 at three frequencies. In (b), the fibre optic loss includes a 30 dB fixed loss due to E/O and O/E conversion. Figure and caption adapted from [21].

This fact that optical fibres display frequency-independent loss and dispersion across entire microwave bands, made them a highly attractive platform for signal processing. This realization first took place in 1976, when Wilner and van den Heuvel proposed that processing the microwave signal while it was in the optical domain, travelling along the fibre as in Fig. 1.4(b), could lead to order-of-magnitude improvements in the amount of information able to be processed [26]. Over the following years, this concept was demonstrated through a number of pioneering experiments in 1980's[27–32] and 90's [33–35], in the context of delay and filtering. It was at the turn of the century however, that MWP signal processors became more advanced, by making use of a wider variety of optical components, such as fibre gratings [36]. Since then, the field of MWP signal processing has grown immensely, both in the number of demonstrated functionalities, and in the means used to achieve them [12–14, 37, 38]. These are discussed further in Sec. 1.4.

1.2.2 *Recent Trends*

Today, RF and microwave signals continue to play an important role in many technologies, and our everyday lives us well, as shown by our increasing dependence on wireless connectivity for interactions, work, and leisure. This trend comes at the cost of a growing demand for data and bandwidth, which is constantly pushing the boundaries of current electronic-based technologies. MWP presents a solution that offers the capability for immense data rates, enabled by the ultra-wideband capabilities of photonics transporting and processing signals.

RoF technology is increasingly being used to provide high-speed wireless data services in large, crowded buildings such as shopping malls, hospitals, and stadiums. MWP is also redefining network architectures, to increase wireless infrastructure while driving down power consumption with the use of pico- or femto-cells; these consist of low-cost/low-power remote antenna units which cover small areas, and increase capacity by enabling wireless frequency reuse [39]. This so called cloud radio access network achieves dynamic shared resource allocation, leading to a more efficient and greener network, and has been identified as a key technology for next-generation 5G cellular networks. Other disruptive technologies for meeting the traffic and data-rate expectations of 5G are the implementation of massive multiple-input, multiple-output systems at mobile base stations (i.e. phased arrays for focusing signals) as well as a move away from conventional low-frequency bands to higher frequency millimetre bands. Even in these regards, the RF frequency-transparency of MWP can help [40, 41]. Indeed, a wireless communication system with

100 Gbit/s data rates was demonstrated by using photonics to generate a high-frequency microwave carrier [16].

With regards to MWP signal processing, the current trend now lies towards integration of the various optical components onto a single chip, together with all the driving electronics. Since their inception, MWP circuits have relied on discrete optoelectronic devices, as well as optical fibres and fibre-based components. As such, while achieving higher overall performance compared to their electronic counterparts, they could not compete in terms of size and power consumption. Instead, the use of photonic integrated circuit technology in MWP has the power to lead to enhanced robustness, as well as reductions in size, weight, and power consumption. Moreover, the possibility for large-scale fabrication can significantly reduce the cost of these circuits [42]. Because of their enhanced performance, integrated MWP signal processors have been identified as a promising technology for future radio access networks [39]. However, this field is still in its infancy and current research is focused on pushing the boundaries of what can be achieved using this technology, as well as investigating a suitable material platform which can form the foundation of MWP circuits.

1.3 MICROWAVE PHOTONIC LINKS

MWP links are essentially analog links. Admittedly, the vast majority of communication and signal processing systems nowadays handle information in digital format. Nevertheless, we live in an analog world, and any digital communication system is in fact simply an analog system where each signal is composed of a discrete set of frequencies (or a discrete set of analog signals). On top of this, there are still a number of applications (e.g. phased-array radars, radio astronomy) where pure analog transmission is the only available option, due to the limitations of current ADCs [21]. Therefore, analog MWP systems and their corresponding figures of merit remain relevant to this day. These are considered next.

1.3.1 *Components*

Most MWP systems, whether they are performing some signal processing function, or simply transferring information as in an RoF link, make use of the same basic components, shown in Fig. 1.6. As previously stated, one definition of MWP is the use of optical components and techniques for processing microwave signals. Therefore, the first function performed by most MWP systems is to convert the microwave signal to an optical signal, normally through modulation of a laser source.

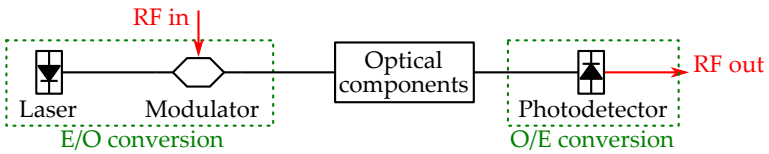

Fig. 1.6. Basic structure of an MWP system, composed of a light source (i.e. laser), a modulator, and a photodetector.

In MWP, the desirable characteristics of the laser used to generate the optical carrier are a high output power with low intensity noise. Laser intensity noise arises mainly due to emissions of spontaneous and stimulated photons in time. The requirement of high output power with low noise is quantified by the laser relative intensity noise (RIN), defined as the variance of the optical power fluctuations, divided by the square of the mean optical power. Distributed feedback (DFB) semiconductor diode lasers satisfy this requirement, and for this they are commonly used in MWP systems. A RIN value of -155 dB/Hz is typical for an unmodulated DFB laser, but values as low as -170 dB/Hz have been reported for a high 180 mW output power [43]. The wavelength of the laser output is, in principle, immaterial to the operation of the MWP system. However, most optical communication systems and components (optical amplifiers in particular) are designed to operate in the C-band (around 1.55 μm), so that the laser is normally selected to operate in this region. Laser diodes have the added benefit of having relatively low threshold currents and high electrical-to-optical conversion efficiencies, compared to other types of lasers, meaning they can be operated at relatively low current levels [44].

Modulation of the laser output can occur in one of two ways. External modulation relies on a separate modulator, as shown in Fig. 1.6, and is the most commonly used in MWP systems today. Alternatively, the earliest MWP systems made use of direct modulation, where the input RF signal is applied to the laser directly, dispensing with the modulator. This is done by superimposing the signal waveform onto a direct current (DC) bias to drive the laser, as shown in Fig. 1.7. The resulting output optical power, ideally, becomes proportional to the input RF signal. The use of direct modulation places additional requirements on the optical source; primary among these are a high slope efficiency (to minimize electrical-to-optical conversion losses), and a linear current-power characteristic (to minimize nonlinear distortions in the conversion process). In practice, the slope efficiency is dependent on the frequency of the input RF signal, exhibiting a low-pass response (due to the photon and free carrier lifetimes in the gain medium). For this, the main drawback of using direct modulation is the limited modulation bandwidth, typically less than 30 GHz [12, 45]. Despite these disadvantages, the simplicity and low cost of

direct modulation systems continues today to fuel research into high-speed sources for MWP photonic applications [46].

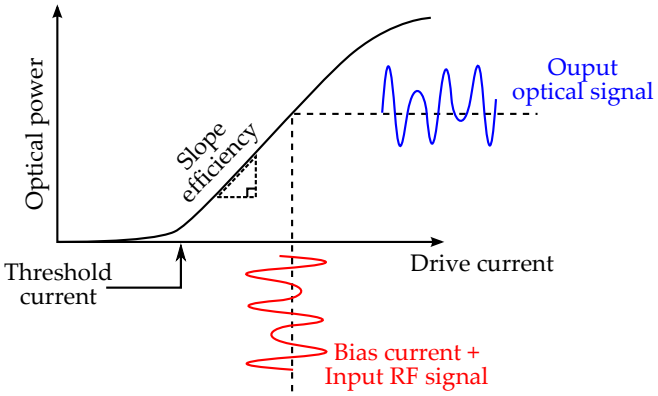

Fig. 1.7. Typical current-power characteristic for a laser diode. Direct modulation of the laser output power is achieved by modulating the drive current.

The most common approach to perform electrical-to-optical conversion is to use external modulation, where a continuous wave (CW) laser is modulated by an electro-optic modulator (EOM). This decoupling of the laser from the modulation process relaxes the requirements on the laser source. Most importantly however, the modulation bandwidth becomes independent from the laser characteristics, solving the main limitation of directly modulated systems. This opens the way for processing high-frequency millimetre wave microwave signals, with modulation bandwidths surpassing 145 GHz having been demonstrated in polymer materials [47]. There are numerous physical mechanisms that can be exploited in materials to achieve optical modulation, including electrooptic, electroabsorption, acoustooptic, and magnetooptic effects. In MWP, the most commonly used technology is crystal $LiNbO_3$. This relies on the Pockel's effect, where the electric field of the input RF signal modulates the phase of the optical carrier. By adding an interferometric structure, such phase modulation can be converted to intensity modulation. This configuration, known as a Mach-Zehnder modulator (MZM), is the most prevalent modulation architecture used in MWP. The transfer characteristic of an MZM, shown in Fig. 1.8, can be expressed as

$$P_o = P_i \frac{1}{2L_{ff}} \left[1 + cos\left(\frac{\pi V_m}{V_\pi} \right) \right] \tag{1.1}$$

where P_o is the output optical power, P_i is the input optical power into the modulator, L_{ff} is the modulator insertion loss, V_m is the driving voltage, composed of a DC bias voltage plus the voltage of the input RF signal, and V_π is a modulator parameter known as the switching voltage. In order to minimize nonlinear distortions in the output optical signal, one should bias the modulator halfway between a minimum and a maximum transmission point, known as quadrature. Desirable characteristics for a modulator are a low V_π across a

wide bandwidth, for maximizing the slope efficiency, and a low insertion loss. These requirements however are actually conflicting: in the common travelling-wave structure, a lower V_π is easily achieved by increasing the electrodes' lengths, but at the expense of a reduction in bandwidth and an increase in insertion loss. Commercially available MZMs exhibit V_π values in the range 3.5–4.5 V, but values as low as 1.33 V at 12 GHz have been reported [48], and more recently 0.45 V at 18 GHz in a III–V MZM operating at 870 nm wavelength [49]. One key aspect of external modulation is that the slope efficiency can also be increased simply by increasing the input optical power into the modulator, as indicated by Eq. (1.1). This revelation has revolutionized system performance and has enabled the realization of MWP links where the input RF signal experienced up to 24 dB net gain without the aid of amplifiers [48].

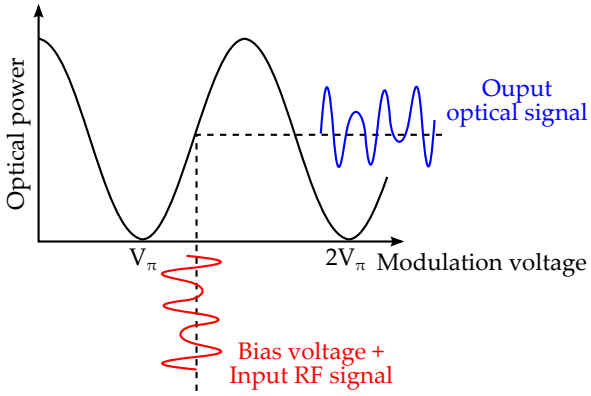

Fig. 1.8. Typical voltage-power characteristic for an MZM. Unlike directly-modulated lasers, which are current-driven, external modulators are voltage-driven.

In MWP, once the optical signal has been processed, it needs to be converted back to the electrical domain. This is done using a photodetector, whose power-current characteristic is shown in Fig. 1.9. These generate an electrical current, $i(t)$, which is directly proportional to their input optical power:

$$i(t) \propto \mathcal{R} \left| E(t) \right|^2 \tag{1.2}$$

where $\mathcal{R}$ is the responsivity, and $E(t)$ is the input optical field. The vast majority of MWP systems to date rely on the P-I-N photodiode structure, where an intrinsic semiconductor layer is sandwiched between p-doped and an n-doped layers. Ideal characteristics for such photodetectors are a high responsivity and bandwidth, but in practice these cannot be achieved simultaneously due to design trade-offs. A notable achievement in this regard was the demonstration of a P-I-N photodetector with 172 GHz bandwidth, and a high 76 GHz bandwidth-efficiency product [50]. It is also desirable for the device to have a highly linear power-current characteristic, in order to avoid

nonlinear distortions. Finally, as shall be seen in Sec. 1.3.3, the link gain of externally modulated MWP systems in general improves by using high optical signal powers, so that photodetectors must also have a high power-handling capability. Uni-travelling carrier photodiodes are an alternative to conventional P-I-N structures, capable of handling high optical powers with large bandwidths and high output electrical power [51]. These have been used to demonstrate MWP links with high 27.8 dB link gain at 6 GHz [52], as well as the generation of high-power microwave signals [53].

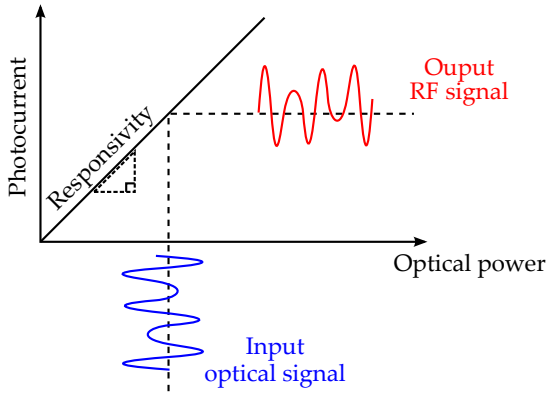

Fig. 1.9. Typical power-current characteristic for a photodiode.

1.3.2 *Modulation Types*

In general, the modulation type in a communication system also determines the detection scheme. The majority of MWP systems use intensity modulation, followed by direct detection, where the only property of the signal which is registered is its intensity. This is in stark contrast to current RF receivers, which are coherent receivers and therefore capable of detecting the signal's amplitude, frequency, and phase [44]. Coherent detection in MWP is possible [54, 55], but it is significantly more complex than direct detection, and for less frequently used. For this, direct detection is the only mechanism considered here.

Most, if not all, modulation schemes in MWP are rooted in external phase modulation. That is, they rely on modulating the phase of the optical carrier. This is also true of intensity modulation, arguably the most common modulation type. The basic structure of an intensity modulator, illustrated in Fig. 1.10(a), is known as an MZM, where a phase modulator is inserted into one arm (or sometimes, both arms) of an interferometer. The electric field fed into the phase modulator is composed of the input RF signal, V_{RF}, and a DC bias voltage, V_b. The spectrum of the optical signal at the output of the modulator is shown in Fig. 1.10(b), comprising the optical carrier, and two modulation sidebands which are exact copies of the input RF signal spectrum.

In intensity modulation, the optical carrier is in phase with the two sidebands. The ratio between the carrier and the sidebands' powers can be controlled by adjusting the DC bias voltage. For example, setting $V_b = V_\pi$ causes the carrier to be suppressed at the output, while $V_b = 2V_\pi$ results in the maximum carrier output power. The nonlinearity of the modulator transfer function, shown in Fig. 1.8, causes the generation of higher-order sidebands, at the harmonics of the first-order sideband. In signal transmission systems (e.g. RoF) this effect is usually undesired, and can be minimized by biasing the modulator at quadrature, i.e. $V_b = V_\pi/2$. There are however applications, particularly in signal processing, where higher-order sideband generation is desirable for making frequency combs [56, 57], and a different modulator bias point may be selected accordingly.

Fig. 1.10. (a) Structure of an intensity modulator; PM: phase modulator. (b) Optical spectrum of an intensity-modulated signal, comprising a carrier and two modulation sidebands in phase.

The simplest type of modulation is pure phase modulation, achieved by using a phase modulator as shown in Fig. 1.11(a). One advantage of this scheme is that no DC bias voltage is required, which solves the bias-drift problem inherent to intensity modulators, making the modulated optical signal more stable [58]. The optical spectrum of a phase-modulated signal, shown in Fig. 1.11(a) consists of the optical carrier and two sidebands. However, unlike intensity modulation, the optical sidebands are 180° out of phase. This is the reason why direct detection of a phase-modulated signal yields no RF output: the mixing products of the sidebands with the optical carrier interfere destructively. Because of this, frequency discrimination is necessary in phase-modulated direct detection links [59]. Nevertheless, the unique features of this scheme have made it attractive in a number of MWP signal processors, including filters [60]. An alternative class of phase modulators which has gained attention in MWP signal processing are known as polarization modulators [61]. These modulators are based on the photoelastic effect; they generate a phase-modulated signal where the two sidebands, as well as being out of phase, also have orthogonal polarization states.

The main problem with both intensity and phase modulation schemes is that, when the modulated signal propagates through a dispersive element (such as a long length of fibre), dispersion breaks the phase relationship between the modulation sidebands. This is a problem especially in applications that rely on signal distribution of intensity-modulated signals; at some RF signal frequencies, the modulation

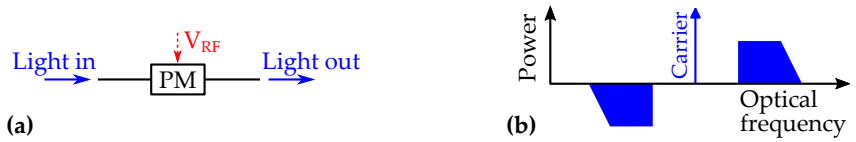

Fig. 1.11. (a) Structure of an phase modulator; PM: phase modulator. (b) Optical spectrum of a phase-modulated signal, comprising a carrier and two modulation sidebands in antiphase.

sidebands will have an antiphase relationship (i.e. they will appear to have been phase-modulated), so that the mixing products at the photodetector will cancel out, giving a null output at those particular signal frequencies. This problem, known as dispersion-induced fading, can be solved by making use of single sideband (SSB) modulation, where the modulated signal is composed of the optical carrier and a single sideband, as shown in Fig. 1.12(a). In this way, dispersive effects change the phase relationship between the carrier and modulation sideband, but at the photodetector, only one mixing product is generated, and its power remains constant. For this reason, and due to its higher spectral efficiency, SSB modulation is commonly employed in RoF systems. Moreover, SSB modulation is also useful for signal processing techniques, such as optical carrier processing (see Sec. 4.2.2). SSB modulation can be achieved by using dual-drive or dual-parallel MZMs (see Sec. 3.3), where the RF signal is fed to the modulator through a 90° RF hybrid coupler. An alternative technique is to send the output of a phase modulator to an optical bandstop filter, where one of the modulation sidebands can be removed.

Fig. 1.12. Optical spectrum of (a) an SSB-modulated signal. (b) a signal modulated with a complex modulation type, where the amplitude and phases of the carrier and sidebands can be independently adjusted.

A number of recent works [62, 63], have highlighted the importance of using more complex modulation schemes, where the amplitude and phase of carrier and of the modulation sidebands can be independently controlled. Such a scheme, illustrated in Fig. 1.12(b), is ideal for signal processing applications such as phase shifting and filtering. In MWP, signal processors work mainly by processing the amplitude and phase of the optical modulated signal. Therefore, the ability to tailor the amplitude and phase of each individual spectrum component enables the realization of powerful multi-purpose signal processors. Techniques for synthesizing such modulation spectra are discussed further in Chapter 3.

1.3.3 *Figures of Merit*

Determination of the level of performance of an MWP link or signal processor is largely dependent on its functionality. Nevertheless, there are a number of general figures of merit which can be used for assessing the performance of most MWP systems. These are the link gain, the noise figure, and the spurious-free dynamic range (SFDR). What follows lays the foundations for understanding both link gain and noise figure, which are of interest in this work. Excellent in-depth derivations of all figure of merits can be found in [21, 44].

The link gain, g_{link}, is the ratio of the output RF signal power delivered to the load (with real impedance R_L), and the input RF signal power available at the source (with real impedance R_S):

$$g_{\text{link}}(\Omega) = \frac{P_{\text{RF,out}}(\Omega)}{P_{\text{RF,in}}(\Omega)} \tag{1.3}$$

where Ω is the frequency of the RF signal. The link gain is clearly frequency-dependent, and is determined by the frequency response of the optical and electrical components which make up the MWP link. In practice, one wants to maximize the link gain, and avoid power loss of the RF signal being transported or processed. A good intuition for achieving this can be gained by considering the basic MWP link from Fig. 1.6. Assuming the modulator is an MZM, the link gain is given by [64]

$$g_{\text{link}} = \left(\frac{\pi \mathcal{R} R_L P_i \sin \phi_b}{2 L V_{\pi,\text{RF}}} \right)^2 \tag{1.4}$$

where

$$\phi_b = \frac{\pi V_B}{V_{\pi,\text{DC}}}$$

is the bias angle of the MZM. The switching voltage of the modulator from Eq. (1.1) does in fact depend on the frequency of the driving RF signal; to take this into account, this parameter is usually split into the DC switching voltage, $V_{\pi,\text{DC}}$, and the RF switching voltage $V_{\pi,\text{RF}}$, at a given frequency Ω. V_B is the DC bias voltage to the modulator, and L takes into account the modulator insertion loss L_{ff} as well as other optical losses which affect both carrier and sidebands as they travel towards the photodetector. This expression is valid provided that the input RF driving voltage is considerably smaller than $V_{\pi,\text{RF}}$.

Equation (1.4) reveals a number of important features about the link gain of an MWP system. One such feature, proprietary to the modulator used being an MZM, is that the link gain increases when this is biased at quadrature, where $\phi_b = \pi/2$. Of more relevance to this work however are the more general features, which hold true even when the modulator is not an MZM. These are that the link gain increases

with the responsivity of the photodetector, and that the link gain is highly sensitive to both the optical power launched into the modulator, as well as to the optical losses present in the link. The reason for this square relationship between optical losses and link gain is that, broadband optical losses which affect both carrier and sidebands (e.g. fibre propagation losses) are squared at the photodetector, where the carrier and the sidebands mix with each other. As such, the link gain of an MWP system is extremely sensitive to optical losses, and values for g_{link} ranging from -20 to -40 dB are not uncommon. A similar argument can be used for the optical input power into the modulator.

The second figure of merit of interest to this work is the noise figure, NF, defined as

$$\text{NF} = 10\log_{10}\left(\frac{\text{SNR}_{\text{in}}}{\text{SNR}_{\text{out}}}\right). \tag{1.5}$$

That is, the noise figure is the deterioration in the signal-to-noise ratio (SNR) of the RF signal at the input, compared to the output, of the MWP link. This definition suggests that there are two variables which affect the noise figure: the loss in signal power along the MWP link (quantified by the link gain g_{link} at that particular signal's frequency), and the noise added to the signal along the link. The main sources of noise in MWP links are thermal noise, shot noise, and RIN. Thermal noise is due to thermally induced, random movements of charge carriers in conductors. Shot noise is generated at the photodetector due to the random arrival of photons which generate random fluctuations in the detected photocurrent. RIN arises from random emissions of spontaneous and stimulated photons in the gain medium of the laser. Optical amplifiers, present in most laboratory setups, constitute an additional noise source due to amplified spontaneous emission (ASE), which often dominates over other noise sources. The noise figure can be expressed in terms of link parameters [64]

$$\text{NF} = 10\log_{10}\left(\frac{p_N}{g_{\text{link}}kTB}\right) \tag{1.6}$$

where p_N is the total noise power, k is Boltzmann's constant, T is the absolute temperature, and B is the bandwidth across which the noise and signal powers are being measured.

It can be shown that, even in the ideal case of a lossless link ($g_{\text{link}} = 1$) and when noise sources such as RIN and ASE are negligible, the minimum noise figure of an MWP link is 3 dB [64]. This is due the unavoidable thermal noise generated in the ohmic components in the circuits of the modulator and photodetector. The current record for the lowest noise figure is 3.2 dB at a signal frequency of 2 GHz [65]. In general however, noise figure values as high as 30 dB are considered typical in MWP systems. In most cases, the main reason for such high noise figure values is not so much the large amounts of noise, but the high losses experienced by the RF signal as it is processed by

the link [66]. Therefore, the most effective way to reduce the noise figure in practice is to increase the link gain without increasing noise sources [64]. This can be achieved, for instance, by minimizing the signal losses (particularly optical losses) and by using a modulator with a low $V_{\pi,\mathrm{RF}}$.

1.4 MICROWAVE PHOTONIC SIGNAL PROCESSING

Today, RoF systems are driving most of the applications of MWP to the real world [67]. An added benefit of transporting RF signals in optical form is the wide range of signal processing functionalities made possible through the wideband capacities of photonics [37]. MWP signal processing is a thriving area of research, and over the years has led to the demonstration of a large number of functionalities, some of which are very complex or not even possible to implement directly using electronics [13]. What follows is a brief overview of some of the most important breakthroughs in this field.

1.4.1 *Filtering*

RF and microwave filters are ubiquitous components, used in all communication systems. The function of filters is to suppress all frequencies that fall in the stopband while transmitting all frequencies within the passband. The most commonly used filters in microwave systems are bandpass and bandstop filters. Bandpass filters are frequently used to select required channels, while bandstop filters work to remove unwanted frequencies such as interferers. A desirable characteristic for these filters is the ability to tune the centre frequency of the passband or stopband across wide, gigahertz frequency bands, without compromising the filter performance. Such tunability is extremely difficult to achieve with electronics, but readily achievable in photonics [68, 69].

The most popular architecture for implementing MWP filters relies on the same principle as discrete-time signal processors. The operational principle for such filters is shown in Fig. 1.13(a). Initially, the input RF signal to be filtered is converted to an optical signal through modulation. Multiple copies (taps) of the optical signal are then delayed, weighed, and recombined at the photodetector. The resulting RF transfer function $H(\Omega)$ is given by

$$H(\Omega) = \sum_{n=0}^{N-1} h(n) e^{-jn\Omega T} \tag{1.7}$$

where Ω is the RF signal frequency, N is the number of taps, $h(n)$ is the complex coefficient (i.e. amplitude and phase) of the n^{th} tap, and T is the time delay between successive taps. By controlling the number of taps, the time delay between the taps, and their amplitude,

it is possible to configure the response of the system to implement a vast number of functionalities. In fact, the main advantage of this filter architecture is that it allows reconfiguration of the filter response [70], enabling the realization, theoretically, of any filter shape desired.

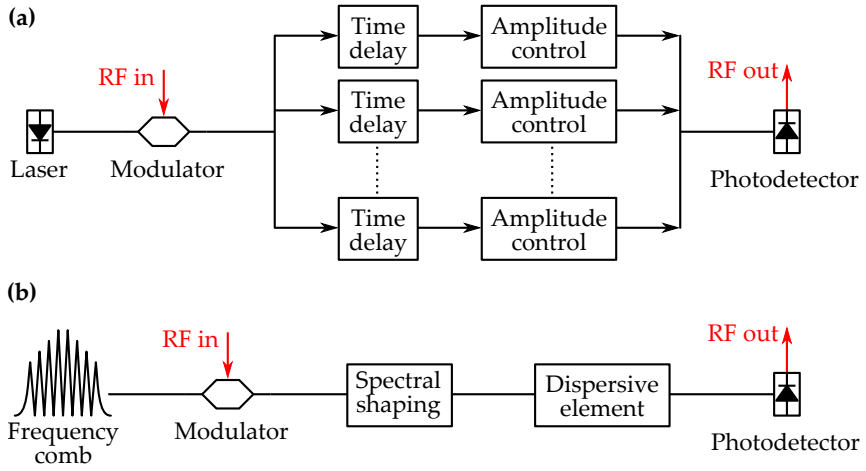

Fig. 1.13. (a) Basic principle and (b) typical structure of incoherent MWP filters.

In order to maintain a stable filter response in the presence of environmental fluctuations, these filters are operated in the incoherent regime, to avoid optical interference when the taps are recombined at the photodetector. For this reason, such filters are known as *incoherent* filters [68]. The typical structure of such incoherent filters is shown in Fig. 1.13(b). In general, the taps are generated by modulation of a frequency comb [15], a broadband light source [71], or a laser array [72]. A dispersive element can then be used to introduce a differential delay between the taps. The dispersive element has been implemented using bulky components, such as lengths of fibres, but also with a highly compact photonic crystal delay line [72]. When operating in the incoherent regime, all taps have positive coefficients. However, generation of taps with complex coefficients is desirable to achieve a more flexible filter response, tunable in frequency without alteration of the filter characteristics [70]. Such complex-coefficient filters have been implemented using MZMs [73], polarization modulators [74], non-uniformly tap delays [75], and Fourier-domain optical processor (FD-OP)s [76, 77].

One significant limitation of incoherent filters, observable from Eq. (1.7), is that their response is periodic, the period or free spectral range (FSR), being equal to $1/T$. This FSR, clearly visible in Fig. 1.14, is normally less than 10 GHz, and limits the bandwidth of the analog signals which can be processed by the filter. While solutions to this problem have been proposed, such as by using electronic filters to select one single filter period [78] or by using multi-wavelength

taps (i.e. a continuous-time impulse response) [79–81], these are not faultless and often further complicate the filter implementation, ultimately limiting the frequency tuning range of the filter response. Since frequency tunability is the main motivation behind MWP filters, this represents a significant drawback of multi-tap filters.

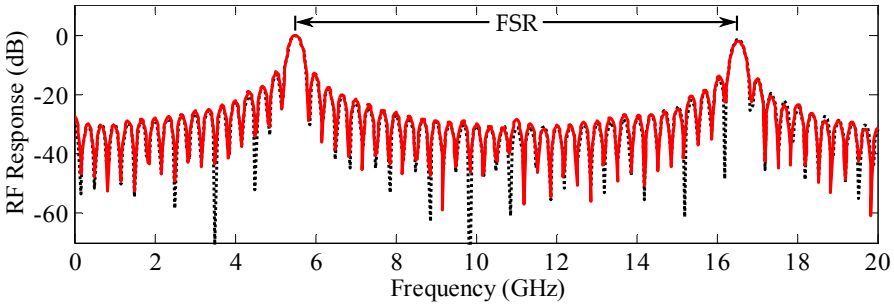

Fig. 1.14. Measured and calculated (dotted) MWP filter response. Figure adapted from [77].

Coherent MWP filters rely on a different architecture from their incoherent counterparts, shown in Fig. 1.15, where the modulated optical signal is sent through one or more optical filters. The optical filter then affects the modulation sidebands so that, after photodetection, the desired filter response is achieved. This filter architecture, as well as being considerably simpler and requiring fewer components than multi-tap architectures, can also be used to solve the periodic response problem. One of the earliest implementations relied on using two Fabry-Perot resonators as the optical filters [82]. A significantly different technique relies on phase modulation and a Bragg grating [60] or a ring resonator [83], to obtain phase-to-intensity modulation conversion within the grating resonance, and obtain a bandpass response. This phase modulation approach has become particularly popular for implementing narrowband bandstop, or notch, MWP filters, and is discussed in more detail in Chapter 3. While the filter architecture from Fig. 1.15 can be used to implement wideband tunable MWP filters, its performance is highly dependent on the characteristic of the optical filter employed. Unfortunately, optical filters display relatively wide resonances, of the order of hundreds of megahertz, or even gigahertz, and the corresponding MWP filter response suffers from a low selectivity and exceedingly broad response. A solution to this problem, discussed in Sec. 1.4.3, is to rely on optical nonlinearities such as stimulated Brillouin scattering.

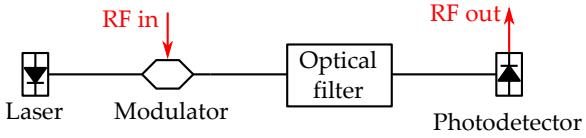

Fig. 1.15. Structure of a coherent MWP filter.

1.4.2 *Time Delay and Phase Shifting*

Time delay and phase shifting are essential functionalities in signal processing (e.g. as in multi-tap filters) and in phase-array antennas for beamforming. These find applications in radar, but also in Wi-Fi wireless technology, where beamforming can enable dramatic improvements in terms of performance, reliability, coverage, and range. Soon after their inception, optical fibres were recognized as far superior delay lines than RF coaxial cables, mainly because they enabled large delays with low losses (0.04 dB/μs). The use of long fibre lengths for time delay is possible but not ideal due to the bulk of such long spools; a more elegant solution relies on using a recirculating delay line architecture, where the optical signal continuously travels around a loop [84]. While being well-suited for optical memory and buffering, such architectures are not ideal for beamforming applications, where the ability to quickly tune the delay is essential. Tunable time delay in this context has been demonstrated through slow light in photonic crystal fibres [85], gratings [86], switched fibre arrays [87], and free-space techniques [88]. A recent promising demonstration uses a new method called complementary phase-shifted spectra (CPSS) to mimic the characteristics of true time delay [89]. It relies on a delay interferometer in combination with a phase modulator, offering the potential for full integration, as well achieving continuously tunable delay with picosecond settling time, which is important for fast beam-steering.

1.4.3 *Role of Optical Nonlinearities*

Since their origin, MWP signal processors have largely relied on using linear effects, such as delay and dispersion, and linear devices, such as optical couplers, fibre Bragg gratings, and MZMs biased for linear operation. In the context of MWP, it is desirable to process the input signal without adding nonlinear distortions to the resulting output signal. Such distortions are referred to as *RF nonlinearities* because their parasitic effects are manifested in the electrical domain. In most MWP links, these nonlinearities arise due to the nonlinear response of the various link components, especially the modulator and photodetector. There is another type of nonlinearities, known as *optical nonlinearities*, which arise from the nonlinear interaction of the optical fields with the molecules of the transmission medium. Optical nonlinearities, upon photodetection, can generate RF nonlinearities, and for this they have largely been seen as undesirable. However, when properly managed, nonlinear optical effects present unique features, which make them highly attractive for realizing signal processing functionalities inaccessible in the linear regime [90]. In this work, the role of optical nonlinearities is to enhance signal processing without introducing additional RF nonlinearities in the electrical domain.

Excitation of nonlinear effects normally involves launching a high-power light beam, known as the *pump*, into the medium (e.g. fibre). The nonlinear response of the medium can then be used to affect, or process, the optical carrier or the modulation sidebands which make up the signal. Nonlinear optical effects manifest themselves in a vast array of physical phenomena, and exhibit a wide range of properties. However, two optical nonlinearities are predominantly used in MWP systems. These are stimulated Brillouin scattering and four-wave mixing.

Stimulated Brillouin scattering (SBS) is the strongest nonlinearity in optical fibres and the easiest to excite, normally requiring pump powers of a few milliwatts. It arises from the interaction of light with acoustic phonons in the medium, and it results in a gain resonance being induced at a Stokes frequency (i.e. a frequency down-shifted from that of the pump). One essential feature of SBS is that, owing to the relatively long lifetime of acoustic phonons, the linewidth of its gain resonance is very small, of the order of 30 MHz in silica fibres. The narrow linewidth of SBS has proven important in a wide number of MWP applications, beginning in 1997 with the use of SBS in an optoelectronic oscillator for the generation of microwave signals [91], and soon after for frequency multiplication [92] and signal amplification [93]. SBS is also an ideal mechanism for optical carrier processing (see Sec. 4.2.2), which has been effectively used implementing phase shifters [94, 95], complex-coefficient incoherent filters [96, 97], and separate carrier tuning [98–100], which finds applications in reconfigurable filters and phased array antennas. Finally, perhaps the most natural application of SBS is in MWP filtering. A vast range of MWP filters have been demonstrated, with different specifications such as bandpass with narrow passbands [101–104], wide passband [105, 106], and notch [63, 103, 107]. More recently however, there is a strong push to harness the SBS interaction in shorter, integrated platforms, instead of kilometres of fibre [108].

Another prevalent optical nonlinearity, four-wave mixing (FWM) occurs due to the distortions in the electron cloud surrounding the molecules of the medium, as the light field passes through it. This distinction in the mechanism used for sourcing the nonlinearity causes FWM and SBS to exhibit entirely different behaviours, particularly regarding the time scales required to build up the interaction; whereas SBS is a slow process, occurring over nanoseconds, FWM is considered an ultrafast process, as it can occur over femtosecond periods. It is this property of FWM that has placed it at the centre of research into ultrafast optical signal processing for the past two decades, with applications to parametric amplifiers, wavelength conversion, signal regeneration, and switching [109]. FWM also has a long history in MWP, where its mixer-effect can be used to augment the number of taps in multi-tap filters, improving the filter response [15, 110, 111].

FWM has also found utility in a wide range of applications such as frequency multiplication [112–114], arbitrary waveform generation [115], channelized RF receivers [116], and instantaneous frequency measurement [117–120]. Recently FWM has been used to eliminate distortions in a phase-modulated MWP link, with demonstration of a 19 dB improvement in the link SFDR at 1 Hz frequency [121]. This demonstration highlights the feasibility of optical nonlinearities, not only for enhanced signal processing, but also for maintaining the signal linearity, which is essential when processing analog signals.

1.5 INTEGRATED MICROWAVE PHOTONICS

While research into MWP signal processing has been active for the past four decades, its application to real-world systems has gathered serious attention only in the past couple of years. The main obstacle in this regard was the fact that the vast majority of MWP systems demonstrated to date relied on discrete components, occupying large volumes, suffering from reduced reliability due to the various interconnections, and requiring high costs for packaging. This situation is somewhat reminiscent of electronics in the early twentieth century. Electronic circuits became truly viable only after the creation of components capable of being integrated onto a single chip (e.g. solid-state transistors). This ability greatly reduced production costs, improved performance, and enabled the realization of more complex architectures capable of more powerful functionalities.

In the same way, integration of MWP circuits is the key to bringing these technologies closer to commercialization [42, 122]. First of all, photonic integrated circuits require significantly less packaging; this fact, together with the possibility for large scale production would significantly drive down manufacturing costs. Secondly, the possibility of integrating all circuit elements onto a single chip would reduce inter-component coupling losses, which is of utmost importance for increasing the system link gain as well as achieving a more energy-efficient circuit. Moreover, the inherently low size and weight benefits integrated MWP circuits would make them more attractive in a vast range of applications, such as in defence and aviation. All these benefits would be additional to the wideband processing capabilities of MWP circuits.

The roadmap towards integration of MWP circuits is not fully aligned with current mainstream research in photonic integrated circuit technology [123, 124], which caters mainly for digital communication. In this last field, signal fidelity is compromised to maximize processing speed, component counts, and the number of functionalities on a single chip. This trend, while acceptable for digital applications, is not suited to analog processors like in MWP, where preserving the signal quality (e.g. by minimizing losses, noise figure, and distortions) is

paramount. In this context, the more stringent requirement of MWP circuits highlight the importance for selection of a material platform capable of supporting the required functionality (e.g. nonlinear effects, light generation, light detection), but also of meeting the needs of MWP processors, particularly for low loss. Next we discuss some of the more popular technologies which have been recently used to demonstrated MWP systems, and how these technologies meet the required criteria.

1.5.1 *Indium Phosphide*

Indium phosphide (InP) is attractive due its inherent support of active functionalities such as light generation, modulation, amplification, and detection, meaning it has the potential for monolithic integration of a complete MWP link. Various MWP functionalities [124] have been demonstrated in this platform, such as phase/amplitude control of microwave signals for phased-array antennas [125], programmable filters [126, 127] and frequency measurement systems [128] using ring resonator structures, optical phase-locked loops for coherent detection schemes [129], and a frequency discriminator for phase-to-intensity modulation conversion, including optical detectors [130]. The main limitation of InP comes from its high propagation loss, in the range of 1–2 dB/cm. This can be compensated with active components such as semiconductor optical amplifiers, but at the expense of further deterioration of the noise figure.

1.5.2 *Silica*

Silica planar lightwave circuits (PLCs) are popular due to their low propagation loss ($<$ 1 dB/m), low cost, and compatibility with manufacturing processes used for silicon integrated circuits [131]. These properties make this a suitable platform for tunable delay lines [132], with applications to beamforming [133, 134], but other functionalities have also been demonstrated, such as frequency discrimination [135] and arbitrary waveform generation [136]. The main limitation of silica comes from its relatively low refractive index, which in turn leads to a low core-cladding index contrast. Because of this, silica waveguides typically have large micrometre mode areas and large millimetre bending radii, resulting in large chip sizes. More compact circuits can be realized with Hydex, a doped silica with a higher 1.5–1.9 refractive index. Due to its moderate nonlinearity (five times higher than for pure silica) and negligible nonlinear loss, Hydex is also a suitable platform for nonlinear optics [137], and has been used to demonstrate an all-optical RF spectrum analyzer based on cross-phase modulation [138].

1.5.3 *Silicon*

Silicon is a highly attractive and thriving platform, widely available and compatible with mature complementary metal-oxide semiconductor (CMOS) technology, opening the possibility for seamless integration of both optical and electronic components onto the same chip. The silicon on insulator (SOI) platform is the most common fabrication approach, where the functional silicon elements are situated on top of an insulator, typically made from SiO_2. Silicon's high refractive index ($n = 3.45$) compared to silica ($n = 1.45$) enables strong optical confinement in small waveguides, leading to more compact circuits. There are two main types of SOI waveguides used in MWP. Rib waveguides have large core areas, with widths ranging from 1–8 μm, which allow them to exhibit relatively low 0.1–0.5 dB/cm propagation losses, but with a large bending radius of hundreds of micrometers [139, 140]. SOI rib waveguides have been extensively used in MWP to demonstrate delay lines [140–142] and filters using passive components, such as Mach-Zehnder interferometers and ring resonators [143–147], as shown in Fig. 1.16. Another type of common SOI waveguides has a strip geometry, with width dimensions ranging from 0.3 to 1.5 μm and heights of 0.2 to 1.5 μm. These silicon *nanowires* can achieve considerably smaller bending radii, at the cost of higher 1–3 dB/cm propagation losses. As well as more compact circuits, one of the reasons for reducing waveguide dimensions is the possibility of efficiently exploiting silicon's large nonlinearity [148]. Indeed, FWM in a silicon nanowire was used to demonstrate a reconfigurable MWP filter [111], and two-photon absorption for ultrawideband (UWB) signal generation [149]. Nevertheless, silicon's high nonlinear loss (see Sec. 2.3.2) represents a major limitation to its widespread use in MWP.

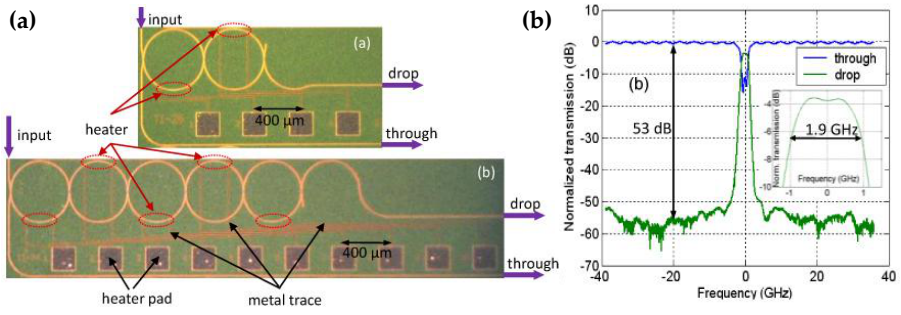

Fig. 1.16. (a) Optical images of fully fabricated second (top) and fifth (bottom) -order SOI ring filters. (b) Transmission spectrum for the fifth-order ring filter after optimization of the heating power. Figure and caption adapted from [145].

1.5.4 *Silicon Nitride*

Silicon nitride (Si_3N_4) is a mature technology for MWP that has led to the implementation of a wide array of functionalities [150]. Its appeal stems from its ultralow loss (0.045 dB/m at 1.58 μm, which is a record for a planar waveguide [151]) and its compatibility with CMOS fabrication processes. Different waveguide geometries have been realized, shown in Fig. 1.17, with different characteristics to best suit a number of applications. The box-shaped geometry (Fig. 1.17, left), offers low polarization birefringence due to its symmetrical layout [152]. A large library of standard optical components is available in this geometry, which has been used to fabricate programmable optical beamformers [153–156] and frequency discriminators for phase-modulated MWP links [157]. The double-stripe geometry (Fig. 1.17, centre) is standardized for MWP applications due to its tight bending radii and low propagation losses at 1.55 μm, and has enabled the realization of MWP filters with sub-1 cm^2 footprints [158]. The single-stripe geometry (Fig. 1.17, right), boasts the lowest propagation losses, and is thus best suited to making delay lines [151]. Silicon nitride has recently gained attention as a suitable platform for nonlinear optics, due to its negligible nonlinear losses, its transparency across a broad wavelength range (from 0.405 to 2.35 nm), and its moderate nonlinearity (ten times that of silica) [137].

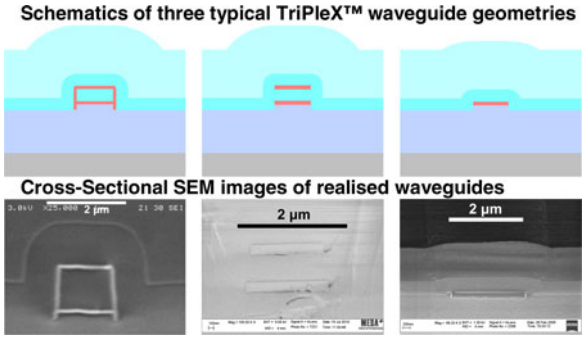

Fig. 1.17. Schematics (top row) and corresponding scanning electron microscope images of realized Si_3N_4/SiO_2 structures (bottom row) of three typical single-mode channel layouts–a symmetrical, box-shaped layout with minimal modal birefringence (left), and two asymmetrical layouts with large modal birefringence: the double-stripe layout (centre) and the single-stripe layout (right). Figure and caption adapted from [159].

1.5.5 *Chalcogenide*

Chalcogenides, and As_2S_3 in particular, have recently found widespread use in MWP signal processors [160] due to their excellent nonlinear characteristics (100 times stronger than silica), with negligible nonlinear loss [161]. In particular, chalcogenide is currently the only plat-

form capable of supporting strong SBS interactions in a chip-scale length. This ability has led to the demonstration of SBS-based tunable bandpass filters [162], narrowband notch filters [163, 164], wideband phase shifters [165], and microwave sources [166]. Currently, the most commonly used chalcogenide waveguides have a rib geometry with 2–4 μm widths, and a low 0.3 dB/cm propagation loss.

1.6 SCOPE OF THIS THESIS

Nonlinear optical effects provide a range of useful functionalities which simply cannot be achieved with linear optical devices. However, access to these functions requires high optical powers, in order to excite the desired nonlinear interactions. To alleviate these high-power requirements, MWP signal processors rely on hundreds of meters, or even kilometres, of fibre lengths to stimulate the desired nonlinear interactions. As previously stated, the use of long fibre spools is not desirable, as it increases the instabilities and bulkiness of the system. Real-world applications would greatly benefit from having the nonlinear interaction occur in a short, sub-centimetre, integrated platform. This would constitute the first step towards achieving a fully-integrated MWP signal processor.

The requirements for applications in MWP, particularly for analog signal processing, are very different from those in high-capacity optical communication systems, where the bulk of nonlinear optics research is currently focused. In MWP, the signal content is normally contained in a frequency range spanning a few tens of gigahertz; as such, nonlinear interactions only need occur over a couple nanometres of bandwidth. This greatly eases the phase matching requirements which are needed for efficient nonlinear interactions. On the other hand nonlinear interactions in MWP are hindered by the fact that most MWP systems rely on interactions between CW fields (i.e. CW carriers and pumps). This places a limit on the available power (either because of the source or because of parasitic SBS), which in turn limits the strength of the interaction. Moreover, CW fields are highly susceptible to the effects of nonlinear loss, such as free-carrier absorption (FCA) in silicon, which greatly reduces the efficiency of the nonlinearity as well as deteriorating the link gain. Therefore, MWP processors require careful design of the nonlinear platform, as well as clever manipulation of the interacting fields, so as to fully exploit the effect of the nonlinearity with minimum power requirements.

This thesis presents the use of on-chip nonlinear interactions for achieving a number of MWP signal processing functions.

Chapter 2 provides a background for understanding the origin of optical nonlinearities. Three nonlinear optical effects are considered in detail in the context of MWP: nonlinear absorption, four-wave mixing, and stimulated Brillouin scattering.

Chapter 3 deals with implementing narrowband MWP notch filters through the use of on-chip SBS. There are two main architectures that are utilized for implementing MWP notch filters. The first relies on the use of optical notch filters, while the second relies on clever manipulation of the modulation sidebands to obtain destructive interference in the filter stopband. It is shown that the second approach, while more complicated, achieves significantly better performance (in terms of suppression and narrow bandwidth) with orders-of-magnitude lower SBS pump power. This is of utmost importance when the SBS interaction occurs on-chip, where power handling is of concern, and where a different factors ultimately limit the strength of the SBS process. The properties of the filter: suppression, frequency tuning, bandwidth tuning, insertion loss, and stability are also studied in detail.

Chapter 4 presents the use of SBS as an effective tool for performing optical carrier processing, with emphasis on its applications to phase shifting. Two different MWP phase shifter architectures are presented. The first utilizes an SBS pump configuration first introduced in 2006, where SBS gain and loss resonances are simultaneously harnessed on-chip and induced on an optical carrier. This results in a tunable phase-shifter with low power fluctuations. The technique for tuning the phase shift is altered from previous demonstrations, making it more energy-efficient and thus more suited to on-chip operation. The insertion loss of the phase shifter is also studied in detail. The second phase shifter architecture utilizes a new SBS pump configuration, and achieves a large tunable phase shift with record-low output power fluctuations, over an ultrawide bandwidth.

Chapter 5 presents the use of on-chip FWM for doing instantaneous frequency measurement. Two architectures for performing instantaneous frequency measurement are discussed, one relying on power-fading effects, the other on interferometry. It is shown that interferometric approaches have an advantage in that their response can be easily reconfigured to alter their characteristics. It is shown that FWM is highly effective in implementing an interferometric system capable of extremely high microwave frequency measurements, and that its performance is directly related to the power of the generated mixing idlers. It is for this reason that the integrated platform used as the mixing medium is chosen to be a long, thick silicon waveguide, capable of supporting high optical powers with low propagation losses, and modest nonlinearity. The instantaneous frequency measurement system implemented using this platform is shown to achieve record-low measurement error over an ultrawide bandwidth. The chapter concludes by providing a detailed plan of how the whole system could be monolithically integrated onto a silicon chip.

Chapter 6 provides a summary of the work presented in the previous chapters, and discusses future directions for building on these results.

2

NONLINEAR OPTICS FOR MICROWAVE PHOTONICS

2.1 INTRODUCTION

Optics is a branch in physics which deals with the properties and behaviour of light. By light here we mean electromagnetic waves whose wavelengths fall into one of three regions: infrared (0.76 to 300 μm), visible (390 to 760 nm), or ultraviolet (10 to 390 nm). *Photonics* is a branch within optics which deals with the control of photons (i.e. packets of light energy), just like *electronics* deals with the control of charges; except that photons behave very differently to charges. Charges can affect each other (e.g. like charges repel), while photons simply do not interact with other photons. They do however interact with matter.

As an example, one can consider the scenario illustrated in Fig. 2.1(a). One light beam $x_1(t)$ is sent into a medium; it interacts with the medium, and leaves it as a light beam $y_1(t)$ which is most likely weaker due to energy loss. The same process can be repeated with a different light beam $x_2(t)$, with the output beam labelled $y_2(t)$. The interesting question now is, what happens when both light beams are launched into the medium simultaneously? The vast majority of the times, if the input is a superposition of both beams, $x_1(t) + x_2(t)$, the output is simply a superposition of the original output beams $y_1(t) + y_2(t)$, shown in Fig. 2.1(b). That is, each light beam acts as if the other was not there. This is known as *linear* optics.

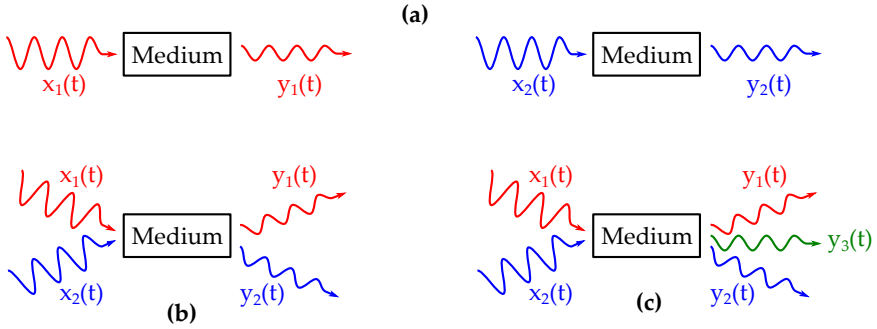

Fig. 2.1. (a) Light beams entering a medium individually. (b) Linear optical interaction, where the light beams coexist without interacting. (c) Nonlinear optical interaction, where the light beams interact with each other.

There are however certain situations, under the right conditions, where this is not the case. Sometimes, launching two light beams in the medium causes a third light beam, $y_3(t)$, to come out, depicted

in Fig. 2.1(c). In these situations, combining the two light beams at the input causes them to behave differently than if they were alone, almost as if they "felt" each other's presence. This is known as *nonlinear* optics, where the medium acts as a mediator between the photons, allowing them to interact. In turn, this leads to the possibility of manipulating light with light, which is of practical interest for many applications, including microwave photonic (MWP).

This chapter gives the underlying principles of two types of optical nonlinearities which have found widespread use in MWP. These are Kerr nonlinearities, such as self-induced effects and four-wave mixing, where the light interacts with the electrons in the atoms of the medium. The second type of nonlinearity to be studied is stimulated Brillouin scattering, where the light interacts with the medium's molecules through acoustic vibrations. The different mechanisms which give rise to these nonlinearities cause them to exhibit very different properties which can be exploited for diverse applications.

2.2 ORIGIN OF THE NONLINEARITY

Light is an electromagnetic wave described by two vector fields: an electric field $\mathbf{E}(\mathbf{r}, t)$ and a magnetic field $\mathbf{H}(\mathbf{r}, t)$, where $\mathbf{r}$ is the position vector, and t denotes time. As such, its behaviour is governed by Maxwell's equations

$$\nabla \times \mathbf{E} = -\frac{\partial \mathbf{B}}{\partial t} \tag{2.1}$$

$$\nabla \times \mathbf{H} = \frac{\partial \mathbf{D}}{\partial t} + \mathbf{J} \tag{2.2}$$

$$\nabla \cdot \mathbf{D} = \rho \tag{2.3}$$

$$\nabla \cdot \mathbf{B} = 0 \tag{2.4}$$

where $\rho(\mathbf{r}, t)$ is the free charge density, and $\mathbf{J}(\mathbf{r}, t)$ the electric current density. The vector fields $\mathbf{D}(\mathbf{r}, t)$ and $\mathbf{B}(\mathbf{r}, t)$ are known as the electric and magnetic flux densities, respectively. The physical significance of these flux densities can be understood in terms of the constitutive relations

$$\mathbf{D} = \epsilon_0 \mathbf{E} + \mathbf{P} \tag{2.5}$$

$$\mathbf{B} = \mu_0 \left(\mathbf{H} + \mathbf{M} \right) \tag{2.6}$$

where $\mu_0 = 4\pi \times 10^{-7}$ henry/m is the permeability of free-space, and $\epsilon_0 = 8.854 \times 10^{-12}$ farad/m is the permittivity of free-space. The vector fields $\mathbf{P}(\mathbf{r}, t)$ and $\mathbf{M}(\mathbf{r}, t)$ are known as the polarization and magnetization densities, respectively. They basically define how light interacts with matter. For example, in the presence of an electric field, the electron clouds surrounding the nuclei of the atoms in the

medium experience a force which distorts them, and the atoms become polarized. They are said to have acquired a *dipole moment*. The average electric dipole moment per unit volume is a macroscopic field known as the polarization density, $\mathbf{P}(\mathbf{r}, t)$. An analogous mechanism describes the formation of magnetic dipoles in the presence of a magnetic field, with $\mathbf{M}(\mathbf{r}, t)$ being the average magnetic dipole moment per unit volume.

In MWP, the optical signal is usually guided by dielectric materials, where all charges are bound to specific atoms or molecules so that $\rho(\mathbf{r}, t) = 0$. The absence of free charges also means that no currents can easily flow so that $\mathbf{J}(\mathbf{r}, t) = 0$ and $\mathbf{M}(\mathbf{r}, t) = 0$. With these simplifications, we combine Eqs. (2.1)–(2.6) into one single wave equation. The process begins by taking the curl of Eq. (2.1) and applying the vector identity $\nabla \times \nabla \times \mathbf{A} = \nabla (\nabla \cdot \mathbf{A}) - \nabla^2 \mathbf{A}$:

$$\nabla (\nabla \cdot \mathbf{E}) - \nabla^2 \mathbf{E} = -\frac{\partial}{\partial t} (\nabla \times \mathbf{B}) . \tag{2.7}$$

Further substitution of Eqs. (2.2), (2.5), and (2.6) leads to

$$\nabla (\nabla \cdot \mathbf{E}) - \nabla^2 \mathbf{E} = -\mu_0 \frac{\partial^2 \mathbf{D}}{\partial t^2}. \tag{2.8}$$

Next comes the crucial step in the derivation. It requires some assumption about the nature of the polarization density. By definition, $\mathbf{P} = N\mathbf{p}$, where N is the average density of dipole moments, and $\mathbf{p}$ is the dipole moment induced by an electric field $\mathbf{E}$ on an individual atom. Using the simple Lorentz model of the atom, the dipole moment is equal to $\mathbf{p} = -e\mathbf{x}$, where $\mathbf{x}$ is the displacement of a charge e due to the force it feels from the electric field. This force, $e\mathbf{E}$ must be exactly balanced by an equal and opposite force $-e\mathbf{E}$, as the electron tries to return to its equilibrium position. Provided $|\mathbf{x}|$ is small, the restoring force is proportional to the displacement: $|\mathbf{x}| \propto -e\,|\mathbf{E}|$ (Hooke's law). This thought process indicates that the polarization density is somehow proportional to the electric field:

$$\mathbf{P} = \epsilon_0 \chi^{(1)} \mathbf{E} \tag{2.9}$$

where $\chi^{(1)}$ is known as the linear susceptibility. This is a very convenient notation because it allows all material properties (losses, dispersion, homogeneity, isotropy, linearity) to be fully described by χ. Our next assumption is that the majority of the optical power is concentrated in the core of a waveguide, wherein the core has a uniform $\chi^{(1)}$ profile. Examples of such waveguides include step-index fibres, as well as the on-chip waveguides used for the experiments in Chapters 3, 4, and 5. This assumption allows us to invoke the homogeneous medium approximation (i.e. $\chi^{(1)}$ is not a function of position). An additional assumption is that the core of the waveguide is isotropic, such that $\mathbf{P}$ is independent of the polarization of $\mathbf{E}$ (i.e.

$\chi^{(1)}$ is a scalar). This last assumption is valid for most non-crystalline materials, which will be used throughout this work. Because of the homogeneity and isotropicity assumptions, it is simple to show that $\nabla \cdot \mathbf{E} = 0$, and the first term on the left hand side of Eq. (2.8) disappears. Substitution of Eqs. (2.9) and (2.5) into (2.8) gives

$$\nabla^2 \mathbf{E} - \frac{n^2}{c^2} \frac{\partial^2 \mathbf{E}}{\partial t^2} = 0, \tag{2.10}$$

where $n = \sqrt{1 + \chi^{(1)}}$ is the refractive index, and $c = 1/\sqrt{\mu_0 \epsilon_0}$ is the speed of light.

This second-order, homogeneous, partial differential equation is known as the wave equation. One of its central properties is that it is linear, confirming the premise that light waves do not interact with each other. The key assumption in its derivation was that the polarization density of the medium is directly proportional to the electric field. This in turn was based on the premise that the displacements of the electron clouds of the atoms in the medium are very small. This may well be true for small electric fields, but not for large ones. When the intensity of the electric field becomes sufficiently high, the relationship between the charges' displacements and the electric field ceases to be linear and becomes significantly more complex. This is the field of nonlinear optics.

In nonlinear optics, the actual functional relation between polarization density and electric field is unknown. For this, it is standard practice to express the susceptibility as a power-series expansion in $\mathbf{E}(\mathbf{r}, t)$

$$\chi = \chi^{(1)} + \chi^{(2)} \mathbf{E} + \chi^{(3)} \mathbf{E}^2 + \cdots \tag{2.11}$$

where $\chi^{(1)}, \chi^{(2)}, \ldots$ denote the various expansion orders of the susceptibility. In writing this expansion, it is specifically assumed that the optical field strength is significantly smaller than the interatomic or crystalline fields [167] present in the medium. This assumption is generally true for guided-wave nonlinear optics used in MWP signal processing, even when focused laser light is used. This expression replaces $\chi^{(1)}$ in Eq. (2.9):

$$\begin{aligned} \mathbf{P} &= \epsilon_0 \chi^{(1)} \mathbf{E} + \epsilon_0 \chi^{(2)} \mathbf{E}^2 + \epsilon_0 \chi^{(3)} \mathbf{E}^3 + \cdots \\ &= \mathbf{P}^{\mathrm{L}} + \mathbf{P}^{\mathrm{NL}} \end{aligned} \tag{2.12}$$

where $\mathbf{P}^{\mathrm{L}}$ is defined as in Eq. (2.9). The wave equation must now be derived again starting from Eq. (2.8). In doing this, it is clear that the term $\nabla \cdot \mathbf{E}$ no longer vanishes, even for the case of a homogeneous, isotropic medium. Nevertheless, it can still be assumed to be negligible, especially when the slowly varying amplitude approximation (see Sec. 2.3) is valid [168].

$$\nabla^2 \mathbf{E} - \frac{n^2}{c^2} \frac{\partial^2 \mathbf{E}}{\partial t^2} = \mu_0 \frac{\partial^2 \mathbf{P}^{\mathrm{NL}}}{\partial t^2} \tag{2.13}$$

is the wave equation in nonlinear optics. This equation has two central features. The first is that it is not a linear equation, due to the higher powers of $\mathbf{E}$ that appear in the $\mathbf{P}^{\mathrm{NL}}$ term. The second is that it is not a homogeneous wave equation; the term on the right hand side is non-zero and it acts as a source for the generation of new waves. As an example, consider the case where the input electric field into some nonlinear medium oscillates with frequency ω, i.e. $E(t) \propto e^{j\omega t}$. Substitution of this field into Eq. (2.12) reveals that the $\mathbf{P}^{\mathrm{NL}}$ term oscillates at multiple frequencies which are harmonics of the input field frequency: $2\omega, 3\omega, \ldots$. Due to the wave equation, each of these oscillating terms will start driving new electric fields oscillating with the same frequency. This basic example reveals the key feature of nonlinear optics. That is, the medium's response contains frequency components which differ from the frequency of the input optical field. In other words, a nonlinear interaction leads to the generation of fields with new frequencies, through energy exchanges.

Nonlinear optics is a very rich field. There is a large number of nonlinear optical effects resulting from the seemingly simple Eq. (2.12), each effect displaying a different behaviour, and whole books have been written on the topic [109, 168]. Nonlinear effects are broadly categorized by the order of the nonlinear susceptibility which gives rise to them. For example, nonlinearities due to $\chi^{(2)}$ are known as second-order nonlinearities and include second harmonic generation, three-wave mixing, and the electro-optic effect; third-order nonlinearities arise from $\chi^{(3)}$, such as self-phase modulation, cross-phase modulation, four-wave mixing, and third harmonic generation. Furthermore, some nonlinear effects are stronger than others. This can be understood in terms of Eq. (2.12); in order for this expression to have physical significance, it must converge, and in order for it to converge one obvious requirement is that $\chi^{(1)}\mathbf{E} \gg \chi^{(2)}\mathbf{E}^2 \gg \chi^{(3)}\mathbf{E}^3 \gg \cdots$. That is, linear effects (e.g. absorption, dispersion) due to $\chi^{(1)}$ are the strongest light-matter interactions. Optical nonlinearities require much higher powers, which explains why they were observed experimentally only after the invention of the laser in 1960. Among the various nonlinearities, the strongest in general are the second-order processes. However, there are certain materials which exhibit centrosymmetry (i.e. the properties of the medium are not altered by the transformation $\mathbf{r} \to -\mathbf{r}$), so that the relation between $\mathbf{P}$ and $\mathbf{E}$, i.e. Eq. (2.12), must exhibit odd symmetry. In these media, all even-order effects, e.g. $\chi^{(2)}, \chi^{(4)}, \ldots$ must vanish, so that the strongest nonlinearities are actually third-order effects. Centrosymmetric media include a variety of materials used for integrated platforms, such as silicon, silica, silicon nitride, and chalcogenide, as well as most optical fibres.

The most commonly used optical nonlinearities in MWP are two third-order effects: four-wave mixing and stimulated Brillouin scattering. These are explored in the next sections, along with a third nonlin-

earity known as two-photon absorption. In most cases, this last effect is undesirable, being the ultimate obstacle to improving the performance of integrated MWP signal processors in certain platforms, such as silicon.

2.3 SELF-INDUCED EFFECTS

Self-induced effects are caused by odd-order terms of the nonlinear polarization in Eq. (2.12). In centrosymmetric media, considered in this work, the dominant odd-order nonlinear term is due to $\chi^{(3)}$. Third-order self-induced effects include self-phase modulation and nonlinear loss. This latter effect in particular is important when evaluating different nonlinear media for MWP, where losses ultimately limit the overall performance.

The derivation that follows is useful for familiarising with the use of Eq. (2.13), and how it is used to study other nonlinear effect. We begin by assuming that the input optical field into the medium is described by

$$E(z,t) = \frac{1}{2} A e^{j(\omega t - kz)} + \text{c.c.} \tag{2.14}$$

where A is the (complex) electric field amplitude, k is the wave vector magnitude, ω is the angular frequency, and *c.c.* denotes the complex conjugate. Writing the field in this form presupposes certain properties of the nature of the wave. The first is that the field is a scalar, which assumes that all waves in the medium are linearly polarized in the same direction. The second is that the field is monochromatic (i.e. A is not a function of time); while this is not necessarily true in practice, most applications in MWP rely on continuous wave (CW) optical waves, and even when this is not the case, any pulse can be written as a Fourier compositions of Eq. (2.14). Finally, it assumes that the wave is a plane wave; again, this may not be the case in practice, but plane waves form a complete set so that superpositions can be used to describe arbitrary beams.

In the centrosymmetric medium under consideration, third-order processes are the dominant sources of nonlinearities, so that the nonlinear polarization can be written as

$$\begin{aligned} P^{\text{NL}}(z,t) &= \epsilon_0 \chi^{(3)} E^3(z,t) \\ &= \frac{\epsilon_0 \chi^{(3)}}{8} A^3 e^{j(3\omega t - 3kz)} + \frac{3\epsilon_0 \chi^{(3)}}{8} |A|^2 A e^{j(\omega t - kz)} + \text{c.c.} \end{aligned}$$

This expression shows that the nonlinear polarization term oscillates with two frequencies: that equal to the frequency of the input optical field ω, and a third-harmonic component at 3ω. This harmonic component can be neglected in practice due to the fact that nonlinear interactions are weak, and different processes do not appreciably affect each other. This statement is further supported by a probable lack

of phase matching (see Sec. 2.4), meaning that the 3ω process does not occur efficiently. For this, only the ω component of the nonlinear polarization is substituted in Eq. (2.13). Before doing this however, it is useful to state a common assumption made in nonlinear optics, known as the slowly varying amplitude approximation (SVEA)

$$\left| k\frac{dA}{dz} \right| \gg \left| \frac{d^2A}{dz^2} \right|, \tag{2.15}$$

which basically states that the change in the field amplitude occurs gradually, over many optical cycles. With these approximations, Eq. (2.13) yields

$$\frac{dA}{dz} = -j\frac{3\omega}{8cn}\chi^{(3)} |A|^2 A. \tag{2.16}$$

Greater insight into the evolution of the optical field can be gained by expanding the complex amplitude into a space-dependent amplitude $u(z)$ and phase $\phi(z)$

$$A = u(z)e^{j\phi(z)}$$

and substituting into Eq. (2.16)

$$\frac{du}{dz} + ju\frac{d\phi}{dz} = -j\frac{3\omega}{8cn}\chi^{(3)}u^3. \tag{2.17}$$

We now make the generalization that the third-order susceptibility is complex: $\chi^{(3)} = \chi_R^{(3)} - j\chi_I^{(3)}$. This results in two ordinary differential equations which describe the evolution of phase and amplitude of the input field as it propagates along the nonlinear medium:

$$\frac{d\phi}{dz} = -\frac{3\omega}{8cn}\chi_R^{(3)}u^2 \tag{2.18}$$

$$\frac{du}{dz} = -\frac{3\omega}{8cn}\chi_I^{(3)}u^3. \tag{2.19}$$

2.3.1 *Self-Phase Modulation*

Equation (2.18) shows how the nonlinear polarization acts to affect the phase of the field that is inducing it in the first place. This process is known as self-phase modulation (SPM). The self-phase shift due to SPM as the field travels along a short medium length Δz, is given by

$$\Delta\phi^{\mathrm{NL}} = -\frac{3\omega}{8cn}\chi_R^{(3)}u^2\Delta z. \tag{2.20}$$

However, the phase of the field also changes linearly due to its travelling wave nature:

$$\Delta\phi^{\mathrm{L}} = -k\Delta z = -\frac{\omega}{c}n\Delta z. \tag{2.21}$$

The total phase shift undergone by the field is a sum of these two contributions

$$\begin{aligned}\Delta\phi &= \Delta\phi^{\mathrm{NL}} + \Delta\phi^{\mathrm{L}} \\ &= -\frac{\omega}{c}\left(n + \frac{3}{8n}\chi_R^{(3)}u^2\right)\Delta z.\end{aligned} \tag{2.22}$$

Comparison of Eqs. (2.21) and (2.22) suggests that the nonlinear phase shift is equivalent to a change in the refractive index of the medium, proportional to the intensity of the field. The total refractive index can then be written as

$$n_{\mathrm{total}} = n + n_2 I \tag{2.23}$$

where I is the time-averaged intensity for monochromatic plane waves given by

$$I = \frac{n\epsilon_0 c}{2}u^2 \tag{2.24}$$

and

$$n_2 = \frac{3}{4\epsilon_0 n^2 c}\chi_R^{(3)} \tag{2.25}$$

is known as the Kerr coefficient (or nonlinear index). As shall be seen in Sec. 2.4, the Kerr coefficient is an important measure of the strength of the nonlinearity of a given medium. Another commonly used parameter is given by

$$\gamma = k\frac{n_2}{A_{\mathrm{eff}}}, \tag{2.26}$$

which is a geometry-dependent measure of the nonlinearity for a given platform, where A_{eff} is the effective mode area of the waveguide.

Due to its automatically phase-matched nature (see Sec. 2.4), SPM can be readily used to estimate the Kerr coefficient of a medium. SPM, essentially, causes a change $\Delta\phi^{\mathrm{NL}}$ in the phase of a wave proportional to wave's power. When applied to optical pulses, the time-dependent nature of the pulse power introduces a time component in $\Delta\phi^{\mathrm{NL}}$, which in turn causes a change in the instantaneous frequency of the pulse

$$\Delta\omega(t) = \frac{\partial\Delta\phi^{\mathrm{NL}}}{\partial t}. \tag{2.27}$$

The time dependence in the instantaneous frequency of a wave is known as frequency chirping. The SPM-induced frequency chirp causes new frequencies to be generated as the pulse propagates along the medium. These new frequencies can in turn lead to spectral broadening or narrowing. In the case of unchirped input pulses, SPM always

leads to spectral broadening. For Gaussian pulses, an estimate of this spectral broadening is given by [169]

$$\Delta\omega_{\max} = \frac{0.86}{T_0} k n_2 I_0 L_{\text{eff}} \tag{2.28}$$

where T_0 is the full width at half maximum (FWHM) of the pulse period, I_0 is the peak intensity of the pulse, and $L_{\text{eff}} = (1 - e^{-\alpha L})/\alpha$ is the effective length of the medium, L is the physical length of the medium, and α is its linear absorption coefficient. Experimental observations of such SPM-induced spectral broadening is provided in Fig. 5.9.

2.3.2 *Nonlinear Losses*

The main sources of nonlinear loss in optical waveguides are multi-photon absorption processes. More specifically, in $\chi^{(3)}$-media (i.e. centrosymmetric media), the dominant nonlinear loss mechanism is two-photon absorption (TPA). TPA is a process where two photons are absorbed simultaneously, exciting an atom to a higher energy state. In a dielectric or a semiconductor, TPA only occurs when the photon energy is at least half of the bandgap energy, E_g. MWP, like most optical communication systems, normally relies on optical wavelengths in the vicinity of 1550 nm. At this wavelength, photons carry an energy of 0.8 eV, meaning that TPA does not occur in silica fibres ($E_g = 8.9$ eV), but it does occur in silicon waveguides ($E_g = 1.12$ eV).

The nonlinear loss mechanism due to $\chi^{(3)}$ is described by Eq. 2.19. This equation can be re-written in terms of intensity:

$$\frac{dI}{dz} = -\beta I^2 \tag{2.29}$$

where

$$\beta = \frac{3\omega}{2\epsilon_0 n^2 c^2} \chi_I^{(3)} \tag{2.30}$$

is the TPA coefficient.

Throughout this whole derivation, the effect of linear losses has not been taken into account. At this point however, it is useful to include it in the space-evolution of the field intensity:

$$\frac{dI}{dz} = -\alpha I - \beta I^2 \tag{2.31}$$

where α is the linear absorption coefficient. While $\alpha \gg \beta$, it is clear that for high light intensities, the TPA term dominates and eventually saturates the power that leaves the waveguide. This is a serious problem in MWP, where the link gain of the system has a square-dependence on the optical loss.

The effect of TPA nonlinear absorption is made considerably worse when the two absorbed photons excite an electron from the valence band to the conduction band (as occurs in silicon [148, 170]). The dynamics of free carriers induced by TPA can be described by the Drude model and results in the following rate equation for the free carrier density N_c:

$$\frac{\partial N_c}{\partial t} = \frac{\beta}{2\hbar\omega} I^2 - \frac{N_c}{\tau_c} \tag{2.32}$$

where τ_c is the free-carrier lifetime. The effect of free carriers on the optical fields in the medium is modelled by adding both a real and an imaginary term to the linear susceptibility $\chi^{(1)}$. For the purpose of this work however is it sufficient to know that free carriers cause a change in the linear refractive index of the medium, opposite in sign to the change due to the Kerr effect. Therefore, free carriers effectively reduce the real part of $\chi^{(3)}$, which is not desirable when nonlinearities are being exploited for signal processing. Moreover, free carriers also act to increase the linear absorption, an effect known as free-carrier absorption (FCA):

$$\frac{dI}{dz} = -\alpha I - \alpha_{\mathrm{FC}} I - \beta I^2 \tag{2.33}$$

where α_{FC} is the free-carrier absorption coefficient, which is directly proportional to the free-carrier concentration N_c. While FCA is not a nonlinear absorption process in itself, the fact that N_c depends on the optical intensity (due to TPA) means that TPA-induced free carriers are a source of nonlinear loss.

Optical generation of free-carriers may be desirable for active light control, for instance, when making fast optical switches or modulators. However, to this day, this has not found applications in MWP, where free carriers are largely seen as a nuisance that limit the optical power into a device and ultimately, reduce the link gain of the system. This is clearly seen in Fig. 2.2, where TPA-induced free carriers are the main source of output power saturation, in as standard silicon nanowire. Methods for reducing the effect of free carriers typically involve pulsing the optical field, using pulse widths lower than the free-carrier lifetime ($\tau_c > 1$ ns in silicon) and pulse repetition periods longer than the lifetime. This however slows down the whole system, and does not work when CW light, as required in most MWP systems. An alternative approach is to remove the carriers by applying a lateral electric field across the waveguide. The field can be applied through ohmic contacts, or by implementing a metal-semiconductor metal lateral Schottky junction [171] or, in the case of a group-IV semiconductor waveguide, by laterally doping the waveguide to obtain a p-i-n junction.

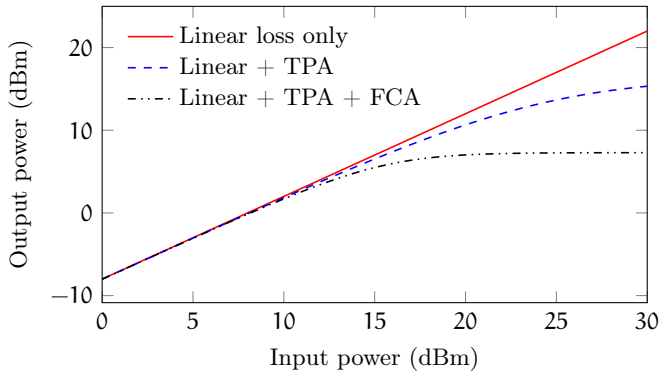

Fig. 2.2. Simulated output power for a 4 cm long, silicon nanowire with 0.1 μm^2 mode area, 2 dB/cm linear loss, $\beta = 2$ cm/GW, $\alpha_{FC} = 1.45 \times 10^{-17}$ $cm^2 \times N_c$, and $\tau_c = 3$ ns.

2.4 FOUR-WAVE MIXING

Four-wave mixing (FWM) arises from the interaction of four waves due to the $\chi^{(3)}$ term in Eq. (2.12). In the most general case, all four interacting waves have different frequencies, but strictly speaking, only three of the four waves' frequencies need differ. As the name implies, this is a nonlinear mixing process, which can be used for generating new optical frequencies, or for copying the information encoded on one carrier to a different optical carrier. The principal features of FWM can be better understood by considering its effect on an optical field composed of three different CW waves:

$$E(z,t) = \frac{1}{2}\left[A_1 e^{j(\omega_1 t - k_1 z)} + A_2 e^{j(\omega_2 t - k_2 z)} + A_3 e^{j(\omega_3 t - k_3 z)}\right] + \text{c.c.} \tag{2.34}$$

with $\omega_1 < \omega_2 < \omega_3$. Upon propagation through a medium where the $\chi^{(3)}$ nonlinearity dominates, the nonlinear polarization

$$P^{NL}(z,t) = \epsilon_0 \chi^{(3)} E^3(z,t)$$

is composed of a large number of frequency terms. Only the terms oscillating with a frequency which is a combination of at least two different frequencies (e.g. $\omega_1 + \omega_2 + \omega_3$, or $2\omega_2 - \omega_1$) are referred to as FWM processes. In theory, each of these terms in the nonlinear polarization has the potential of becoming a source for a new optical field. In practice however, only a few, if any, of these terms manage to actually drive new frequencies, due to a condition known as phase matching, described later. Here we consider the polarization term with frequency $\omega_4 := -\omega_1 + \omega_2 + \omega_3$, and assume that such a

field is generated by the nonlinearity. The steady-state optical field then needs to be rewritten as

$$E(z,t) = \frac{1}{2}\Big[A_1 e^{j(\omega_1 t - k_1 z)} + A_2 e^{j(\omega_2 t - k_2 z)} + A_3 e^{j(\omega_3 t - k_3 z)} + A_4 e^{j(\omega_4 t - k_4 z)}\Big] + \text{c.c.} \tag{2.35}$$

The question now is how all these frequencies interact via the $\chi^{(3)}$ nonlinearity. To answer this question, one needs to find all the nonlinear polarization terms oscillating with frequency equal to one of the terms present in the field. For example, the nonlinear polarization oscillating with frequency ω_1 is

$$P^{\text{NL}}(\omega_1) = \frac{3\epsilon_0\chi^{(3)}}{8}\Big[\left(|A_1|^2 + 2|A_2|^2 + 2|A_3|^2 + 2|A_4|^2\right)A_1 e^{-jk_1 z} + 2A_2 A_3 A_4^* e^{-(k_2+k_3-k_4)z}\Big] + \text{c.c.} \tag{2.36}$$

Equation (2.36) shows that the nonlinear polarization for the field at ω_1 results in a number of nonlinear effects. The first term on the right hand side of Eq. (2.36) results in SPM and, if $\chi^{(3)}$ is complex, nonlinear losses. The three terms after the first are cross effects; these are similar to self-induced effects (they also cause a phase shift and nonlinear loss), but are due to optical fields at different frequencies than the one they are affecting. It is important to note that all of these effects have the same spatial wavelength as the field they are affecting (i.e. $\propto e^{-jk_1 z}$); because of this, these terms are *automatically phase matched*. The last term on the right hand side of Eq. (2.36) is that which causes FWM. It involves energy exchange between the different fields, and its spatial wavelength, determined by $k_2 + k_3 - k_4$, may differ from k_1. As we shall see, this difference has a dramatic effect on the efficiency of the FWM process.

Similar expressions from that of Eq. (2.36) may be found for the nonlinear polarizations oscillating with frequencies ω_2, ω_3, and ω_4. Upon substitution of these expressions in the wave equation (2.21), one finds four coupled mode equations describing the evolution in space of the three input fields and the newly generated field:

$$\frac{dA_1}{dz} = -j\frac{3\omega_1\chi^{(3)}}{8n_1 c}\Big[\left(|A_1|^2 + 2|A_2|^2 + 2|A_3|^2 + 2|A_4|^2\right)A_1 + 2A_2 A_3 A_4^* e^{j\Delta k z}\Big] \tag{2.37}$$

$$\frac{dA_2}{dz} = -j\frac{3\omega_2\chi^{(3)}}{8n_2 c}\Big[\left(|A_2|^2 + 2|A_1|^2 + 2|A_3|^2 + 2|A_4|^2\right)A_2 + 2A_1 A_3^* A_4 e^{-j\Delta k z}\Big] \tag{2.38}$$

$$\frac{dA_3}{dz} = -j\frac{3\omega_3\chi^{(3)}}{8n_3c}\left[\left(|A_3|^2 + 2|A_1|^2 + 2|A_2|^2 + 2|A_4|^2\right)A_3 + 2A_1A_2^*A_4e^{-j\Delta kz}\right] \tag{2.39}$$

$$\frac{dA_4}{dz} = -j\frac{3\omega_4\chi^{(3)}}{8n_4c}\left[\left(|A_4|^2 + 2|A_1|^2 + 2|A_2|^2 + 2|A_3|^2\right)A_4 + 2A_1^*A_2A_3e^{j\Delta kz}\right] \tag{2.40}$$

where $n_i = n(\omega_i)$ for $i = 1, 2, 3, 4$ is to take into account the dispersion of the medium, and

$$\Delta k = k_1 - k_2 - k_3 + k_4 \tag{2.41}$$

is known as the phase mismatch. It is clear that in order for the new field component at ω_4 to grow, the requirement is that $\Delta k = 0$. This is known as the phase matching condition. It basically states that the driving force (i.e. the polarization) must be in phase with the driven field along the whole length of interaction. When this is the case, energy flows efficiently from the polarization to the newly generated field, allowing it to experience parametric amplification. If however phase matching is not satisfied, the direction of energy flow continuously switches between the polarization and the new field, and no growth occurs.

Phase matching depends on the direction of propagation of the different fields, given by the direction of the wavevector $\mathbf{k}_i$. In most waveguides however, light is confined in two dimensions such that all fields can be assumed to travel in just one of two directions: forward or backward. For the example above, assuming all fields are co-propagating, the phase matching condition can be rewritten as

$$n_2\omega_2 - n_1\omega_1 = n_4\omega_4 - n_3\omega_3$$

which shows that, essentially, phase matching depends on the dispersion of the waveguide, i.e. the dependence of the refractive index on the optical frequency. In the ideal case of a nondispersive medium, phase matching is automatically satisfied. In practice however, all materials exhibit dispersion, making phase matching a nontrivial process. Phase matching is particularly difficult between waves with very different frequencies, which is why FWM normally excites waves which are nearest in frequency to those of the input fields (e.g. $\omega_4 := -\omega_1 + \omega_2 + \omega_3$) and not those which are farthest (e.g. $\omega_4 := \omega_1 + \omega_2 + \omega_3$).

In broad terms, dispersion can be split between normal (where the refractive index increases with increasing frequency) and anomalous (where the refractive index decreases with increasing frequency). For

the purpose of this work, it is sufficient to know that the most efficient FWM occurs when all interacting waves have frequencies which lie in a region of small anomalous dispersion. For phase matching however, what is important is the total dispersion of a given medium: the sum of the material dispersion and the waveguide dispersion. For low-index contrast waveguides, with large mode areas in the order of micrometres, the total dispersion is mainly determined by the material dispersion. For waveguides that have a high index contrast however, where the mode can be confined to nanometre-sized areas, waveguide dispersion plays an increasingly important role. This can be used for engineering the total dispersion of the waveguide. For example, bulk silicon exhibits normal dispersion, but the dispersion of a rectangular silicon waveguide is anomalous at 1550 nm wavelengths when its height is 220 nm, and its width is in the range between 440 and 540 nm. Such dispersion-engineered silicon nanowires have played an important role in nonlinear optics in the past decade [148].

It can be seen from Eqs. (2.37)–(2.40) that, provided phase matching is satisfied, FWM can lead to energy exchanges between the different frequency components. The convention is to name the two strongest waves the *pumps*, the weakest input wave the *signal*, and the fourth wave, which is being generated, the *idler*. There are two standard configurations, shown in Fig. 2.3, in which FWM is normally studied; nondegenerate FWM is when all four interacting waves have different frequencies. Degenerate FWM is a subset of the previous case that occurs when both pumps have the same frequency.

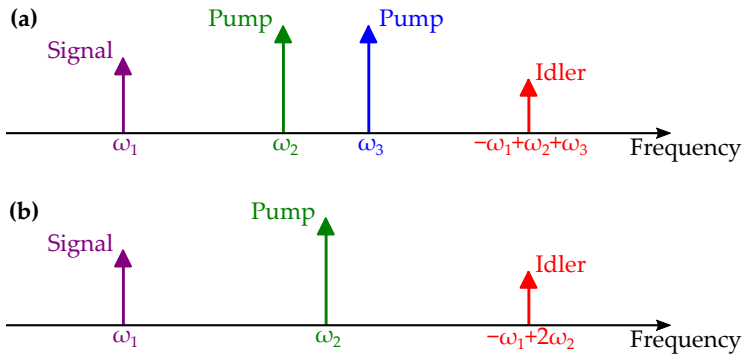

Fig. 2.3. (a) Nondegenerate and (b) degenerate FWM processes, where two pump photons mix with one signal photon to generate an idler photon.

It is easy to imagine how the FWM process could be used as an amplifier, where the pumps give their energy to both signal and idler. In MWP however, FWM is normally used for generating new frequency components (e.g. for tap generation in multi-tap filters). In such situations, the idler is not introduced at the input of the medium, but it grows due to noise fluctuations in the electromagnetic field of the medium. In MWP therefore, the parameter of interest to define the strength of the FWM interaction is the conversion efficiency. This is

defined as the ratio of the output idler intensity, $I_I(L)$, to the input signal intensity $P_S(0)$, and is given by

$$\frac{I_I(L)}{I_S(0)} = \frac{2\omega_I^2}{\epsilon_0 n c^3} n_2 I_P^2(0) L^2 \text{sinc}\left(\frac{\kappa L}{2}\right) \tag{2.42}$$

where ω_I is the idler frequency, $I_P(0)$ is the input pump power, L is the length of the interaction medium, and κ is the sum of linear phase mismatch Δk and nonlinear phase shifts experienced by the idler field due to the combination of self- and cross-induced effects. Clearly, the conversion efficiency increases with the pump power. A fundamental limitation to this trend however occurs due to pump depletion effects. Moreover, in practice other nonlinear processes (e.g. stimulated Brillouin scattering and nonlinear losses) can play a significant role in limiting the maximum achievable conversion efficiency for a given structure. A comparison of some of the highest conversion efficiencies achieved in various integrated platforms for CW operation is provided in Sec. 5.3.

2.4.1 *Material Platforms for FWM*

For harnessing FWM, the most important requirement on the material medium is for $\chi^{(3)}$ to be the dominant source of nonlinearity (i.e. that the medium be centrosymmetric). Optical fibres are one such medium, and observations of FWM were reported soon after low-loss optical fibres became available [172]. More recently, FWM interactions have been demonstrated in a vast number of integrated platforms, including silicon [173], chalcogenide (ChG) [174], doped silica glass [175], silicon nitride [176], AlGaAs [177], and diamond [178]. While nonlinear absorption effects are normally not observed in silica fibres, the introduction of new material platforms has uncovered that this effect can be detrimental to FWM. In fact, FCA is the main obstacle to achieve high conversion efficiencies [179]. For this, the suitability of materials as FWM platforms is normally determined by their nonlinear figure of merit (FOM), defined as the ratio of the real to the imaginary part of the third-order susceptibility, or

$$\text{FOM} = \frac{1}{\lambda}\frac{n_2}{\beta} \tag{2.43}$$

where λ is the wavelength of the pump. Efficient generation of new frequencies through FWM requires that this FOM be high.

ChG devices offer FOMs which are among the highest reported to date; for instance, As_2S_3 rib waveguides exhibit FOMs in excess of 300 [161]. This is due to their high Kerr coefficient and negligible TPA (hence no free-carrier effects) at 1.55 μm telecommunication wavelengths. A different platform, GaAs, is a semiconductor with a very large Kerr nonlinearity and very low linear absorption, both of which

are important properties for nonlinear interactions. However, it also has a very high TPA coefficient due to its direct bandgap. This can be tailored through the addition of aluminium to the compound during epitaxial growth. The result, AlGaAs, has the similar nonlinear performance to GaAs, but with a much lower TPA coefficient in the telecommunication band, and has been used to demonstrated record-high FWM conversion efficiency with the lowest pump/length combination [180]. Both silicon nitride and Hydex glass have also displayed high FOMs, as well as being complementary metal-oxide semiconductor (CMOS)-compatible [137]. However, their Kerr coefficient is relatively low compared to other platforms (approximately a hundred times less than ChG) and thus require large powers for stimulating nonlinear effect. Silicon is the ultimate CMOS compatible material, and it does have a high Kerr coefficient (comparable to that of ChG). Its main drawback however is a large TPA coefficient which drives its FOM below 1 [148]. Nevertheless, the appeal of silicon has driven researchers to design highly nonlinear waveguides with anomalous dispersion so as to fully exploit this platform [181], as well as to consider variations such as hydrogenated amorphous silicon [182].

Table 2.1 shows a comparison of the nonlinear performance of different integrated platforms, including standard silica single-mode fibre (SMF) for comparison. It is important to note that the value of the FOM is purely indicative, and the platform most suited to a given application in general depends on the application itself. For example, as will be discussed in Chapter 5, in MWP applications such as instantaneous frequency measurement, both the Kerr coefficient, n_2, and the linear propagation loss, α, (which is not accounted for by the FOM) play a central role in determining the overall performance. In fact, it has been noted that some applications may benefit from using platforms with lower nonlinearities but also lower losses (e.g. Si_3N_4), and maintain a moderate conversion efficiency by employing longer waveguide lengths [183]. A similar concept is applied in Chapter 5 by using a thick silicon platform, with lower losses (and lower nonlinearity) than conventional silicon nanowires [184].

2.5 STIMULATED BRILLOUIN SCATTERING

Stimulated Brillouin scattering (SBS) is an inelastic scattering process that results from the interaction between an optical and an acoustic wave [168], where the acoustic wave is generated from the light itself. While SBS is a third-order nonlinearity, it does not originate from the $\chi^{(3)}$ term of the nonlinear polarization. Its origin instead is due to a combination of three mechanisms: (1) electrostriction, the tendency of a material to be compressed in the presence of an optical intensity gradient; (2) thermal or quantum-mechanical zero-point effects; (3) radiation pressure, exerted by the optical field at the boundaries of

Table 2.1. Kerr nonlinearity and nonlinear FOM for different platforms.

Platform	α (dB/cm)	n_2 (m^2/W)	β (cm/GW)	FOM
Silica SMF [109]	Negligible	2.6×10^{-20}	Negligible	Large
As_2S_3 rib [161]	0.6	3×10^{-18}	6.2×10^{-4}	312
Crystalline Si [185]	2	4.5×10^{-18}	0.9	0.3
Amorphous Si [186]	4.5	2.1×10^{-17}	0.25	5
SiN [137]	0.4	2.6×10^{-19}	Negligible	Large
Hydex [137]	0.06	1.3×10^{-19}	Negligible	Large
AlGaAs [187]	4.5	2×10^{-17}	Negligible	Large

the waveguide. At microscales, the dominant SBS mechanism is electrostriction; since this is the regime where most of this work is based, this is considered next.

When an optical wave, known as the pump, is launched into a medium, it encounters thermally generated acoustic phonons. These are random time-varying fluctuations of the medium density. Due to the photoelastic effect, these density fluctuations result in localized fluctuations in the material's refractive index, causing the pump wave to scatter. This process, illustrated in Fig. 2.4(a), is known as spontaneous Brillouin scattering. Efficient scattering occurs only in the backward direction (opposite the direction of the pump). Moreover, conservation of energy dictates that the scattered wave must have a lower frequency than that of the pump, and is thus called the "Stokes" wave. If the power of the pump wave is increased above a certain threshold, the scattered Stokes wave builds up and is resonantly amplified. This is known as SBS.

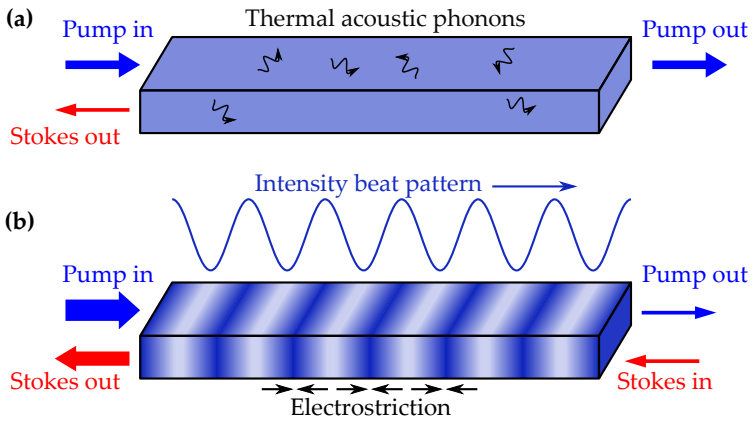

Fig. 2.4. (a) Spontaneous and (b) stimulated Brillouin scattering.

The process which leads to SBS is better understood by considering an alternative configuration, shown in Fig. 2.4(b), which occurs when an external Stokes wave is input to the medium from the opposite

side to that of the pump. As they counterpropagate, the interference between the pump and Stokes waves produces an intensity beat pattern along the length of the medium. Due to electrostriction, regions of the medium subjected to high intensities are compressed, while all other regions are rarefied, forming a density grating along the medium. If the optical field comprising the optical pump and Stokes waves is written as

$$E(z,t) = \frac{1}{2}A_p e^{j(\omega_p t - k_p z)} + \frac{1}{2}A_s e^{j(\omega_s t + k_s z)} + \text{c.c.} \tag{2.44}$$

the intensity beat pattern, being proportional to $|E(z,t)|^2$, contains frequency $|\omega_p \pm \omega_s|$ and wave vector magnitudes $|k_p \mp k_s|$. By varying the frequency of either pump or Stokes waves, it is possible to find a point where the ω/k value of the beat pattern matches the dispersion relation for an acoustic field supported by the medium. At this point, the beat pattern, and hence the density grating, moves along the medium in the same direction as the pump, and is therefore called an acoustic wave. This sets up a positive feedback mechanism where the Stokes wave is resonantly amplified by the scattering of the pump, and the stronger Stokes wave strengthens the beat pattern, amplifying the acoustic wave.

The evolution of the acoustic field $\Delta\rho$ in the medium is described by the equation

$$\frac{\partial^2 \Delta\rho}{\partial t^2} - \Gamma\nabla^2\frac{\partial \Delta\rho}{\partial t} - v^2\nabla^2\Delta\rho = -\frac{1}{2}\gamma_e \nabla^2 E^2 \tag{2.45}$$

where Γ is the acoustic damping parameter, v is the acoustic velocity, and γ_e is called the electrostrictive coefficient, defined as

$$\gamma_e = \epsilon_0 \rho_0 \frac{\partial \chi}{\partial \rho}\bigg|_{\rho_0} \tag{2.46}$$

where ρ_0 denotes the mean density of the medium. The source term on the right hand side of Eq. (2.45) therefore accounts for electrostriction; this term actually contains two frequency components, $|\omega_p \pm \omega_s|$, however only the $|\omega_p - \omega_s|$ component makes physical sense since it is not possible for an acoustic wave to be driven with frequency $|\omega_p + \omega_s|$. By assuming an acoustic field of the form

$$\Delta\rho(z,t) = \frac{1}{2}\Delta\rho_0 e^{j(\Omega t - qz)} + \text{c.c.}, \tag{2.47}$$

it is possible to solve Eq. (2.45) for the steady-state acoustic field amplitude $\Delta\rho_0$ by assuming it does not vary substantially across an acoustic wavelength, as well as by making the SVEA for the optical fields:

$$\Delta\rho_0 = \frac{\gamma_e q^2 A_p A_s^*}{2\left(\Omega_B^2 - \Omega^2 - i\Gamma_B\Omega\right)} \tag{2.48}$$

where $\Omega = \omega_p - \omega_s$ and $q = k_p + k_s$ are the frequency and the wave vector magnitude of the acoustic field, respectively. $\Omega_B = vq^2$ is known as the Brillouin frequency shift, while $\Gamma_B = vq$ is known as the Brillouin frequency shift.

Now that the mechanism for generating the acoustic field has been defined, we look at how this field interacts with the optical waves. Equation (2.46) indicates that the nonlinear polarization term in SBS is given be

$$P^{\mathrm{NL}}(z,t) = \frac{\gamma_e}{\rho_0}\Delta\rho_0(z,t)E(z,t). \tag{2.49}$$

Substituting this expression into the driven wave equation (2.13), and making the SVEA, one can derive two steady-state coupled mode equations, for both pump and Stokes waves:

$$\frac{dA_p}{dz} = \frac{\omega_s\gamma_e^2\epsilon_0 q^2}{2nc\rho_0}\left[\frac{-\Omega\Gamma_B + j\left(\Omega_B^2 - \Omega^2\right)}{\Omega^2\Gamma_B^2 + \left(\Omega_B^2 - \Omega^2\right)^2}\right]|A_s|^2 A_p - \frac{\alpha}{2}A_p \tag{2.50}$$

$$\frac{dA_s}{dz} = \frac{\omega_s\gamma_e^2\epsilon_0 q^2}{2nc\rho_0}\left[\frac{-\Omega\Gamma_B - j\left(\Omega_B^2 - \Omega^2\right)}{\Omega^2\Gamma_B^2 + \left(\Omega_B^2 - \Omega^2\right)^2}\right]|A_p|^2 A_s + \frac{\alpha}{2}A_s. \tag{2.51}$$

For the purpose of this work however, it is more convenient to express these equations in terms of the powers P_p, P_s, and phases θ_p, θ_s, of the pump and Stokes waves, respectively

$$\frac{dP_p}{dz} = -\frac{g_0}{A_{\mathrm{eff}}}\left[\frac{\Gamma_B^2}{4(\Omega-\Omega_B)^2 + \Gamma_B^2}\right]P_pP_s - \alpha P_p \tag{2.52}$$

$$\frac{dP_s}{dz} = -\frac{g_0}{A_{\mathrm{eff}}}\left[\frac{\Gamma_B^2}{4(\Omega-\Omega_B)^2 + \Gamma_B^2}\right]P_pP_s - \alpha P_s \tag{2.53}$$

$$\frac{d\theta_p}{dz} = \frac{g_0\Gamma_B}{A_{\mathrm{eff}}}\left[\frac{\Omega-\Omega_B}{4(\Omega-\Omega_B)^2 + \Gamma_B^2}\right]P_s \tag{2.54}$$

$$\frac{d\theta_s}{dz} = -\frac{g_0\Gamma_B}{A_{\mathrm{eff}}}\left[\frac{\Omega-\Omega_B}{4(\Omega-\Omega_B)^2 + \Gamma_B^2}\right]P_p \tag{2.55}$$

where g_0 is known as the Brillouin gain coefficient

$$g_0 = \eta\frac{\gamma_e^2\omega_p^2}{nvc^3\rho_0\Gamma_B}. \tag{2.56}$$

Here, η is a dimensionless quantity between 0 and 1, which measures the overlap between the optical and acoustic modes.

These equations show that, in the SBS interaction, the Stokes wave (travelling in the $-z$-direction) is amplified, while the pump wave (travelling in the $+z$-direction) is depleted. From the point of view of the Stokes wave, SBS induces a gain resonance at a frequency downshifted from that of the pump by an amount Ω_B. However, from the

point of view of the pump wave, SBS induces a loss resonance at a frequency down-shifted from that of the pump by an amount Ω_B. The frequency response of both gain and loss resonances, comprising of amplitude and phase responses, is illustrated in Fig. 2.5 and, in the undepleted pump approximation (see Sec. 2.5.1), can be expressed mathematically as

$$|H(\Omega)| = \exp\left[\frac{G}{2} \times \frac{\Gamma_B^2}{4(\Omega - \Omega_B)^2 + \Gamma_B^2}\right] \tag{2.57}$$

$$\angle H(\Omega) = G \times \Gamma_B \frac{\Omega - \Omega_B}{4(\Omega - \Omega_B)^2 + \Gamma_B^2} \tag{2.58}$$

where

$$G = \pm \frac{g_0 P_p(0) L_{\text{eff}}}{A_{\text{eff}}} \tag{2.59}$$

is known as the SBS strength parameter (positive for gain, negative for loss), and $L_{\text{eff}} = (1 - e^{-\alpha L})/\alpha$ is the effective length of the medium.

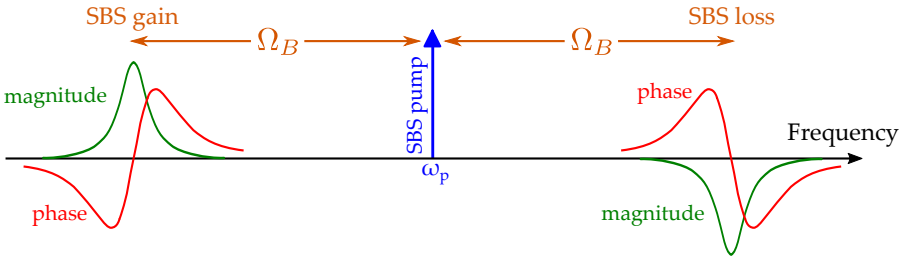

Fig. 2.5. SBS frequency response induced by a pump wave. It consists of a gain resonance at the Stokes frequency, and a loss resonance at the anti-Stokes frequency.

It is important to note that these resonances only affect pump or probe waves propagating in opposite directions. This is known as backward SBS, and it occurs due to the interaction of light with longitudinal acoustic modes. An analogous mechanism, where pump and Stokes co-propagate, or forward SBS, is possible if, instead of being longitudinal, the acoustic mode is transverse. Such modes are supported only in certain waveguide geometries [188], such as suspended-core multi-structured optical fibres [189]. Nevertheless, for the most commonly used optical waveguides (e.g. silica SMF), the longitudinal acoustic mode is dominant so that the backward SBS interaction is the strongest.

The unique property of SBS, which makes it such an interesting process for MWP signal processing, is the extremely narrow linewidth of its resonances. In optical waveguides, the Brillouin linewidth, Γ_B, is in the range of a few tens of megahertz (in silica fibres $\Gamma_B \sim 30$ MHz). To date, very few other optical elements or effects can generate such narrow resonances. For instance, optical resonators are able to reach

linewidths as low as 10 MHz [190], but require considerable fabrication efforts and the circulating power build-up can constitute a significant challenge. In SBS instead, the linewidth is determined by the acoustic properties of the medium (e.g. speed of sound), and narrow, megahertz linewidths occur naturally in most optical waveguides.

2.5.1 *Linearity of SBS Interaction*

The linearity of SBS refers to the linearity of the (gain or loss) frequency responses induced by the SBS process. It may seem contradictory to discuss the linearity of a nonlinear process; however we note that most (if not all) systems in existence are inherently nonlinear, and are considered linear only under certain conditions. As explained previously, a large number of applications in MWP make use of the SBS resonances for signal processing. SBS can therefore be considered as a system, with frequency response depicted in Fig. 2.5. In signal processing, and analog signal processing in particular, it is essential that the systems used be linear. It is then necessary to understand the conditions under which SBS acts as a linear system.

We begin by considering the SBS coupled mode equations (2.52) and (2.53) for the optical field powers, when the pump and Stokes frequency are separated precisely by the Brillouin frequency shift, i.e. $\omega_p - \omega_s = \Omega_B$:

$$\frac{dP_p}{dz} = -\frac{g_0}{A_{\text{eff}}} P_p P_s - \alpha P_p \tag{2.60}$$

$$\frac{dP_s}{dz} = -\frac{g_0}{A_{\text{eff}}} P_p P_s - \alpha P_s. \tag{2.61}$$

These equations must be solved numerically, with boundary conditions $P_p(0)$ (the input pump power) and $P_s(L)$ (the input Stokes power), where L is the physical length of the SBS medium. However, an analytic solution exists by assuming that no pump depletion occurs due to SBS, i.e.

$$\frac{dP_p}{dz} \approx -\alpha P_p. \tag{2.62}$$

With this approximation, it is simple to show that the power evolution of the Stokes wave along the medium is given by

$$P_s(z) = P_s(L) e^{\alpha(z-L)} \exp\left[\frac{g_0 P_p(0)}{\alpha A_{\text{eff}}} \left(e^{-\alpha z} - e^{-\alpha L}\right)\right] \tag{2.63}$$

which corresponds to a total SBS gain of

$$\frac{P_s(0)}{P_s(L)} e^{\alpha L} = e^G. \tag{2.64}$$

The information provided by Eq. (2.64) is extremely important. This equation states that, when the SBS pump is not depleted, the SBS gain

experienced by the Stokes wave is linear (i.e. it is not a function of the Stokes power itself). The question now is, under what conditions is the SBS pump undepleted? An obvious condition is that the Stokes power be small, formalized as $P_s(0)/P_p(0) \to 0$ [191]. However, this is a strong condition, which can be relaxed provided that other requirements are met.

An analytic expression describing the condition required for linearity can be obtained by studying Eqs. (2.60) and (2.61). The general solution to Eq. (2.60) is

$$P_p(z) = P_p(0) \exp\left[-\int_0^z \left(\frac{g_0}{A_{\text{eff}}} P_s(\zeta) + \alpha\right) d\zeta\right]. \tag{2.65}$$

If the pump power is not depleted due to SBS, then as the pump wave travels through the medium, the only mechanism which reduces the pump power is the intrinsic propagation loss, meaning that the pump power reaching the end of the medium of length L is equal to $P_p(0)e^{-\alpha L}$. This approximation, together with Eq. (2.65) can be used to obtain the formal condition required for the undepleted pummp to hold:

$$\frac{g_0}{A_{\text{eff}}} \int_0^z P_s(\zeta) d\zeta \ll 1. \tag{2.66}$$

The integral in Eq. (2.66) can only be evaluated numerically, because there is no known analytic solution to the coupled equations (2.60) and (2.61). However, it is possible to go one step further. Assuming condition (2.66) is true, then a good approximation to $P_s(z)$ is given by Eq. (2.63). By examining Eq. (2.63), it is clear that $P_s(z)$ can grow to be quite large, thereby contradicting the assumption that Eq. (2.66) is true. Therefore, while condition (2.66) implies Eq. (2.63), Eq. (2.63) does not imply condition (2.66).

For this, in the case that the Stokes power launched into the medium is very small, a good approximation to $P_s(z)$ is given by Eq. (2.63). Provided that the approximation satisfies the condition given in Eq. (2.66), then the approximation can be taken as being accurate. If the approximation does not satisfy condition (2.66), then by contradiction, the approximation is no longer accurate and SBS is not occurring linearly. By substituting Eq. (2.63) into Eq. (2.66), we find

$$\frac{g_0}{A_{\text{eff}}} \int_0^z P_s(\zeta) d\zeta = \Upsilon P_s(L) \tag{2.67}$$

where

$$\Upsilon = \frac{K}{P_p(0)} \left\{1 - e^{-\alpha L} \exp\left(-Ke^{-\alpha L}\right) \cdot \left[e^K + K\text{Ei}\left(Ke^{-\alpha L}\right) - K\text{Ei}(K)\right]\right\} \tag{2.68}$$

is the linearity parameter,

$$K = \frac{g_0}{\alpha A_{\text{eff}}} P_p(0)$$

and

$$\mathrm{Ei}(x) = \int_{-\infty}^{x} \frac{e^{\zeta}}{\zeta} d\zeta$$

is a special function known as the exponential integral.

The linearity parameter Y gives a measure of the amount of pump depletion, or of how linear an SBS interaction is, from the point of view of the Stokes wave. The SBS interaction is seen as a system, characterized by the medium loss α, length L, area A_{eff}, gain coefficient g_0, and the input pump power $P_p(0)$. Y then describes the linearity of this system, in terms of the system parameters, with smaller values signifying a greater linearity.

An example of how the system parameters affect the linearity of the SBS interaction, Fig. 2.6 shows the SBS gain experienced by the Stokes wave for different SBS medium lengths. For all cases, the medium properties were kept constant (other than the length). This was achieved by taking a long strand of standard silica SMF, and cutting it up into multiple shorter sections. The input pump power was then set such that a weak Stokes wave experience 30 dB of SBS gain. As shown in the figure, this was the case for low input Stokes powers and, in this regime, the whole system could be considered as linear. As the Stokes power was increased above a certain threshold however, the gain experienced by the Stokes wave reduced. This was the depleted-pump regime, where the interaction resembled that of a nonlinear system.

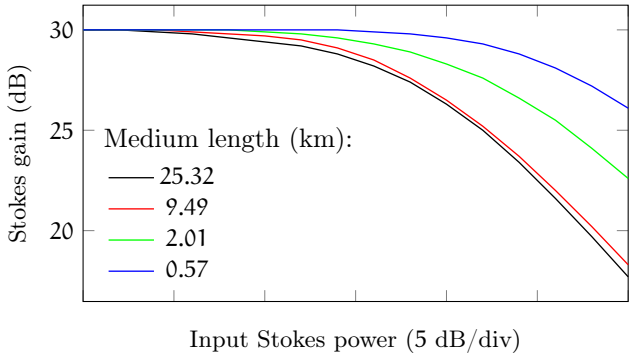

Fig. 2.6. Measured SBS gain on the Stokes wave, as a function of Stokes power, for different SMF lengths.

.

This experiment indicates that, when all other medium properties are maintained constant, shorter media result in more linear SBS interactions, where pump depletion occurs for higher input Stokes powers. In fact, this matches theoretical predictions obtained using Eq. 2.68, shown in Fig. 2.7(a). The greater linearity at shorter medium lengths comes at the cost of a higher input pump power, required to achieve the same level of SBS gain, as shown in Fig. 2.7(b). The simulation illustrated in Fig. 2.7(a) also suggests that the linearity of the system improves for medium lengths greater than 20 km. This is simply

because, as the medium length is increased, the Stokes power undergoes greater propagation losses before it begins being amplified by SBS. Therefore, greater Stokes powers can be launched into longer media, without greatly depleting the pump. This is confirmed by the fact that the 3 dB cut-off for longer media increases exponentially with medium length, similar to the propagation loss. These results show that, when using SBS for MWP signal processing, it is advantageous to operate in shorter media, which is aligned with the current push to move to integrated platforms.

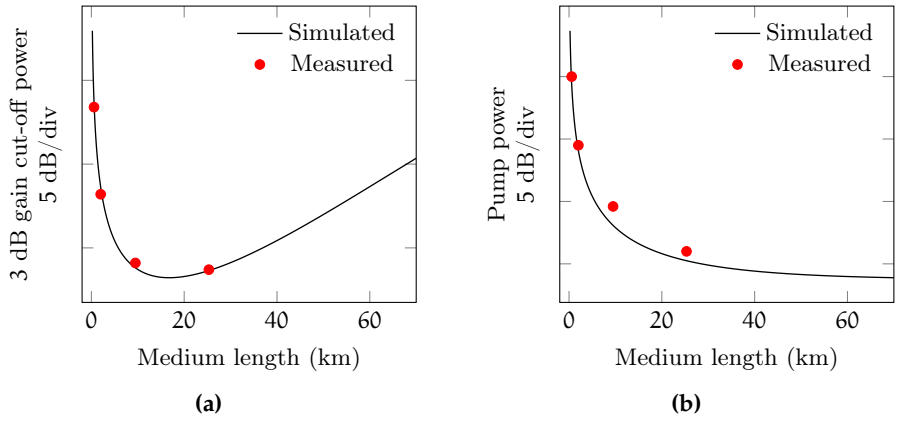

Fig. 2.7. (a) Input Stokes power at which the SBS gain drops by 3 dB. The simulated curve is proportional to 1/Y. (b) Input pump power required to obtain 30 dB of Stokes gain in the undepleted-pump regime.

2.5.2 *Material Platforms for SBS*

Since the its initial observation in optical fibres in 1972 [192], SBS has proven to be extremely useful in a number of areas; notably in ultra-narrow-bandwidth lasers [193–196], sensing [197], slow and fast-light [198–200], and, as discussed previously, in MWP signal processing. In the past, the conventional platform for SBS interactions has been silica-based SMF [188]. The properties of this material are such that, in order to observe significant SBS with modest pump powers ($\sim$ 10-100 mW CW), hundreds if not thousands of metres of fibre are needed. This poses a major obstacle to the application of SBS to real-world systems, since long spools of fibre, as well as being relatively bulky, are highly sensitive to environmental fluctuations like temperature and pressure. The ability to efficiently harness SBS in a short, chip-scale platform represents a significant milestone in the field of photonic signal processing, opening opportunities for integration of a vast array of functionalities.

In recent years, substantial effort has focused on the development of a material platform where SBS can be harnessed over short length scales [108, 201, 202]. Since SBS is, fundamentally, an interaction be-

tween optical and acoustic modes, the main requirement on the material is that both optical and acoustic modes be confined for long enough that the two fields can interact. This requirement is far from trivial; optical and acoustic waves are fundamentally different (one being electromagnetic, the other mechanical), and waveguides capable of confining light are not necessarily capable of confining sound.

It is clear, by observing Eq. (2.59) that, for a given material, the strength of the SBS process depends on the material's Brillouin gain coefficient g_0. This parameter, given by Eq. (2.56) is a function of a number of physical properties of the material. In order to maximize the SBS strength, the material needs to have a low density, a low speed of sound and, most importantly, a high refractive index. This last requirement comes from the fact that the electrostrictive constant scales to the fourth power of the refractive index [168]

$$\gamma_e \sim (n^2 - 1)(n^2 + 2)/3. \tag{2.69}$$

In addition, since the Brillouin linewidth Γ_B is inversely proportional to the phonon lifetime, the material should have a small acoustic damping parameter.

Control of the material properties is difficult in most cases. It is however possible to tailor the waveguide geometry so as to maximize the strength of the SBS interaction, as suggested by Eq. (2.59). While increasing the interaction length L_{eff} is not always possible in photonic integrated circuits, on-chip waveguides are capable of significantly lower optical mode areas A_{eff} compared to standard fibres. The reduction of the effective optical mode area is desirable for two reasons; firstly, it leads to a direct increase in the optical intensity; secondly, at the nanoscale, radiation pressure can lead to great enhancement of the SBS strength [203]. Furthermore, the requirement that both optical and acoustic modes remain confined can be satisfied by appropriate selection of the waveguide's core and cladding materials. It is well-known that for optical guidance, the core must have a higher refractive index than the cladding. In an analogous manner, acoustic confinement requires a large acoustic impedance mismatch between the core and the cladding [204]. The acoustic impedance of a material is a quantity related to the velocity of sound in that material. Therefore, essentially, acoustic confinement occurs when the velocities of sound in the core and the cladding are sufficiently different. If this is not the case, the density wave generated by SBS leaks from the core of the waveguide before the light can interact with it, so that $\eta = 0$, and SBS does not occur. The efficiency of the SBS process is highly dependent on this confinement.

The first demonstration of on-chip SBS occurred in a ChG As_2S_3 rib waveguide, only 7 cm long [205]. ChG is a soft glass with a large refractive index ($n = 2.45$ in [205]) and large electrostrictive constant. These properties lead to a high Brillouin gain coefficient $g_0 \sim 7.4 \times$

10^{-10} m/W, more than 30 times that of silica fibres. Combining a high acousto-optic overlap (using a polymer cladding) with a small 2.3 μm^2 optical mode area, this geometry, shown in Fig. 2.8, is ideal for efficiently harnessing SBS, and SBS strengths up to $G = 5.3$ have been observed [206]. This has led to numerous important demonstrations of integrated functionalities, including lasers [207], slow and fast light [206], frequency combs [208, 209], and MWP signal processors [162, 164–166].

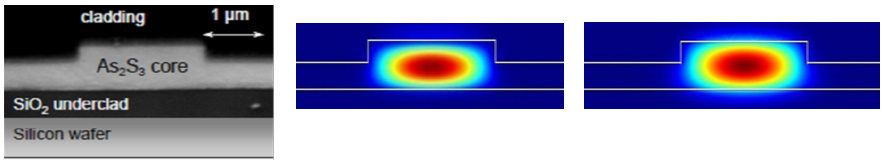

Fig. 2.8. Optical microscope image of a typical ChG rib waveguide, together with simulations of the optical and acoustic modes, showing strong confinement of both fields. Figure adapted from [162].

Table 2.2. SBS parameters for different platforms.

Platform	Gain coefficient, g_0 (m/W)	Linewidth, Γ_B (MHz)	Frequency shift, Ω_B (GHz)
Silica SMF [188]	$1–4 \times 10^{-11}$	~ 30	10–11
As_2S_3 rib waveguide [205]	7.2×10^{-10}	34	7.7
Silicon nanowire[1] [210]	3.2×10^{-10}	30–40	9.2
Si/Si_3N_4 hybrid[1] [211]	2.3×10^{-10}	–	1–18[2]

1 Values are for forward SBS.
2 Dependent on waveguide width.

Silicon is the preferred platform for making photonic integrated circuits, due to its compatibility with CMOS technology, which enables large-scale fabrication of nano-photonic devices at relatively low cost. While silicon's large refractive index ($n = 3.5$) suggests a large Brillouin gain coefficient, SBS in this material has eluded researchers for a number of years. The main cause of this is the fact in silicon on insulator (SOI) devices, the low acoustic impedance mismatch between the silicon waveguide and the silica substrate causes the acoustic mode to leak. This complication was solved by suspending the waveguide in air, and reducing its mode area, so that boundary effects such as radiation pressure could enhance the strength of the SBS process [203, 212, 213]. A Si-Si_3N_4 hybrid structure was used to demonstrate

SBS in a silicon waveguide [211], however the acoustic mode was confined in the silicon nitride, and the measured SBS strength was very low, $G = 0.09$. The first demonstration of significant SBS in a waveguide where both optical and acoustic modes were confined in silicon, took place recently [210]. A waveguide was partially suspended to confine both modes, and the observed SBS strength was $G = 1$, which is still lower than required for most applications. Furthermore, a recent study has demonstrated that nonlinear losses in silicon severely limit the maximum observable SBS strength [214]. This fact, combined with the mechanical constraints of suspended structures, required for acousto-optic confinement, diminish silicon's appeal for SBS-based signal processing.

Table 2.2 shows the SBS characteristics of various integrated platforms demonstrated to date, including standard silica SMF for comparison. These values are for single-pass structures (i.e. where the SBS medium is not embedded in a resonator), as used in MWP applications. It is important to note that ChG, as well as displaying the highest reported Brillouin gain coefficient, unlike silicon-based devices does not require suspension of the waveguide core in order to achieve acoustic confinement. For these reasons, ChG offers the most robust and efficient platform for harnessing SBS on-chip and is the platform of choice for the work presented in Chapters 3 and 4.

3

ULTRAHIGH SELECTIVITY NOTCH FILTER USING ON-CHIP STIMULATED BRILLOUIN SCATTERING

3.1 INTRODUCTION

Microwave filters are used in most microwave systems to select certain frequency components (i.e. channels), while suppressing others. In this chapter, the focus is on notch filters, which suppress a very narrow band of frequencies, without affecting signals falling outside this band. Notch filters find application in electronic warfare (e.g. preventing receiver jamming [215]) or, as shown in Fig. 3.1(a), in any communication system where there is a need to remove self-interference, frequency parasitics, or spurious bands, before sending the signal to the receiver.

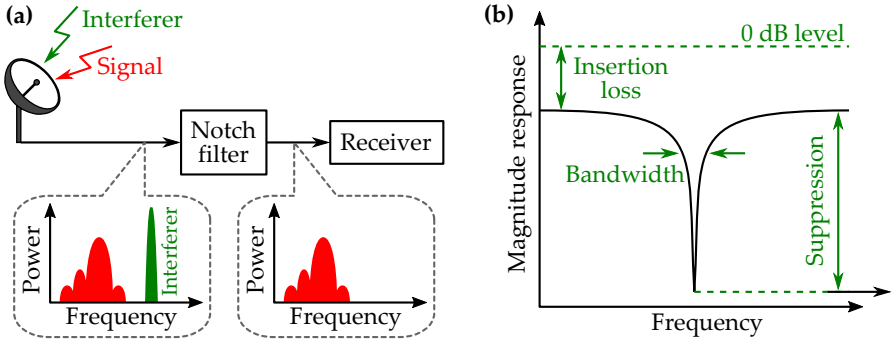

Fig. 3.1. (a) Notch filter being used to suppress an interferer, while letting the signal through to the receiver. (b) Typical notch filter magnitude response, including filter parameters.

Figure 3.1(b) shows the typical response for a notch filter. Desirable characteristics for these filters depend on the application, but in general include a low 0 dB insertion loss, a narrow bandwidth in the kHz-MHz range, and a high suppression. Furthermore, the increasing bandwidth capacity of modern systems has raised demand for notch filters where the frequency of the notch can be tuned over entire microwave bands without compromising the filter performance. As described in Chapter 1, this remains an obstacle for electronic filters, but is achievable with the aid of photonics.

There are two main types of microwave photonic (MWP) notch filters. The first type rely on the same principle as incoherent filters described in Sec. 1.4.1 [72, 74, 216–218]. The appeal of these filters, due to their flexibility, is diminished by a number of serious limitations. These include a high system complexity, a restricted tuning range, and a trade-off between notch bandwidth and free spectral

range (FSR), which greatly limits the operational bandwidth of the filter.

The second type of MWP notch filters rely on the coherent approach whose structure and operating principle are shown in Fig. 3.2. Conversion of the input radio frequency (RF) to the optical domain can occur through intensity modulation but, in the simplest cases, involves single sideband (SSB) modulation. An optical notch filter is then used to filter the optical signal, before it is finally detected with a photodetector (PD). The various implementations of this technique have differed in the type of optical notch filter they employed, with demonstrations using ring resonators [144, 147, 219] or Lyot filters relying on the birefringence of a polarization-maintaining fibre and a phase modulator [220]. The fundamental feature in all these demonstrations, inherent to this type of filter, is the fact that the electrical notch response is a copy of the optical filter's notch response. Due to their simplicity, coherent MWP notch filters are an attractive alternative to multi-tap filters, solving their main limiting trade-off between notch bandwidth and frequency tuning range [70].

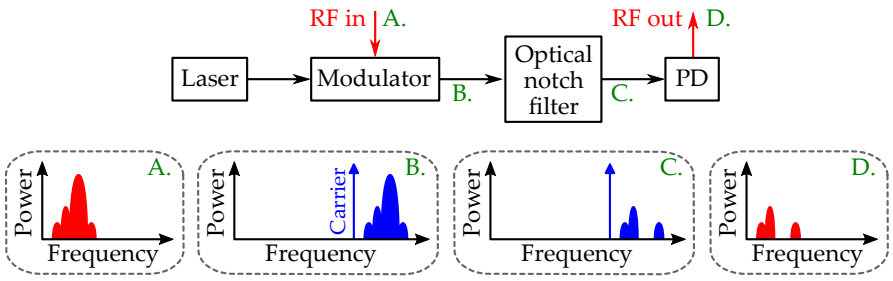

Fig. 3.2. Structure (above) and operating principle (below) of coherent MWP notch filters.

Clearly, the frequency response of coherent MWP notch filters is greatly dependent on the response of the optical notch filters they employ. Unfortunately however, commonly used resonator optical filters suffer from a trade-off between resolution and peak suppression [145, 190, 221], which is reflected in the electrical response of the MWP filter. In order to alleviate this problem, one solution is to use optical filters with extremely narrow linewidths. The loss resonance generated by a stimulated Brillouin scattering (SBS) interaction is one such filter. Indeed, the SBS loss resonance has been used for this very purpose [163], and the resulting MWP filter displayed a 3-dB bandwidth equal to 121.5 MHz (in an As_2S_2 waveguide), which is an order of magnitude lower than that achieved with other optical notch filters [144, 147, 219, 220]. The main obstacle with SBS-based notch filters is the high pump powers they require, in the order of tens or hundreds of milliwatts. This is especially true when the SBS process occurs on-chip, where shorter interaction lengths necessitate substantial

increases in the pump powers, in order to maintain strong SBS resonances.

Cancellation notch filters are a new class of coherent MWP notch filters, which have shown the ability of achieving very high suppressions, independently of the optical notch filter strength. As shown in Fig. 3.3, these use a very similar structure to electrical-to-optical mapping filters. The main difference lies in the spectrum of the modulated optical signal, and how it is processed. Instead of SSB modulation, the modulator is used to generate two optical sidebands. The key lies in the phase and amplitude relationship between the sidebands; they must be in antiphase (i.e. π-out-of-phase), and they must not have the same amplitude. Some optical resonance is then used to equalise the amplitude of the sidebands over the band of the signal which needs to be suppressed. At the photodetector, the mixing between the optical carrier and the optical sidebands generates two RF mixing products. Due to their antiphase relationship, these mixing products interfere destructively. However, complete destructive interference occurs only in the frequency band where the mixing products have the same amplitude (i.e. the filter stopband). Outside of this band (i.e. the filter passband), the mixing products do not completely cancel out, and the RF signal is still present.

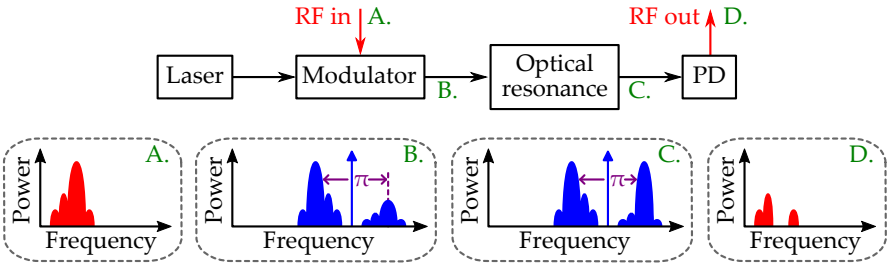

Fig. 3.3. Structure (above) and operating principle (below) of cancellation MWP notch filters. Note the antiphase relationship between the optical sidebands.

While demonstrations of MWP cancellation filters have made use of different optical resonances, from ring resonators [222, 223] to gratings [224, 225], the most promising results have been achieved with SBS [63, 107, 164]. There are two main reasons for this: the SBS linewidth being more narrow than any other resonance, and the ability to easily tune the bandwidth of the resulting notch response, as demonstrated in [164]. In addition, the notch response of cancellation filters is generated solely through destructive interference, meaning that these filters are theoretically capable of ultra-high suppression, irrespective of the strength of the optical resonance. This fact is of vital importance when the SBS interaction occurs in certain integrated platforms such as silicon nanowires, where nonlinear losses greatly inhibit the magnitude of the resonance (e.g. 4 dB in silicon) [214], making it unsuitable for most conventional applications. The smart

optical processing of cancellation filters however enables the exploitation of even the weakest optical resonances, and the realization of ultra-high suppression MWP notch filters.

The next section provides a detailed explanation of the how MWP cancellation filters work, together with the conditions that must be satisfied by the optical signal spectrum in order to obtain high suppression notch responses. In Section 3.3, a cancellation MWP notch filter using on-chip SBS is presented, together with demonstrations of bandwidth tuning, centre frequency tuning, and insertion loss reduction. Finally, Section 3.4 investigates how the destructive interference effect used for forming the notch impacts the stability of the filter. An alternative technique for implementing MWP cancellation filters is presented, with demonstrations of great improvements in the long-term stability.

3.2 WORKING PRINCIPLE

Cancellation filters rely on destructive interference in the electrical domain to provide a high-extinction notch response. The two interfering RF signals are generated by mixing an optical carrier with two optical sidebands, which contain the RF signal content. Therefore, the optical field $E_B(t)$ at the output of the modulator (i.e. step B in Fig. 3.3) must consist of two modulation sidebands, and an optical carrier, written as

$$\begin{aligned} E_B(t) = E_C e^{j\omega_c t + j\theta_C} + E_L e^{j(\omega_c - \omega_{RF})t + j\theta_L} \\ + E_U e^{j(\omega_c + \omega_{RF})t + j\theta_U} + \text{c.c.} \end{aligned} \tag{3.1}$$

where E_C, E_L, E_U are the magnitudes, and $\theta_C, \theta_L, \theta_U$ are the phases of the carrier, lower, and upper frequency sidebands, respectively. The carrier frequency is denoted by ω_c, while ω_{RF} is the frequency of the RF signal into the modulator. If the input RF signal is composed of multiple frequencies, Eq. (3.1) can be rewritten as a sum over all input RF frequencies.

This optical field then encounters the optical resonance. It is important to note that the optical resonance does not affect the whole field. Only the portion of the field spectrum which falls within the resonance linewidth "sees" the resonance. This is shown in Fig. 3.4(a), where the resonance, with complex response $G_R e^{j\phi_R}$, affects a narrow band of the upper sideband. In the figure, this happens only for optical frequencies $\omega_c + \omega_{RF}$ which match the resonance frequency ω_R. When this happens, the processed optical field becomes

$$\begin{aligned} E_C(t) =& E_C e^{j\omega_c t + j\theta_C} + E_L e^{j(\omega_c - \omega_{RF})t + j\theta_L} \\ &+ \begin{cases} G_R E_U e^{j(\omega_c + \omega_{RF})t + j\theta_U + j\phi_R} & \text{for } \omega_c + \omega_{RF} = \omega_R \\ E_U e^{j(\omega_c + \omega_{RF})t + j\theta_U} & \text{otherwise} \end{cases} + \text{c.c.} \end{aligned} \tag{3.2}$$

where G_R is the amplitude gain, while ϕ_R is the phase shift provided by the optical resonance.

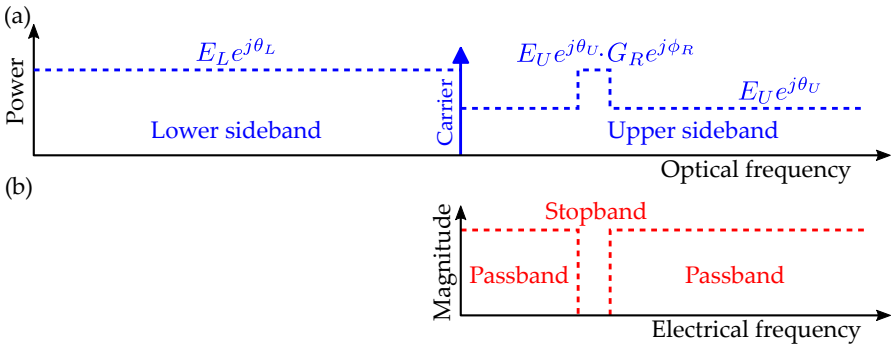

Fig. 3.4. (a) Optical signal spectrum after having been processed by the optical resonance. (b) The resulting notch filter response, after photodetection of the signal shown in (a). The portion of the sideband affected by the optical resonance corresponds to the notch frequency in the electrical domain.

Finally, upon reaching the photodetector, the processed optical field undergoes heterodyning detection. The generated output RF signal, $i_{\text{out}}(t)$ is directly proportional to the detected optical power. At this point, we are interested only in the portion of the optical signal affected by the resonance, since this is the portion that undergoes destructive interference, resulting in a notch as shown in Fig. 3.4(b). Assuming $E_C \gg E_L, E_U$, the mixing products generated upon photodetection are

$$\begin{aligned} i_{\text{out}}(t) &\propto E_D(t) E_D^*(t) \\ &\propto E_L \cos(\omega_{\text{RF}} t + \theta_C - \theta_L) \\ &\quad + G_R E_U \cos(\omega_{\text{RF}} t - \theta_C + \theta_U + \phi_R) \end{aligned} \tag{3.3}$$

where the * symbol denotes the complex conjugate operator. It is clear that for the two mixing products in Eq. (3.3) to cancel out, they must have the same amplitude

$$E_L = G_R E_U \tag{3.4}$$

and they must be π-out-of-phase

$$2\theta_C - \theta_L - \theta_U - \phi_R = \pm\pi. \tag{3.5}$$

Equations (3.4) and (3.5) are the amplitude and phase conditions, respectively, which must be satisfied by the RF mixing products in order to obtain a notch response. When these are satisfied, perfect signal cancellation at the output of the filter occurs, and the notch depth is, theoretically, infinitely large, independently from the strength of the optical resonance.

3.3 NOTCH FILTER WITH DPMZM FOR SPECTRAL TAILORING OF SIDEBANDS

The previous section derives the requirements on the phase and amplitude of the carrier and modulation sidebands [i.e. Eqs. (3.4) and (3.5)], which must be satisfied in order to obtain a notch response for a given optical resonance $G_R e^{j\phi_R}$. These requirements can be summarized as follows: (1) the modulator needs to generate a dual-sideband modulated carrier; (2) the amplitude and phase of the modulation sidebands need to be independently adjustable such that the sidebands have equal amplitude and opposite phase in the range of frequencies affected by the optical resonance. Both of these requirements can be satisfied simultaneously when the modulator used is a dual-parallel Mach-Zehnder modulator (DPMZM).

A DPMZM is a device comprising five optical phase electro-optic modulators (EOMs) [226], as shown in Fig. 3.5. Two pairs of phase modulators are connected to form two parallel Mach-Zehnder structures in a push-pull configuration. Each of these has both an RF and a DC input. An RF hybrid coupler is used so that the signals fed to the Mach-Zehnder structures are 90° out of phase. In the lower arm, a phase modulator is DC-biased, to act as a broadband optical phase shifter. In the small-signal regime, the output of a DPMZM consists of two sidebands and an optical carrier, with phasor representation given by

$$\begin{aligned} E_C e^{j\theta_C} =& J_0(m_{RF1}V_{RF}) \cos\left(\frac{\theta_A}{2}\right) \exp\left(j\frac{\theta_A}{2}\right) \\ &+ J_0(m_{RF2}V_{RF}) \cos\left(\frac{\theta_B}{2}\right) \exp\left(j\frac{\theta_B}{2} + j\theta_C\right) \end{aligned} \tag{3.6}$$

$$\begin{aligned} E_L e^{j\theta_L} =& - J_1(m_{RF1}V_{RF}) \sin\left(\frac{\theta_A}{2}\right) \exp\left(j\frac{\theta_A - \pi}{2}\right) \\ &+ J_1(m_{RF2}V_{RF}) \sin\left(\frac{\theta_B}{2}\right) \exp\left(j\frac{\theta_B}{2} + j\theta_C\right) \end{aligned} \tag{3.7}$$

$$\begin{aligned} E_U e^{j\theta_U} =& J_1(m_{RF1}V_{RF}) \sin\left(\frac{\theta_A}{2}\right) \exp\left(j\frac{\theta_A - \pi}{2}\right) \\ &+ J_1(m_{RF2}V_{RF}) \sin\left(\frac{\theta_B}{2}\right) \exp\left(j\frac{\theta_B}{2} + j\theta_C\right) \end{aligned} \tag{3.8}$$

where $J_n(\cdot)$ is an n^{th}-order Bessel function of the first kind, m_{RF1} and m_{RF2} are the modulation indices for the two Mach-Zehnder structures present in the DPMZM, V_{RF} is the amplitude of the input RF signal, and $\theta_i = m_{\text{DC}} V_i$, where $i = A, B, C$ and m_{DC} is the DC modulation index. By varying the DC bias voltages V_A, V_B and V_C to the DPMZM, it is possible to control the phase and amplitude of the output fields.

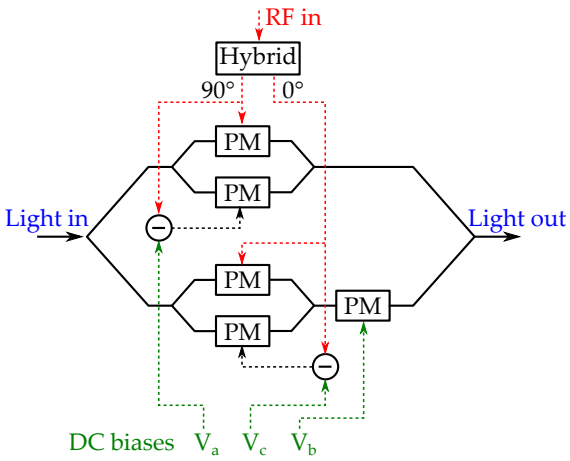

Fig. 3.5. Structure of a DPMZM. PM: phase modulator.

A DPMZM is convenient for electrical-to-optical conversion of the input RF signal in a cancellation MWP filter since it offers a convenient way for synthesizing an optical signal which satisfies the required amplitude and phase conditions expressed in Eqs. (3.4) and (3.5). In fact, DPMZMs have also been used for achieving SSB-modulated signals to be utilized in the more conventional coherent MWP notch filters from Fig. 3.2 [163]. Therefore, when using a DPMZM, one effectively has the option of implementing either a cancellation or a coherent notch filter. In the current work, this is convenient as it permits a direct comparison between these two different filtering techniques, simply by adjusting the DC bias voltages.

The experimental setup of an MWP cancellation notch filter using a DPMZM for the sideband tailoring is shown in Fig. 3.6. In this particular setup, the optical resonance is provided by SBS in a chalcogenide (ChG) optical waveguide. Two separate distributed feedback (DFB) lasers are used for generating the SBS pump and probe waves. The probe laser is sent through a DPMZM, where it is modulated by the input RF signal to be filtered. The modulated signal's power is then adjusted with an erbium-doped fibre amplifier (EDFA), before it is launched into the ChG waveguide. Here the SBS interaction affects one of the modulation sidebands, as shown if Fig. 3.4, after which the optical signal is detected by a PD. A polarisation controller (PC) is used before the DPMZM to minimise its insertion loss. Similarly, two PCs are used for both pump and probe waves entering the chip, both to minimise coupling losses to the waveguide, and to maximise the strength of the SBS interaction. Finally, a vector network analyser (VNA) is used to measure the electrical frequency response of the whole system.

The ChG waveguide used here is a 6.5 cm long, As_2S_3 rib waveguide, with cross section dimensions of 4 μm $\times$ 0.85 μm, and 2.3 μm^2 optical mode area. Due to its material properties and its high confinement of both optical and acoustic modes, it exhibits a large Brillouin gain coefficient $g_0 = 0.74 \times 10^{-9}$ m/W [205]. Coupling to the waveguide is

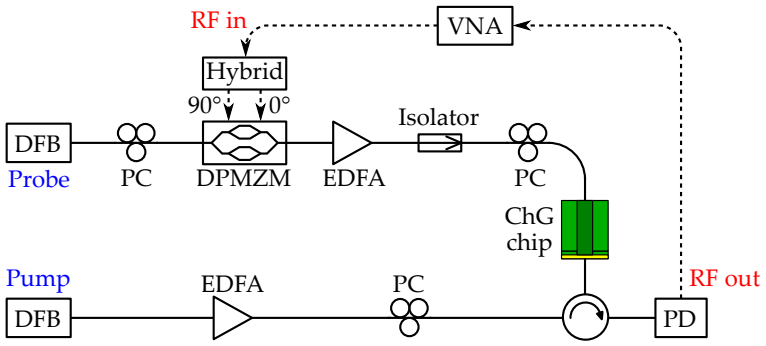

Fig. 3.6. Experimental setup for a cancellation notch filter, where the EOM is a DPMZM, and SBS is used as the optical resonance. DFB: distributed feedback laser; PC: polarisation controller; EDFA: erbium-doped fibre amplifier; ChG: chalcogenide; PD: photodetector; VNA: vector network analyser.

achieved through the use of lensed fibres, for a typical insertion loss of 9.5 dB, comprising 0.3 dB/cm propagation loss, and 3.5 dB/facet coupling loss.

Figures 3.7(a) and (b) show the optical power spectrum at the output of the modulator, where the optical carrier wavelength is 1550.4 nm, and the input RF signal is a 15 GHz tone. Figure 3.7(a) depicts an SSB-modulated signal, where only the upper frequency sideband is present (the lower sideband, being 100 times weaker, is considered suppressed). In Fig. 3.7(b) however, both sidebands are present, but their powers differ by 1 dB, and they are in antiphase.

An optical-to-electrical mapping filter can be implemented using the modulated signal from Fig. 3.7(a). Indeed, the response for such a filter is shown in Fig. 3.7(c), where the SBS loss resonance is used as the optical notch filter. For the current ChG waveguide, 350 mW of pump power correspond to an SBS loss resonance 20 dB deep. This depth is exactly matched by the response of the notch filter. If the pump power is reduced from 350 mW to 8 mW, the suppression of the notch filter reduces to 1 dB, much too low for any application. However, if this 1 dB SBS resonance is used to equalise the sidebands from the spectrum in Fig. 3.7(b), the cancellation conditions (3.4) and (3.5) are satisfied, and destructive interference occurs in the electrical domain. The resulting notch response has an ultra-high suppression surpassing 55 dB, limited by the noise floor of the system.

It is clear, from Fig. 3.7(c), that the response of the cancellation filter is much closer to that of an ideal notch filter. The importance of this result can be further appreciated by considering a situation resembling a real-world application of notch filters. Figure 3.8 shows two spectra where a desired signal is in the vicinity of a much stronger, unwanted interferer. In this experiment, the desired signal was generated by modulating an RF tone with a frequency of 11.982 GHz and power of -9 dBm. The modulation signal was a triangular waveform with 30 kHz frequency and 1 V peak-to-peak amplitude generated

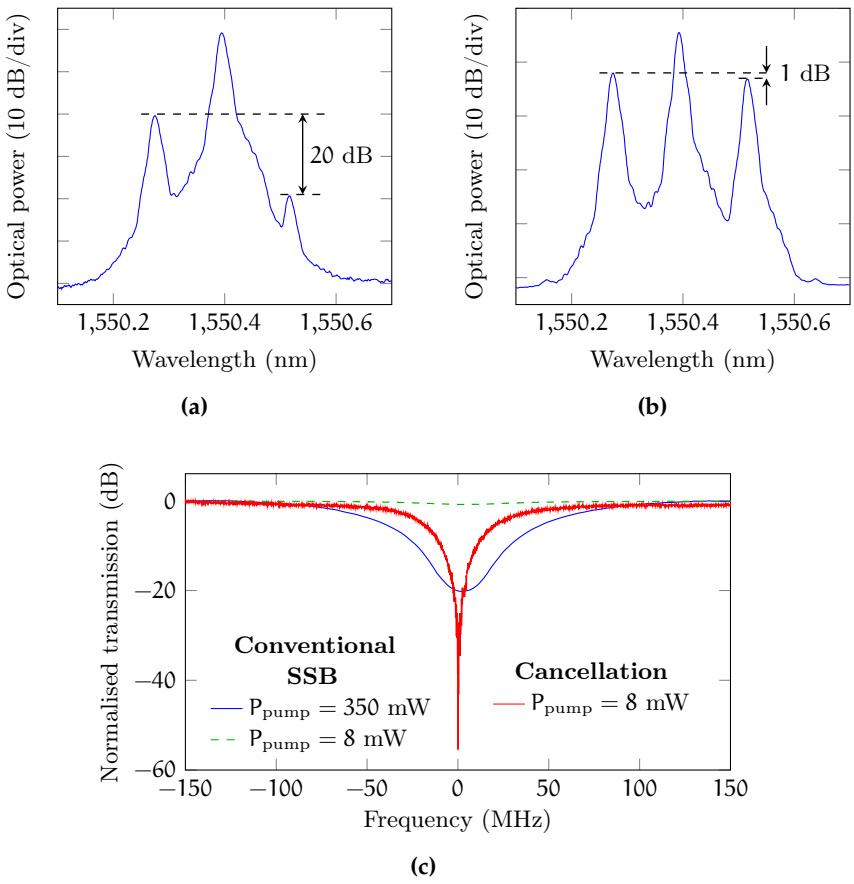

Fig. 3.7. Optical power spectrum at the output of the DPMZM for (a) SSB modulation; (b) phase modulation with unmatched sidebands. (c) Corresponding VNA traces depicting filter responses for the conventional coherent (SSB-based) and cancellation filters. For the same low pump power (8 mW), the SSB filter yields 0.8 dB suppression, while the cancellation filter yields 55 dB suppression.

using an arbitrary waveform generator. This created a band-limited signal with 1 MHz width and peak power of −21 dBm. The unwanted interferer was instead generated using a separate RF source, with frequency 12.002 GHz and 0 dBm output power. These two RF signals were then combined to simulate the input into an antenna, for instance, where the desired signal is contaminated by a much stronger, unwanted interferer. If this signal were to be detected as is, the interferer, being 100 times stronger, would completely mask the target signal. It is in situations such as this that notch filters become necessary.

To compare the efficacy of both conventional SSB-based and cancellation filter, the desired signal and unwanted interferer were simultaneously input to the DPMZM, maintaining the setup shown in Fig. 3.6. Other than adjusting the DPMZM biases, the SSB-based filter was generated by using the SBS loss resonance with 28 dBm pump power

at the chip facet creating 17 dB of peak suppression. The cancellation filter was created using 4 dB of SBS gain from 21 dBm of pump power at the chip facet. The chip insertion loss in these measurement was 8.8 dB. In both measurements, the filter response was aligned to achieve maximum suppression at the unwanted interferer frequency of 12.002 GHz.

The output RF spectra, after filtering with the current SSB-based and cancellation filters are shown in Figs. 3.8(a) and (b), respectively. These were measured with an electrical spectrum analyser, across a 50 MHz span, with 100 MHz resolution bandwidth. As expected, in the conventional filter case, the interferer power was reduced by 17 dB, but the signal also experienced a high 9 dB attenuation. In contrast, the cancellation filter was able to completely remove the interferer, imparting it with 47 dB attenuation, while the signal was only attenuated by 2 dB. These measurements clearly demonstrate the superior response of cancellation filters which, using a weaker optical resonance, are able to achieve ultrahigh suppression across a narrower bandwidth, compared to conventional MWP filters.

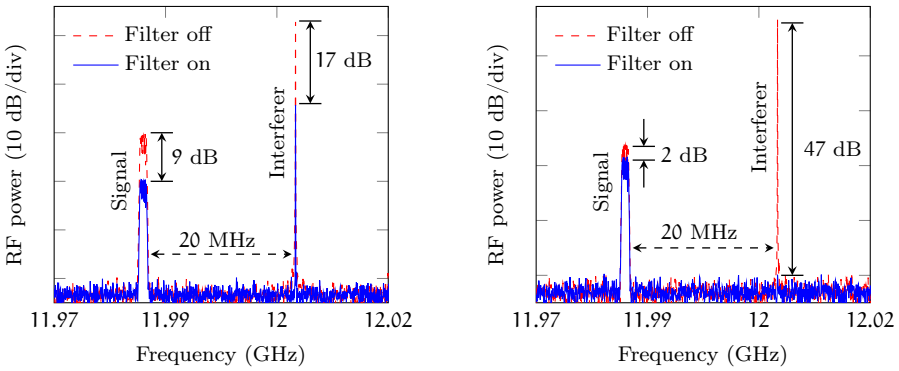

Fig. 3.8. Input and output spectra of a typical microwave signal, and an interferer, after undergoing filtering with through SBS in a (a) conventional SSB-based filter; (b) cancellation filter.

3.3.1 *Bandwidth Tuning*

The bandwidth of the electrical notch response is, to a good approximation, equal to the bandwidth of the optical resonance. When SBS is used as the optical resonance, control of the SBS bandwidth therefore can be used for tuning the notch bandwidth. There is a general understanding in the literature that the bandwidth of the SBS gain or loss resonance can only be adjusted through tuning of SBS linewidth Γ_B, which is a material property of the SBS medium [227, 228]. While such tuning is possible, it requires modifications of the acoustic properties of the SBS medium (e.g. through temperature changes), which

is not always a convenient option. In fact, a way exists to tune the SBS resonance which does not involve any such changes to the SBS medium.

To understand how this is possible, it is important to distinguish between the SBS linewidth Γ_B, and the bandwidth of the SBS resonance. The former is, by definition, the full width at half maximum (FWHM) of the Lorentzian function present in the exponent in Eq. (2.57). The latter is the FWHM of the SBS resonance, which comprises the whole of Eq. (2.57). By using this equation, it is simple to show that the bandwidth of the SBS resonance is given by

$$\Delta\omega_{\text{SBS}} = \Gamma_B \sqrt{\frac{G}{\ln(e^G + 1) - \ln 2} - 1}. \tag{3.9}$$

This expression shows that the bandwidth of the SBS resonance can be controlled simply by changing the strength of the SBS interaction, G (e.g. by changing the SBS pump power). Moreover, the bandwidth depends on whether the optical resonance is achieved using the SBS gain ($G > 0$) or loss ($G < 0$) response.

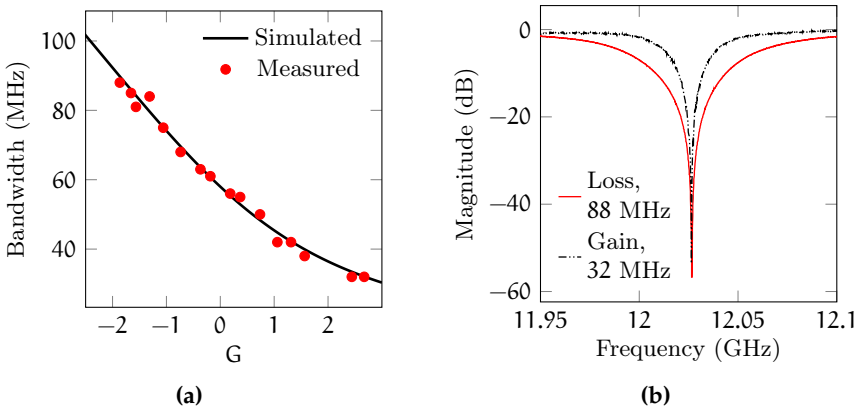

Fig. 3.9. (a) Simulation (line) and measurement (dots) of the cancellation filter bandwidth, as a function of SBS strength G. (b) Electrical response of the cancellation filter using SBS loss ($G < 0$, red) and SBS gain ($G > 0$, black) as the optical resonance.

Figure 3.9 demonstrates tuning the bandwidth of the cancellation notch filter setup from Fig. 3.6 by varying the SBS pump power (i.e. the SBS strength G). The measured values closely match the trend calculated using Eq. (3.9), with $\Gamma_B = 58$ MHz for the ChG chip used in the experiment.

These measurements show two great advantages that cancellation notch filters have over optical-to-electrical mapping filters. The first is that cancellation notch filters are not limited to rely on optical notch filters (i.e. loss resonances), to achieve filtering. The fact that they can exploit both loss and gain resonances (as in SBS) means that they can achieve an extended bandwidth tuning range. The second

and main advantage is that, in cancellation filters, the notch bandwidth is independent from the notch suppression. Conventional MWP notch filters, where the electrical response matches the response of the optical notch filter used, suffer from an inherent trade-off between suppression and bandwidth. For cancellation filters however, the suppression is solely dependent on how well Eqs. (3.4) and (3.5) are satisfied, while the optical resonance determines the width of the notch. For this reason, cancellation notch filters can simultaneously achieve high suppression and a narrow bandwidth.

3.3.2 *Notch Frequency Tuning*

One of the main advantages that MWP notch filters have over electronic-based notch filters is the ability to tune the notch frequency over wide bandwidths, without loss in performance. This means that the same notch filter can be used for filtering signals over many microwave bands.

Considering the filter setup from Fig. 3.6, the optical resonance used for sideband equalisation can be provided either by the SBS gain or the SBS loss responses. For a pump frequency ω_p, and Brillouin frequency shift Ω_B, the SBS loss resonance occurs at frequency $\omega_p + \Omega_B$. The electrical frequency of the notch, ω_{notch}, is given by

$$\omega_{\text{notch}} = \left|\omega_p + \Omega_B - \omega_c\right| \tag{3.10}$$

where ω_c is the carrier frequency. If instead the SBS gain resonance is used for sideband equalisation, the notch frequency occurs at

$$\omega_{\text{notch}} = \left|\omega_p - \Omega_B - \omega_c\right|. \tag{3.11}$$

These expressions clearly show that, whether SBS gain or loss is used, tuning of the notch frequency simply requires one to tune the frequency of either the carrier or of the SBS pump. In practice, this can be done with sub-kilohertz accuracy [107]. The Brillouin frequency shift depends on the material properties and can therefore be considered constant for a given platform. Nevertheless, its value can be altered by applying a strain or by changing the temperature of the SBS medium [229–232], providing another possible way of tuning the notch frequency.

Figure 3.10 demonstrates tuning of the centre notch frequency by changing the SBS pump frequency. As can be seen, the filter performance (in terms of bandwidth and suppression) remains unaltered as the centre frequency is tuned. The enormous tuning range of lasers means that, in principle, the notch frequency could be continuously tuned across the whole RF and microwave spectra. In practice however, this range is reduced due to the limited bandwidth of the modulator and of the PD.

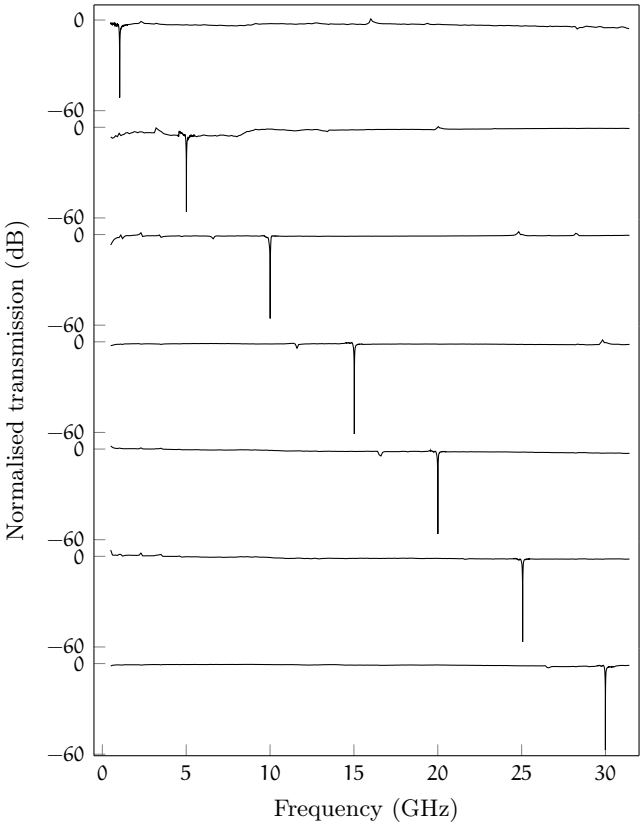

Fig. 3.10. Tuning of the notch frequency by tuning of the SBS pump laser's wavelength.

3.3.3 *Insertion Loss*

In the stopband of a cancellation filter, the optical resonance causes the mixing products to interfere destructively, leading to an ultra-high suppression region. This same principle however is the cause for the main drawback of such filters. That is, partial destructive interference in the passband causes the link gain, or insertion loss, of cancellation filters to degrade beyond the norm for conventional MWP notch filters.

The reason behind this insertion loss degradation effect is illustrated in Fig. 3.11(a). In general, in an SBS-based cancellation notch filter, the phase and amplitude of the sidebands are tailored such that the electrical notch response coincides with the centre of the SBS gain (or loss) resonance. The main reason for doing this is that the notch response obtained in this manner is symmetric in frequency. However, at the centre of the SBS resonance, the SBS phase contribution is zero, so that in order to achieve a cancellation notch, the modulation sidebands must be generated out of phase. Essentially the modulation format is similar to phase modulation, and the RF mixing products, being in antiphase, interfere destructively in both the stopband and the passband, increasing the filter insertion loss.

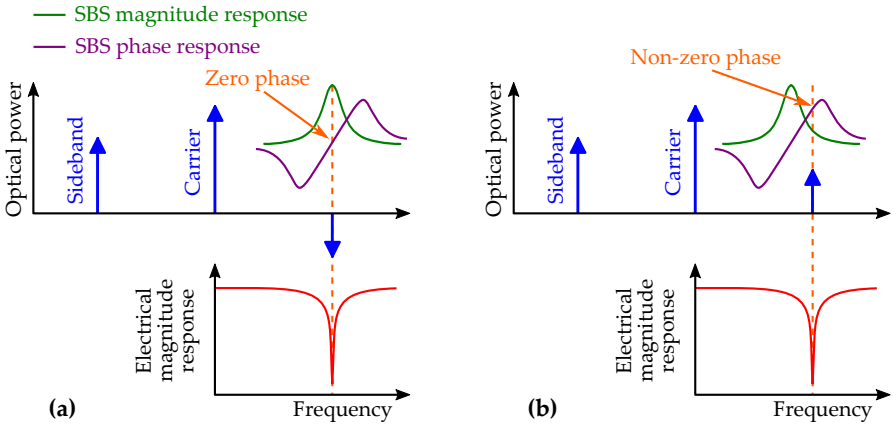

Fig. 3.11. Optical signal spectrum and resulting electrical notch response when the cancellation condition is satisfied (a) in the centre of the SBS gain resonance, where $\phi_R = 0$; (b) off-centre from the SBS gain resonance, where $\phi_R \neq 0$.

This reasoning suggests that if the phase and amplitude conditions (3.4) and (3.5) were to be satisfied at a frequency detuned from the SBS resonance centre, the insertion loss of the filter could be reduced. This principle, illustrated in Fig. 3.11(b), relies on using both the amplitude and the phase contributions of SBS to achieve a notch response. In this way, the mixing products are in antiphase only in the filter stopband, and they no longer destructively interfere in the passband. In general however, this technique does not lead to an insertion loss reduction.

This effect can be understood in terms of the mixing products in the filter passband. The output RF power in the filter passband, away from the frequency of the optical resonance, is

$$P_{\text{RF,out}} \propto \left| E_C E_L e^{j(\theta_C - \theta_L)} + E_C E_U e^{j(\theta_U - \theta_C)} \right|^2. \tag{3.12}$$

Due to the phase and amplitude conditions (3.4) and (3.5) which must be satisfied by the sidebands and carrier, this expression can be rewritten as

$$P_{\text{RF,out}} \propto E_C^2 E_U^2 \left| 1 - G_R e^{j\phi_R} \right|^2 \tag{3.13}$$

and since the sideband amplitude level is, in the small signal approximation, directly proportional to the input RF power, the insertion loss of a cancellation filter can be expressed as

$$\begin{aligned} \text{Insertion loss} &= \left. \frac{P_{\text{RF,in}}}{P_{\text{RF,out}}} \right|_{\text{passband}} \\ &\propto \frac{1}{E_C^2 \left| 1 - G_R e^{j\phi_R} \right|^2}. \end{aligned} \tag{3.14}$$

Equation (3.14) highlights the two independent variables which can be adjusted to control the filter insertion loss: the optical carrier power,

E_C^2, and the phase and amplitude contribution of the optical resonance at the frequency where the cancellation conditions (3.4) and (3.5) are satisfied, $G_R e^{j\phi_R}$.

When the cancellation conditions are satisfied in the centre of the SBS gain or loss resonance, SBS gives a zero phase contribution according to Eq. (2.58), and $\phi_R = 0$. If however, by altering the DC bias voltages of the DPMZM, one changes the phase and amplitude relations between the modulation sidebands, it is possible that cancellation conditions (3.4) and (3.5) are satisfied at a frequency detuned from the SBS centre, where $\phi_R \neq 0$. The actual phase contribution from the SBS in this case depends both on the SBS strength parameter G, and on the amount of detuning. Using Eq. 3.14, Fig. 3.12 simulates the effect that such frequency detuning has on the insertion loss of an SBS-based cancellation filter. The quantity being plotted is the insertion loss degradation of the cancellation filter relative to a conventional SSB-based coherent MWP notch filter.

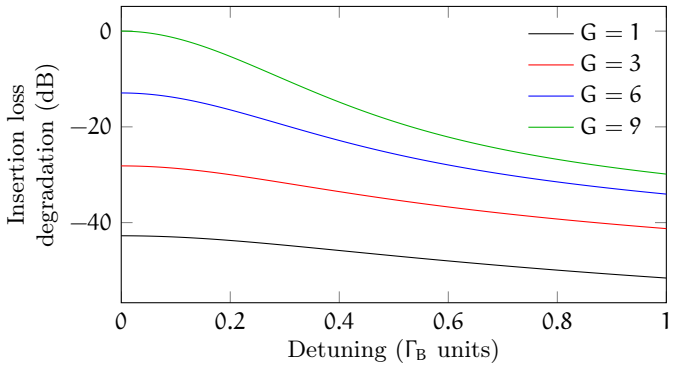

Fig. 3.12. Degradation of the insertion loss of a cancellation filter, compared to a conventional SSB-based MWP filter, as the cancellation conditions are satisfied at a frequency detuned from the centre of the SBS resonance. The detuning is given in units of the SBS linewidth Γ_B. The curves indicate different levels of SBS strength G.

The trend displayed by these simulations is that the insertion loss degrades the least when a stronger SBS resonance (with higher G parameter) is used to achieve cancellation. This is simply because, according to the amplitude condition (3.4), as the SBS strength is increased, so does the mismatch between the two sidebands' powers. Effectively, for a very strong SBS resonance, the optical signal spectrum approaches that of an SSB-modulated signal, and the destructive interference of the RF mixing products in the passband becomes negligible. In this way, the insertion loss of a cancellation filter can is approximately equivalent to that of a conventional SSB-based MWP notch filter. Unfortunately however, using strong SBS resonances is not practical, particularly when the SBS interaction occurs on-chip. The simulations also indicate that the insertion loss of a cancellation filter is minimum when the cancellation condition occurs at the centre of

the SBS resonance. The reason for this is that, while it is true that away from the SBS centre, the modulation sidebands no longer have to be in antiphase, the fact that the SBS magnitude contribution reduces off-centre means that the mismatch between the sideband's powers must also reduce, so that the signal spectrum no longer resembles that of an SSB-modulated signal.

The simulation from Fig. 3.12 were performed assuming that, as the cancellation conditions are satisfied away from the centre of the SBS resonance, the only signal parameters which change are the phase and amplitude of the modulation sidebands. In practice however, this is not the case, particularly when the modulator used is a DPMZM. That is, when the bias voltages of a DPMZM are changed to tune the phase and amplitude of the modulation sidebands such that the cancellation condition is satisfied away from the resonance centre, it is not just the sidebands' fields which change, but also the field of the optical carrier. This effect is important because, according to Eq. (3.14), the carrier power has an effect on the filter insertion loss.

By taking into account the effect of the DPMZM, the simulations in Fig. 3.13(a) indicate that when the strength of the SBS resonance is $G > 4$, the insertion loss of an SBS-based cancellation filter improves if the cancellation conditions are satisfied at a frequency detuned from the centre of the resonance. This is due to the amplitude and phase requirements on the sidebands, which cause the modulator to operate at a bias point where the carrier power is high, reducing the overall insertion loss. When using a DPMZM therefore, achieving the notch away from the centre of SBS resonance can reduce the insertion loss of the cancellation filter to the same level as that of conventional SSB-based MWP notch filters, as shown in Fig. 3.13(b). However, the fact that this technique relies on using a DPMZM, and that it only works for relatively high SBS strengths, make it unsuitable for general operation, such as when the SBS strength needs to be continuously varied (e.g. for tuning the notch bandwidth).

A different technique for reducing the insertion loss of a cancellation filter is to increase the optical power into the modulator (i.e. the optical carrier power), as suggested by Eq. (3.14). In fact this is a very general, well-known technique, previously explained in Sec. 1.3.3, effective not just when using a DPMZM, or in the case of cancellation filters, but of any MWP filter as well. However, the unique properties of cancellation filters cause this technique to be particularly effective and of great importance when operating on-chip.

To understand the principle behind this insertion loss reducing technique, it is important to note that for various reasons, such as photosensitivity [161], heating [162], or intensity-dependent losses [210], many on-chip devices are not suited to handle high optical power. In the case of an SBS-based notch filter, this is particularly problematic because it is not just the optical signal propagating along the chip,

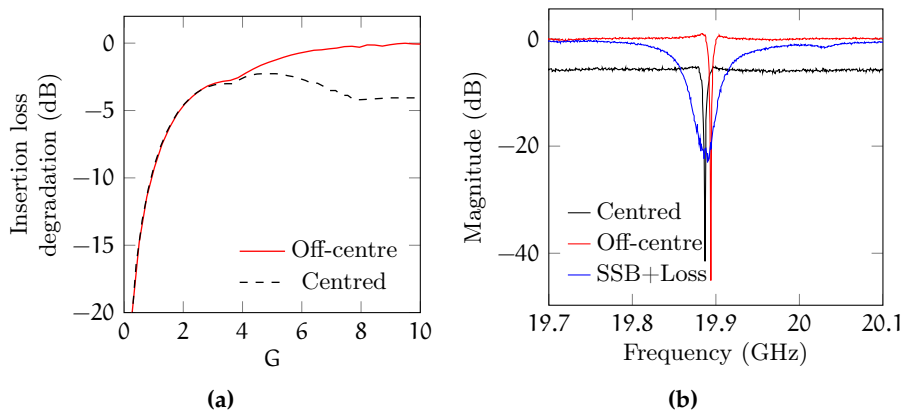

Fig. 3.13. (a) Simulation of the insertion loss degradation of a DPMZM-based cancellation filter for cancellation conditions satisfied off-centre (red) and in the centre (black) of the SBS resonance. (b) Filter response for a cancellation filter where the cancellation conditions are satisfied in the centre (black) and 7 MHz off-centre (red) of the SBS resonance. The response of an SSB-based notch filter (blue) is shown for comparison.

but the SBS pump power as well. In these situations, a limited power budget must be distributed between the waves that undergo the SBS interaction in the chip: the pump and the signal. Since cancellation filters are able to function even with minimal resonances (i.e. low SBS pump powers), more power can be budgeted for the signal carrier, reducing the insertion loss.

This power budgeting procedure is demonstrated in Fig. 3.14, which shows amplitude responses for the filter setup from Fig. 3.6. The blue curve shows the response of an SSB-based optical-to-electrical mapping filter, where 25 dBm of power is allocated to the SBS pump. Such high optical power for the pump is indispensable in such filters, where the amount of suppression scales with the SBS strength G. In order to avoid damage to the chip, the signal is given 20 dBm of power before being launched into the ChG waveguide. This corresponds to an RF insertion loss of -37.7 dBm, obtained with 3 mA of current at the PD. The optical power distribution is then reversed in order to obtain the cancellation notch response (red curve). The SBS pump power, now being 20 dBm, results in only 4 dB of SBS gain, which is converted to 55 dB of RF suppression. The 25 dBm signal, once detected, generates 10 mA of average current, achieving a 6 dB improvement in the filter insertion loss compared to the SSB-filter case. Therefore, SBS-based cancellation notch filters allow for efficient redistribution of the optical power from the SBS pump to the carrier, which is an effective technique for reducing the insertion loss when operating on-chip.

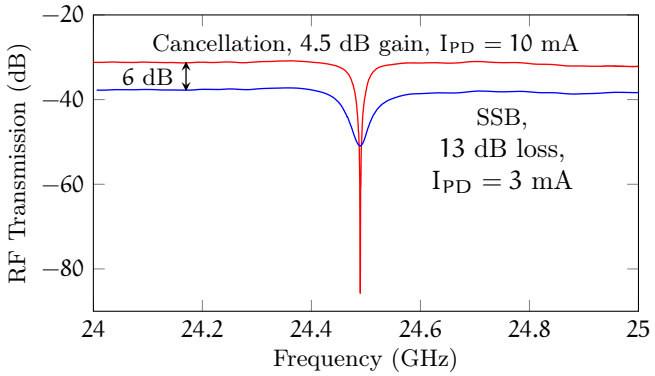

Fig. 3.14. Filter insertion loss reducing through optical power redistribution. Experiments are for an optical power budget of 500 mW at the facets of the optical chip. Blue trace: conventional SSB-based approach with 25 dBm of input pump power and 20 dBm of signal power. Red trace: cancellation approach with 20 dBm of pump power and 25 dBm of signal power. I_{PD} is the detected photocurrent.

3.3.4 *Noise Figure*

There is an inherent advantage to using SBS for notch filtering. This is that the noise figure of the filter, as measured in the passband, is largely unaffected by the noise generated through the SBS process.

SBS leads to the generation of noise due to spontaneous Brillouin scattering of a pump wave off of thermally-excited sound waves [233]. This process, although inefficient, is rapidly reinforced through the interaction of the spontaneously scattered field with the pump wave. Such interaction results in an unwanted, secondary SBS process leading to noise formation in the vicinity of the Stokes and anti-Stokes frequencies, relative to the pump wave.

Early studies with Brillouin fibre amplifiers indicated that such amplifiers suffered from significantly higher noise figures, compared to other types of amplifiers, such as those based on Raman scattering [234, 235]. In those studies, the higher SBS noise figure was partly attributed to the narrow Brillouin linewidth, which causes all the SBS-generated noise to be concentrated in a relatively small band.

However, the fact that the SBS-generated noise spans only the Brillouin linewidth is advantageous when SBS is used for notch filtering. In this situation, the Brillouin linewidth corresponds to the filter stopband, while the filter passband remains unaffected by the SBS process and the associated noise. Such would not be the case for an SBS-based MWP bandpass filter, where the signal of interest coincides with the SBS gain spectrum.

For this reason, the noise figure of the notch filter can be said to be equivalent to that of a standard MWP link. As explained in Sec. 1.3.3, the insertion loss typically dominates the noise figure of such links. Therefore, the single most important step towards reducing the noise

figure of the filter is to reduce the insertion loss, using the techniques discussed in Sec. 3.3.3.

Having discussed the most important figures of merit of the present notch filter, we proceed to compare its performance with other state-of-the-art on-chip MWP notch filters. The results, summarized in Table 3.1, show that the present SBS-based cancellation notch filter is capable of a bandwidth almost two orders of magnitude lower than any other MWP filter. In fact, the bandwidth of the SBS-based cancellation notch filter is comparable to that of low-loss electronic filters [236], while maintaining the large tuning range characteristic of photonics. The present filter also exhibits the highest quality factor, defined as the ratio of the filter's 3 dB bandwidth to the central frequency of the resonance. Currently, the main challenge is to reduce the filter insertion loss (and hence the noise figure), which at 30 dB is comparable to other MWP implementations but still too large for real-world applications. One possible approach would be to reduce the losses in the system, currently dominated by the insertion loss of the ChG waveguide. This is measured in the experiment of Sec. 3.3 to equal 9.5 dB, thus accounting for a 19 dB deterioration in the link gain. Chip packaging followed by well-designed pre- and post-amplification stages could see the filter insertion loss drop to levels on par with traditional electronic filters.

Table 3.1. Performance comparison of different on-chip MWP notch filters. Type a: cancellation; Type i: incoherent; Type c: coherent; Type e: electronic.

Technology	Type	Bandwidth (MHz)	Tuning range (GHz)	Insertion loss (dB)	Highest Q
SBS (this work)	a	33–88	1–30	30	375
Photonic crystal [72]	i	1000	10–30	45	N/A
Si_3N_4 ring [222]	a	247–850	2–8	30	28
Si ring [144]	c	910	2–15	N/A	16
Si ring [147]	c	6000	2.5–17.5	N/A	1.84
MEMS [236]	e	9.7	3.4–3.8	0.3	345

3.4 NOTCH FILTER USING OPTICAL PROCESSOR FOR STABILITY ENHANCEMENT

It is well known that the bias point of a lithium niobate modulator, such as a DPMZM, drifts over time due to charging effects, or due to

ambient changes such as variations of temperature and polarisation [237]. While in conventional operation, such as for the generation of differential quadrature phase shift keying (DQPSK) signals, the drift can be compensated with a bias controller, this is not the case when the desired output is a signal which satisfies Eqs. (3.4) and (3.5). To understand this, Fig. 3.15 shows the procedure for obtaining a high-suppression notch response by varying the DPMZM biases. This process requires all three bias voltages to be varied and, as shown in Fig. 3.15(b), not in the vicinity of points where a bias controller would be able to lock into (e.g. quadrature, null, or peak). Furthermore, the fact that the bias voltages do not always vary monotonically hinders the implementation of a feedback-based control mechanism.

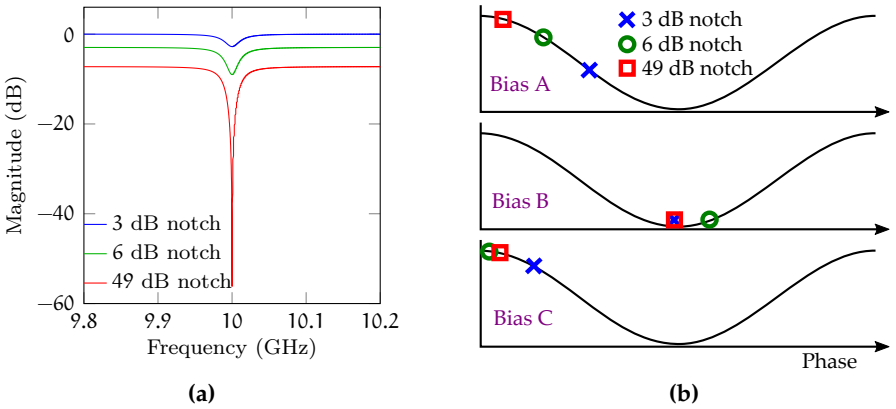

Fig. 3.15. (a) Simulation of a DPMZM-based cancellation notch filter. The different curves show the filter response for different DPMZM bias points, as shown in (b).

This problem is exacerbated further by the fact that any fluctuations in the system (e.g. tuning of the notch frequency, or fluctuations in the optical resonance) need to be followed by proper adjustments of the DPMZM bias voltages, so that a high notch suppression can be maintained. Therefore, in most situations, the DPMZM bias voltages need to be continually adjusted, preventing the DPMZM response from stabilizing to a fixed point. This in turn introduces a time drift in the DPMZM transfer function, which comprises an additional source of instability.

A possible solution to this obstacle is to replace the DPMZM with a phase modulator, followed by a Fourier-domain optical processor (FD-OP) [238], as shown in Fig. 3.16. There are two main advantages that follow from this novel configuration. The first is that a phase modulator does not need to be biased, hence removing the main source of instability. The second key advantage is that, by using a FD-OP composed of a two-dimensional liquid crystal on silicon (LCoS) array, the phase and amplitude relations can be independently con-

trolled, greatly simplifying the process of satisfying Eqs. (3.4) and (3.5).

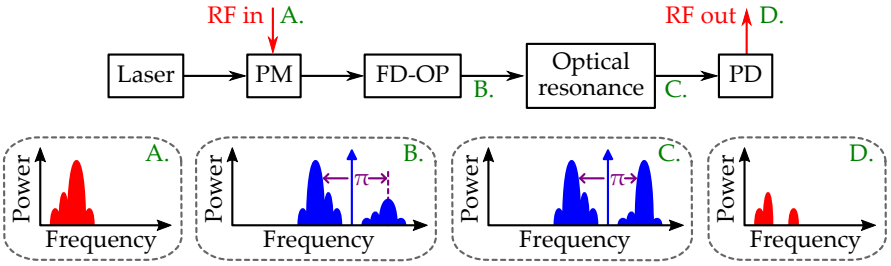

Fig. 3.16. Structure (above) and operating principle (below) of cancellation filters, where a FD-OP is used to satisfy the cancellation conditions.

To appreciate the simplified approach, we examine the field at the output of the phase modulator,

$$E_C e^{j\theta_C} = J_0(m_{RF} V_{RF}) \tag{3.15}$$

$$E_L e^{j\theta_U} = -J_1(m_{RF} V_{RF}) \tag{3.16}$$

$$E_U e^{j\theta_U} = J_1(m_{RF} V_{RF}) \tag{3.17}$$

together with the frequency response $H_{\mathrm{OP}}(\omega)$ of the FD-OP:

$$H_{\mathrm{OP}}(\omega) = \begin{cases} 1 & \text{for } E_C, E_{L/U} \\ A e^{j\phi} & \text{for } E_{U/L} \end{cases} \tag{3.18}$$

where $0 < A < 1$ and $-\pi < \phi \leq \pi$ are parameters whose value can be independently controlled. Equations (3.15)–(3.17) show that the carrier and sidebands generated by the phase modulator automatically satisfy Eq. (3.5). Ideally therefore, the FD-OP need only be used to control the amplitude of one of the sidebands, with $\phi = 0$, to satisfy Eq. (3.4). The procedure for maximizing the notch suppression is shown in Fig. 3.17. It involves using the FD-OP to attenuate only one of the sidebands; as the attenuation approaches the value of the optical resonance, the notch suppression increases. The fact that the procedure requires control of a single variable (i.e. FD-OP attenuation), and that its value is changed monotonically, greatly simplifies the task of implementing automatic feedback control of the notch suppression.

A proof-of-principle experiment can be carried out to test the performance of the new cancellation filter configuration, and measure its stability. In this experiment, the optical resonance is provided by SBS in an optical fibre in order to remove additional instabilities which arise when on-chip SBS is used (e.g. through coupling loss fluctuations).

Figure 3.18 shows the experimental setup of an MWP cancellation filter where the DPMZM is replaced by a phase modulator, followed by an FD-OP. Two DFB lasers, operated in continuous wave (CW) mode with 20 dBm output power, are used to generate the SBS pump and

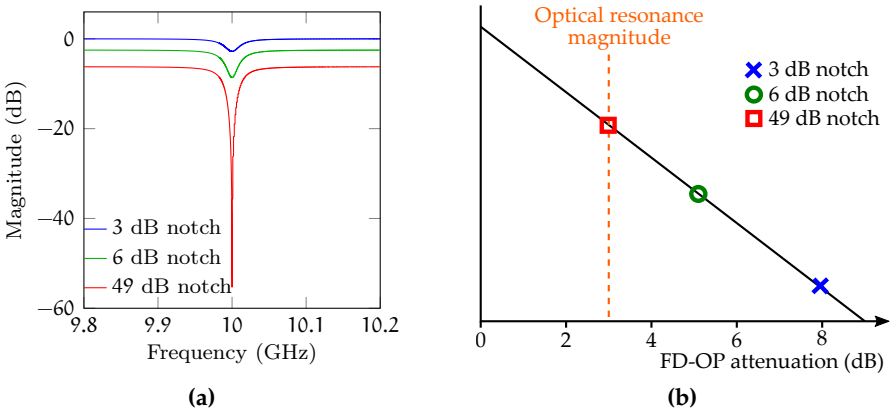

Fig. 3.17. (a) Simulation of a cancellation notch filter using a phase modulator in combination with an FD-OP to sideband tailoring. The phase modulator causes Eq. (3.5) to be automatically satisfied. Equation (3.4) is satisfied by using the FD-OP to attenuate one of the sidebands. (b) The different FD-OP attenuations, approaching the magnitude of the optical resonance, to maximize the notch suppression.

probe waves. The probe laser, with 1550 nm wavelength, is sent through a phase modulator, where it is modulated by the input RF signal supplied by a VNA. The phase-modulated signal then passes through the FD-OP, implemented with a Finisar waveshaper 4000s (denoted as WS in Fig. 3.18). This waveshaper is used to attenuate one of the sidebands, without affecting the carrier or the other sideband. The main advantage of using the waveshaper however, is that it is capable of providing a constant, flat phase contribution across the whole phase-modulated signal spectrum. This allows it to compensate for imperfections in the phase modulator, which would otherwise prevent the field from satisfying Eq. (3.5), and form a notch response. Finally, the signal is launched into a 1.6 km length of single-mode fibre (SMF), where the SBS interaction occurs, before being detected at the PD. The frequency of the laser used for generating the SBS pump wave is set such that the SBS gain resonance occurs on the attenuated sideband. In this way, the amplitudes of the sidebands are equalized only over a frequency range approximately equal to the SBS linewidth ($\sim$ 35 MHz), resulting in a narrowband notch response in the electrical domain. While, in this particular experiment, the optical signal has to travel through more than 1 km of fibre, fibre dispersion does not have a significant effect on the filter passband due to the modulation format used for the cancellation filter, where one of the sidebands is considerably stronger than the other. Effectively, the signal spectrum resembles that of an SSB-modulated signal, which is immune to fibre dispersion.

It is important to note that the notch filter response and characteristics achieved here are, for all intents and purposes, equivalent to those

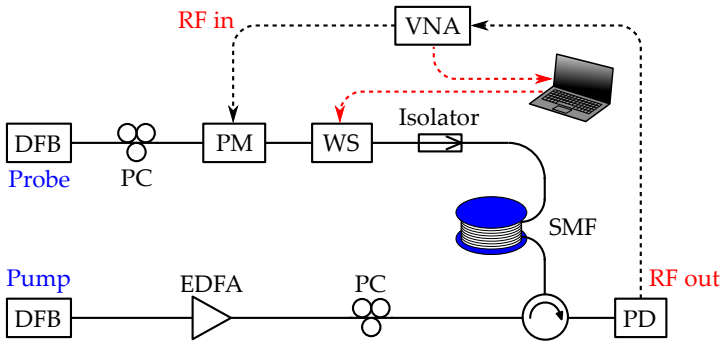

Fig. 3.18. Experimental setup for the cancellation filter, with a phase modulator (PM) and a waveshaper (WS) used for tailoring the sidebands' spectra. The filter response is measured with a VNA. The SBS interaction occurs in a 1.6 km spool of SMF. PCs are used to minimize losses, and to maximize the strength of the SBS interaction.

from Sec. 3.3. The mechanisms for controlling the notch frequency, bandwidth, and insertion loss are the same as those described previously and for this, they are not reiterated here. The only difference between the two notch filter implementations is the technique used for tailoring the phase and amplitude of the sidebands so as to obtain a cancellation notch response. Other than filter stability however, all other filter characteristics are transparent to the sideband tailoring method used.

In order to measure the stability of the filter response, the system is initially optimized to achieve maximum notch suppression. This involves setting the waveshaper attenuation to match the magnitude of the SBS resonance (5 dB). The system is then left running freely for a 24 hour period in an uncontrolled environment, subject to temperature and pressure fluctuations, and the filter response continually monitored. This 24-hour measurement is repeated with a computer program monitoring the notch filter response over time, and actively adjusting the waveshaper attenuation to maintain maximum notch suppression. This active control loop involves using the VNA to continuously measure the magnitude response of the filter. The VNA trace is then input to a computer program which measures the filter suppression (defined as the ratio of maximum to minimum transmission). If the measured value is found to be below a predetermined minimum suppression level, the program sends a control signal to the waveshaper, which adjusts its attenuation and the corresponding ratio between the modulation sidebands. A hill climbing algorithm is used to determined whether the waveshaper suppression has to be increased or decreased. The speed of the control process is approximately 3 seconds, mainly limited by the response time of the waveshaper.

These long-term measurements are repeated also using the DPMZM-based cancellation filter topology (using the same setup as Fig. 3.18,

but with a DPMZM replacing the phase modulator and waveshaper). This allows for a direct comparison between the stability of these two filter topologies. Figure 3.19 shows the measured filter responses at the start of the measurement (i.e. with optimized notch filter suppression), and after 12 and 24 hours of continuous operation, for all three sideband tailoring methods. The drift in the centre frequency of the notch is due to the free-running arrangement of the pump and probe lasers. Over the 24 hour measurement period, the maximum laser frequency drift is measured as 15 MHz. In the DPMZM measurements, shown in Fig. 3.19(a), the notch frequency drift is larger than this value due to the inherent instability of the DPMZM output. This instability causes the phase relations between the sidebands to deviate from the ideal antiphase state of Eq. (3.5), such that the destructive interference of the RF mixing products occurs at a frequency offset from the SBS resonance centre, where its phase contribution is non-zero.

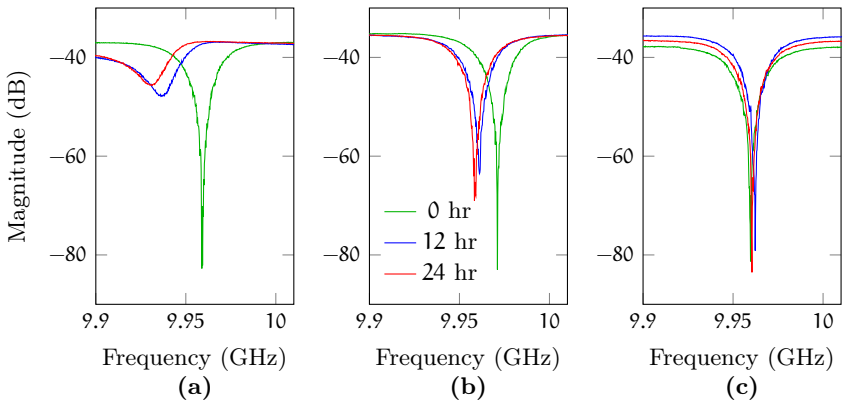

Fig. 3.19. Measurements of the notch filter response after 12 hour intervals of continuous operation. Sideband tailoring was performed using a (a) DPMZM; (b) phase modulator in combination with a waveshaper; (c) phase modulator in combination with waveshaper, driven by software to actively control the waveshaper attenuation.

Figure 3.20 shows the measurement of the notch filter suppression across the whole 24-hour period. The main source of instability during each 24-hour period is a drift in the SBS pump power and polarization. This causes fluctuations in the SBS resonance amplitude, which in turn causes Eq. (3.4) to no longer hold true. From the measurements however it is clear that the DPMZM implementation has an additional source of instability, due to bias drifts, which causes the filter response to deteriorate more rapidly. The inherently unstable nature of the DPMZM, combined with the high complexity of its response, present a major obstacle to realizing software control for filter stabilization. On the contrary, the simplicity of the phase modulator and waveshaper implementation enable the realization of active software control, which greatly stabilizes the filter response.

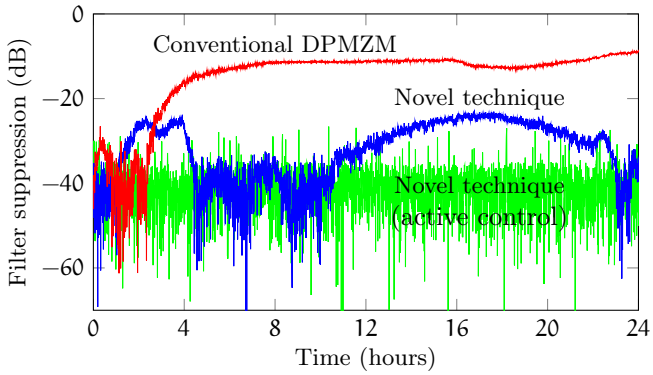

Fig. 3.20. Measurement of the notch filter suppression over a 24 period of continuous operation. The three plots denote different methods for tailoring the sidebands' spectra.

While, on average, the filter suppression obtained with the active control method achieves higher suppression than the other two methods, it is clear that its value also experiences more fluctuations. It is important to note that any suppression beyond 50 dB in this experiment is subject to the noise floor of the system, and therefore varies randomly. The fluctuations that occur for suppression values lower than 40 dB however are due to the active control algorithm, which on average requires multiple iteration steps to correct the waveshaper attenuation to maximize the filter's suppression. The correction algorithm itself is relatively simple, and designed only as a proof of concept.

It is important to note that the stabilization approach presented here is most effective at dealing with fluctuations which result in an amplitude and phase imbalance between the SBS process and the signal field (i.e. whereby the cancellation condition no longer holds). Such fluctuations include pump power fluctuations and polarization drifts, which act to change the SBS gain experienced by the signal. Other types of fluctuations, and most importantly, coupling fluctuations when using on-chip SBS, require other types of control mechanisms (e.g. mechanical control) not covered in this work. Ideally however, this last type of fluctuations would be completely removed through proper packaging of the SBS medium. It is noted that even in such ideal cases, thermal effects due to high optical powers would still play a role in destabilizing the filter response. However, even thermal effects simply result in amplitude and phase imbalances, which are correctable using an FD-OP as taught in this work.

3.5 SUMMARY

In this chapter, an MWP cancellation notch, using on-chip SBS, has been presented. SBS is ideal for implementing MWP notch filters, be-

cause its narrow linewidth enables the realization of highly selective notch filters, with a very sharp notch response. However, the high pump powers required by SBS interactions, particularly in integrated platforms, present a major obstacle which stymies further development of SBS-based integrated MWP notch filters.

Cancellation filters offer a solution to this problem. These filters rely on precise tailoring of the phase and amplitude of the field at the output of the modulator, to achieve ultra-high suppression notch responses, independently from the strength of the optical resonance. This allows for the realization of high-performance notch filters using minimal SBS pump power. Furthermore, the simpler structure of these filters, relative to more common incoherent MWP notch filters, facilitates the tuning of the response over tens of gigahertz, limited only by the equipments used. Tuning of the notch bandwidth is also possible by varying the strength of the SBS process. The insertion loss of these filters, being their main drawback, can be improved beyond the levels attainable by conventional MWP notch filters, by smart budgeting of the optical power inside the waveguide.

Finally, the instability of conventional cancellation filters has been identified, and a solution has been presented. This uses an FD-OP to control the phase and amplitude of the optical signal, directly in the optical domain. This novel approach for independent tailoring of the phase and amplitude of the optical carrier and modulation sidebands could define the new waves of MWP processing, not only for filtering [223], but also for other signal processing such as phase shifting [239] and link gain optimization. In the near future, approaches to integrate this tailoring functionality in a photonic chip will gain significant attention to redefine the field of linear and nonlinear integrated microwave photonics [160].

4

TUNABLE PHASE SHIFTERS USING STIMULATED BRILLOUIN SCATTERING

4.1 INTRODUCTION

Phase shifters are used to shift the phase of a signal by a constant amount across the whole signal spectrum. An important application of radio frequency (RF) phase shifters is in phased array antenna systems [240], as shown in Fig. 4.1(a), where the direction of a radiated signal is controlled by shifting the phase of the multiple signals feeding the antennas. In this way, beam steering simply requires electrical adjustment of different phase shifts, removing the need for physical adjustment of the antenna's orientation. This enables fast steering of the radiated beam, which is very useful for radar. Another example application is in frequency translators, which employ phase shifters to periodically add a phase contribution to a signal, thereby changing its frequency without the need for nonlinear mixing. Phase shifting however is a fundamental signal processing function which can be used as a building block for numerous more complex functionalities, including crosstalk cancellation, Doppler simulation, and the ubiquitous filtering.

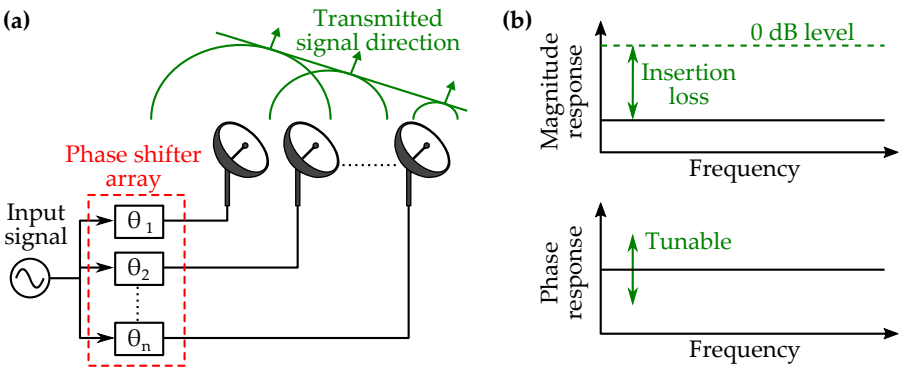

Fig. 4.1. (a) Multiple phase shifters being used to control the phase of the radiating elements, and steer a beam in a given direction. (b) Frequency response of a phase shifter, where the phase shift constant across the whole bandwidth, while the magnitude response remains fixed.

Figure 4.1(b) illustrates the ideal frequency response for a phase shifter. Ideally, RF phase shifters should provide a constant phase shift across their whole operational bandwidth. The phase shift should be continuously tunable across the whole 0–360° range. Moreover, they should exhibit a 0 dB insertion loss, and their amplitude response should not vary as the phase shift is tuned. A vast number of tech-

nologies are currently in use for making electronic phase shifters [240]. Ferrite phase shifters are popular for applications which require high power handling, and operations beyond 60 GHz [241]. Diode phase shifters offer fast, nanosecond switching speeds, but mainly operate across bandwidths lower than 5 GHz [242]. Ferroelectric phase shifters have recently gained attention due to their low drive power and fast switching speeds [243]. At present however, none of these technologies is capable of concurrently achieving all the aforementioned phase shifter requirements.

Microwave photonic (MWP) phase shifters exploit the huge bandwidth potential and reconfigurability of photonics to overcome the shortcomings of electronic implementations [13]. Electro-optic modulators [62, 244–247], stimulated Brillouin scattering [94, 95, 248, 249], cross-phase modulation [250], semiconductor optical amplifiers (SOAs) [251, 252], Fourier-domain optical processors (FD-OPs) [239], and Bragg gratings [253–256] have all been shown capable of achieving tunable phase shifts over multi-GHz bands. More recently, integrated MWP phase shifters have been demonstrated using ring resonators [155, 257, 258], as well as integrated waveguide Bragg gratings [259, 260] and colloidal quantum dots [261]. Numerical computations using silicon graphene waveguides have also shown very promising results [262], but have yet to be confirmed in practice.

The majority of MWP phase shifters to date have made use of optical carrier processing. This technique relies on shifting the phase of the optical carrier of an single sideband (SSB)-modulated optical signal. Upon heterodyne photodection, the phase shift on the optical carrier is mapped, through mixing, onto the phase of the whole RF signal spectrum [263]. The fact that the phase shift only needs to be imparted on the optical carrier and therefore is independent from the bandwidth of the input RF signal, makes this is a very powerful technique for implementing phase shifters with, theoretically, unlimited RF bandwidth capacity [94].

In order for optical carrier processing to work effectively, the mechanism used to shift the phase of the carrier must be narrowband so as to not distort the optical sideband. In addition, it must not affect the amplitude of the carrier, to prevent power fluctuations at the output of the phase shifter as the phase shift is tuned. While achieving impressive results, all prior on-chip phase shifter demonstrations have not met either of these requirements, resulting in suboptimal operation.

Alternatively, stimulated Brillouin scattering (SBS) is ideal for optical carrier processing due to its narrow linewidth [264], allowing it to process the optical carrier without distorting the optical sideband. Moreover, SBS is unique in its ability to simultaneously provide gain and loss resonances, which can be used for shifting the phase of an optical carrier without changing its amplitude [94]. For this reason,

SBS opens the possibility for realizing wideband MWP phase shifters with equal amplitude in all phase states.

This chapter presents the use of two different architectures for SBS-based phase shifters, both of which rely on optical carrier processing. Section 4.2 presents the different architectures which have been used for implementing MWP phase shifters based on SBS. Section 4.3 demonstrates the first MWP phase shifter using on-chip SBS by implementing an architecture first introduced in [94]. The technique is refined to be more energy-efficient and thus more suited to on-chip implementation. In addition, the effect of SBS pump depletion on the phase shifter insertion loss is analysed, and it is shown that shorter, integrated platforms are, in principle, capable of lower insertion losses compared to long fibre-based implementations. Section 4.4 presents a novel architecture, where a different SBS pump configuration enables the demonstrations of the first ultra-wideband MWP phase shifter with independently reconfigurable amplitude and phase responses.

4.2 SBS-BASED PHASE SHIFTER ARCHITECTURES

4.2.1 *Vector-Sum Technique*

In the vector-sum phase shifter architecture, two copies of the signal whose phase is to be shifted, are added together [265]. The two copies have the same frequency, but different amplitudes and phases. This operation can be described by the well-known sinusoidal relation

$$A\sin(\omega t) + B\sin(\omega t + \Delta\phi) = C\sin(\omega t + \theta) \tag{4.1}$$

where the phase, θ, of the output signal is a function of $\Delta\phi$ and of A/B. Tuning of the phase shift is therefore achieved by adjusting the amplitude ratio and the phase difference between the two signal copies.

This same principle is used in vector-sum MWP phase shifters [249, 266–268], shown in Fig. 4.2. The input RF signal modulates an optical carrier, generating two optical sidebands. The phase and the amplitude of one of the sidebands is then adjusted using some optical component, such as an optical delay line [266–268], or an optical resonance such as SBS [249]. Finally, at the photodetector, the beating between the two sidebands and the carrier generate two RF mixing products which take the form of Eq. (4.1), and result in a phase-shifted RF signal.

The use of SBS for the sideband processing mechanism of a vector-sum phase shifter has been demonstrated [249], but exhibits a number of deficiencies. The main obstacle is due to the narrow SBS linewidth, which greatly restricts the bandwidth of any input RF signal. In order for the phase shift to be truly wideband, the phase of the whole optical sideband spectrum must be shifted through the sideband pro-

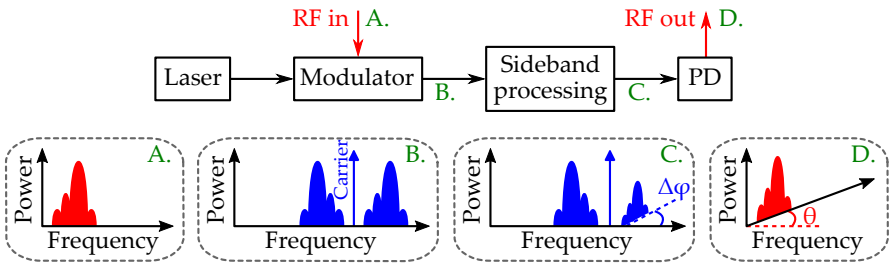

Fig. 4.2. Structure (above) and operating principle (below) of phase shifters based on the vector-sum principle.

cessing mechanism. The fact that the SBS linewidth is of the order of tens of megahertz, causes the bandwidth of the phase shifter to also fall in this range. Since the main advantage that MWP phase shifters have over electronic-based phase shifters is their potential for wideband operation, the limitation introduced by SBS is an overwhelming drawback. Broadening of the SBS resonance, while possible [106], is only a partial solution because the SBS phase response on the optical sideband would cause each frequency component to experience a different phase shift $\Delta\phi$, and the phase of the output RF signal would also be similarly distorted.

A second obstacle, inherent to all vector-sum approaches is that, it is not just the phase of the RF signal which is shifted; its amplitude is also affected. Because of this, tuning of the phase shift causes power fluctuations at the output of the phase shifter. This effect was also observed in [249]. Because of these disadvantages, vector-sum techniques have not received significant attention in the field of MWP phase shifters. Instead, most demonstrations have relied on optical carrier processing.

4.2.2 *Optical Carrier Processing*

Chapter 3 presented the use of SBS for implementing highly selective notch filters, with a narrow bandwidth unachievable through other means. In fact, the popularity of SBS for MWP filtering hinges on its narrow linewidth. It seems contradictory therefore to consider SBS as a tool for wideband signal processing. Nevertheless, this is in fact possible through the use of optical carrier processing [264].

In optical carrier processing, the SBS response acts on the optical carrier, and not on the optical modulation sidebands, as shown in Fig. 4.3. In order to avoid being affected by the resonance, the frequencies of the modulation sidebands should be far enough away from the carrier, so that they do not "see" the optical resonance. This places a limit on the lowest RF signal frequencies that can be modulated onto the carrier, effectively limiting the RF bandwidth of the MWP signal processor. To minimize this limit, the response of the optical resonance must be as narrow as possible. The narrow linewidth of

SBS is ideal for this, and has been used in this context to demonstrate compensation of dispersion-induced signal fading [269], generation of triangular-shaped pulses [270], and phase shifters [94, 95, 165, 248].

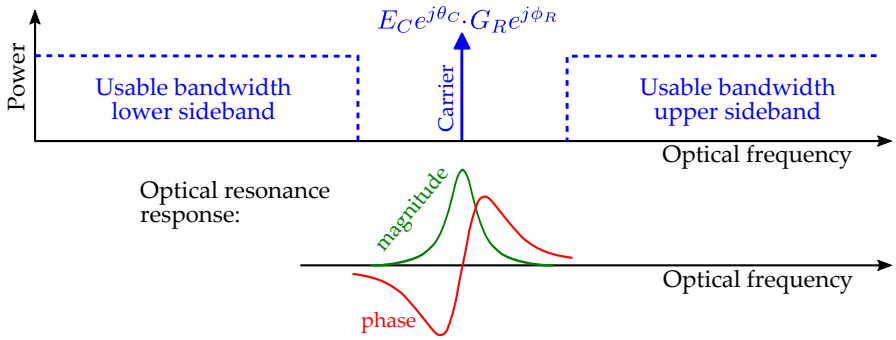

Fig. 4.3. Optical carrier being affected by an optical resonance. To avoid distortion, the optical resonance must not affect the modulation sidebands.

The basic structure of a phase shifter making use of optical carrier processing is shown in Fig. 4.4. SSB modulation is used to convert the input RF signal to the optical domain. The optical field $E_B(t)$ at the output of the modulator can be described by

$$E_B(t) = E_C e^{j\omega_c t + j\theta_C} + E_U e^{j(\omega_c + \omega_{RF})t + j\theta_U} + \text{c.c.} \tag{4.2}$$

An optical resonance $G_R e^{j\phi_R}$ is then used to shift the phase of the optical carrier:

$$E_C(t) = G_R E_C e^{j\omega_c t + j\theta_C + j\phi_R} + E_U e^{j(\omega_c + \omega_{RF})t + j\theta_U} + \text{c.c.} \tag{4.3}$$

At the photodetector (PD), the carrier and the sideband mix to generate the output RF signal

$$\begin{aligned} i_{out} &\propto E_C(t) E_C^*(t) \\ &\propto G_R E_C E_U \cos(\omega_{RF} t - \theta_C + \theta_U - \phi_R). \end{aligned} \tag{4.4}$$

As can be seen, the mixing process causes the phase shift ϕ_R on the optical carrier to be mapped onto the output RF signal. It is important to note that in this derivation, no restrictions were placed on the frequency of the RF signal, ω_{RF}. Therefore, this phase-mapping process works, in principle, for all RF frequencies. In this fact lies the strength of optical carrier processing, because it converts a narrowband optical phase shift into an ultra-wideband phase shift, independent from the bandwidth of the input RF signal.

Observation of Eq. (4.4) reveals another property of optical carrier processing. Not only is the phase of the optical resonance mapped onto the output RF signal, but also its amplitude contribution G_R. This causes a complication when the phase of the output signal needs to be tuned. Tuning of the phase shift in the electrical domain simply

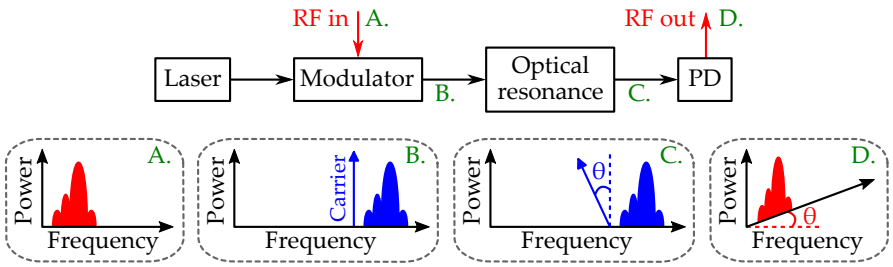

Fig. 4.4. Structure (above) and operating principle (below) of phase shifters based on optical carrier processing.

requires changing the phase response of the optical resonance at the optical carrier frequency. However, in general the phase and the amplitude responses of an optical resonance are directly linked (through the Kramers-Kronig relations) meaning that, as ϕ_R changes, so does G_R. This causes the power of the output RF signal to fluctuate (i.e. the phase shifter exhibits a different amplitude response in different phase states). Such an effect should be minimized in practice. Ideally, the optical resonance should have a flat amplitude, or amplitude-transparent response. For all integrated MWP phase shifters to date, this requirement has proven impossible to reach using resonances provided by ring resonators or gratings, for instance, but has been achieved with SBS.

4.3 AMPLITUDE-TRANSPARENT PHASE SHIFTER

4.3.1 *Working Principle*

The application of SBS as an amplitude-transparent phase shifting mechanism was introduced by Loayssa and Lahoz [94]. The technique relies on counter-propagating an SSB-modulated signal with two pump waves. The frequencies of the two pumps are symmetrically up and down-shifted from that of the carrier by Ω, in the vicinity of the Brillouin frequency shift Ω_B, as shown in Fig. 4.5. Pump 1 then acts as an SBS Stokes wave, and induces a loss resonance on the carrier, while Pump 2 acts as an SBS pump wave, inducing a gain resonance on the carrier.

The evolution of the carrier power P_c, and phase θ_c, together with the power of Pump 1 P_{p1}, and Pump 2 P_{p2}, can be obtained through

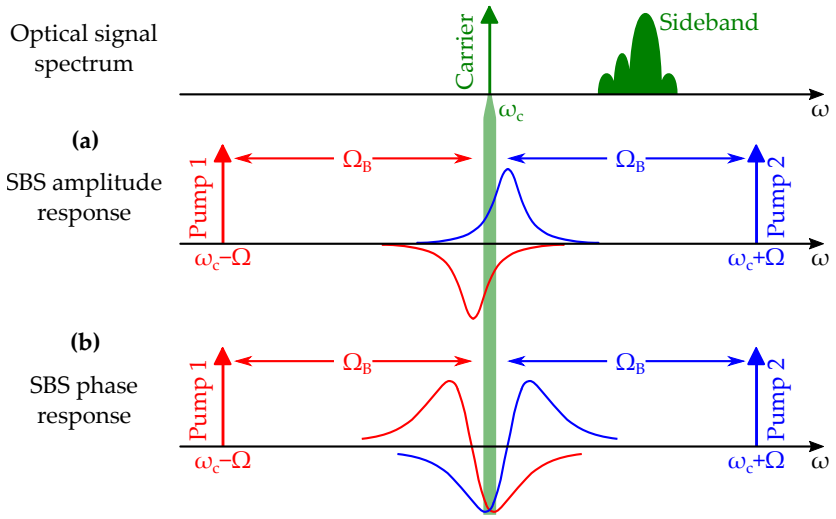

Fig. 4.5. Operating principle for the SBS-based MWP phase shifter, as presented in [94]. (a) The gain and loss resonances from an SBS Stokes (Pump 1) and pump (Pump 2) wave cancel out, while (b) their phase contributions add up, at the carrier frequency.

manipulation of the steady-state SBS coupled mode equations (2.52)–(2.55), and is described by

$$\frac{dP_{p1}}{dz} = \frac{g_0}{A_{\text{eff}}}\left[\frac{\Gamma_B^2}{4(\Omega-\Omega_B)^2+\Gamma_B^2}\right]P_{p1}P_c - \alpha P_{p1} \tag{4.5}$$

$$\frac{dP_{p2}}{dz} = -\frac{g_0}{A_{\text{eff}}}\left[\frac{\Gamma_B^2}{4(\Omega-\Omega_B)^2+\Gamma_B^2}\right]P_{p2}P_c - \alpha P_{p2} \tag{4.6}$$

$$\frac{dP_c}{dz} = \frac{g_0}{A_{\text{eff}}}\left[\frac{\Gamma_B^2}{4(\Omega-\Omega_B)^2+\Gamma_B^2}\right](P_{p1}-P_{p2})P_c + \alpha P_c \tag{4.7}$$

$$\frac{d\theta_c}{dz} = \frac{g_0\Gamma_B}{A_{\text{eff}}}\left[\frac{\Omega-\Omega_B}{4(\Omega-\Omega_B)^2+\Gamma_B^2}\right](P_{p1}+P_{p2}). \tag{4.8}$$

Here g_0 is Brillouin gain coefficient, A_{eff} is the effective optical mode area, Γ_B is the Brillouin linewidth, and α is the loss coefficient of the medium. In the above expressions, the carrier is assumed to be travelling in the $-z$-direction, opposite to Pump 1 and 2, which travel along the $+z$-direction.

It is clear that if the powers of Pump 1 and 2 are equal throughout the whole SBS medium, i.e.,

$$P_{p1}(z) = P_{p2}(z) \tag{4.9}$$

the first term on the right-hand side of Eq. (4.7) vanishes, and the SBS amplitude contributions cancel out at the carrier frequency. This amplitude response cancellation, depicted in Fig. 4.5(a), implies that the carrier power is not affected by the SBS process. Equation (4.9) requires that both Pump 1 and 2 be launched into the medium with the same power, i.e. $P_{p1}(0) = P_{p2}(0)$, and that they evolve in the same

manner as they propagate along the medium. This last statement is satisfied when the first term on the right-hand side of Eqs. (4.5) and (4.6) vanishes such that

$$\frac{dP_{p1}}{dz} \approx \frac{dP_{p2}}{dz} \approx -\alpha P_{p1}. \tag{4.10}$$

This equation represents the undepleted pump condition [271]. This is a key requirement for phase shifter operation because it implies that for the phase shifter amplitude response to remain unchanged in all phase states, both SBS interactions must operate in the linear regime (i.e. without pump depletion).

The total phase shift ϕ experienced by the carrier is the sum of the phase responses due to the two SBS interactions, as shown in Fig. 4.5(b), and can be found by integrating Eq. (4.8) over the length L of the SBS medium. In [94], tuning of the phase shift in the range $\pm 180°$ was achieved by simultaneously varying the frequency of Pump 1 and 2, as shown in Fig. 4.6(a), while their input power remained fixed at

$$P_{p1}(0) = P_{p2}(0) = \frac{2\pi A_{\text{eff}}}{g_0 L_{\text{eff}}} \tag{4.11}$$

where $L_{\text{eff}} = \frac{1}{\alpha}(1 - e^{-\alpha L})$ is the effective length of the medium. This has the effect of changing the value of Ω such that the optical carrier accesses a different point of the SBS phase response. It is clear that this method is highly inefficient since even small phase shifts require high SBS pump powers.

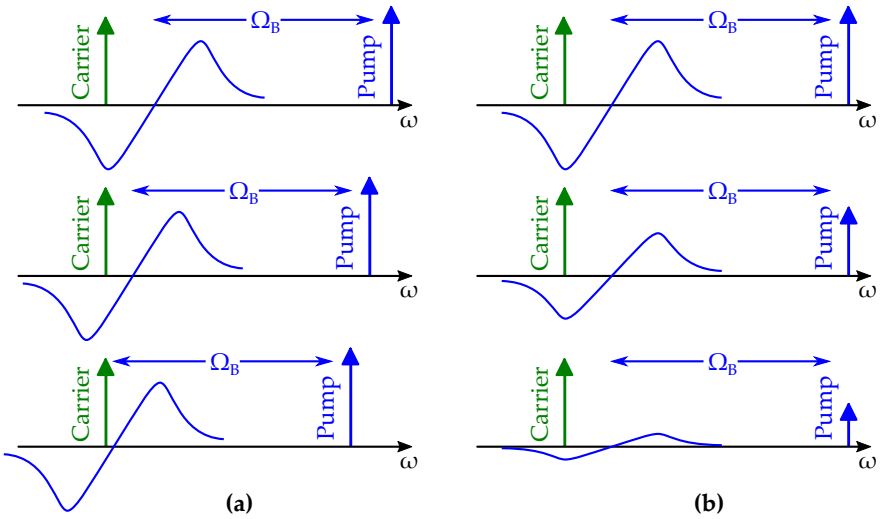

Fig. 4.6. Phase shift tuning mechanism using (a) pump frequency tuning technique from [94]; (b) novel pump power tuning technique.

A more energy-efficient method for tuning the phase shift is to exploit the maximum phase shift provided by the SBS phase response, and is illustrated in Fig. 4.6(b). By fixing the frequencies of Pump 1 and 2, such that

$$\Omega = \Omega_B \pm \frac{\Gamma_B}{2} \tag{4.12}$$

the carrier always has access to the maximum (or minimum) phase shift, for a given power of Pump 1 and 2. The phase shift is then tuned by simultaneously varying the powers of Pump 1 and 2:

$$P_{p1}(0) = P_{p2}(0) = \frac{2A_{\text{eff}}}{g_0 L_{\text{eff}}} |\phi| . \tag{4.13}$$

Using this new technique, the amount of pump power becomes proportional to the amount of desired phase shift, making it less power-consumptive, and alleviating the burden on the SBS medium.

4.3.2 *Demonstration Using On-Chip SBS*

The experimental setup used to implement the SBS-based phase shifter is shown in Fig. 4.7. A distributed feedback (DFB) laser is biased for continuous wave (CW) operation with 1550 nm wavelength, and 20 dBm output power; the laser output is then split equally between two branches. With reference to Fig. 4.7, the upper branch is used to generate the SSB-modulated carrier. A swept-frequency RF signal is generated using a vector network analyser (VNA), and fed to a dual-parallel Mach-Zehnder modulator (DPMZM) through a 90° hybrid coupler. The DPMZM is biased for SSB operation, and the resulting optical signal is amplified using an erbium-doped fibre amplifier (EDFA), before being coupled to a 6.5 cm long As_2S_3 rib waveguide, through lensed fibres. The waveguide has a cross section of 0.85×4 μm, a mode area of 2.3 μm^2, and a high SBS gain coefficient ($g_0 \sim 7.4 \times 10^{-10}$ m/W) [205]. The total waveguide insertion loss is 10 dB, comprising of 4 dB/facet coupling loss, and 0.3 dB/cm propagation loss.

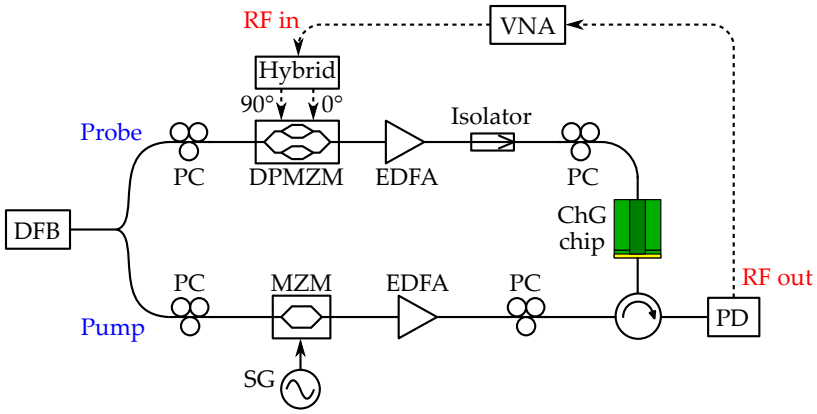

Fig. 4.7. Experimental setup for the MWP phase shifter using on-chip SBS. The pump configuration for shifting the phase of the carrier is shown in Fig. 4.5.

With reference to Fig. 4.7, the lower branch of the setup is used to generate Pump 1 and 2, as shown in Fig. 4.5. This is achieved by biasing a Mach-Zehnder modulator (MZM) for intensity modulation,

with suppressed carrier. The modulation process generates two sidebands with frequency $\omega_c \pm \Omega$, where ω_c is the frequency of the laser output, while Ω is the frequency of the RF signal being fed to the MZM by a signal generator (SG). This pump field is amplified by an EDFA and coupled to the chip, where it counterpropagates with the SSB-modulated carrier.

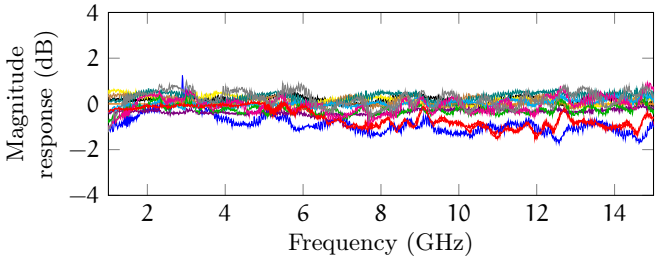

(a)

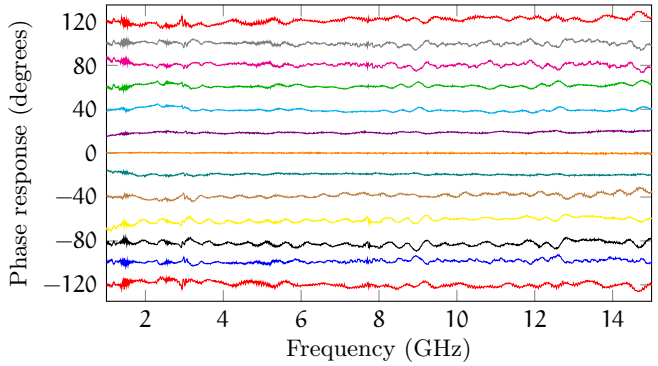

(b)

Fig. 4.8. Measured (normalized) frequency response for the MWP phase shifter using on-chip SBS.

The SBS interactions between Pump 1 and 2 and the carrier result in a phase shift on the carrier. The frequency of the SG is set to 7.637 GHz and 7.695 GHz, for negative and positive phase shifts, respectively. For the chalcogenide (ChG) waveguide used in the experiment, these values equal to $\Omega_B \pm \Gamma_B/2$ which, as explained in Sec. 4.3.1, correspond to the SBS interactions with the most efficient phase shift for a given power of Pump 1 and 2. The frequency response for the phase shifter is shown in Fig. 4.8. The phase shift can be continuously tuned over a 240° range, simply by varying the power of Pump 1 and 2, as depicted in Fig. 4.6(b). The maximum SBS pump power on the facet of the waveguide is 31 dBm (28 dBm for both Pump 1 and 2), corresponding to a ±120° phase shift. Tuning of the phase shift results in ±1.5 dB fluctuations in the magnitude response. This is partly due to the reflection of the residual carrier of the SBS pump field, which interferes with the signal carrier at the PD, causing the RF output signal level to vary over time. Another source of power fluctuation is the polarization pulling effect of SBS on the signal carrier

[272], which causes the carrier to experience a different polarization-dependent loss as the phase shift is tuned. These power fluctuations could be improved by integration of all the components onto a single chip. Nevertheless, the current phase shifter displays lower fluctuations, for the given phase shift tuning range, compared to all other on-chip MWP photonic phase shifters demonstrated to date, as shown in Table 4.1.

Table 4.1. Performance comparison of different on-chip MWP phase shifters. N/A bandwidth values are due to measurements at a single RF frequency.

Technology	Bandwidth (GHz)	Phase range (degrees)	Power fluctuation (dB)
SBS (this work)	1–15	240	3
Si microrings [257]	N/A	360	2
Si microrings [258]	16–23	360	N/A
Si grating [260]	22–29	160	6
SOA [251]	20–40	360	N/A
SOA [252]	N/A	360	40
Si_3N_4 rings [155]	1–2.4	360	N/A
Quantum dot [261]	0.01–25	36.5	1

4.3.3 *Bandwidth Limitation*

The measurements of the frequency response of the phase shifter shown in Fig. 4.8 cover a frequency span ranging from 1 to 15 GHz. For the current experiment, the lower frequency limit is set by the 90° hybrid coupler used for feeding the input RF signal to the DPMZM. The upper frequency limit is instead equal to twice the Brillouin frequency shift Ω_B of the medium ($\sim$ 7.6 GHz in ChG). This limit is a direct consequence of the pump configuration used by the phase shifter.

This can be understood by observing Fig. 4.9, which shows the two SBS pumps, and the various responses they stimulate. Each pump, with frequency ω_p, generates two SBS resonances: a loss resonance at an anti-Stokes frequency $\omega_p + \Omega_B$, and a gain resonance at the Stokes frequency $\omega_p - \Omega_B$. Optical carrier processing requires that only the carrier "sees" the optical resonance. This however is not the case when the frequency of the input RF signal is in the vicinity of $2\Omega_B$. At this frequency, the optical sideband experiences an unwanted SBS response. This is manifested as a glitch in the electrical amplitude and phase responses of the phase shifter, shown in Fig. 4.10.

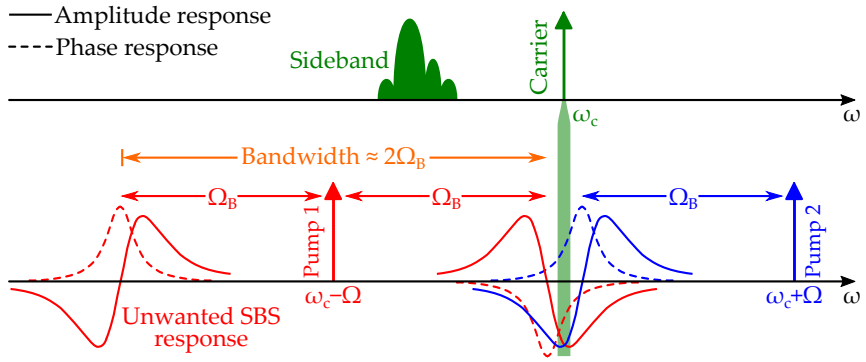

Fig. 4.9. SBS pump configuration for the amplitude-transparent phase shifter. The unwanted SBS response on the sideband occurs at a frequency $2\Omega_B$ distant from the optical carrier. Note that if the SSB-modulated signal contains an upper-frequency sideband, the unwanted SBS response is a loss resonance.

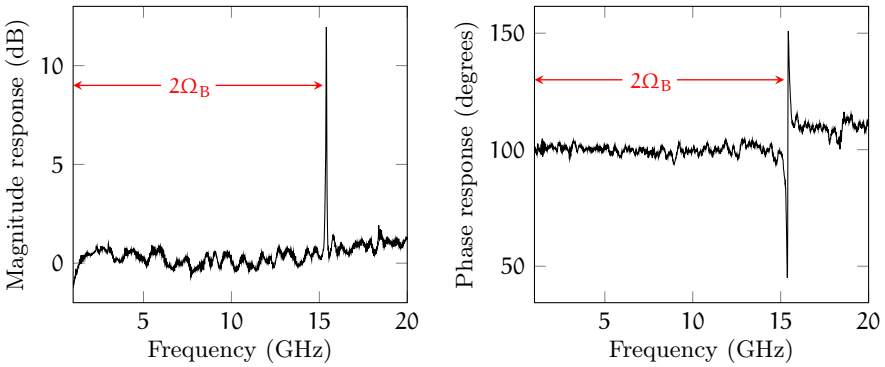

Fig. 4.10. (a) Magnitude and (b) phase response of the MWP phase shifter using the SBS pump configuration from Fig. 4.5. In this example, the SBS occurs in a ChG rib waveguide ($\Omega_B \sim 7.6$ GHz), and the phase shifter is in the 100° phase state.

It is important to note that the glitch in the frequency response only occurs over a bandwidth equal to the SBS linewidth. It can therefore be argued that the RF bandwidth of the phase shifter is unlimited, for RF frequencies above $2\Omega_B$. Nevertheless, the unwanted SBS resonance causes an inconvenient disruption in the bandwidth of operation. An architecture for an SBS-based phase shifter which solves this problem is presented in Sec. 4.4.

4.3.4 *Insertion Loss*

Minimization of the insertion loss is a design challenge which must be addressed, in order to enhance the performance and signal-to-noise ratio of the phase shifter. Following optimization of the system, the most effective way to reduce the insertion loss is to increase the

optical power into the modulator since, when using external modulation, the link gain is proportional to the square of the optical input power [44]. However, the fact that the SBS interaction is occurring on the carrier places an upper limit on the maximum carrier power.

It was shown in Sec. 4.3.1 that, in order to avoid RF power fluctuations as the phase shift is tuned, the powers of both SBS pumps must remain approximately unchanged by their SBS interactions with the carrier. This condition is expressed mathematically by Eq. (4.10) and is essentially equivalent to the undepleted pump condition [168]. As shown in Fig. 4.11(a), in this regime the energy transfer between the carrier and the two SBS pumps is negligible, and the interaction can be viewed as a linear system. In order for this assumption to hold, the carrier power must remain below a certain value, which depends on a number of factors including the properties of the medium, given by [271]

$$\frac{g_0}{A_{\text{eff}}} \cdot \frac{\Gamma_B^2}{4(\Omega - \Omega_B)^2 + \Gamma_B^2} \int_0^L P_c(\zeta, \Omega) d\zeta \ll 1. \tag{4.14}$$

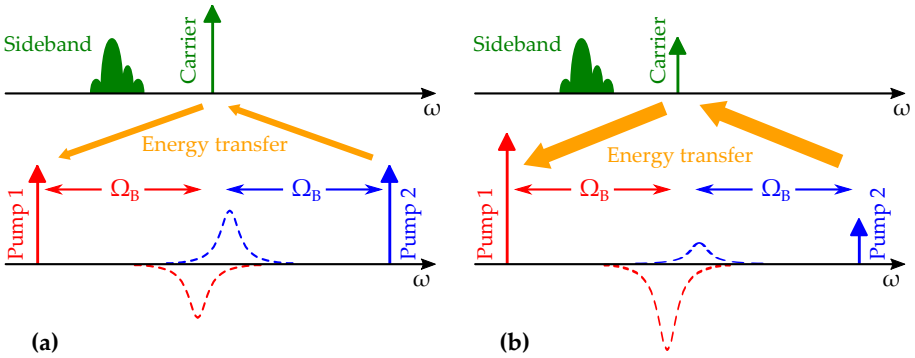

Fig. 4.11. (a) For low carrier powers, the energy transfer between the carrier and the SBS pumps is negligible, and the phase shifter acts as a linear system. (b) For high carrier powers, SBS pump depletion causes the carrier to experience a net loss, as energy is transferred to Pump 1, and the phase shifter acts as a nonlinear system.

If Eq. (4.14) is not satisfied, as tends to happen for high carrier powers, the SBS interaction between Pump 2 and the carrier causes Pump 2 to deplete, resulting in a decrease in the gain resonance on the carrier. On the contrary, the SBS interaction between Pump 1 and the carrier causes Pump 1 to be amplified, corresponding to an increase in the loss resonance on the carrier, as can be shown with Eqs. (4.5)-(4.7). In this regime, illustrated in Fig. 4.11(b), the amplitude contributions from Pump 1 and 2 on the carrier no longer cancel out, and the carrier experiences a net loss. Therefore, increasing the optical signal power into the waveguide increases the amount of pump depletion, resulting in a higher net loss on the carrier (i.e. carrier depletion), which ultimately limits the output power of the optical carrier.

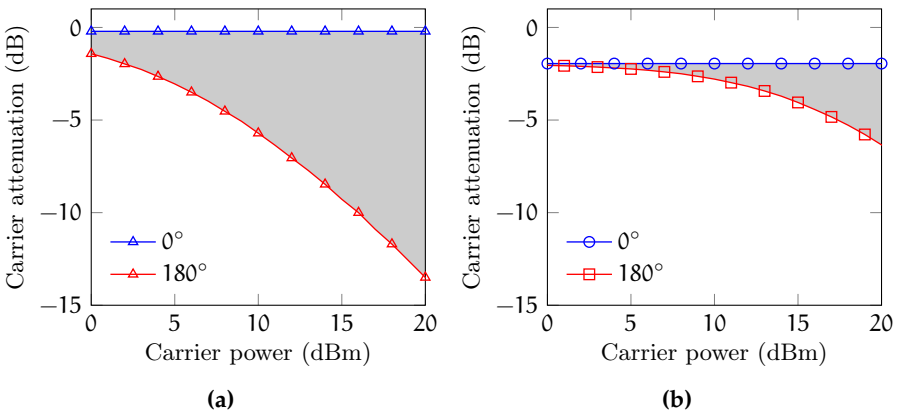

Fig. 4.12. Simulated carrier attenuation, as a function of carrier power and phase shift for different SBS media: (a) 1 km standard silica SMF; (b) 6.5 cm ChG rib waveguide.

Figure 4.12 simulates the effect of increasing the optical power into the waveguide, when the SBS interaction occurs in a 1 km length of standard silica SMF, or in the 6.5 cm long ChG rib waveguide from Fig. 4.7. The corresponding increase in the carrier power is counteracted by SBS depletion of the optical carrier, which in turn leads to a higher degradation of the insertion loss of the phase shifter. The curves indicate the trends for the two extreme phase shifts: 0° and 180°; the shaded regions indicate where the curves would lie for all other phase shifts (including the negative ones). The simulations do not include the additional attenuation due to spontaneous Brillouin scattering, and therefore represent a best-case scenario. They show that a 1 km spool of silica fibre is more susceptible to SBS carrier depletion, meaning that chip implementations allow operation at higher carrier powers, with more potential for reducing the insertion loss. It is important to note that when the pump power launched into the medium is the same for both chip and fibre cases, the length of the fibre can be reduced to 71 m. In this instance, the depletion threshold for both fibre and chip implementations is the same. Nevertheless, on-chip operation is more attractive for enabling the realisation of multiple functionalities on the same device.

Further examination of Eq. (4.14) reveals that it is not just the medium parameters which have an effect on the amount of carrier depletion. The evolution of the carrier power along the SBS medium also has an effect. The magnitude of this effect in turn depends on the SBS pump powers. In this context, it is useful to compare how the technique used for tuning the phase shift affects the insertion loss. Figures 4.13(a) and(b) simulate the carrier depletion for the frequency-tuning (see Fig. 4.6(a)) and the power-tuning (see Fig. 4.6(b)) techniques, respectively. The frequency-tuning technique always requires high pow-

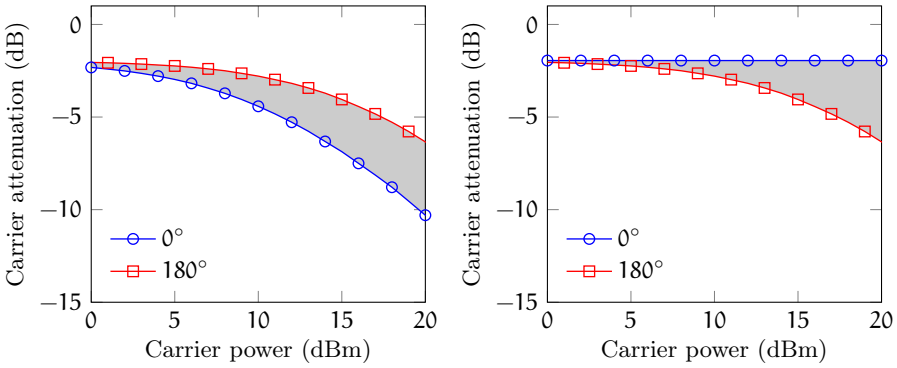

Fig. 4.13. Simulated carrier attenuation, as a function of carrier power and phase shift for different phase shift tuning mechanisms: (a) frequency-tuning mechanism from [94]; (b) power-tuning mechanism.

ers, even for low phase shifts, and is thus more susceptible to carrier depletion than the power-tuning technique presented here.

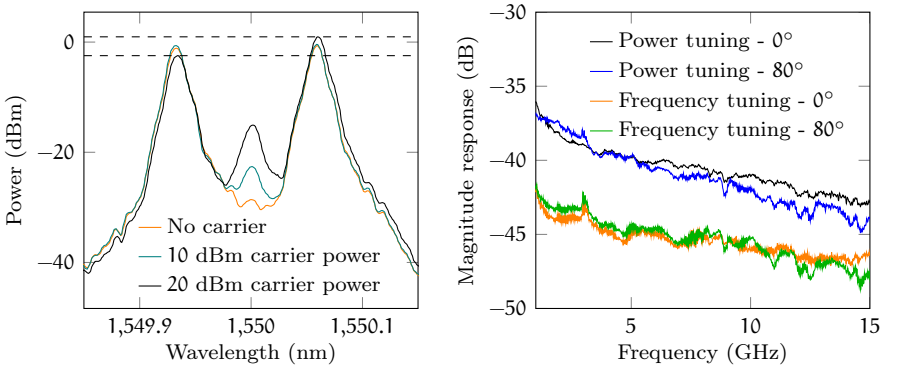

Fig. 4.14. (a) Pump spectra after the SBS interactions, for different carrier powers. (b) Phase shifter magnitude response using both the power-tuning and the frequency-tuning technique for tuning the phase shift. The carrier power launched into the ChG waveguide is 20 dBm.

An experiment can be performed to observe the effect of a high carrier power on the operation of the phase shifter for the two phase shifting mechanisms. The experimental setup is the same as in Fig. 4.7. It involves increasing the power of the carrier launched into the ChG waveguide. The pump spectrum after the SBS interaction is recorded and is shown in Fig. 4.14(a). If no carrier depletion occurs, Eq. (4.10) is satisfied, and both SBS pumps evolve in the same way, exiting the waveguide with the same power. This is the case for low carrier powers. For the current experiment however, when the launched carrier power reaches 20 dBm, the pumps exit the waveguide with different powers, Pump 1 having been amplified, while Pump 2 is attenu-

ated, due to SBS. It is in this case that carrier depletion occurs. Figure 4.14(b) shows the measured, unnormalized magnitude response of the phase shifter in this region of operation, for two different phase shifts, with tuning achieved using either the power-tuning, or the frequency-tuning technique. As expected, this last technique suffers from higher carrier depletion, leading to a larger insertion loss, for high carrier powers. Alternatively, the power-tuning technique for tuning the phase shift delays the insertion loss degradation to higher carrier powers, thus allowing a further increase in the link gain of the phase shifter, as well as achieving more efficient operation.

Finally, it is worth noting that while SBS carrier depletion sets an upper limit on the maximum carrier power, it does not necessarily limit the minimum achievable insertion loss. This is because the insertion loss of the filter depends on the power of both the carrier and the sideband. Therefore, it is possible to increase the link gain of the phase shifter simply by increasing the power of the optical sideband. Since the sideband is not affected by the SBS process, it cannot induce pump depletion. The relatively high insertion loss illustrated in Fig. 4.14(b) (greater than 35 dB), could then be significantly reduced. One possible approach for doing this would be to generate the optical signal by using SSB modulation with quasi-suppressed carrier. Subsequent optical amplification would then allow one to arbitrarily amplify the sideband power (and hence reduce the insertion loss) without inducing SBS carrier depletion.

4.4 ULTRA-WIDEBAND PHASE SHIFTER

4.4.1 *Working Principle*

The phase shifter presented in Sec. 4.3 was initially introduced in 2006 by Loayssa and Lahoz [94], using SBS in fibre. For a number of years, this technique was accepted as being the only way of using SBS for achieving an amplitude-transparent phase shifter. It wasn't until 2014 that a different SBS-based phase shifter architecture was proposed. The novel structure still relied on optical carrier processing, but made use of a different pump configuration to overcome the bandwidth limitation of the previous demonstration, while retaining amplitude transparency.

The SBS pump configuration used in this new technique can be seen in Fig. 4.15. Two SBS pumps are chosen with higher frequencies than that of the carrier, ω_c, to induce SBS gain resonances in its vicinity. With reference to Fig. 4.15, Pump 1 causes both the amplitude and the phase of the carrier to vary through its SBS interaction. The SBS interaction due to Pump 2 has a similar effect. However, by choosing the frequency of Pump 2 to be exactly Ω_B higher than that of the carrier, its phase contribution at the carrier frequency is null [see

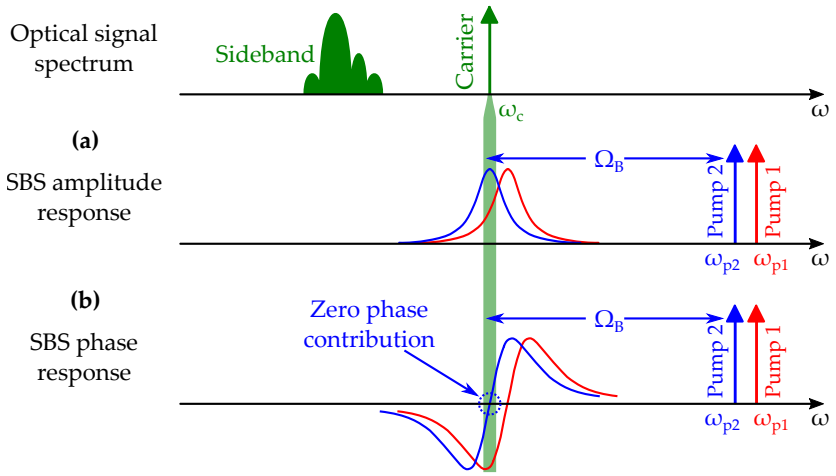

Fig. 4.15. Operating principle for the SBS-based MWP phase shifter, using the novel pump configuration. (a) Two gain resonances from two separate SBS pumps are adjusted to maintain the same carrier amplitude in all phase states. (b) The frequency of Pump 1 is such that its phase contribution on the carrier is 0°, so that just the SBS response from Pump 2 works to shift the carrier phase.

Eq. (2.58)]. In this way, the frequency and power of Pump 1 can be adjusted to control the phase shift on the optical carrier, while adjustments in the power of Pump 2 can compensate for any fluctuations in the carrier power caused by tuning its phase. Once the carrier and sideband reach the photodetector, any phase shift on the optical carrier is mapped onto the output RF signal spectrum through mixing. More importantly, with this new pump configuration the sideband never sees any SBS resonances, so that the RF operational bandwidth for this phase shifter is, theoretically, unlimited.

In order to maximize the efficiency of the phase shifter, the frequency of Pump 1, ω_{p1}, must be set such that the carrier always "sees" the maximum (or minimum) phase shift, for a given pump power. By differentiating Eq. (2.58) with respect to Ω, it is simple to show that, for any given pump power, the frequency of maximum or minimum phase shift is always equal to

$$\omega_{p1} = \begin{cases} \omega_c + \Omega_B + \Gamma_B/2 & \text{for } \phi < 0 \\ \omega_c + \Omega_B - \Gamma_B/2 & \text{for } \phi \geq 0 \end{cases}. \tag{4.15}$$

For these frequencies, the response on the carrier due to its SBS interaction with Pump 1, can be calculated using Eqs. (2.57) and (2.58):

$$H_1(\omega_c) = e^{G_1/2} \cdot e^{\pm jG_1/4} \tag{4.16}$$

where G_1 is the strength of the SBS process due to Pump 1 [see Eq. (2.59)], and the sign of the phase contribution depends on the which of the frequencies from Eq. (4.15) is being used.

The frequency of Pump 2, ω_{p2} should remain fixed at

$$\omega_{p2} = \omega_c + \Omega_B \tag{4.17}$$

in all phase states. At this frequency, the response it induces on the carrier can be calculated using Eqs. (2.57) and (2.58) to be

$$H_2(\omega_c) = e^{G_2} \tag{4.18}$$

where G_2 is the strength of the SBS process due to Pump 2. The fact that the response is a real number indicates that this SBS process has no effect on the phase of the carrier.

Assuming that the two SBS processes due to Pumps 1 and 2 are linear processes, their effect on the optical carrier can be expressed as a combination of two linear systems whose response is described by Eqs. (4.16) and (4.18):

$$H_{\text{total}}(\omega_c) = e^{G_1/2+G_2} \cdot e^{\pm jG_1/4}. \tag{4.19}$$

This expression can be used to calculate the SBS strengths, i.e. pump powers, required to achieve a given phase shift ϕ, while maintaining a constant carrier power in all phase states:

$$G_1 = 4\,|\phi| \tag{4.20}$$

$$G_2 = 2\pi - 2\,|\phi| \tag{4.21}$$

for $-\pi < \phi \leq \pi$.

The validity of Eq. (4.19) hinges on the condition that the SBS interactions due to Pump 1 and 2 remain linear processes. This in turn requires that both pumps are not significantly depleted as they interact with the carrier [271]. Pump depletion can be avoided by using a low carrier power at the input of the SBS medium. This does not have a significant effect on the insertion loss of the phase shifter due to the fact that SBS gain is being used to shift the phase, so that the carrier is amplified before reaching the photodetector. Furthermore, while the phase shifter requires a low input carrier power, it does not impose any restrictions on the power of the optical sideband. Increasing the power of the optical sideband could then compensate for any increase in the insertion loss due to a reduced carrier power.

4.4.2 *Demonstration Using SBS in Fibre*

The novel SBS phase shifter can be demonstrated with the setup shown in Fig. 4.16. A tunable DFB semiconductor laser diode, with 500 kHz linewidth, is biased for CW operation with 1550 nm wavelength and 20 dBm output power. A 3 dB coupler is used to split the laser power between the two branches of the setup. With reference to Fig. 4.16, the lower branch is used to prepare the two SBS pumps. An MZM biased

for suppressed-carrier operation is fed with two RF tones. These are generated using two separate signal generators (SG1 and SG2), which allow for precise control of the frequency and power of the two SBS pumps. The output of the intensity modulator is then composed of four lines: two each for the upper and lower sidebands. Since the phase shifter requires the SBS pumps to be at a frequency higher than that of the optical carrier, the two lines corresponding to the upper frequency sideband can be selected with an optical bandpass filter (BPF). The two pumps can then be amplified using an EDFA before being sent through 2.3 km of standard silica SMF.

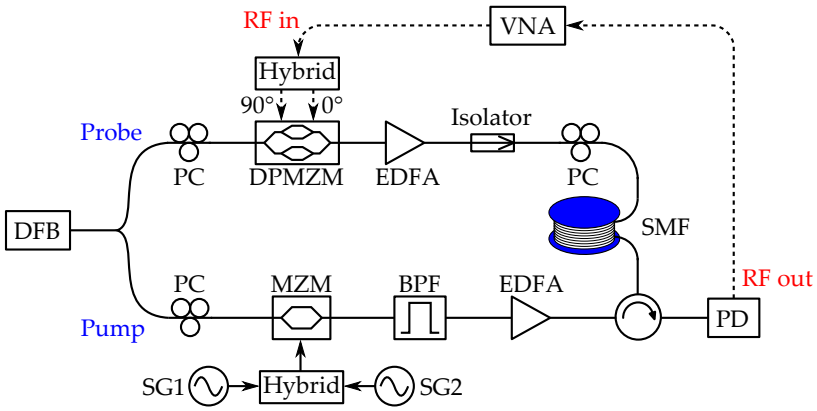

Fig. 4.16. Experimental setup for the MWP phase shifter using the novel SBS configuration from Fig. 4.15.

In the upper branch, referring to Fig. 4.16, the optical carrier is modulated with an the input RF signal, using a DPMZM, biased for SSB modulation. A low-noise EDFA then amplifies the optical signal before it is launched into the SMF. An optical isolator is placed at the output of the signal EDFA to prevent the two SBS pumps from injection locking the amplifier. The SBS interaction occurs along the SBS medium (in this case an SMF) where the carrier's phase and amplitude are affected according to Eq. (4.19). At the PD, the carrier and the sideband mix, and the sideband spectrum is down-converted back to the electrical domain. A VNA can be used to provide the input RF signal, and to measure the electrical frequency response of the phase shifter by comparing it to the output RF signal.

The electrical response of the system, shown in Fig. 4.17, measured with the VNA, spans from 1.5 GHz to 31 GHz. The lower frequency limit is set by the hybrid coupler used for feeding the RF signal to the DPMZM, while the upper frequency limit is due to the limited bandwidth of the DPMZM. The slight irregularity in the frequency response at 2.5 GHz remained visible even when both SBS pumps were turned off, and is therefore attributed to the response of the underlying photonic link. Not accounting for this irregularity, which is not caused by the operation principle, the amplitude response remains remarkably unchanged for different phase shifts, the variation being

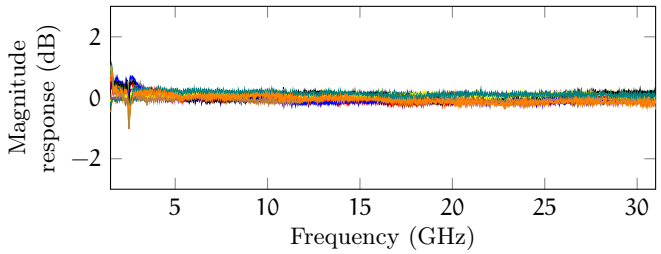

(a)

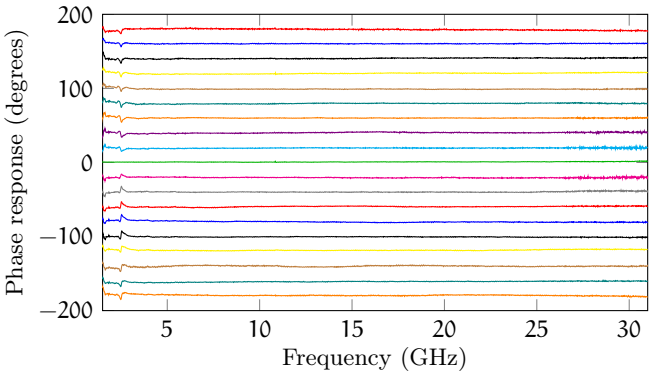

(b)

Fig. 4.17. Measured (normalized) frequency response for the MWP phase shifter using the novel SBS pump configuration.

less than ± 0.25 dB. The phase response is also flat, with less than 2° ripple over the whole measurement span. The phase shift could be continuously tuned in the range $\pm 180^\circ$.

The frequency and power of the two SBS pumps is controlled solely through the RF signal generators. The frequency of the SG used for the generating Pump 2 was set to 10.83 GHz, corresponding to the Brillouin frequency shift of the fibre. The phase pump frequency was set to 10.81 GHz for positive phase shifts, and to 10.85 GHz for negative phase shifts. The fact that both the pumps and the SSB signal are generated using the same carrier laser, means that any drifts in the laser wavelength affects both branches in the same way, thus improving the stability of the system. The parameters of the SMF used as the SBS medium were measured to be $L = 2.3$ km, $g_0 = 2.0 \times 10^{-11}$ m/W, $\alpha = 0.2$ dB/km, and $A_{\text{eff}} \approx 78$ μm^2. These values meant that the power of the Pump 1 reached a peak value of 14.0 dBm when providing $\pm 180^\circ$ phase shift, while the maximum power of Pump 2 was 10.2 dBm, for 0° phase shift. A comparison between experimental and theoretical gain, calculated using (4.20) and (4.21), is shown in Fig. 4.18. For all phase shifts, the combined magnitude response of Pump 1 and 2, results in the carrier power being amplified by a factor of $e^{2\pi}$, or 27.3 dB.

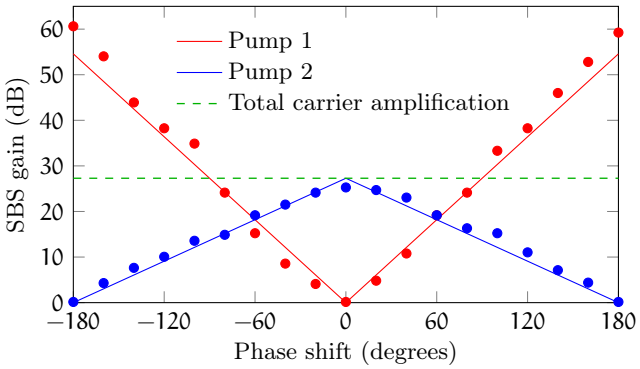

Fig. 4.18. Theoretical (line) and experimental (circle) SBS line centre gain for a given phase shifter state.

4.5 SUMMARY

The narrow linewidth of SBS makes it an ideal tool for implementing wideband MWP phase shifters through optical carrier processing. In this chapter, two SBS-based MWP phase shifters were presented, both making use of optical carrier processing, but with different SBS pump configurations.

The first phase shifter represents the first MWP phase shifter using on-chip SBS. It exploits a pump configuration first introduced in [94] to achieve low ±1.5 dB power fluctuations as the phase shift is continuously tuned across a 240° range, which is a record for a MWP phase shifter using an on-chip mechanism. These record-low power fluctuations are enabled by the unique ability of SBS to generate both gain and loss resonances, allowing it to shift the phase of an optical carrier without changing its amplitude. The pump configuration used by this phase shifter, while effective in minimizing power fluctuations, causes an interruption its usable bandwidth at a frequency of $2\Omega_B$.

It is also shown that power fluctuations at the output of the phase shifter are due to SBS pump depletion. Since the SBS occurs on the optical carrier, depletion can be avoided by using a low carrier power, which is actually undesirable since it limits the insertion loss of the phase shifter. This effect is shown to be more prominent in fibre than on chip, meaning that integration has the capacity for higher performance at high optical signal powers, and promises greater improvements in the insertion loss of the phase shifter, which is essential for practical applications.

The second phase shifter uses a novel SBS pump configuration which enables unprecedented control over the amplitude and phase of an optical carrier, and overcomes the bandwidth limitation of the previous approach. Independent control of the electrical amplitude and phase response is achieved simply by adjusting the power of two SBS pumps. This is used to demonstrate an MWP phase shifter with con-

tinuously tunable 360° phase shift tuning range and minimal power fluctuations less than ±0.25 dB over a 29.5 GHz span. The RF bandwidth of this phase shifter is however, theoretically unlimited due to the high time-bandwidth product of photonic signal processing.

Integration of this phase shifter would enable applicability to real-world systems, and lead to improved robustness, as well as a reduction in size, weight, cost, and power consumption [42]. Thus far, the highest SBS gain demonstrated on-chip is 23 dB, in a 7 cm long ChG rib waveguide [206]. According to Eq. (4.19), this would allow a maximum ±76° phase shift. The high SBS gain required by this technique highlights the importance of current research into high-SBS-gain materials [108].

5

FREQUENCY MEASUREMENT SYSTEM USING ON-CHIP FOUR-WAVE MIXING

5.1 INTRODUCTION

The ability to monitor a given portion of the microwave spectrum and to measure the frequency of an unknown signal, is a basic requirement for the operation and testing of wireless systems. In particular, the ability to do so in real-time, known as instantaneous frequency measurement (IFM), is crucial for Radar receivers used in electronic warfare (EW) [273] and biomedical technology [274, 275]. Figure 5.1(a) depicts a scenario where an IFM system is deployed in a Radar receiver for measuring the frequency of the Radar signal reflected from a moving target. The Doppler shift on the reflected wave allows the determination of the target's velocity. Another application of IFM to EW involves preventing receiver jamming, by quickly identifying the jammer frequency and directing a notch filter to suppress it [276].

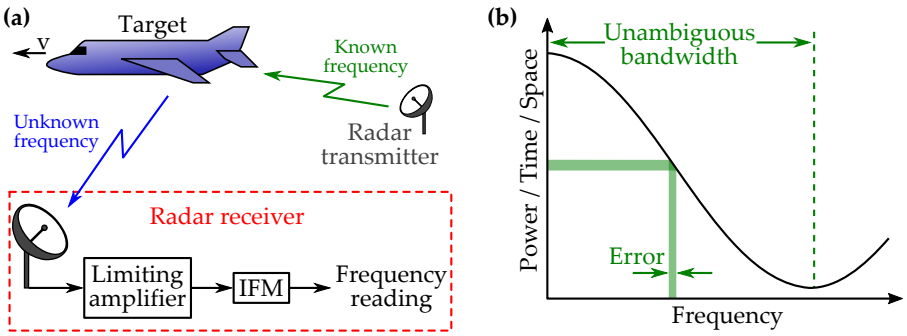

Fig. 5.1. (a) IFM receiver used for detecting the Doppler shift on a reflected signal, allowing determination of the target's velocity. (b) Transfer function of a frequency measurement system, where the unknown frequency of the input signal is mapped to a variable such as power, time, or space.

The applications just described highlight two key requirements for IFM systems: fast measurement speed and high instantaneous bandwidth. This is different from conventional frequency measurement devices, such as swept-tuned electrical spectrum analysers. These are capable of monitoring large bandwidths, but they do this by sweeping through a sequence of smaller frequency bands. Consequently, their instantaneous bandwidth is low (e.g. they have a small probability of detecting a pulse shorter than their sweep time). Spectrum analysers which instead rely on the fast Fourier transform algorithm can, in principle, achieve large instantaneous bandwidths, but in practice

are limited by electronic sampling speeds and their bandwidth rarely surpasses 1 GHz.

On the other hand, IFM systems trade-off the high measurement accuracy of conventional spectrum analysers for large, multi-GHz, instantaneous bandwidths. They do this by mapping the frequency of an input signal to a more easily measurable quantity, such as power, time, or space. The typical response, or mapping function, of an IFM system is shown in Fig. 5.1(b). This mapping function is, in general, not monotonic, meaning that a given power/time/space measurement might map to more than one frequency value. The range of frequencies for which there is a one-to-one correspondence between the measured variable and the output frequency value, is known as the unambiguous bandwidth. Any uncertainty in the measured variable directly translates to an uncertainty in the output frequency value. This uncertainty is known as the error of the measurement. It is directly linked to the measurement resolution, which indicates the minimum frequency spacing required to distinguish two different signals.

Modern electronic-based IFM systems are capable of fast measurement times (< 50 ns), with high accuracy ($< 1\%$ of the measurement bandwidth), sufficient for most applications [273]. However, they are also heavily limited by the instantaneous bandwidth they can monitor, normally around 18 GHz [277, 278]. Moreover, they are considerably bulky and complex, requiring multiple mixers, and are plagued by high power consumption. The use of photonics for implementing microwave IFM not only achieves greatly improved instantaneous bandwidth, but can also lead to simpler, smaller, and more efficient systems.

Some of the earliest photonics-based IFM systems relied on frequency-to-space mapping [279–281]. The underlying principle of these devices is based on an optical channeliser, which acts as an array of optical filters, splitting the signal and sending different portions of its spectrum (i.e. channels) to different paths. After electrical-to-optical conversion, the signal is spatially demultiplexed using the channeliser. Each channel is then measured using a low-speed photodetector (PD). A non-zero reading at a given PD signifies an event (i.e. frequency) detected for that particular channel. The advantage of such IFM systems is their ability to detect multiple frequencies simultaneously. Their main limitation however lies in their key component; the IFM resolution is derived from the channeliser channel-spacing and optical channelisers normally posses channel spacings of multiple tens of gigahertz. A channeliser with megahertz frequency spacing has been demonstrated with stimulated Brillouin scattering (SBS) [282], but in order to achieve multiple gigahertz of instantaneous bandwidth, such a device would require prohibitive amounts power to generate hundreds of SBS pumps.

Other photonics-based approaches rely on frequency-to-time mapping. A number of demonstrations make use of the "scanning receiver" approach [283–286] where the centre frequency of a bandpass filter is continuously scanned across the frequency band of interest. A different type of frequency-to-time IFM systems works by delaying the optical signal by an amount dependent on its frequency, either through the use of a dispersive medium [287], or by embedding a frequency shifter within a recirculating delay line [288, 289]. Frequency-to-time mapping IFM systems are capable of measuring multiple frequencies simultaneously, with high accuracy, at the cost of a high measurement delay, typically of the order of microseconds.

Frequency-to-power mapping IFM systems are the most common. They are also the simplest, requiring the least number of components, and the least expensive since power measurement is a very basic functionality. A number of these systems have been implemented using the power fading approach [290–299], where the signal frequency is extracted by measuring its attenuation at the output of an optical filter whose response has been carefully characterized. Other implementations make use of interferometric approaches [117–120, 300–304]. Both of these architectures are explained in more detail in Sec. 5.2.

As previously discussed in Chapter 1, integration is important for microwave photonic (MWP) signal processors. This is especially true in the case of IFM, where smaller circuits can significantly reduce the measurement latency. The aforementioned characteristics of frequency-to-power mapping IFM cause these systems to be the most prone to integration, and they have in fact been recently demonstrated in a number of integrated platforms [128, 305–307]. However, all of these previous on-chip demonstrations obtained a measurement by exploiting the frequency response of various optical components (e.g. ring resonators and gratings), which limited their bandwidth to values below 10 GHz [128, 305, 306], or caused their measurement error to exceed 2% [307]. Nonlinear optical interactions have the potential to broaden the frequency measurement range beyond these limits, and with higher accuracy. The key lies in efficiently harnessing optical mixing in a nonlinear platform with low losses. To date, this requirements have only been met by optical fibres, and previous nonlinear optics-based IFM systems relied on hundreds of meters of fibre for these interactions [117–120].

This chapter presents the use of a low-loss, thick silicon on insulator (SOI) platform for efficiently harnessing nonlinear optical mixing. The unique properties of this platform lead to an on-chip frequency-to-power mapping IFM system with record-high instantaneous bandwidth and sub-1% measurement error. Sec. 5.2 provides a detailed description of the different power-mapping IFM architectures. Optical mixing uses an interference approach to perform IFM, and the working principle behind this is explained in Sec. 5.3, along with

the demonstration of the first on-chip IFM system relying on this approach to achieve record performance. This section also lays out a road-map for creating an IFM system that is monolithically integrated in a silicon chip.

5.2 POWER MAPPING IFM ARCHITECTURES

5.2.1 *Power Fading Approach*

The power fading approach is the most intuitive of all photonics-based IFM systems. In its simplest form, it involves sending the signal into an optical element offering some frequency selectivity or discrimination, e.g. an optical filter such as a grating. The power of the signal at the output of said optical element is then measured. Prior knowledge of the frequency response of said element can then be used to estimate the signal frequency. Figure 5.2 shows the typical structure of an IFM system relying on power fading. It is important to note that these systems are only capable of measuring one frequency at any given time. Therefore, it is assumed that the power of the input radio frequency (RF) signal is concentrated at the one unknown frequency Ω. This signal modulates a continuous wave (CW) laser. Different modulation schemes have been used but most commonly consist of single sideband (SSB) or double sideband (DSB) modulation. The next step is the core functionality of the structure, where the signal is affected by the response of the frequency-selective element. In the first frequency-to-power mapping demonstration, this response was provided by a length of dispersive fibre [290]. As the signal travelled along the fibre, dispersion caused the modulation sidebands to experience equal but opposite phase shifts, relative to the carrier phase. Upon photodetection, the RF mixing products would also have equal but opposite phases, and their interference determined the power of the output RF signal. Since in a dispersive element, the phase shift is frequency-dependent, the power of the output RF signal could be used to first estimate the phase shift θ, and then the unknown frequency Ω .

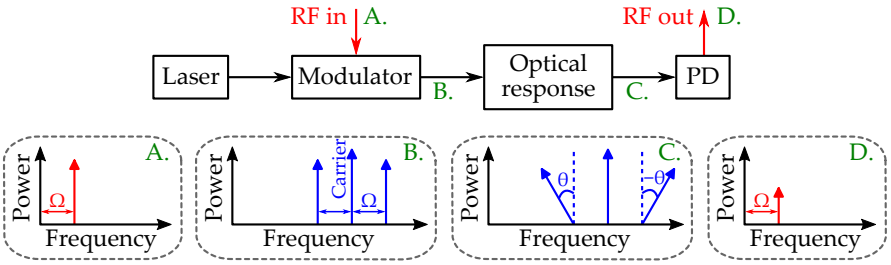

Fig. 5.2. Structure (above) and operating principle (below) of photonics-based IFM systems relying on the power fading approach.

Following its first demonstration in 2006, the optical response in IFM systems has been provided using a variety of devices, including interferometers [291–293, 297, 299], gratings [294], and SBS [298]. In particular, all on-chip IFM demonstrations to date have relied on the power fading approach through the use of optical filters such as ring resonators [128, 305], microdisks [306], or integrated Bragg gratings [307].

When an optical filter is used as the source of the optical response, frequency-to-power mapping is achieved by selecting a carrier wavelength such that the modulation sideband falls within the filter resonance, as shown in Fig. 5.3(a). The filter is then characterized by sweeping the frequency of a known input RF signal, and measuring the power at the output of the IFM system. This process generates a function which relates the frequency of the input signal to the power of the output signal, and is called an amplitude comparison function (ACF). In the simplest cases, the ACF has the same profile as the filter response, shown in Fig. 5.3(b). During standard operation, when the input signal frequency is unknown, the measured output signal power is compared to the predetermined ACF.

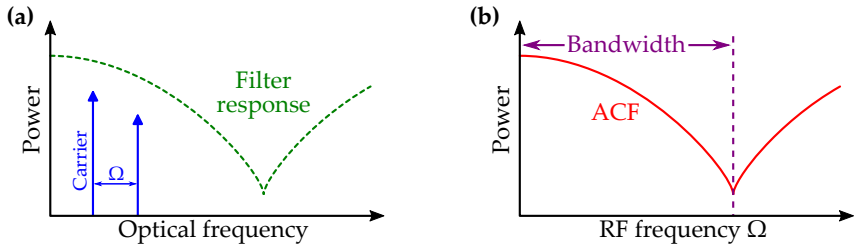

Fig. 5.3. (a) Operating principle of a power fading IFM system where the input SSB-modulated signal is passed through an optical filter. (b) Sweeping the input RF signal frequency Ω across a predetermined range, and measuring the output power, yields the ACF of the IFM system.

The problem with this approach is that the output signal power depends not only on the frequency, but also on the power of the input RF signal. For example, in a linear system, if the power of the input signal is doubled, the power of the output RF signal is also doubled. In this case, use of the ACF gives erroneous results. There are two main solutions to this problem. The solution employed by electronic-based IFM systems is to send the input RF signal through an electrical limiting amplifier, before measuring its frequency [273]. Limiting amplifiers are designed to provide the same output level, independently from the input power. This method however, causes the bandwidth of the IFM system to be restricted by the bandwidth of the limiting amplifier. The second approach, increasingly used by photonics-based IFM systems, is to split the modulated carrier, and process it with two different linear optical responses. The outputs from the two responses are then detected separately, using two PDs.

Taking the ratio of the output powers then normalizes the ACF, eliminating any dependence on the input signal power. While requiring more components, demonstrations have cleverly adapted to exploit the multiple responses displayed by a single optical filter, such as the drop and through ports of a ring resonator [305], or the transmitted and reflected outputs of a grating [294, 307].

It is clear that the performance of the IFM system is directly related to its ACF which in turn depends on the optical response used. The two IFM features which are most affected by the optical response are the measurement bandwidth and the resolution. The measurement bandwidth depends in part on the bandwidth of the optical response, but its main limitations comes from the periodicity of the ACF. This is shown in Fig. 5.3(b), where the frequency measurement bandwidth is equal to the portion of the ACF where there is a one-to-one relation between the input frequency Ω and the output power. The resolution of the measurement gives an indication of the minimum frequency step that can be distinguished by the IFM system (i.e. the measurement accuracy). If two input signals differ in frequency by an amount $\Delta\Omega$, and the power readings at the output of the IFM system differ by an amount ΔP, the resolution is given by

$$\text{Resolution} = \left| \lim_{\Delta\Omega \to 0} \frac{\Delta P}{\Delta \Omega} \right| \tag{5.1}$$

which is equivalent to the slope of the ACF. In order for the IFM system to possess the highest measurement accuracy across the broadest measurement bandwidth, it is desirable to simultaneously maximize the width and the slope of the ACF. This however is not always possible and in fact, these two requirements are often conflicting. As an example, most on-chip IFM systems have made use of ring resonators, and their response is quite similar to that shown in Fig. 5.3(a). When using these filters, increasing the measurement bandwidth (or horizontally "stretching" the ACF) necessarily reduces the slope of the ACF. All frequency-to-power mapping IFM systems suffer from an inherent trade-off between measurement bandwidth and resolution.

5.2.2 *Interference-Based IFM*

Interferometric approaches are commonly used by electronic IFM systems. Their typical structure is shown in Fig. 5.4(a). They operate by splitting the input RF signal along two paths. One of these paths has a longer travel time, so that the signal it carries is delayed by some predetermined amount Δt, relative to the other path. Finally, the two signal copies are recombined at the output, either through superposition or mixing. The response of the IFM system is depicted in Fig. 5.4(b), where the output power varies sinusoidally as a function of the input signal frequency Ω. This response can be considered as an

ACF, defined by the differential delay Δt. The main obstacle faced by electronic implementations is that the couplers and mixers used are required to function over multiple tens of gigahertz bandwidth. This is a major challenge in electronics but not in photonics, where nonlinear optical mixing has been used to demonstrate IFM systems with 40 GHz bandwidth [117], limited only be the electronic measurement equipment.

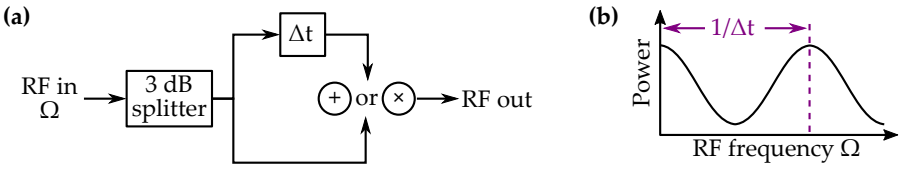

Fig. 5.4. (a) Typical structure of an interference-based IFM system, where two copies of the input signal to be measured are differentially delayed and recombined either through superposition or mixing. (b) Response of an interferometric-based IFM system, where the output signal power is a function of the input signal frequency.

In order to understand the properties of interference-based IFM systems, the output power can be written in its simplest form as

$$P_{\text{out}}(\Omega) \propto \cos(\Omega \Delta t). \tag{5.2}$$

This is periodic in frequency, the period being equal to $1/\Delta t$. In order to obtain an unambiguous value from the IFM, it is necessary to restrict the range of input frequencies such that there is always a one-to-one correspondence between the input frequency and the output power. For this, the actual measurement bandwidth is equal to half of the period, or

$$\text{Bandwidth} = \frac{1}{2\Delta t}, \tag{5.3}$$

which is inversely proportional to Δt. The measurement resolution, given by Eq. (5.1), for a sinusoidal ACF can be expressed as

$$\text{Resolution} \propto \Delta t \sin(\Omega \Delta t), \tag{5.4}$$

which is directly proportional to Δt.

These two expressions show a similarity between interferometric and power fading IFM systems; that is, there is an inherent trade-off between measurement bandwidth and resolution. However, unlike power fading IFM systems where the system response is fixed by the properties of the optical response, the response of interferometric IFM systems can be reconfigured by adjusting the delay Δt. This process is illustrated in Fig. 5.5. A short delay Δt results in the system response shown in Fig. 5.5(a), with a wide measurement bandwidth and a low resolution (i.e. a large error or uncertainty in the measurement). Subsequent increase of the delay, shown in Fig. 5.5(b), reduces the period

of the system response and a given power reading no longer maps to a single frequency value, but to multiple frequencies, residing in different bands. In order for such a measurement to be meaningful, the user must possess some prior knowledge of the input RF signal (e.g. the input signal frequency might be known to reside in Band 4). The reduction in unambiguous bandwidth however also increases the slope of the response, thus improving the resolution and accuracy of the system.

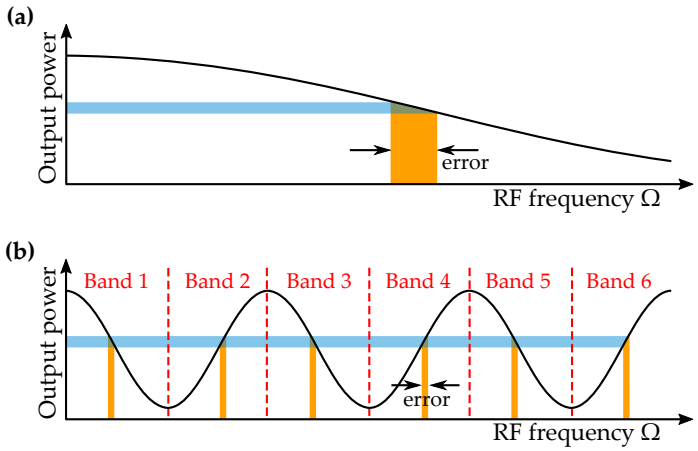

Fig. 5.5. Response of an interferometric frequency-to-power mapping IFM system, where the differential delay Δt is changed from a low value in (a), to a high value in (b).

As demonstrated in [120], it is possible to design an algorithm which maximizes the measurement accuracy across the broadest bandwidth by dynamically varying Δt. The algorithm is quite intuitive, involving consecutive increases in the value of Δt as more knowledge is acquired about the input RF signal. For example, when an unknown RF signal is first detected, no prior knowledge of it exists, and Δt should be set to its lowest possible value as to give an unambiguous, but rough, estimate of its frequency. With this information, the signal can be re-measured with a higher value of Δt, so as to give a more accurate estimate of its frequency. The information from the first, rough measurement is then used to remove the ambiguity from the second, more accurate measurement. This process is repeated until the error in the measurement is deemed sufficiently low. Therefore, the reconfigurability of interference-based IFM systems enables them to circumvent the inherent bandwidth/error trade-off.

5.3 IFM WITH OPTICAL MIXING

5.3.1 *Working Principle*

Nonlinear optical mixing was first applied to microwave IFM in 2009 [117], the motivation behind it being that it enabled the implemen-

tation of an extremely high frequency, interference-based IFM system. Nonlinear optical mixing processes (such as four-wave mixing (FWM)) can easily operate over hundreds of gigahertz of bandwidth, so that the resulting IFM system has no inherent RF measurement bandwidth limitation. The system works by generating two mixing products (i.e. idlers) at the same frequency, causing them to interfere. Measurement of the optical idler power can then be used for estimating the frequency of the input RF signal.

The basic structure of an IFM system relying on optical mixing is shown in Fig. 5.6(a). Two lasers are used to generate two CW optical carriers at two different frequencies ω_1 and ω_2, shown in Fig. 5.6(b), part A. These two carriers are then sent to two separate modulators, where they undergo intensity modulation by the same RF signal whose frequency, Ω, is to be determined. The combined optical spectra at the output of the two modulators are shown in part B of Fig. 5.6(b), and can be written in terms of complex fields as

$$\begin{aligned} E_B(t) = &\left(C_1 + S_1 e^{-j\Omega t} + S_1 e^{j\Omega t}\right) e^{j\omega_1 t + j\phi_{R1}} \\ &+ \left(C_2 + S_2 e^{-j\Omega t} + S_2 e^{j\Omega t}\right) e^{j\omega_2 t + j\phi_{R2}} + \text{c.c.} \end{aligned} \tag{5.5}$$

where C_1 and C_2 are the complex amplitudes of the two carriers, while S_1 and S_2 are the complex amplitudes of the modulation sidebands. For generality, phase terms ϕ_{R1} and ϕ_{R2} are added to the two separate signal fields to model the effect of any phase fluctuations occurring along the structure (including due to the lasers not being phase-locked).

The signal carried by ω_2 is then delayed by a known amount Δt, so that the combined field becomes

$$\begin{aligned} E_C(t) = &\left(C_1 + S_1 e^{-j\Omega t} + S_1 e^{j\Omega t}\right) e^{j\omega_1 t + j\phi_{R1}} \\ &+ \left(C_2 + S_2 e^{-j\Omega t + j\Omega\Delta t} + S_2 e^{j\Omega t - j\Omega\Delta t}\right) \\ &\cdot e^{j\omega_2 (t-\Delta t) + j\phi_{R2}} + \text{c.c.} \end{aligned} \tag{5.6}$$

The delay effectively causes the sidebands on the second carrier to experience equal but opposite phase shifts, relative to the carrier phase, shown in Fig. 5.6(b), part C.

Up until this stage, the two optical signals have been kept separate, so that no interaction occurs between them. The next process is to combine them and mix these signals together. The mixing occurs due to FWM which is a third-order optical nonlinearity. After mixing therefore, the field is proportional to the cube of the combined field:

$$E_D(t) \propto E_C^3(t). \tag{5.7}$$

Mixing has the effect of generating new frequency components, called idlers. A number of these idlers can be considered as copies of the

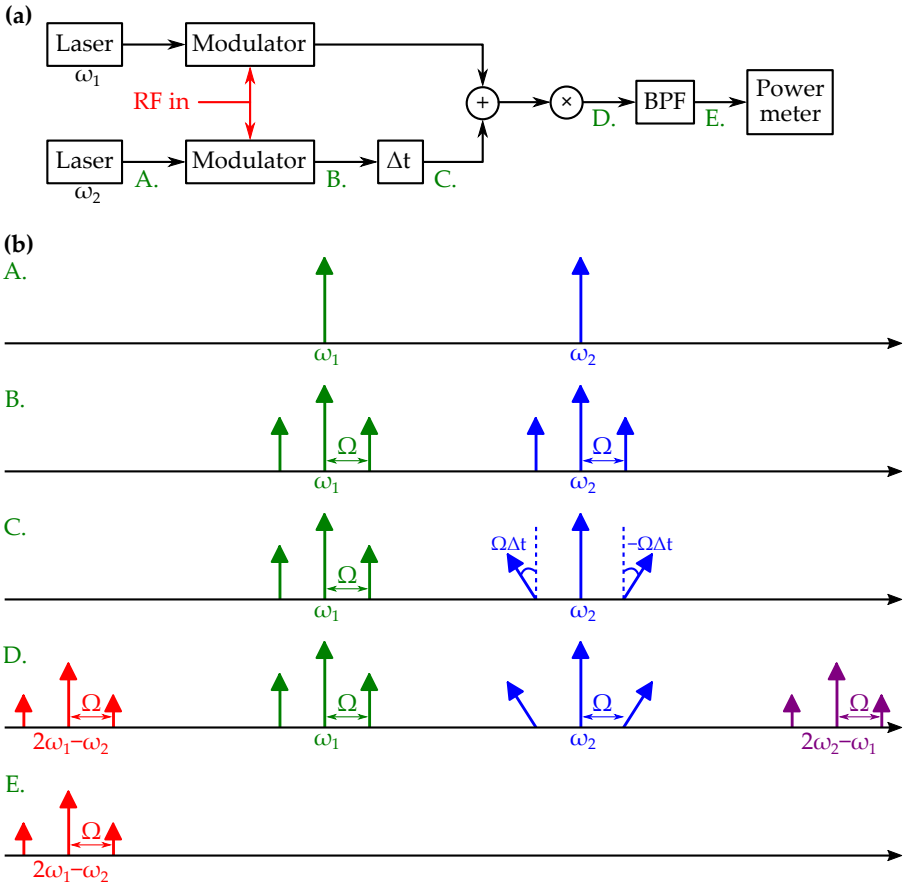

Fig. 5.6. (a) Structure and (b) operating principle of an IFM system based on optical mixing. A: The system relies on using two CW optical carriers at separate frequencies. B: The two optical carriers are modulated using the same input RF signal with frequency Ω. C: One of the two modulated carriers is delayed relative to the other, and the sidebands experience frequency-dependent phase shifts. D: The two modulated carriers interact via FWM, generating idler channels. E: One of these idler channels is selected with a BPF, and its power measured.

original optical signals, comprising their own carrier and modulation sidebands. These copies occur in the vicinity of frequencies $2\omega_1 - \omega_2$ and $2\omega_2 - \omega_1$, shown in Fig. 5.6(b), part D. An optical BPF is then used to select one of these signal copies while suppressing all other frequency components. Finally, the output of the BPF, shown in part E of Fig. 5.6(b), is sent into an optical power meter (i.e. a low-speed PD). The function of the power meter is to output a DC voltage proportional to the optical power of the signal at its input. It is this DC voltage which allows for the estimation of the frequency Ω of the input RF signal.

In order to understand the relationship between these two quantities, we focus on the formation of only one of the idler sidebands, more specifically, the upper sideband of the idler, which has frequency $2\omega_1 - \omega_2 + \Omega$. We know that this sideband forms due to the

mixing of any combination of three frequency components of the field described by Eq. (5.6). To simplify the procedure however, it is convenient to assume that the original optical carriers are significantly stronger than the modulation sidebands, i.e. $|C_i| \gg |S_i|$, with $i = 1, 2$, so that any mixing product of order $|S_i|^2$ or $|S_i|^3$ can be neglected. With this simplification, there are only two mixing processes which contribute to the formation of the upper sideband of the idler:

$$E(2\omega_1 - \omega_2 + \Omega) = \begin{cases} E(\omega_1)E(\omega_1)E^*(\omega_2 - \Omega) & \text{degenerate} \\ E(\omega_1)E(\omega_1 + \Omega)E^*(\omega_2) & \text{non-degenerate} \end{cases} \tag{5.8}$$

These two processes are illustrated in Fig. 5.7. The first one is known as a *degenerate* FWM process due to the fact that it is the mixing of only two distinct frequency components, the component with frequency ω_1 appearing twice in the product. The second process instead is *non-degenerate* because all three factors are distinct, residing at different frequencies.

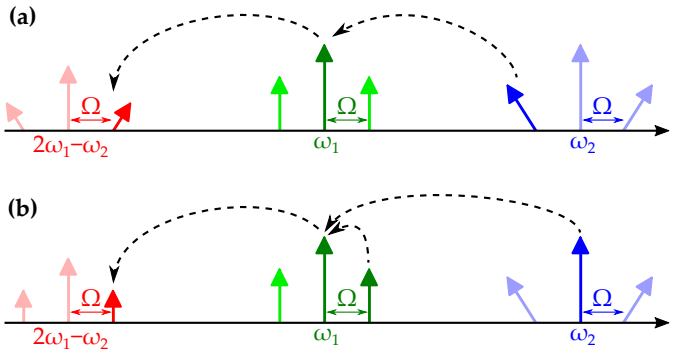

Fig. 5.7. (a) Degenerate and (b) non-degenerate FWM processes which lead to the generation of the upper frequency sideband of the idler.

With this information, it is possible to express the output fields resulting from these two separate FWM processes. For the sake of compactness, these are written in phasor form (it is implicitly assumed that both fields oscillate with frequency $2\omega_1 - \omega_2 + \Omega$)

$$E_{\text{degenerate}} \propto 3C_1^2 S_2^* e^{-j\Omega\Delta t} \cdot e^{j\omega_2\Delta t} \cdot e^{j(2\phi_{R1} - \phi_{R2})} \tag{5.9}$$

$$E_{\text{non-degenerate}} \propto 6C_1 C_2^* S_1 e^{j\omega_2\Delta t} \cdot e^{j(2\phi_{R1} - \phi_{R2})} \tag{5.10}$$

The factors of 3 and 6 are to take into account all possible permutations of the frequency components being multiplied. The total field at the idler frequency $2\omega_1 - \omega_2 + \Omega$ is a coherent sum of these two separate fields:

$$\begin{aligned} E(2\omega_1 - \omega_2 + \Omega) &= E_{\text{degenerate}} + E_{\text{non-degenerate}} \\ &\propto \left(3C_1^2 S_2^* e^{-j\Omega\Delta t} + 6C_1 C_2^* S_1\right) \\ &\quad \cdot e^{j\omega_2\Delta t} \cdot e^{j(2\phi_{R1} - \phi_{R2})} \end{aligned} \tag{5.11}$$

The optical power of this particular idler component can now be calculated

$$\begin{aligned} P(2\omega_1 - \omega_2 + \Omega) &\propto E(2\omega_1 - \omega_2 + \Omega) \cdot E^*(2\omega_1 - \omega_2 + \Omega) \\ &\propto 9\,|C_1|^4\,|S_2|^2 + 36\,|C_1|^2\,|C_2|^2\,|S_1|^2 \\ &\quad + 36\,|C_1|^2\,|C_1|\,|C_2|\,|S_1|\,|S_2| \\ &\quad \cdot \cos(\angle C_1 - \angle S_1 + \angle C_2 - \angle S_2 - \Omega\Delta t) \end{aligned} \tag{5.12}$$

This expression highlights a number of key properties of the IFM system. Of main importance is the fact that the idler power varies sinusoidally with the RF frequency; this is shown by the $\Omega\Delta t$ term inside the cosine of Eq. (5.12). Another key point is that the idler power is stable; while the laser phase fluctuations affect the idler phase through the $e^{j(2\phi_{R1}-\phi_{R2})}$ term in Eq. (5.11), these fluctuations have no effect on the idler power. The only phases which have an effect on the idler power are the phase differences between the two carriers and their respective sidebands, i.e. terms $\angle C_1 - \angle S_1$ and $\angle C_2 - \angle S_2$ in Eq. (5.12). Neglecting dispersion effects, these phase differences however are constant throughout the system, and therefore do not cause instabilities.

In the IFM system from Fig. 5.6(a) however, it is not just the power of the upper idler sideband which is being measured. Also the powers of the idler carrier (frequency $2\omega_1 - \omega_2$) and of the lower idler sideband (frequency $2\omega_1 - \omega_2 - \Omega$) are detected by the power meter. The expression for the lower idler sideband can be found by using a procedure analogous to that for the upper idler sideband above. It is simple to show that also the lower sideband's power fluctuates sinusoidally as a function of $\Omega\Delta t$. On the other hand, the power of the idler carrier is not affected by the input RF frequency. The reason for this is that the idler component with frequency $2\omega_1 - \omega_2$ results from a single, degenerate FWM process and not from two distinct processes as is the case for the idler sidebands. For this reason, the power of the idler carrier can be modelled as a constant term. Therefore, in the ideal case where all the fields are in phase (i.e. $\angle C_1 = \angle S_1 = \angle C_2 = \angle S_2$), the total power detected using the power meter can be described by the following function

$$P_{\text{total}} = A + B\cos(\Omega\Delta t) \tag{5.13}$$

for some constants A and B, with $A > B$. This expression constitutes the ACF of the IFM system. It clearly shows that, once the system has been characterized, i.e. A, B, and Δt are known, an optical power meter can be used to estimate the unknown RF frequency Ω.

The above derivation serves to demonstrate that the IFM system from Fig. 5.6(a) relies on nonlinear optical mixing to generate two idlers at the same frequency, causing them to interfere. As such, it is considered a frequency-to-power mapping, interference-based IFM

system. Indeed, the ACF described by Eq. (5.13) displays a number of properties inherent to interferometric systems, such as a trade-off between measurement bandwidth and resolution regulated by the differential delay Δt (see Sec. 5.2.2). Another important characteristic of this expression however is that it offers an alternative way of increasing the measurement resolution, without reducing the unambiguous bandwidth. It involves increasing the "visibility" of the interference pattern by maximizing the value of B. This has the effect of increasing the slope of the ACF which, according to Eq. (5.1), is directly proportional to the measurement resolution. Equation (5.12) suggests that the most effective way of achieving this is by increasing the power of the optical carrier at ω_1. Of equal importance however, is the efficiency of the FWM process. Equation 5.13 is, essentially, the power of the mixing idler, and both A and B have a strong dependence on the nonlinearity of the mixing medium. For this, in order to optimize the performance of the IFM system, one should choose a mixing medium which maximizes the strength of the generated idlers.

5.3.2 *Chip Implementation and Characterization*

Since their first demonstration, IFM systems using nonlinear optical mixing have gathered significant attention, and have evolved to implement remoted IFM receivers [118], to enable amplitude-independent operation [119], and to demonstrate a reconfigurable IFM system with enhanced measurement accuracy across a broad bandwidth [120]. The wideband mixing process employed by all these prior demonstrations was FWM in a length of silica highly nonlinear fibre (HNLF). The relatively low nonlinearity of this type of fibre however meant its length had to span several hundreds of meters. An IFM system with a component which is hundreds of meters long is bound to experience relatively long measurement latencies (i.e. microseconds) as the signal travels through it, while real-world applications can only afford nanosecond delays [273]. Therefore, the first step towards improving the system performance is to identify a nonlinear platform where a strong mixing idler can be generated over a short length.

Dispersion-engineered chalcogenide (ChG) rib waveguides provide a possible solution, having a higher figure of merit (FOM) than most other nonlinear platforms [161], and have been used to demonstrate an impressive 30 dB idler gain over a 6.5 cm length [174]. However, this required the pump wave to be pulsed in order to limit the average power inside the ChG waveguide and the associated thermal effects. More recently, AlGaAs was shown capable of very high conversion efficiencies using CW pumps (as required for IFM) [177, 308], and holds the current record for highest conversion efficiency in the shortest device length, with the lowest pump power (-8.7 dB in a 3 mm long waveguide, using 145 mW of pump power) [180]. While promising,

both of these platforms have the drawback of not being compatible with current complementary metal-oxide semiconductor (CMOS) fabrication processes. In order to gain this advantage, one must rely on silicon as the FWM medium. Silicon nanowires have been shown capable of high conversion efficiencies up to −12 dB in 2 cm of crystalline silicon [309], or −13 dB in 8 mm of hydrogenated amorphous silicon [310]. However, current nanowires are plagued by high propagation losses and low CW power handling, due to the onset of nonlinear losses. Moreover, their small core areas greatly increases fibre-to-chip coupling losses. The combination of all these factors means that, while the conversion efficiency is high, the output idler power may actually be quite low. This is a serious constraint in FWM-based IFM, where the power of the generated idler plays a direct role in determining the slope of the ACF and the corresponding IFM performance. For this kind of application, the FWM medium is required to display the optimum combination between conversion efficiency and propagation losses which leads to the highest possible idler power. Therefore, for IFM, thick, micrometer-sized silicon waveguides may prove a better candidate than more standard silicon nanowires.

Silicon photonic waveguides with micrometer cross-sections have been in use for a number of years [311–316]. They offer linear propagation losses as low as 0.09 dB/cm [316], compared to 1–3 dB/cm for smaller silicon nanowires. Their larger core area leads to significantly lower fibre-to-chip coupling losses and a higher nonlinear loss threshold, but also hinders optical nonlinearities due to a lower light intensity. This drawback is normally counteracted by increasing the interaction length through the use of longer waveguides. For on-chip operation however, this is not feasible since waveguides with micrometer cores require bending radii with millimetre or even centimetre dimensions (to avoid coupling to higher order modes), which lead to impractically large chips. For this reason, thick waveguides are usually constrained to lengths of a few centimetres, and are not suited to the observation of nonlinear effects. Nonetheless, a breakthrough in this regard has been recently demonstrated through the use of Euler bends, where the bending radius varies continuously along the whole bend. This design has led to the integration of micrometer thick silicon waveguides with micrometer-scale bending radii, comparable to those of smaller silicon nanowires [316]. This advance enables the realization of ultra-compact low-loss thick silicon waveguides with long lengths, capable of supporting nonlinear interactions.

One such waveguide is used as the FWM medium in this particular demonstration of IFM. The waveguide has a large mode area of 2.7 μm^2, and a long 35 cm length, with a small footprint. The whole 35 cm spiral, shown in Fig. 5.8(a), occupies less than 3 mm^2 surface area on an SOI chip. The waveguide has a strip geometry, shown in Fig. 5.8(b), with cross-section dimensions of 3×1.875 μm. As pre-

viously explained, this large size leads to a low 0.15 dB/cm linear propagation loss, as well as low 1.5 dB/facet fibre-to-chip coupling losses. While the strip is multi-moded, coupling from the fibre occurs through a single-mode rib waveguide [317, 318] which then tapers into the strip waveguide, as shown in Fig. 5.8(c). This ensures excitation of the fundamental mode.

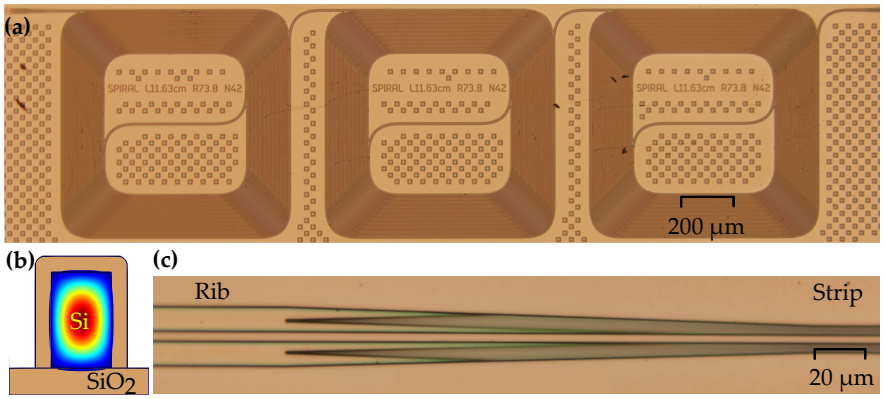

Fig. 5.8. (a) 35 cm long, thick silicon spiral top view. (b) Simulation of the fundamental mode for the 3×1.875 μm silicon strip waveguide. (c) Rib-to-strip converter for coupling to the fundamental mode.

The nonlinear optical properties of the waveguide were measured through a series of self-phase modulation (SPM) and FWM experiments. Figure 5.9(a) shows the SPM-induced broadening of a picosecond-duration pulse as it propagates along the waveguide. Measurement of the pulse broadening for different input pulse peak powers, shown in Fig. 5.9(b), was used in conjunction with Eq. (2.28) to estimate the nonlinear parameter of the waveguide to be $\gamma \sim 1.8$ m^{-1}W^{-1}. This value corresponds to a Kerr coefficient of $n_2 \sim 1.2 \times 10^{-18}$ m^{2}W^{-1}, which is slightly lower than for a typical silicon waveguide, possibly due to the change in crystal orientation that occurs in the spiral bends [319]. A similar experiment with picosecond pulses was used to measure the nonlinear loss of the waveguide, neglecting free-carrier effects. The result, shown in Fig. 5.10, was fit with Eq. (2.33) to obtain a two-photon absorption (TPA) coefficient $\beta \sim 0.23$ cm/GW. This value is comparable to that for amorphous silicon, but thick silicon has the advantage of exhibiting a significantly lower linear propagation loss [186].

The relevant FWM parameters of the thick silicon waveguide were measured in the CW regime, as required by the IFM system. Figure 5.11(a) shows the measured FWM conversion efficiency of the spiral, for different input pump powers with 1550 nm wavelength. The maximum achieved conversion efficiency (defined as the output idler power divided by the input signal power) was -18.7 dB, using an input pump power of 20.5 dBm, shown in Fig. 5.11(b). This is an encouraging value, when considering the high powers supported by the

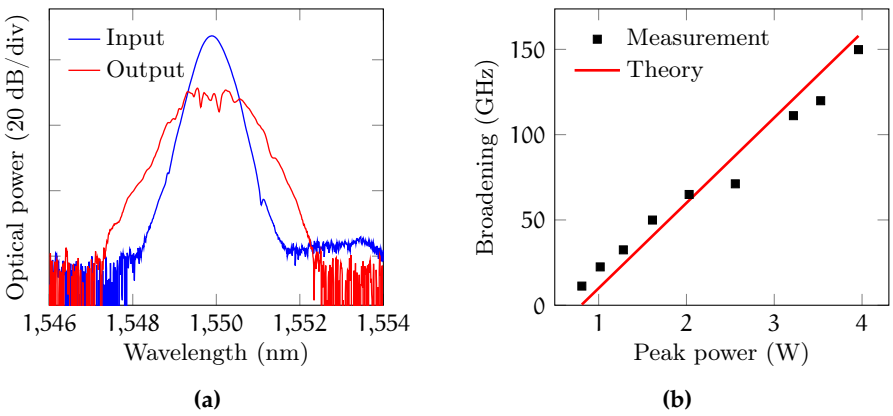

Fig. 5.9. (a) Pulse spectra at the input and output of the thick silicon waveguide. The pulse characteristics are 6.29 ps period, with 38.6 MHz repetition rate, and 4.0 W peak input power. (b) SPM pulse broadening at the waveguide output, for different input peak powers.

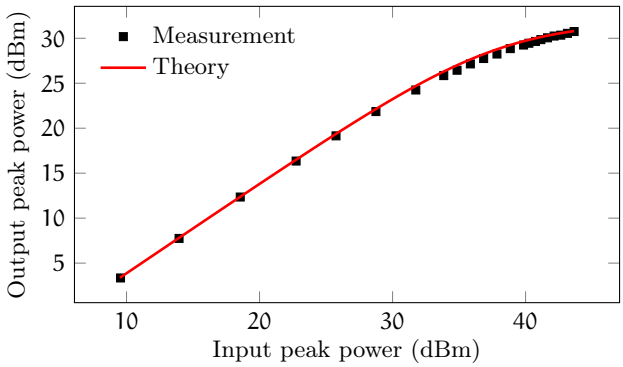

Fig. 5.10. Pulsed output-input power characteristic of the thick silicon waveguide showing the onset of nonlinear losses, mainly due to TPA. The pulse characteristics are 6.29 ps period, with 38.6 MHz repetition rate, and 11.9 W peak input power.

waveguide, promising a high idler power as required for IFM. Finally, the waveguide dispersion at a 1550 nm wavelength was measured to be normal, leading to an FWM 3-dB bandwidth of 6 nm. This value is however sufficient for most microwave photonic applications, where the signal content is in the range of 1–100 GHz, or less than 2 nm.

The structure presented in Fig. 5.6(a), while useful for understanding the principle of mixing-based IFM systems, is not an efficient design. All demonstrations to date have instead relied on the architecture shown in Fig. 5.12(a). Here the modulator, being the most expensive component, is shared by the two optical carriers. A dispersive element (such as a chirped fibre Bragg grating) is then used to delay one of the modulated signals, before both are launched into the FWM medium, usually a length of HNLF. In this setup, since the signals are always co-propagating, it is important to ascertain that no mixing

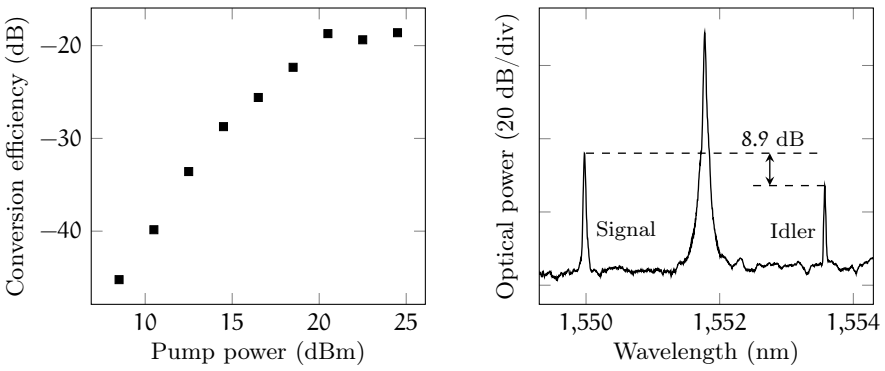

Fig. 5.11. (a) Measured conversion efficiency (output idler power divided by the input signal power) as a function of input FWM pump power. Pump and signal wavelengths at 1550 and 1552 nm, respectively. (b) Optical spectrum at the output of the waveguide for the highest measured conversion efficiency.

occurs before the actual FWM medium. This can be done by minimizing the propagation length preceding the HNLF. Of higher concern however is the method used to tune the differential delay Δt, which normally involves tuning of the carrier wavelengths. This method, while elegant, is a relatively slow process, requiring microseconds or even milliseconds to complete. Such long tuning times are not suited to fast reconfiguration of the system response (described in Sec. 5.2.2), impairing the key advantage that interference-based IFM systems have over other IFM techniques. The structure shown in Fig. 5.12(b) solves this problem by physically separating the two modulated carriers with a coarse wavelength division multiplexer (CWDM), and delaying one of them with a tunable delay element. Since true time delay elements have been shown capable of picosecond tuning speeds [89], this novel structure facilitates fast switching of the system between high-bandwidth and high-resolution measurement states.

The experimental setup used to implement the mixing-based IFM system is shown in Fig. 5.13, and it is based on the structure from Fig. 5.12(b). Two distributed feedback (DFB) lasers are used to generate the optical carriers, with wavelengths of 1550.0 and 1551.7 nm. The CW outputs from these lasers are launched into an Mach-Zehnder modulator (MZM) where they undergo intensity modulation by the input RF signal. The modulated signals are then amplified with an erbium-doped fibre amplifier (EDFA) before being demultiplexed with a CWDM. The CWDM has 200 GHz channel spacing and a 3 dB insertion loss. The advantage of placing the EDFA before CWDM is that any amplified spontaneous emission (ASE) is filtered out, as well as any parasitic FWM that might occur in the EDFA. After being demultiplexed, the signals are differentially delayed by propagating along

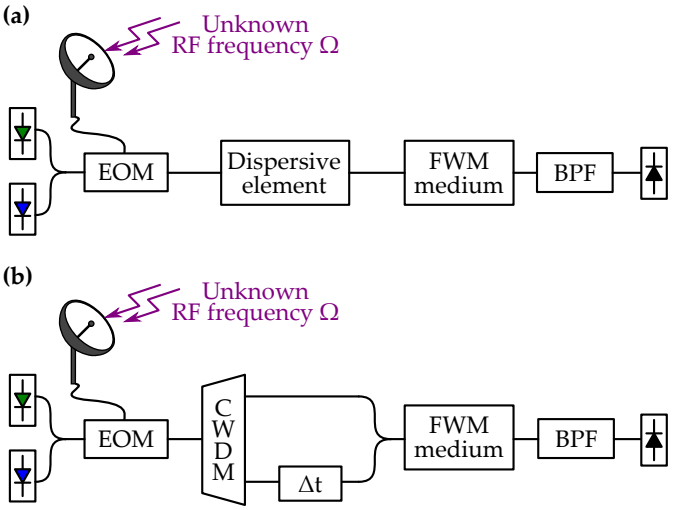

Fig. 5.12. Basic structure of an IFM system based on optical mixing, where the modulator is shared by the two optical carriers and where the delay is implemented using a (a) dispersive element; (b) tunable delay mechanism.

different path lengths. The delay Δt can be easily tuned by adjusting the path length difference through a tunable delay line (TDL). The two signals are then recombined before being launched into the 35 cm long, thick silicon spiral previously described. At the output of the chip, a tunable optical BPF is used to select one of the mixing idler signals (i.e. idler carrier and idler sidebands), whose power is measured with an optical power meter.

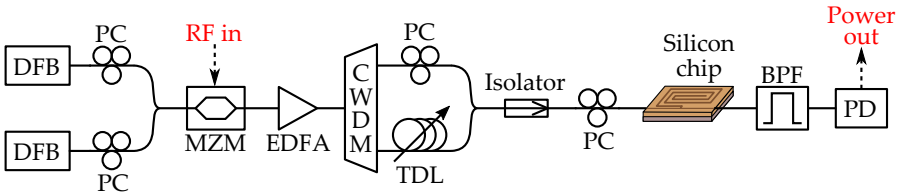

Fig. 5.13. Experimental setup for the mixing-based IFM system. The FWM occurs in the 35 cm long, thick silicon spiral depicted in Fig. 5.8

.

The gain of the EDFA is set such that both optical carriers enter the silicon waveguide with 18.7 dBm power, resulting in a FWM conversion efficiency of -30.1 dB. This differs from the value expected using Fig. 5.11 due to both FWM pump and signal (carrier at ω_1 and ω_2, respectively) having the same power, so that pump depletion occurs. Figure 5.14 shows the optical spectrum at the output of the waveguide, when the microwave input frequency is $\Omega/2\pi = 40$ GHz. The spectrum is shown for two separate differential delays corresponding to $\Delta t = 0$ and $\Delta t = 12.5$ ps. These two delay values, achieved by adjusting the TDL, are chosen specifically so as to vary the product $\Omega\Delta t$ between 0 and π. According to Eq. (5.13), these two points correspond to maximum and minimum idler sidebands power, respectively. This

is clearly visible in Fig. 5.14, where there is a 10 dB power contrast for the idler sidebands as the delay is tuned. These results confirm the theory presented in Sec. 5.3.1.

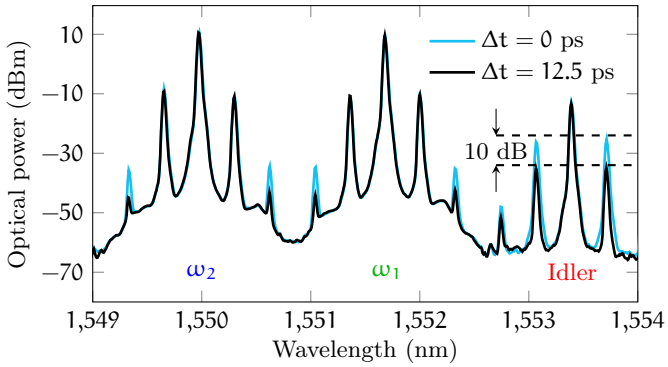

Fig. 5.14. Optical spectra at the output of the silicon waveguide for two different delay Δt values. The input microwave signal frequency is 40 GHz. The 10 dB power difference in the idler sidebands is a manifestation of the interference effect between the idlers generated through degenerate and non-degenerate FWM.

5.3.3 *IFM Experiment*

In this particular experiment, the input RF signal was supplied by an RF signal generator (Keysight Technologies, N5183 MXG Microwave Analog Signal Generator), with a maximum frequency of 40 GHz. In order to provide an unambiguous frequency measurement across the whole 40 GHz bandwidth, the differential delay could not exceed 12.5 ps, according to Eq. (5.3). Taking into account the frequency roll-off of the MZM, the delay that gives the highest resolution (i.e. highest ACF slope) across this bandwidth was found to be $\Delta t = 8.3$ ps. With this delay, the system is characterized by sweepingRF signal generator from 0 to 40 GHz, with a constant 15 dBm output power, and measuring the generated idler power. This measurement is shown in Fig. 5.15(a), together with a theoretical fit. This fit becomes the ACF used to estimate unknown frequencies in the measurement range.

A second experiment is then carried out to test the performance of the system. It involves setting the RF signal source to frequency-hop randomly 1000 times across the whole 40 GHz bandwidth, and measuring the output power of the idler. The measured power values are then input into the ACF which maps them to a unique frequency value. It is important to note that while each power measurement consists of a single-shot measurement, averaging occurs in practice due to the limited time response of the power metre. Because of this limitation, in the experiment frequency hops are separated by a 0.3 s interval. While such delay between measurements is typically too large for real-world applications, it is not inherent to the IFM technique (FWM

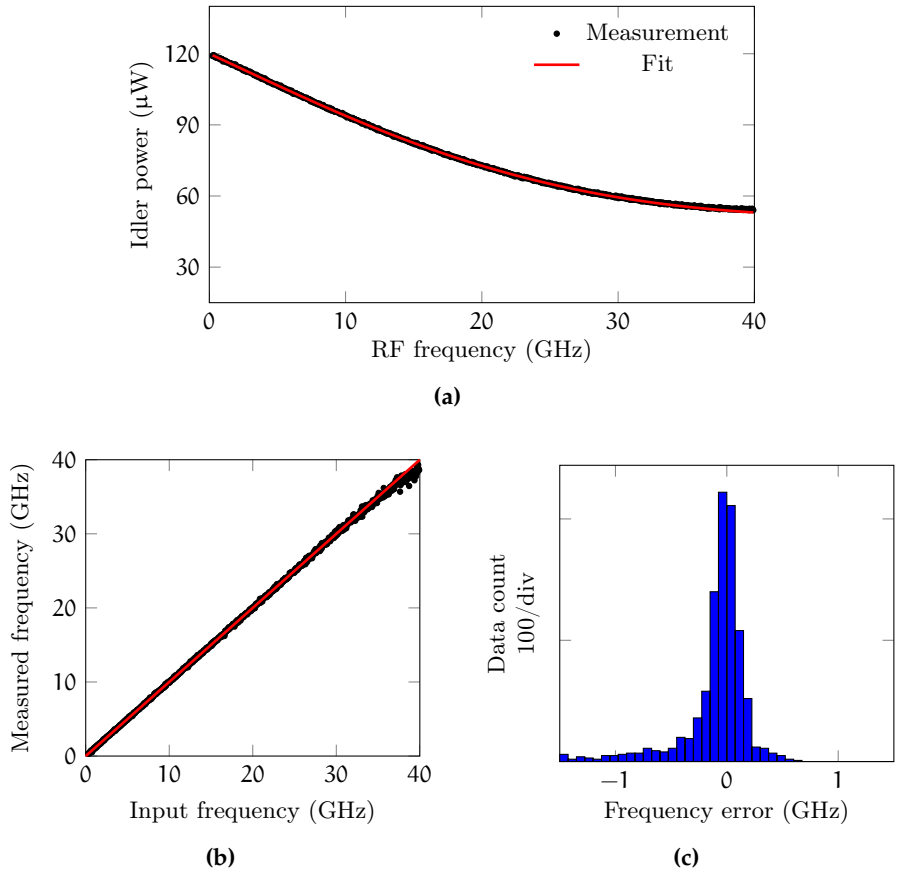

Fig. 5.15. Mixing-based IFM system with $\Delta t = 8.3$ ps. (a) Measured system response (dots) and fit (line). (b) Frequency estimation measurement across a 40 GHz frequency band. (c) Histogram of the frequency measurement error with 318.9 MHz rms value.

being an ultra-fast process) and can therefore be improved by using a faster photodetector.

A comparison of the measured frequency values versus the actual input signal frequency is shown in Fig. 5.15(b). Figure 5.15(c) displays a histogram of the error for this experiment. The rms value of the frequency estimation error is 318.9 MHz, corresponding to 0.8% of the 40 GHz measurement bandwidth. This combination of wide measurement bandwidth (limited only by the range of the RF signal generator), and sub-1% error, is a record for an on-chip IFM system, as shown in Table 5.1. It is clear, by examining Fig. 5.15(b), that the largest discrepancy between the measured frequency and the actual frequency occurs for frequency values above 30 GHz. This is not a coincidence; it is due to the fact that the slope of the ACF is lowest in this frequency range. This is evidence of the close relationship which exists between the slope of the ACF and the measurement resolution, or error.

To confirm this relationship, the IFM experiment is repeated, but with a higher differential delay, chosen arbitrarily to equal $\Delta t = 69.4$

Table 5.1. Performance comparison of different on-chip MWP IFM systems.

Technology	Range (GHz)	Error (MHz)	Error/ bandwidth (%)
FWM (this work)	0–40	318.9 rms	0.8
Ring resonator [305]	0.5–4	93.6 rms	2.7
InP Mach-Zehnder interferometer [128]	5–15	$<$ 200 rms	2.0
Si microdisk [306]	9–19	$\pm$200	2.0
Si Bragg grating [307]	0–32	755 rms	2.4
Echelle diffractive grating [281]	0–15	200	1.3

ps. As a result, the system response is reconfigured, with the new ACF shown in Fig. 5.16(a). The decaying sinusoid nature, not expected from Eq. (5.13), is due to the frequency roll-off of the modulator and the RF cables used to deliver the signal to the MZM. In order to avoid measurement ambiguities, each linear region of the ACF is assigned to a particular frequency band. This results in six, 7.2 GHz bands, where the input RF signal is swept randomly, and its frequency estimated by comparing the output idler power to the ACF for that particular frequency band. The results of this measurement, shown in Figs. 5.16(b) and (c) exhibit a much lower frequency estimation error, with an rms value of 40.2 MHz, or 0.56% of the 7.2 GHz measurement bandwidth. Therefore, reconfiguration of the system response can be used to switch between measurement states with wide unambiguous bandwidths (small Δt values), or states with high measurement accuracy (large Δt values). Fast reconfiguration of the delay Δt would therefore open the way to achieving the first IFM system which overcomes the bandwidth/resolution trade-off.

5.3.4 *Potential for Integration*

The ability to harness nonlinear optical processes efficiently, in a low-loss integrated platform, is fundamental for a wide variety of microwave photonic applications [42]. This is particularly true of FWM-based IFM where, as shown in Sec. 5.3.3, the generated idler power has a direct effect on the measurement error. This work has shown that long, thick silicon waveguides exhibit all of these properties, while being able to maintain low footprints and a high nonlinear loss threshold.

Nevertheless, to be able to monolithically integrate all critical components of the IFM system, one will need to combine the thick silicon

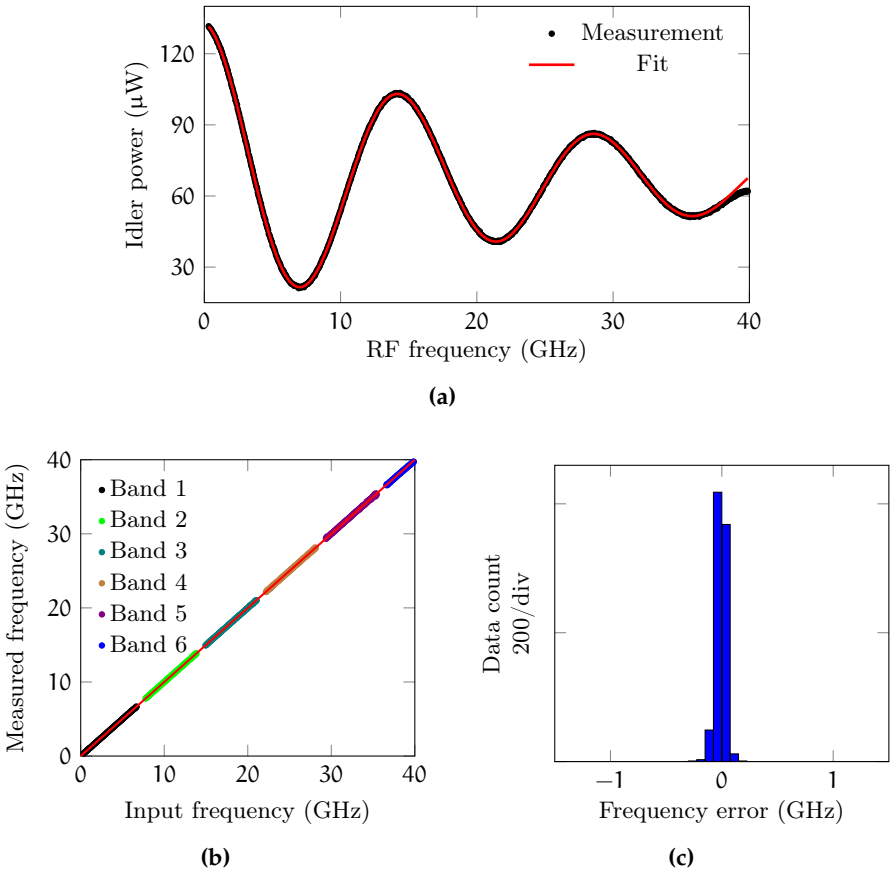

Fig. 5.16. Mixing-based IFM system with $\Delta t = 69.4$ ps. (a) Measured system response (dots) and fit (line). (b) Frequency estimation measurement across six separate 7.2 GHz frequency bands. (c) Histogram of the frequency measurement error with 40.2 MHz rms value.

platform with a more standard SOI technology. One such technology is 220 nm SOI (i.e. thin SOI), which enables access to a full library of active and passive components.

A vision of the layout of a future fully-integrated SOI FWM-based IFM system is presented in Fig. 5.17, featuring a single transition from thin to thick silicon. This transition could be implemented using a section of tapered rib waveguide that minimizes the excitation of higher order modes [317], or even through photonic wire bonding [320]. Alternatively, one could integrate the thin SOI die onto the thick SOI die through flip chip bonding [321].

The thick silicon part of the chip houses the FWM waveguide, BPF, and photodetector. An important advantages of the current FWM-based IFM scheme is that it requires only a simple low-speed PD, unlike other frequency-to-power mapping IFM systems. Such a device has already been demonstrated using vertical p-i-n germanium, integrated on a thick SOI waveguide [322]. Bandpass filters composed of cascaded Mach-Zehnder interferometers have also been demon-

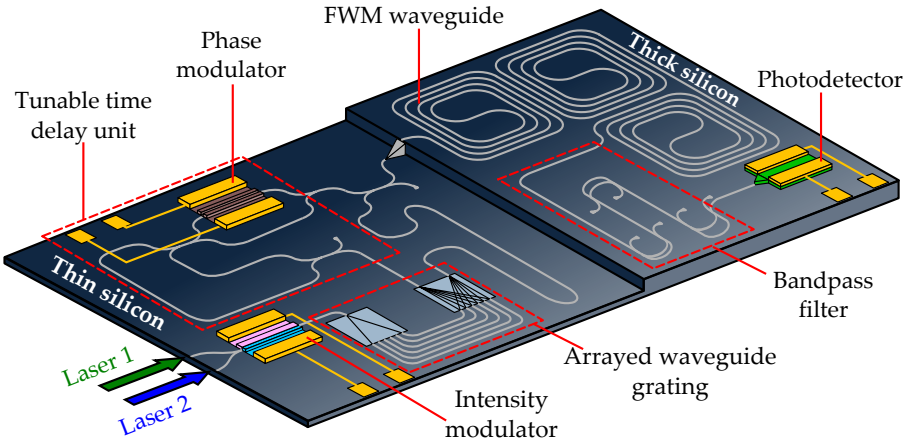

Fig. 5.17. Future vision of the SOI integrated FWM-based IFM system. The chip is divided into thin and thick silicon sections. The RF input signal is applied to the intensity modulator. The tunable time delay unit consists of an optical delay interferometer and a phase modulator [89]. Tuning of Δt is achieved by varying the voltage input to the phase modulator. The photodetector outputs a DC voltage proportional to the idler power, which is then mapped to an estimate for the RF input signal frequency.

strated in thick silicon [323]. For these components, Euler bends will need to be implemented so as to maintain a low footprint.

The thin silicon section of the chip hosts the electro-optic modulator (EOM)s, and arrayed waveguide grating. The intensity modulator used by the input RF signal would be implemented using doped thin SOI technology. Such MZMs have been shown capable of high performance, with low 1.6 dB insertion loss, and wide 27.8 GHz bandwidth [324]. Demultiplexing of the two channels would occur in an arrayed waveguide grating, which have also been demonstrated in thin SOI with 200 GHz channel spacing [325]. Finally, tunable time delay could be realized using a novel approach [89], employing an optical delay interferometer and a phase modulator. High-speed phase modulators have been implemented using silicon-organic hybrid technology [326], and would allow for fast tuning of the Δt delay. Such a chip, boasting fast tunable delay and compact size will result in the first ultra-low latency and highly accurate IFM system with bandwidth and capabilities beyond what is achievable using state-of-the-art RF technologies.

5.4 SUMMARY

In this chapter, a frequency-to-power mapping IFM system using on-chip FWM has been presented. Prior on-chip IFM demonstrations all relied on optical filters, such as integrated ring resonators or Bragg gratings, to map the frequency of an unknown RF signal to an RF power level. Their measurement bandwidth however was severely

limited by the response of these filters, and by the bandwidth/resolution trade-off inherent to frequency-to-power mapping IFM systems. Nonlinear optical mixing has the ability to greatly extend the measurement bandwidth and, through fast reconfiguration of the system response, can quickly switch between high-bandwidth and high-resolution measurement modes.

The FWM-based IFM system works on the principle first introduced in [117], where two differentially delayed optical signals are mixed to generate idlers. The interference of the different idlers causes the total idler power to be dependent on the input RF frequency. It is shown that the system performance is directly related to the power of the optical idlers. It is essential therefore to harness FWM in a low-loss, nonlinear platform, in a sub-metre length scale, in order to prevent the long latency which occurs when hundreds of metres of fibre are used.

Here, the FWM medium is implemented with a 35 cm long, thick silicon spiral. While the nonlinear performance of this platform is not a match for more standard silicon nanowires, its overall insertion loss is considerably lower, and its larger core size raises the nonlinear loss threshold, allowing it to support higher optical powers. The combination of these characteristics lead to the generation of an optical idler with enhanced strength, and a record-low 0.8% measurement error across a 40 GHz bandwidth, limited only by the maximum frequency able to be supplied by the RF signal generator. Reconfiguration of the system response can further improve this value to 0.56% over a 7.2 GHz measurement bandwidth. Moreover, the technique for reconfiguring the system is varied from previous fibre-based demonstrations, making it both simpler and faster, opening the way to fast reconfiguration for overcoming the bandwidth/resolution trade-off.

Finally, this chapter presents a proposal for creating the first IFM system that is monolithically integrated in a silicon chip. Integrated devices such as modulators, filters, and photodetectors have all been demonstrated with sufficient performance for this task. In addition, a recent breakthrough in fast-tuning time delay has also been deemed capable of integration. The availability of all the required components is a promising step for the realization of a complete photonics-based microwave IFM system, with bandwidth and resolution unmatched in electronics.

6 CONCLUSIONS AND OUTLOOK

6.1 SUMMARY

Nonlinear optical effects provide a wide range of unique functionalities which can be exploited for a variety of applications, including microwave photonic (MWP). This thesis has presented the use of on-chip nonlinear optics for enabling different MWP signal processors.

The first optical nonlinearity considered here was stimulated Brillouin scattering (SBS). The unique feature of SBS is its ability to generate narrowband gain and loss resonances. These resonances can be used for implementing MWP filters with megahertz bandwidths, which is significantly better than what is possible with the more common multi-tap filter architectures. This work focused on the implementation of MWP notch filters. There are two main problems which arise when using SBS for notch filtering applications: (1) the stopband suppression depends on the SBS pump power, with high pump powers required for large suppressions; (2) the stopband width depends on the suppression, i.e. the bandwidth increases with the suppression. Both of these problems can be solved with the novel technique presented here, where SBS is not used as an optical filter per se, but as a mechanism to equalise the amplitude of two modulation sidebands in antiphase. At the photodetector, the radio frequency (RF) mixing products formed by the beating of the optical carrier with the two sidebands, interfere destructively across the frequency range affected by the SBS process. Therefore, the resulting notch filter attains high (theoretically infinite) suppression, irrespectively of the strength of the SBS resonance or of the pump power. This decoupling of suppression from bandwidth enables tunability of the stopband width simply by varying the SBS strength. Moreover, the fact that low pump powers are sufficient for filter operation permit re-distribution of the optical power from the pump to the signal, enabling improvements in the filter insertion loss.

The narrow linewidth of SBS is not only useful for highly selective filters, but it can also be used for processing the continuous wave (CW) optical carrier used in most MWP links relying on direct detection. This so-called optical carrier processing finds application in the realization of wideband MWP phase shifters. In phase shifting, the aim is to generate a tunable phase shift onto the signal, without affecting its amplitude. Two different MWP phase shifter architectures are presented here. The first makes use of two SBS pumps to generate opposite gain and loss resonances on the optical carrier. This is then

used to demonstrate a tunable on-chip phase shifter with record-low power fluctuations, as a function of phase shift. The second architecture relies on a different SBS pump configuration where the phase and amplitude of the input RF signal can be independently controlled. This second architecture achieves only half of the phase shift compared to the first, but its operational bandwidth, theoretically, covers the whole RF and microwave domain. For both phase shifters, minimization of the insertion loss requires that the SBS pumps not be depleted (i.e. that all SBS interactions be linear). A study of the linearity of SBS from Chapter 2 proves that this requirement can be more easily fulfilled when using shorter platforms, which is in line with the current trend towards integration.

Another optical nonlinearity which has found use in MWP is four-wave mixing (FWM), useful for frequency conversion of wideband signals. One promising application of FWM is for frequency measurement of microwave signals. instantaneous frequency measurement (IFM) systems are used to map the frequency of an unknown RF signal to some more easily measurable variable such as space, time, or power. Currently, frequency-to-power mapping IFM systems offer the best combination of benefits in terms of highest measurement bandwidth and lowest measurement error. The use of FWM in these systems enables extremely high frequency measurement bandwidths, removing the restrictions that normally arise from the use of linear elements such as ring resonators. The performance of these systems can be further improved through integration, where shorter device lengths directly lead to a reduced measurement latency. The key lies in harnessing FWM in an integrated nonlinear platform, with low losses. Contrary to current mainstream approaches which mainly rely on silicon nanowires, the nonlinear platform here is a long thick silicon waveguide. Its unique properties enable the generation of a strong FWM idlers, which in turn result in an enhanced measurement resolution, and a low measurement error. The combination of large bandwidth and low error is a record for an on-chip IFM system, complemented by the ability to dynamically reconfigure the system response enabling the first IFM system capable of measurements across a wide frequency range, with high accuracy.

The next sections investigate possible ways in which these technologies could be improved, as well as providing my personal assessment of the field and its outlook for the future.

6.2 IMPROVEMENTS TO PRESENT WORK

6.2.1 *Notch Filter*

This work has demonstrated the use of SBS for notch filtering, and the results indicated strong performance in terms of suppression and

bandwidth. Future efforts should therefore be directed towards improvement of the link characteristics such as noise figure, link gain, and dynamic range.

One of the main arguments against the use of SBS for signal processing is the high level of noise generated through spontaneous Brillouin scattering. In this regard, the use of SBS for notch filtering is convenient because the SBS noise, having a similar linewidth to the SBS gain or loss resonance, is concentrated at the notch frequency (i.e. the filter stopband). In the filter passband, where the signal of interest resides, the added noise is due to the standard MWP link noise sources. The same argument applies to nonlinear distortions. Therefore, optimization of all these figures of merit depends, not on the SBS process itself, but on careful design of the underlying MWP link through proper selection of the laser, modulator, photodetector, and minimization of losses.

Replacing the dual-parallel Mach-Zehnder modulator (DPMZM) with a phase modulator, as was demonstrated in Sec. 3.4, would be the most significant step towards improving the filter performance in terms of both minimizing nonlinear distortions [327, 328] and maximizing the stability. This however would also need to be accompanied by an Fourier-domain optical processor (FD-OP) to produce an antiphase/unequal amplitude relation between the modulation sidebands as required to obtain RF cancellation at the notch frequency. In this work, the FD-OP was implemented with a Finisar WaveShaper which achieved the required functionality, but was quite bulky, relying on various discrete free-space components. The notch filter would greatly benefit from integration of these components. A recent development is this line was the demonstration of a hybrid free-space/guided-wave FD-OP where an arrayed waveguide grating integrated in a silica planar lightwave circuit (PLC) was used to replace the bulk diffraction grating normally used to disperse the light on the liquid crystal on silicon (LCoS) spatial light modulator (which is the fundamental component in most FD-OPs) [329].

6.2.2 *Phase Shifter*

Presently, the main limitation to the phase shifter is its phase shift tuning range which falls below 360° due to the limited amount of SBS gain which can be harnessed on-chip. There is an intrinsic relationship between the maximum SBS power gain, and the maximum SBS phase shift, which states that for a single SBS pump to induce a tunable ±180° phase shift, a minimum of 54.6 dB gain is required. In the first architecture presented in Sec. 4.3, two SBS pumps both contribute to shifting the phase of the optical carrier, and the SBS gain required to achieve a full 360° tuning range is halved to 27.3 dB. In the second architecture, presented in Sec. 4.4, two pumps are used but only one

of them contributes to shifting the phase of the carrier. Therefore, the amount of gain induced by the phase-shifting pump must equal or surpass 54.6 dB for achieving a 360° phase shift tuning range. Clearly, the first phase shifter architecture is more suited to on-chip operation. However, even in this case the required amount of SBS gain exceeds the maximum value achieved on chip to date, equal to 23 dB in a 7 cm long chalcogenide (ChG) rib waveguide [206].

The high power gains required by these phase shifters highlight the importance of research into into high-SBS-gain materials [108]. To date, the material with the highest SBS gain coefficient suitable to guiding light is As_2S_3, with $g_0 \sim 7.5 \times 10^{-10}$ m/W. This is approximately two times higher than for crystalline Si [210], and twenty times higher than for SiO_2. Other than material investigations, known techniques for increasing the strength of the SBS interaction involve exploiting slow-light effects or optical resonators [209]. As they stand, neither of these techniques is appropriate to SBS-based MWP phase shifting since they may introduce amplitude distortions; however, they do warrant further consideration. For now, the most straightforward way to increase the SBS interaction strength and achieve wider phase shift tuning ranges is to increase the SBS interaction length. For example, provided all other parameters remain constant, a 10 cm ChG waveguide would provide a sufficient amount of gain, with longer lengths further reducing the pump power requirements and resulting in a more energy-efficient device. Such waveguide lengths could be packaged in chips with surface areas less than 2 cm^2 which, while not permitting large-scale integration, would be sufficiently small for mainstream applications like in phased-array antennas.

Another limitation of both phase shifter architectures is in their maximum operational bandwidth. This is due to the fact that both phase shifters rely on processing the optical carrier of an single sideband (SSB)-modulated signal and the most common way of generating this modulation format is through the use of a DPMZM, which in turn necessitates the use of an RF hybrid couplers. These components are the main bottleneck to the maximum RF signal bandwidth which can be processed by the phase shifter. It is however possible to dispense with the RF hybrid coupler, by replacing the DPMZM with a much simpler phase modulator, and using an optical notch filter (or even a bandpass filter) to suppress one of the modulation sidebands and obtain SSB modulation. It is likely that this approach would sacrifice low-frequency operation, due to the relatively slow roll-off of optical filters, but it would allow full exploitation of the great benefits of optical carrier processing, such as extremely high RF frequency operation, limited only by the bandwidth of the modulator and photodetector.

6.2.3 *Instantaneous Frequency Measurement*

The current IFM system relies on knowledge of the input signal power in order to work correctly, i.e. its amplitude comparison function (ACF) is itself a function of the signal power. However, obtaining a measurement which is independent of the power of the input RF signal is important for a wide range of applications. Achieving this in the present FWM-based IFM system, in combination with its current high bandwidth and low error characteristics, would significantly increase its appeal. To cope with a varying input signal power, one could use an electrical limiting amplifier (as done by electronic IFM systems [273]) at the input of the Mach-Zehnder modulator (MZM), or use an all-optical approach whereby multiple idler copies are generated and the ratio of their power is measured [119]. Neither of these approaches is ideal however; the first being restricted by the limited bandwidth of electrical amplifiers, while the second requires a considerable number of extra components, such as four lasers instead of two.

In general, achieving amplitude-independent operation in IFM simply involves taking the ratio of two ACFs. The requirement however is that the ACFs not be scaled versions of each other. In the current IFM system, the first ACF is given by Eq. (5.13) and is obtained by measuring the optical power of the whole idler field. A second ACF could be attained by measuring the optical power of the whole signal field at ω_1 or ω_2 (i.e. one of the original optical signals), as shown in Fig. 6.1. Neglecting the powers of the optical carriers (which are known and can be subtracted out), both ACFs have the same dependence on the input RF signal power (through the optical sidebands' powers). Therefore, taking the ratio of these two ACFs would lead to a third ACF which is amplitude-independent, without sacrificing IFM bandwidth or error. The only additional components required would be a second optical power meter, and an optical bandpass filter to select the signal field centred at ω_1 or ω_2, at the output of the system.

In Chapter 5 it is shown that the IFM system performance improves directly as the generated idler power increases. Therefore, future efforts could also investigate different FWM media which lead to stronger idler generation with lower input signal powers. In this work, a long thick silicon waveguide was chosen as the FWM medium because it supported high idler powers due to its low losses and high nonlinear loss threshold. Nevertheless, this waveguide was not designed for FWM applications and as such, the achieved conversion efficiency was relatively low. One can imagine however that a dispersion-engineered, silicon nanowire, integrated with a p-i-n diode to minimize free-carrier absorption (FCA) effects, could potentially achieve better performance. Such medium would also be consistent with the future vision of integrating the whole IFM system onto a silicon chip.

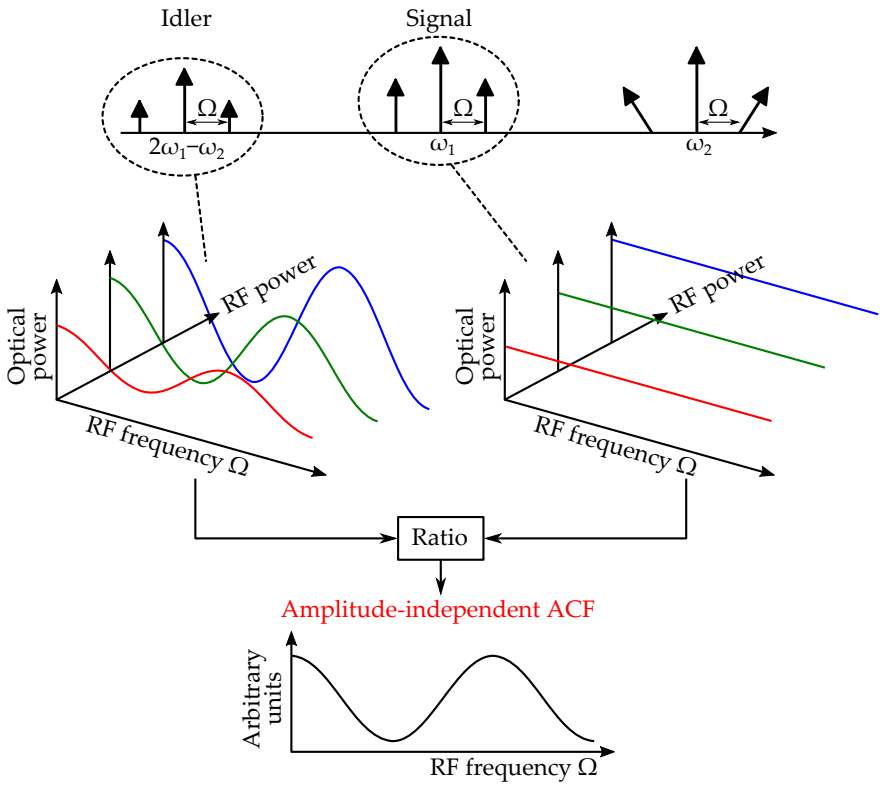

Fig. 6.1. In the FWM-based IFM system, an amplitude-independent ACF can be obtained by measuring the optical power of both idler and signal fields, and taking their ratios.

6.3 ROADMAP TO FULL INTEGRATION

One of the key goals of MWP is the creation of a fully integrated MWP signal processor. This goal is the first, necessary step, to reducing the MWP processor's size, weight, and power consumption, for application to real-world systems [330]. This thesis has demonstrated that on-chip nonlinear optical effects provide an effective means to achieving this goal. The challenge that remains now is integration, not just of the nonlinear medium, but of all the various MWP link components and, in particular, of the laser, the modulator, and the photodetector.

To this end, the main challenge to be addressed is the realization of an integrated photonic circuit, capable of supporting efficient nonlinear optics as well as other functionalities (e.g. modulation, light generation), to the high standard required by MWP. That is, MWP, being directed towards analog applications, places a number of stringent requirements on the various components. For example, in MWP, optical loss reduction is of utmost importance for reducing both power consumption and the noise figure, and current integrated photonic devices such as modulators simply cannot meet these demands.

In order to facilitate the process of integration, in the near future MWP should rely on hybrid solutions, since at present there is no sin-

gle technology platform that offers the best performance in all aspects, and hybrid integration would enable the use of different platforms to optimize performance of each individual component. Moreover, in an effort to minimize optical losses, circuits could rely on large, micrometre-core waveguides such as thick silicon, silicon nitride, or Hydex. Nevertheless, as progress is made in these areas, the objective is to migrate MWP functionalities to monolithic circuits, preferably using small nanowire waveguides, so as to ultimately reduce fabrication costs and achieve more complex devices through high integration density.

While laser sources in silicon are available through hybrid integration with III–V semiconductor gain media, most of these currently exhibit relatively low output powers ~ 10 mW and high -130 dB/Hz relative intensity noise (RIN) [331–333]. Moreover, thermal management is currently a major obstacle to integration of the laser onto the same chip as the other circuit elements [334]. Since the performance of the laser source plays a central role in the performance of the MWP processor as a whole, at this stage it is more convenient to maintain an external source. High-speed 38 GHz modulators however have been demonstrated in micron-scale silicon on insulator (SOI) using the Franz-Keldysh effect [335]. A recent breakthrough has seen the demonstration of the electro-optic effect in Si_3N_4 using a multi-slot waveguide structure, which enabled a modulation bandwidth up to 1 GHz [336]. In a separate experiment, integration of graphene over a silicon nitride ring resonator was used to demonstrate a modulator with 30 GHz bandwidth and high 15 dB per 10 V modulation efficiency [337]. In fact, graphene is predicted to have a significant impact in integrated MWP circuits, promising fast-tunable devices such as phase shifters and true time delay lines [338].

One of the main benefits that follow from integration is the possibility for seamlessly coupling different MWP circuits. Effectively, an MWP circuit is no longer restricted to being a stand-alone device, but can become a building block to a more powerful signal processor. This thesis has demonstrated that nonlinear optics can play a fundamental role in at least some of these building blocks. For example, one could imagine integration of the current FWM-based IFM system together with the SBS-based notch filter. The IFM system could then be used to quickly identify a strong interferer, its output being used to tune the notch filter, directing it to suppress said interferer. This would enable a cooperative signal processor which could find applications in receiver front-ends.

The basic block diagram for such a device is shown in Fig. 6.2. It is based on a complementary metal-oxide semiconductor (CMOS)-compatible platform, such as thick silicon or silicon nitride, hybridly integrated with a ChG waveguide for SBS interactions. The front-end would consist of an optimum combination of linear components (e.g.

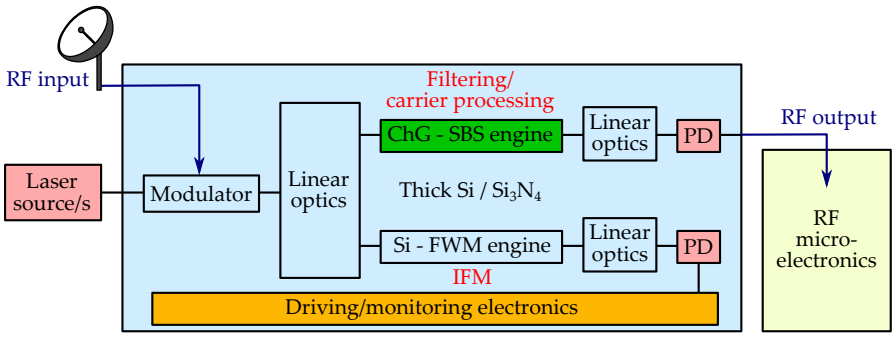

Fig. 6.2. Block diagram of the future vision of a fully-integrated MWP signal processor, consisting of a combination of linear components, nonlinear effects, and driving electronics interfacing with supporting RF circuits.

ring resonators, gratings, arrayed waveguide gratings) and nonlinear optical effects. This would allow one to take full advantage of the unique properties of these different processes. For example, SBS would be used for filtering and optical carrier processing (e.g. phase shifting, modulation conversion), while the linear components could be used for signal conditioning.

Still in MWP, electronic circuits play a fundamental role in the driving of all the various optical components. More importantly, as photonic circuits become more complex, it becomes essential to have electronic circuits monitoring and controlling the response of the various blocks [339]. As demonstrated in Chapter 3, this is critical for stabilization of the MWP processor's response. The use of a CMOS-compatible platform would enable the merging of the photonics and electronics into a single, more robust, functional device.

A final benefit of full photonic integration is the possibility for packaging of both photonic and RF microelectronic circuits into a single component. It is important to note that the aim of MWP is not to replace RF circuits but rather, to complement them, extending their functionalities to cover wider bandwidths for next-generation wireless systems. It is therefore expected that MWP circuits will need to interface, and be supported, by the immense library of RF devices. Integration can reduce the current gap in form-factor between photonic and RF circuits, and lead to fully-packaged RF signal processors with high bandwidth and reconfigurability brought about through the power of photonics.

BIBLIOGRAPHY

[1] B. L. Smith and M.-H. Carpentier, *Microwave engineering handbook* (Van Nostrand Reinhold, New York, 1993), 1st ed.

[2] C. H. Townes and A. L. Schawlow, *Microwave spectroscopy* (Dover Publications, 2012), 2nd ed.

[3] A. Khilo, S. J. Spector, M. E. Grein, A. H. Nejadmalayeri, C. W. Holzwarth, M. Y. Sander, M. S. Dahlem, M. Y. Peng, M. W. Geis, N. A. DiLello, J. U. Yoon, A. Motamedi, J. S. Orcutt, J. P. Wang, C. M. Sorace-Agaskar, M. A. Popović, J. Sun, G.-R. Zhou, H. Byun, J. Chen, J. L. Hoyt, H. I. Smith, R. J. Ram, M. Perrott, T. M. Lyszczarz, E. P. Ippen, and F. X. Kärtner, "Photonic ADC: overcoming the bottleneck of electronic jitter," Opt. Express **20**, 4454–4469 (2012).

[4] S. Chen and J. Zhao, "The requirements, challenges, and technologies for 5g of terrestrial mobile telecommunication," IEEE Commun. Mag. **52**, 36–43 (2014).

[5] C. Caloz, S. Gupta, Q. Zhang, and B. Nikfal, "Analog signal processing: A possible alternative or complement to dominantly digital radio schemes," IEEE Microw. Mag. **14**, 87–103 (2013).

[6] R. A. Pucel, "Design considerations for monolithic microwave circuits," IEEE Trans. Microw. Theory Techn. **29**, 513–534 (1981).

[7] G. Rebeiz and J. B. Muldavin, "RF MEMS switches and switch circuits," IEEE Microw. Mag. **2**, 59–71 (2001).

[8] D. M. Pozar, *Microwave engineering* (Wiley, Hoboken, NJ, 2012), 4th ed.

[9] X.-P. Chen and K. Wu, "Substrate integrated waveguide filters: Design techniques and structure innovations," IEEE Microw. Mag. **15**, 121–133 (2014).

[10] R. Gomez-Garcia and A. Guyette, "Reconfigurable multi-band microwave filters," IEEE Trans. Microw. Theory Techn. **63**, 1294–1307 (2015).

[11] W. Feng, W. Che, and Q. Xue, "The proper balance: Overview of microstrip wideband balance circuits with wideband common mode suppression," IEEE Microw. Mag. **16**, 55–68 (2015).

[12] A. Seeds and K. Williams, "Microwave photonics," J. Lightw. Technol. **24**, 4628–4641 (2006).

[13] J. Capmany and D. Novak, "Microwave photonics combines two worlds," Nat. Photon. **1**, 319–330 (2007).

[14] J. Yao, "Microwave photonics," J. Lightw. Technol. **27**, 314–335 (2009).

[15] V. R. Supradeepa, C. M. Long, R. Wu, F. Ferdous, E. Hamidi, D. E. Leaird, and A. M. Weiner, "Comb-based radiofrequency

photonic filters with rapid tunability and high selectivity," Nat. Photon. **6**, 186–194 (2012).

[16] S. Koenig, D. Lopez-Diaz, J. Antes, F. Boes, R. Henneberger, A. Leuther, A. Tessmann, R. Schmogrow, D. Hillerkuss, R. Palmer, T. Zwick, C. Koos, W. Freude, O. Ambacher, J. Leuthold, and I. Kallfass, "Wireless sub-THz communication system with high data rate," Nat. Photon. **7**, 977–981 (2013).

[17] F. T. M., K. M. S., Q. F., T. J., B. J. C., R. T., L. N., L. A., J. Y., O. C. W., and D. S. A., "Generation of ultrastable microwaves via optical frequency division," Nat. Photon. **5**, 425–429 (2011).

[18] T. Maiman, "Stimulated optical radiation in ruby," Nature **187**, 493–494 (1960).

[19] K. Kao and G. Hockham, "Dielectric-fibre surface waveguides for optical frequencies," Proc. IEEE **113**, 1151–1158 (1966).

[20] Times Microwave Systems, *LMR Wireless Products Catalog* (2014). FBT-600 Flexible Low Loss High Power Communications Coax.

[21] V. J. Urick, J. D. McKinney, and K. J. Williams, *Fundamentals of Microwave Photonics* (Wiley, 2015), 1st ed.

[22] J. Chiddix, "Fiber backbone trunking in cable television networks: an evolutionary adoption of new technology," LCS, IEEE **1**, 32–37 (1990).

[23] A. Cooper, "Fibre/radio for the provision of cordless/mobile telephony services in the access network," Electron. Lett. **26**, 2054–2056 (1990).

[24] J. O'Reilly, P. Lane, M. Capstick, H. Salgado, R. Heidemann, R. Hofstetter, and H. Schmuck, "RACE R2005: microwave optical duplex antenna link," Proc. IEEE **140**, 385–391 (1993).

[25] C. von Helmolt, U. Kruger, K. Kruger, and G. Grosskopf, "A mobile broad-band communication system based on mode-locked lasers," IEEE Trans. Microw. Theory Techn. **45**, 1424–1430 (1997).

[26] K. Wilner and A. van den Heuvel, "Fiber-optic delay lines for microwave signal processing," Proc. IEEE **64**, 805–807 (1976).

[27] K. P. Jackson, J. E. Bowers, S. A. Newton, and C. C. Cutler, "Microbend optical fiber tapped delay line for gigahertz signal processing," Appl. Phys. Lett. **41**, 139–141 (1982).

[28] J. Bowers, S. Newton, W. Sorin, and H. Shaw, "Filter response of single-mode fibre recirculating delay lines," Electron. Lett. **18**, 110–111 (1982).

[29] M. Tur, J. W. Goodman, B. Moslehi, J. E. Bowers, and H. J. Shaw, "Fiber-optic signal processor with applications to matrix-vector multiplication and lattice filtering," Opt. Lett. **7**, 463–465 (1982).

[30] S. Newton, R. Howland, K. Jackson, and H. Shaw, "High-speed pulse-train generation using single-mode-fibre recirculating delay lines," Electron. Lett. **19**, 756–758 (1983).

[31] B. Moslehi, J. W. Goodman, M. Tur, and H. Shaw, "Fiber-optic lattice signal processing," Proc. IEEE **72**, 909–930 (1984).

[32] K. Jackson, S. Newton, B. Moslehi, M. Tur, C. Cutler, J. W. Goodman, and H. Shaw, "Optical fiber delay-line signal processing," IEEE Trans. Microw. Theory Techn. **33**, 193–210 (1985).

[33] D. Norton, S. Johns, C. Keefer, and R. Soref, "Tunable microwave filtering using high dispersion fiber time delays," IEEE Photon. Technol. Lett. **6**, 831–832 (1994).

[34] J. Capmany, J. Cascon, J. Martin, S. Sales, D. Pastor, and J. Marti, "Synthesis of fiber-optic delay line filters," J. Lightwave Technol. **13**, 2003–2012 (1995).

[35] F. Coppinger, S. Yegnanarayanan, P. Trinh, B. Jalali, and I. Newberg, "Nonrecursive tunable photonic filter using wavelength-selective true time delay," IEEE Photon. Technol. Lett. **8**, 1214–1216 (1996).

[36] R. A. Minasian, "Photonic signal processing of high-speed signals using fiber gratings," Opt. Fiber Technol. **6**, 91–108 (2000).

[37] R. Minasian, "Photonic signal processing of microwave signals," IEEE Trans. Microw. Theory Techn. **54**, 832–846 (2006).

[38] R. A. Minasian, E. H. W. Chan, and X. Yi, "Microwave photonic signal processing," Opt. Express **21**, 22918–22936 (2013).

[39] J. Capmany and P. Munoz, "Integrated microwave photonics for radio access networks," J. Lightwave Technol. **32**, 2849–2861 (2014).

[40] G. Gordon, M. Crisp, R. Penty, T. Wilkinson, and I. White, "Feasibility demonstration of a mode-division multiplexed MIMO-enabled radio-over-fiber distributed antenna system," J. Lightwave Technol. **32**, 3521–3528 (2014).

[41] R. Waterhouse and D. Novack, "Realizing 5g: Microwave photonics for 5g mobile wireless systems," IEEE Microw. Mag. **16**, 84–92 (2015).

[42] D. Marpaung, C. Roeloffzen, R. Heideman, A. Leinse, S. Sales, and J. Capmany, "Integrated microwave photonics," Laser Photon. Rev. **7**, 506–538 (2013).

[43] M. Faugeron, M. Tran, O. Parillaud, M. Chtioui, Y. Robert, E. Vinet, A. Enard, J. Jacquet, and F. van Dijk, "High-power tunable dilute mode DFB laser with low RIN and narrow linewidth," IEEE Photon. Technol. Lett. **25**, 7–10 (2013).

[44] C. H. Cox III, *Analog optical links: theory and practice* (Cambridge University Press, 2004), 1st ed.

[45] O. Kjebon, R. Schatz, S. Lourdudoss, S. Nilsson, B. Stalnacke, and L. Backbom, "30 GHz direct modulation bandwidth in detuned loaded InGaAsP DBR lasers at 1.55 μm wavelength," Electron. Lett. **33**, 488–489 (1997).

[46] H. Dalir, A. Matsutani, M. Ahmed, A. Bakry, and F. Koyama, "High frequency modulation of transverse-coupled-cavity VC-

SELs for radio over fiber applications," IEEE Photon. Technol. Lett. **26**, 281–284 (2014).

[47] M. Lee, H. E. Katz, C. Erben, D. M. Gill, P. Gopalan, J. D. Heber, and D. J. McGee, "Broadband modulation of light by using an electro-optic polymer," Science **298**, 1401–1403 (2002).

[48] E. Ackerman, G. Betts, W. Burns, J. Campbell, I. Cox, C.H., N. Duan, J. Prince, M. Regan, and H. Roussell, "Signal-to-noise performance of two analog photonic links using different noise reduction techniques," in "Proc. IEEE/MTT-S Int. Microwave Symp.", (2007), pp. 51–54.

[49] M. Jarrahi, T. Lee, and D. Miller, "Wideband, low driving voltage traveling-wave Mach-Zehnder modulator for RF photonics," IEEE Photon. Technol. Lett. **20**, 517–519 (2008).

[50] K. Giboney, R. Nagarajan, T. E. Reynolds, S. Allen, R. Mirin, M. J. Rodwell, and J. Bowers, "Travelling-wave photodetectors with 172-GHz bandwidth and 76-GHz bandwidth-efficiency product," Photonics Technology Letters, IEEE **7**, 412–414 (1995).

[51] H. Ito, S. Kodama, Y. Muramoto, T. Furuta, T. Nagatsuma, and T. Ishibashi, "High-speed and high-output InP-InGaAs unitraveling-carrier photodiodes," IEEE J. Sel. Topics Quantum Electron. **10**, 709–727 (2004).

[52] X. Xie, K. Li, Q. Zhou, A. Beling, and J. Campbell, "High-gain, low-noise-figure, and high-linearity analog photonic link based on a high-performance photodetector," J. Lightw. Technol. **32**, 4187–4192 (2014).

[53] E. Rouvalis, C. C. Renaud, D. G. Moodie, M. J. Robertson, and A. J. Seeds, "Traveling-wave uni-traveling carrier photodiodes for continuous wave THz generation," Opt. Express **18**, 11105–11110 (2010).

[54] R. Kalman, J. Fan, and L. Kazovsky, "Dynamic range of coherent analog fiber-optic links," J. Lightw. Technol. **12**, 1263–1277 (1994).

[55] B. Cai and A. Seeds, "Optical frequency modulation links: Theory and experiments," IEEE Trans. Microw. Theory Techn. **45**, 505–511 (1997).

[56] l. Gheorma and G. Gopalakrishnan, "Flat frequency comb generation with an integrated dual-parallel modulator," IEEE Photon. Technol. Lett. **19**, 1011–1013 (2007).

[57] S. Ozharar, F. Quinlan, I. Ozdur, S. Gee, and P. Delfyett, "Ultraflat optical comb generation by phase-only modulation of continuous-wave light," IEEE Photon. Technol. Lett. **20**, 36–38 (2008).

[58] L. Zhuang, M. Hoekman, C. Taddei, A. Leinse, R. G. Heideman, A. Hulzinga, J. Verpoorte, R. M. Oldenbeuving, P. W. L. van Dijk, K.-J. Boller, and C. G. H. Roeloffzen, "On-chip microwave

photonic beamformer circuits operating with phase modulation and direct detection," Opt. Express **22**, 17079–17091 (2014).

[59] D. Marpaung, C. Roeloffzen, A. Leinse, and M. Hoekman, "A photonic chip based frequency discriminator for a high performance microwave photonic link," Opt. Express **18**, 27359–27370 (2010).

[60] X. Yi and R. Minasian, "Microwave photonic filter with single bandpass response," Electron. Lett. **45**, 362–363 (2009).

[61] J. D. Bull, N. A. F. Jaeger, H. Kato, M. Fairburn, A. Reid, and P. Ghanipour, "40 GHz electro-optic polarization modulator for fiber optic communications systems," Proc. SPIE **5577**, 133–143 (2004).

[62] E. Chan, W. Zhang, and R. Minasian, "Photonic RF phase shifter based on optical carrier and RF modulation sidebands amplitude and phase control," J. Lightw. Technol. **30**, 3672–3678 (2012).

[63] D. Marpaung, B. Morrison, R. Pant, and B. J. Eggleton, "Frequency agile microwave photonic notch filter with anomalously high stopband rejection," Opt. Lett. **38**, 4300–4303 (2013).

[64] C. Cox, E. Ackerman, G. Betts, and J. Prince, "Limits on the performance of RF-over-fiber links and their impact on device design," IEEE Trans. Microw. Theory Techn. **54**, 906–920 (2006).

[65] H. Roussell, M. Regan, J. Prince, C. Cox, J. Chen, W. Burns, G. Betts, E. Ackerman, and J. C. Campbell, "Gain, noise figure and bandwidth-limited dynamic range of a low-biased external modulation link," in "IEEE Int. Topical Meeting on Microwave Photonics," (2007), pp. 84–87.

[66] C. Cox III, E. Ackerman, and G. Betts, "Relationship between gain and noise figure of an optical analog link," in "IEEE MTT-S Int. Microwave Symposium Digest," , vol. 3 (1996), vol. 3, pp. 1551–1554.

[67] See, "Technology focus on microwave photonics," Nat. Photonics **5**, 723–736 (2011).

[68] J. Capmany, J. Mora, I. Gasulla, J. Sancho, J. Lloret, and S. Sales, "Microwave photonic signal processing," J. Lightwave Technol. **31**, 571–586 (2013).

[69] J. Yao, "Photonics to the rescue: A fresh look at microwave photonic filters," IEEE Microw. Mag. **16**, 46–60 (2015).

[70] J. Capmany, B. Ortega, and D. Pastor, "A tutorial on microwave photonic filters," J. Lightwave Technol. **24**, 201–229 (2006).

[71] X. Xue, X. Zheng, H. Zhang, and B. Zhou, "Widely tunable single-bandpass microwave photonic filter employing a non-sliced broadband optical source," Opt. Express **19**, 18423–18429 (2011).

[72] J. Sancho, J. Bourderionnet, J. Lloret, S. Combrié, I. Gasulla, S. Xavier, S. Sales, P. Colman, G. Lehoucq, D. Dolfi, J. Capmany,

and A. De Rossi, "Integrable microwave filter based on a photonic crystal delay line," Nat. Commun. **3** (2012).

[73] J. Capmany, D. Pastor, A. Martinez, B. Ortega, and S. Sales, "Microwave photonic filters with negative coefficients based on phase inversion in an electro-optic modulator," Opt. Lett. **28**, 1415–1417 (2003).

[74] T.-Y. Kim, C. K. Oh, S.-J. Kim, and C.-S. Park, "Tunable photonic microwave notch filter with negative coefficient based on polarization modulation," IEEE Photon. Technol. Lett. **19**, 907–909 (2007).

[75] Y. Dai and J. Yao, "Nonuniformly-spaced photonic microwave delay-line filter," Opt. Express **16**, 4713–4718 (2008).

[76] F. Xiao, B. Juswardy, and K. Alameh, "Tunable photonic microwave filters based on opto-VLSI processors," IEEE Photon. Technol. Lett. **21**, 751–753 (2009).

[77] L. Li, X. Yi, T. X. H. Huang, and R. A. Minasian, "Distortion-free spectrum sliced microwave photonic signal processor: analysis, design and implementation," Opt. Express **20**, 11517–11528 (2012).

[78] J. Capmany, J. Mora, B. Ortega, and D. Pastor, "High-Q microwave photonic filter with a tuned modulator," Opt. Lett. **30**, 2299–2301 (2005).

[79] J. Mora, B. Ortega, A. Diez, J. Cruz, M. Andres, J. Capmany, and D. Pastor, "Photonic microwave tunable single-bandpass filter based on a Mach-Zehnder interferometer," J. Lightwave Technol. **24**, 2500–2509 (2006).

[80] J. H. Lee and Y. M. Chang, "Detailed theoretical and experimental study on single passband, photonic microwave FIR filter using digital micromirror device and continuous-wave supercontinuum," J. Lightw. Technol. **26**, 2619–2628 (2008).

[81] T. X. H. Huang, X. Yi, and R. A. Minasian, "Single passband microwave photonic filter using continuous-time impulse response," Opt. Express **19**, 6231–6242 (2011).

[82] B. Vidal, M. A. Piqueras, J. Corral, and J. Marti, "Tunable photonic microwave filter based on two parallel Fabry-Perot filters," in "International Topical Meeting on Microwave Photonics, 2005.", (2005), pp. 205–208.

[83] J. Palaci, G. Villanueva, J. Galan, J. Marti, and B. Vidal, "Single bandpass photonic microwave filter based on a notch ring resonator," IEEE Photon. Technol. Lett. **22**, 1276–1278 (2010).

[84] T. Nguyen, E. Chan, and R. Minasian, "Photonic radio frequency memory using frequency shifting recirculating delay line structure," J. Lightw. Technol. **32**, 99–106 (2014).

[85] H. Subbaraman, M. Y. Chen, and R. Chen, "Photonic crystal fiber-based true-time-delay beamformer for multiple RF

beam transmission and reception of an X-band phased-array antenna," J. Lightwave Technol. **26**, 2803–2809 (2008).

[86] Y. O. Barmenkov, J. L. Cruz, A. Díez, and M. V. Andrés, "Electrically tunable photonic true-time-delay line," Opt. Express **18**, 17859–17864 (2010).

[87] J. F. Diehl, J. M. Singley, C. E. Sunderman, and V. J. Urick, "Microwave photonic delay line signal processing," Appl. Opt. **54**, F35–F41 (2015).

[88] R. T. Schermer, F. Bucholtz, and C. A. Villarruel, "Continuously-tunable microwave photonic true-time-delay based on a fiber-coupled beam deflector and diffraction grating," Opt. Express **19**, 5371–5378 (2011).

[89] R. Bonjour, S. A. Gebrewold, D. Hillerkuss, C. Hafner, and J. Leuthold, "Continuously tunable true-time delays with ultra-low settling time," Opt. Express **23**, 6952–6964 (2015).

[90] A. Willner, S. Khaleghi, M. Chitgarha, and O. Yilmaz, "All-optical signal processing," J. Lightw. Technol. **32**, 660–680 (2014).

[91] X. S. Yao, "High-quality microwave signal generation by use of Brillouin scattering in optical fibers," Opt. Lett. **22**, 1329–1331 (1997).

[92] X. Yao, "Phase-to-amplitude modulation conversion using Brillouin selective sideband amplification," IEEE Photon. Technol. Lett. **10**, 264–266 (1998).

[93] X. Yao, "Brillouin selective sideband amplification of microwave photonic signals," IEEE Photon. Technol. Lett. **10**, 138–140 (1998).

[94] A. Loayssa and F. Lahoz, "Broad-band RF photonic phase shifter based on stimulated Brillouin scattering and single-sideband modulation," IEEE Photon. Technol. Lett. **18**, 208–210 (2006).

[95] M. Pagani, D. Marpaung, and B. J. Eggleton, "Ultra-wideband microwave photonic phase shifter with configurable amplitude response," Opt. Lett. **39**, 5854–5857 (2014).

[96] M. Sagues, A. Loayssa, and J. Capmany, "Multitap complex-coefficient incoherent microwave photonic filters based on stimulated Brillouin scattering," IEEE Photon. Technol. Lett. **19**, 1194–1196 (2007).

[97] W. T. Wang, J. G. Liu, H. K. Mei, W. Y. Wang, and N. H. Zhu, "Microwave photonic filter with complex coefficient based on optical carrier phase shift utilizing two stimulated Brillouin scattering pumps," IEEE Photon. J. **7**, 1–8 (2015).

[98] S. Chin, L. Thévenaz, J. Sancho, S. Sales, J. Capmany, P. Berger, J. Bourderionnet, and D. Dolfi, "Broadband true time delay for microwave signal processing, using slow light based on stim-

ulated Brillouin scattering in optical fibers," Opt. Express **18**, 22599–22613 (2010).

[99] J. Sancho, S. Chin, M. Sagues, A. Loayssa, J. Lloret, I. Gasulla, S. Sales, L. Thevenaz, and J. Capmany, "Dynamic microwave photonic filter using separate carrier tuning based on stimulated Brillouin scattering in fibers," IEEE Photon. Technol. Lett. **22**, 1753–1755 (2010).

[100] J. Sancho, N. Primerov, S. Chin, Y. Antman, A. Zadok, S. Sales, and L. Thévenaz, "Tunable and reconfigurable multi-tap microwave photonic filter based on dynamic Brillouin gratings in fibers," Opt. Express **20**, 6157–6162 (2012).

[101] B. Vidal, M. A. Piqueras, and J. Martí, "Tunable and reconfigurable photonic microwave filter based on stimulated Brillouin scattering," Opt. Lett. **32**, 23–25 (2007).

[102] W. Zhang and R. Minasian, "Widely tunable single-passband microwave photonic filter based on stimulated Brillouin scattering," IEEE Photon. Technol. Lett. **23**, 1775–1777 (2011).

[103] W. Zhang and R. A. Minasian, "Switchable and tunable microwave photonic Brillouin-based filter," IEEE Photon. J. **4**, 1443–1455 (2012).

[104] S. Hu, L. Li, X. Yi, and C. Yu, "Ultraflat widely tuned single bandpass filter based on stimulated Brillouin scattering," IEEE Photon. Technol. Lett. **26**, 1466–1469 (2014).

[105] Y. Stern, K. Zhong, T. Schneider, R. Zhang, Y. Ben-Ezra, M. Tur, and A. Zadok, "Tunable sharp and highly selective microwave-photonic band-pass filters based on stimulated Brillouin scattering," Photon. Res. **2**, B18–B25 (2014).

[106] W. Wei, L. Yi, Y. Jaouën, and W. Hu, "Bandwidth-tunable narrowband rectangular optical filter based on stimulated Brillouin scattering in optical fiber," Opt. Express **22**, 23249–23260 (2014).

[107] W. Zhang and R. Minasian, "Ultrawide tunable microwave photonic notch filter based on stimulated Brillouin scattering," IEEE Photon. Technol. Lett. **24**, 1182–1184 (2012).

[108] B. J. Eggleton, C. G. Poulton, and R. Pant, "Inducing and harnessing stimulated brillouin scattering in photonic integrated circuits," Adv. Opt. Photon. **5**, 536–587 (2013).

[109] G. Agrawal, *Nonlinear fiber optics* (Academic Press Inc., 2012), chap. 10, 5th ed.

[110] B. Vidal, J. Palaci, and J. Capmany, "Reconfigurable photonic microwave filter based on four-wave mixing," IEEE Photon. J. **4**, 759–764 (2012).

[111] L. R. Chen, J. Li, M. Spasojevic, and R. Adams, "Nanowires and sidewall Bragg gratings in silicon as enabling technologies for microwave photonic filters," Opt. Express **21**, 19624–19633 (2013).

[112] K. Kitayama, "Highly stabilized millimeter-wave generation by using fiber-optic frequency-tunable comb generator," J. Lightw. Technol. **15**, 883–893 (1997).

[113] A. Wiberg, P. Perez-Millan, M. Andres, and P. Hedekvist, "Microwave-photonic frequency multiplication utilizing optical four-wave mixing and fiber Bragg gratings," J. Lightw. Technol. **24**, 329–334 (2006).

[114] B. Vidal, A. Bockelt, and J. Palaci, "Cascaded four-wave mixing for microwave photonic harmonic multiplication," IEEE Photon. Technol. Lett. **25**, 100–103 (2013).

[115] R. Adams, R. Ashrafi, J. Wang, M. Dizaji, and L. Chen, "RF-arbitrary waveform generation based on microwave photonic filtering," IEEE Photon. J. **6**, 1–8 (2014).

[116] C.-S. Bres, S. Zlatanovic, A. Wiberg, J. Adleman, C. Huynh, E. Jacobs, J. Kvavle, and S. Radic, "Parametric photonic channelized RF receiver," IEEE Photon. Technol. Lett. **23**, 344–346 (2011).

[117] L. A. Bui, M. D. Pelusi, T. D. Vo, N. Sarkhosh, H. Emami, B. J. Eggleton, and A. Mitchell, "Instantaneous frequency measurement system using optical mixing in highly nonlinear fiber," Opt. Express **17**, 22983–22991 (2009).

[118] L. A. Bui and A. Mitchell, "Remoted all optical instantaneous frequency measurement system using nonlinear mixing in highly nonlinear optical fiber," Opt. Express **21**, 8550–8557 (2013).

[119] L. A. Bui and A. Mitchell, "Amplitude independent instantaneous frequency measurement using all optical technique," Opt. Express **21**, 29601–29611 (2013).

[120] H. Emami, M. Ashourian, and M. Ebnali-Heidari, "Dynamically reconfigurable all optical frequency measurement system," J. Lightw. Technol. **32**, 4796–4802 (2014).

[121] A. Bhatia, H.-F. Ting, and M. A. Foster, "Linearization of phase-modulated analog optical links using a four-wave mixing comb source," Opt. Express **22**, 30899–30909 (2014).

[122] J. Capmany, G. Li, C. Lim, and J. Yao, "Microwave photonics: Current challenges towards widespread application," Opt. Express **21**, 22862–22867 (2013).

[123] B. Jalali and S. Fathpour, "Silicon photonics," J. Lightwave Technol. **24**, 4600–4615 (2006).

[124] L. Coldren, S. Nicholes, L. Johansson, S. Ristic, R. Guzzon, E. Norberg, and U. Krishnamachari, "High performance InP-based photonic ICs–a tutorial," J. Lightw. Technol. **29**, 554–570 (2011).

[125] J. Stulemeijer, F. van Vliet, K. Benoist, D. Maat, and M. Smit, "Compact photonic integrated phase and amplitude controller

for phased-array antennas," IEEE Photon. Technol. Lett. **11**, 122–124 (1999).

[126] E. Norberg, R. Guzzon, J. Parker, L. Johansson, and L. Coldren, "Programmable photonic microwave filters monolithically integrated in InP–InGaAsP," J. Lightwave Technol. **29**, 1611–1619 (2011).

[127] R. Guzzon, E. Norberg, and L. Coldren, "Spurious-free dynamic range in photonic integrated circuit filters with semiconductor optical amplifiers," IEEE J. Quantum Electron. **48**, 269–278 (2012).

[128] J. S. Fandiño and P. Muñoz, "Photonics-based microwave frequency measurement using a double-sideband suppressed-carrier modulation and an InP integrated ring-assisted Mach-Zehnder interferometer filter," Opt. Lett. **38**, 4316–4319 (2013).

[129] Y. Li, A. Bhardwaj, R. Wang, S. Jin, L. Coldren, J. Bowers, and P. Herczfeld, "A monolithically integrated ACP-OPLL receiver for RF/photonic links," IEEE Photon. Technol. Lett. **23**, 1475–1477 (2011).

[130] J. S. Fandiño, J. D. Doménech, P. Muñoz, and J. Capmany, "Integrated InP frequency discriminator for phase-modulated microwave photonic links," Opt. Express **21**, 3726–3736 (2013).

[131] Y. Li and C. Henry, "Silica-based optical integrated circuits," Proc. IEEE **143**, 263–280 (1996).

[132] M. Rasras, C. Madsen, M. Cappuzzo, E. Chen, L. Gomez, E. Laskowski, A. Griffin, A. Wong-Foy, A. Gasparyan, A. Kasper, J. Le Grange, and S. Patel, "Integrated resonance-enhanced variable optical delay lines," IEEE Photon. Technol. Lett. **17**, 834–836 (2005).

[133] K. Horikawa, I. Ogawa, H. Ogawa, and T. Kitoh, "Photonic switched true time delay beam forming network integrated on silica waveguide circuits," in "Microwave Symposium Digest, 1995., IEEE MTT-S International," , vol. 1 (1995), vol. 1, pp. 65–68.

[134] G. GROSSKOPF, "Silica based optical beam former for 60 GHz array antennas," Fiber Integrated Opt. **22**, 35–46 (2003).

[135] J. M. Wyrwas, R. Peach, S. Meredith, C. Middleton, M. S. Rasras, K.-Y. Tu, M. P. Earnshaw, F. Pardo, M. A. Cappuzzo, E. Y. Chen, L. T. Gomez, F. Klemens, R. Keller, C. Bolle, L. Zhang, L. Buhl, M. C. Wu, Y. Chen, and R. DeSalvo, "Linear phase-and-frequency-modulated photonic links using optical discriminators," Opt. Express **20**, 26292–26298 (2012).

[136] P. Samadi, L. R. Chen, C. Callender, P. Dumais, S. Jacob, and D. Celo, "RF arbitrary waveform generation using tunable planar lightwave circuits," Opt. Commun. **284**, 3737–3741 (2011).

[137] D. J. Moss, R. Morandotti, and M. Gaeta, Alexander L. amd Lipson, "New CMOS-compatible platforms based on silicon ni-

tride and Hydex for nonlinear optics," Nat. Photon. **7**, 597–607 (2013).

[138] M. Ferrera, C. Reimer, A. Pasquazi, M. Peccianti, M. Clerici, L. Caspani, S. T. Chu, B. E. Little, R. Morandotti, and D. J. Moss, "CMOS compatible integrated all-optical radio frequency spectrum analyzer," Opt. Express **22**, 21488–21498 (2014).

[139] P. Dong, W. Qian, S. Liao, H. Liang, C.-C. Kung, N.-N. Feng, R. Shafiiha, J. Fong, D. Feng, A. V. Krishnamoorthy, and M. Asghari, "Low loss shallow-ridge silicon waveguides," Opt. Express **18**, 14474–14479 (2010).

[140] I. Giuntoni, D. Stolarek, D. I. Kroushkov, J. Bruns, L. Zimmermann, B. Tillack, and K. Petermann, "Continuously tunable delay line based on SOI tapered Bragg gratings," Opt. Express **20**, 11241–11246 (2012).

[141] S. Yegnanarayanan, P. Trinh, F. Coppinger, and B. Jalali, "Compact silicon-based integrated optic time delays," IEEE Photon. Technol. Lett. **9**, 634–635 (1997).

[142] S. Khan, M. A. Baghban, and S. Fathpour, "Electronically tunable silicon photonic delay lines," Opt. Express **19**, 11780–11785 (2011).

[143] M. Rasras, D. Gill, S. Patel, K.-Y. Tu, Y.-k. Chen, A. White, A. T. Pomerene, D. Carothers, M. Grove, D. Sparacin, J. Michel, M. Beals, and L. Kimerling, "Demonstration of a fourth-order pole-zero optical filter integrated using CMOS processes," J. Lightwave Technol. **25**, 87–92 (2007).

[144] M. Rasras, K.-Y. Tu, D. Gill, Y.-k. Chen, A. White, S. Patel, A. Pomerene, D. Carothers, J. Beattie, M. Beals, J. Michel, and L. Kimerling, "Demonstration of a tunable microwave-photonic notch filter using low-loss silicon ring resonators," J. Lightwave Technol. **27**, 2105–2110 (2009).

[145] P. Dong, N.-N. Feng, D. Feng, W. Qian, H. Liang, D. C. Lee, B. J. Luff, T. Banwell, A. Agarwal, P. Toliver, R. Menendez, T. K. Woodward, and M. Asghari, "GHz-bandwidth optical filters based on high-order silicon ring resonators," Opt. Express **18**, 23784–23789 (2010).

[146] N.-N. Feng, P. Dong, D. Feng, W. Qian, H. Liang, D. C. Lee, J. B. Luff, A. Agarwal, T. Banwell, R. Menendez, P. Toliver, T. K. Woodward, and M. Asghari, "Thermally-efficient reconfigurable narrowband RF-photonic filter," Opt. Express **18**, 24648–24653 (2010).

[147] J. Dong, L. Liu, D. Gao, Y. Yu, A. Zheng, T. Yang, and X. Zhang, "Compact notch microwave photonic filters using on-chip integrated microring resonators," IEEE Photon. J. **5**, 5500307–1–8 (2013).

[148] J. Leuthold, C. Koos, and W. Freude, "Nonlinear silicon photonics," Nat. Photon. **4**, 535–544 (2010).

[149] Y. Yue, H. Huang, L. Zhang, J. Wang, J.-Y. Yang, O. F. Yilmaz, J. S. Levy, M. Lipson, and A. E. Willner, "UWB monocycle pulse generation using two-photon absorption in a silicon waveguide," Opt. Lett. **37**, 551–553 (2012).

[150] C. G. H. Roeloffzen, L. Zhuang, C. Taddei, A. Leinse, R. G. Heideman, P. W. L. van Dijk, R. M. Oldenbeuving, D. A. I. Marpaung, M. Burla, and K. J. Boller, "Silicon nitride microwave photonic circuits," Opt. Express **21**, 22937–22961 (2013).

[151] J. F. Bauters, M. J. R. Heck, D. D. John, J. S. Barton, C. M. Bruinink, A. Leinse, R. G. Heideman, D. J. Blumenthal, and J. E. Bowers, "Planar waveguides with less than 0.1 db/m propagation loss fabricated with wafer bonding," Opt. Express **19**, 24090–24101 (2011).

[152] F. Morichetti, A. Melloni, M. Martinelli, R. Heideman, A. Leinse, D. Geuzebroek, and A. Borreman, "Box-shaped dielectric waveguides: A new concept in integrated optics?" J. Lightw. Technol. **25**, 2579–2589 (2007).

[153] A. Meijerink, C. Roeloffzen, R. Meijerink, L. Zhuang, D. Marpaung, M. Bentum, M. Burla, J. Verpoorte, P. Jorna, A. Hulzinga, and W. van Etten, "Novel ring resonator-based integrated photonic beamformer for broadband phased array receive antennas–Part I: Design and performance analysis," J. Lightwave Technol. **28**, 3–18 (2010).

[154] L. Zhuang, C. Roeloffzen, A. Meijerink, M. Burla, D. Marpaung, A. Leinse, M. Hoekman, R. Heideman, and W. van Etten, "Novel ring resonator-based integrated photonic beamformer for broadband phased array receive antennas–Part II: Experimental prototype," J. Lightw. Technol. **28**, 19–31 (2010).

[155] M. Burla, D. Marpaung, L. Zhuang, C. Roeloffzen, M. R. Khan, A. Leinse, M. Hoekman, and R. Heideman, "On-chip CMOS compatible reconfigurable optical delay line with separate carrier tuning for microwave photonic signal processing," Opt. Express **19**, 21475–21484 (2011).

[156] M. Burla, C. G. H. Roeloffzen, L. Zhuang, D. Marpaung, M. R. Khan, P. Maat, K. Dijkstra, A. Leinse, M. Hoekman, and R. Heideman, "System integration and radiation pattern measurements of a phased array antenna employing an integrated photonic beamformer for radio astronomy applications," Appl. Opt. **51**, 789–802 (2012).

[157] D. Marpaung, L. Chevalier, M. Burla, and C. Roeloffzen, "Impulse radio ultrawideband pulse shaper based on a programmable photonic chip frequency discriminator," Opt. Express **19**, 24838–24848 (2011).

[158] L. Zhuang, D. Marpaung, M. Burla, W. Beeker, A. Leinse, and C. Roeloffzen, "Low-loss, high-index-contrast Si_3N_4/SiO_2 opti-

cal waveguides for optical delay lines in microwave photonics signal processing," Opt. Express **19**, 23162–23170 (2011).

[159] R. Heideman, M. Hoekman, and E. Schreuder, "TriPleX-based integrated optical ring resonators for lab-on-a-chip and environmental detection," IEEE J. Sel. Topics Quantum Electron. **18**, 1583–1596 (2012).

[160] D. Marpaung, M. Pagani, B. Morrison, and B. Eggleton, "Nonlinear integrated microwave photonics," J. Lightwave Technol. **32**, 3421–3427 (2014).

[161] B. J. Eggleton, B. Luther-Davies, and K. Richardson, "Chalcogenide photonics," Nat. Photon. **5**, 141–148 (2011).

[162] A. Byrnes, R. Pant, E. Li, D.-Y. Choi, C. G. Poulton, S. Fan, S. Madden, B. Luther-Davies, and B. J. Eggleton, "Photonic chip based tunable and reconfigurable narrowband microwave photonic filter using stimulated Brillouin scattering," Opt. Express **20**, 18836–18845 (2012).

[163] B. Morrison, D. Marpaung, R. Pant, E. Li, D.-Y. Choi, S. Madden, B. Luther-Davies, and B. J. Eggleton, "Tunable microwave photonic notch filter using on-chip stimulated brillouin scattering," Opt. Commun. **313**, 85–89 (2014).

[164] D. Marpaung, B. Morrison, M. Pagani, R. Pant, D.-Y. Choi, B. Luther-Davies, S. J. Madden, and B. J. Eggleton, "Low-power, chip-based stimulated Brillouin scattering microwave photonic filter with ultrahigh selectivity," Optica **2**, 76–83 (2015).

[165] M. Pagani, D. Marpaung, D.-Y. Choi, S. J. Madden, B. Luther-Davies, and B. J. Eggleton, "Tunable wideband microwave photonic phase shifter using on-chip stimulated Brillouin scattering," Opt. Express **22**, 28810–28818 (2014).

[166] R. Pant, D. Marpaung, I. V. Kabakova, B. Morrison, C. G. Poulton, and B. J. Eggleton, "On-chip stimulated brillouin scattering for microwave signal processing and generation," Laser Photon. Rev. **8**, 653–666 (2014).

[167] B. E. A. Saleh and M. C. Teich, *Fundamentals of photonics* (Wiley, Hoboken, NJ, 2007), 2nd ed.

[168] R. W. Boyd, *Nonlinear optics* (Academic Press, 2008), 3rd ed.

[169] G. Agrawal, *Nonlinear fiber optics* (Academic Press Inc., 2012), chap. 4, 5th ed.

[170] O. Boyraz, X. Sang, M. Cazzanelli, and Y. Huang, "Nonlinear Optics in Silicon," in "Handbook of Silicon Photonics," (Taylor & Francis, 2013), Series in Optics and Optoelectronics, pp. 197–248.

[171] L.-D. Haret, X. Checoury, F. Bayle, N. Cazier, P. Boucaud, S. Combrié, and A. de Rossi, "Schottky MSM junctions for carrier depletion in silicon photonic crystal microcavities," Opt. Express **21**, 10324–10334 (2013).

[172] R. H. Stolen, J. E. Bjorkholm, and A. Ashkin, "Phase-matched three-wave mixing in silica fiber optical waveguides," Appl. Phys. Lett. **24**, 308–310 (1974).

[173] H. Fukuda, K. Yamada, T. Shoji, M. Takahashi, T. Tsuchizawa, T. Watanabe, J. Takahashi, and S. Itabashi, "Four-wave mixing in silicon wire waveguides," Opt. Express **13**, 4629–4637 (2005).

[174] M. R. Lamont, B. Luther-Davies, D.-Y. Choi, S. Madden, X. Gai, and B. J. Eggleton, "Net-gain from a parametric amplifier on a chalcogenide optical chip," Opt. Express **16**, 20374–20381 (2008).

[175] M. Ferrera, D. Duchesne, L. Razzari, M. Peccianti, R. Morandotti, P. Cheben, S. Janz, D.-X. Xu, B. E. Little, S. Chu, and D. J. Moss, "Low power four wave mixing in an integrated, micro-ring resonator with Q = 1.2 million," Opt. Express **17**, 14098–14103 (2009).

[176] J. S. Levy, A. Gondarenko, M. A. Foster, A. C. Turner-Foster, A. L. Gaeta, and M. Lipson, "CMOS-compatible multiple-wavelength oscillator for on-chip optical interconnects," Nat. Photon. **4**, 37–40 (2010).

[177] J. J. Wathen, P. Apiratikul, C. J. K. Richardson, G. A. Porkolab, G. M. Carter, and T. E. Murphy, "Efficient continuous-wave four-wave mixing in bandgap-engineered AlGaAs waveguides," Opt. Lett. **39**, 3161–3164 (2014).

[178] B. J. M. Hausmann, I. Bulu, V. Venkataraman, P. Deotare, and M. Loncar, "Diamond nonlinear photonics," Nat. Photon. **8**, 369–374 (2014).

[179] Q. Lin, J. Zhang, P. M. Fauchet, and G. P. Agrawal, "Ultrabroadband parametric generation and wavelength conversion in silicon waveguides," Opt. Express **14**, 4786–4799 (2006).

[180] M. Pu, H. Hu, L. Ottaviano, E. Semenova, D. Vukovic, L. K. Oxenlowe, and K. Yvind, "AlGaAs-on-insulator nanowire with 750 nm FWM bandwidth, −9 dB CW conversion efficiency, and ultrafast operation enabling record Tbaud wavelength conversion," in "Optical Fiber Communication Conference Post Deadline Papers," (OSA, 2015), p. Th5A.3.

[181] M. A. Foster, A. C. Turner, J. E. Sharping, B. S. Schmidt, M. Lipson, and A. L. Gaeta, "Broad-band optical parametric gain on a silicon photonic chip," Nature **441**, 960–963 (2006).

[182] K. Narayanan and S. F. Preble, "Optical nonlinearities in hydrogenated-amorphous silicon waveguides," Opt. Express **18**, 8998–9005 (2010).

[183] C. J. Krückel, V. Torres-Company, P. A. Andrekson, D. T. Spencer, J. F. Bauters, M. J. R. Heck, and J. E. Bowers, "Continuous wave-pumped wavelength conversion in low-loss silicon nitride waveguides," Opt. Lett. **40**, 875–878 (2015).

[184] M. Pagani, B. Morrison, Y. Zhang, A. Casas-Bedoya, T. Aalto, M. Harjanne, M. Kapulainen, B. J. Eggleton, and D. Marpaung, "Low-error and broadband microwave frequency measurement in a silicon chip," Optica **2**, 751–756 (2015).

[185] R. M. Osgood, N. C. Panoiu, J. I. Dadap, X. Liu, X. Chen, I.-W. Hsieh, E. Dulkeith, W. M. Green, and Y. A. Vlasov, "Engineering nonlinearities in nanoscale optical systems: physics and applications in dispersion-engineered silicon nanophotonic wires," Adv. Opt. Photon. **1**, 162–235 (2009).

[186] C. Grillet, L. Carletti, C. Monat, P. Grosse, B. B. Bakir, S. Menezo, J. M. Fedeli, and D. J. Moss, "Amorphous silicon nanowires combining high nonlinearity, FOM and optical stability," Opt. Express **20**, 22609–22615 (2012).

[187] C. Lacava, V. Pusino, P. Minzioni, M. Sorel, and I. Cristiani, "Nonlinear properties of AlGaAs waveguides in continuous wave operation regime," Opt. Express **22**, 5291–5298 (2014).

[188] A. Kobyakov, M. Sauer, and D. Chowdhury, "Stimulated Brillouin scattering in optical fibers," Adv. Opt. Photon. **2**, 1–59 (2010).

[189] M. S. Kang, A. Nazarkin, A. Brenn, and P. S. J. Russell, "Tightly trapped acoustic phonons in photonic crystal fibres as highly nonlinear artificial Raman oscillators," Nat. Phys. **5**, 276–280 (2009).

[190] A. A. Savchenkov, W. Liang, A. B. Matsko, V. S. Ilchenko, D. Seidel, and L. Maleki, "Narrowband tunable photonic notch filter," Opt. Lett. **34**, 1318–1320 (2009).

[191] C. L. Tang, "Saturation and spectral characteristics of the stokes emission in the stimulated Brillouin process," J. Appl. Phys. **37**, 2945–2955 (1966).

[192] E. Ippen and R. Stolen, "Stimulated Brillouin scattering in optical fibers," Appl. Phys. Lett. **21**, 539–541 (1972).

[193] K. O. Hill, B. S. Kawasaki, and D. C. Johnson, "CW Brillouin laser," Appl. Phys. Lett. **28**, 608–609 (1976).

[194] K. S. Abedin, "Brillouin amplification and lasing in a single-mode As_2Se_3 chalcogenide fiber," Opt. Lett. **31**, 1615–1617 (2006).

[195] K. S. Abedin, P. S. Westbrook, J. W. Nicholson, J. Porque, T. Kremp, and X. Liu, "Single-frequency Brillouin distributed feedback fiber laser," Opt. Lett. **37**, 605–607 (2012).

[196] M. Al-Mansoori and M. A. Mahdi, "Multiwavelength L-band Brillouin erbium comb fiber laser utilizing nonlinear amplifying loop mirror," Lightwave Technology, Journal of **27**, 5038–5044 (2009).

[197] X. Bao and L. Chen, "Recent progress in Brillouin scattering based fiber sensors," Sensors **11**, 4152–4187 (2011).

[198] M. González-Herráez, K.-Y. Song, and L. Thévenaz, "Optically controlled slow and fast light in optical fibers using stimulated Brillouin scattering," Appl. Phys. Lett. **87**, 081113 (2005).

[199] Y. Okawachi, M. S. Bigelow, J. E. Sharping, Z. Zhu, A. Schweinsberg, D. J. Gauthier, R. W. Boyd, and A. L. Gaeta, "Tunable all-optical delays via Brillouin slow light in an optical fiber," Phys. Rev. Lett. **94**, 153902 (2005).

[200] K. Y. Song, M. G. Herráez, and L. Thévenaz, "Long optically controlled delays in optical fibers," Opt. Lett. **30**, 1782–1784 (2005).

[201] C. Wolff, R. Soref, C. Poulton, and B. Eggleton, "Germanium as a material for stimulated Brillouin scattering in the mid-infrared," Opt. Express **22**, 30735–30747 (2014).

[202] L. Thevenaz, "Silicon nanophotonics: Good vibrations for light," Nat. Photon. **9**, 144–146 (2015).

[203] P. T. Rakich, C. Reinke, R. Camacho, P. Davids, and Z. Wang, "Giant enhancement of stimulated brillouin scattering in the subwavelength limit," Phys. Rev. X **2**, 011008 (2012).

[204] C. G. Poulton, R. Pant, and B. J. Eggleton, "Acoustic confinement and stimulated Brillouin scattering in integrated optical waveguides," J. Opt. Soc. Am. B **30**, 2657–2664 (2013).

[205] R. Pant, C. G. Poulton, D.-Y. Choi, H. McFarlane, S. Hile, E. Li, L. Thevenaz, B. Luther-Davies, S. J. Madden, and B. J. Eggleton, "On-chip stimulated Brillouin scattering," Opt. Express **19**, 8285–8290 (2011).

[206] R. Pant, A. Byrnes, C. G. Poulton, E. Li, D.-Y. Choi, S. Madden, B. Luther-Davies, and B. J. Eggleton, "Photonic-chip-based tunable slow and fast light via stimulated brillouin scattering," Opt. Lett. **37**, 969–971 (2012).

[207] I. V. Kabakova, R. Pant, D.-Y. Choi, S. Debbarma, B. Luther-Davies, S. J. Madden, and B. J. Eggleton, "Narrow linewidth Brillouin laser based on chalcogenide photonic chip," Opt. Lett. **38**, 3208–3211 (2013).

[208] T. F. S. Büttner, M. Merklein, I. V. Kabakova, D. D. Hudson, D.-Y. Choi, B. Luther-Davies, S. J. Madden, and B. J. Eggleton, "Phase-locked, chip-based, cascaded stimulated Brillouin scattering," Optica **1**, 311–314 (2014).

[209] M. Merklein, I. V. Kabakova, T. F. S. Büttner, D.-Y. Choi, B. Luther-Davies, S. J. Madden, and B. J. Eggleton, "Enhancing and inhibiting stimulated Brillouin scattering in photonic integrated circuits," Nat. Commun. **6** (2015).

[210] R. Van Laer, B. Kuyken, D. Van Thourhout, and R. Baets, "Interaction between light and highly confined hypersound in a silicon photonic nanowire," Nat. Photon. **9**, 199–203 (2015).

[211] H. Shin, W. Qiu, R. Jarecki, J. A. Cox, R. H. Olsson, A. Starbuck, Z. Wang, and P. T. Rakich, "Tailorable stimulated Bril-

louin scattering in nanoscale silicon waveguides," Nat. Commun. **4** (2013).

[212] R. V. Laer, B. Kuyken, D. V. Thourhout, and R. Baets, "Analysis of enhanced stimulated brillouin scattering in silicon slot waveguides," Opt. Lett. **39**, 1242–1245 (2014).

[213] Y. Pennec, V. Laude, N. Papanikolaou, B. Djafari-Rouhani, M. Oudich, S. El Jallal, J. C. Beugnot, J. M. Escalante, and A. Martinez, "Modeling light-sound interaction in nanoscale cavities and waveguides," Nanophotonics **3**, 413–440 (2014).

[214] C. Wolff, P. Gutsche, M. J. Steel, B. J. Eggleton, and C. G. Poulton, "Impact of nonlinear loss on stimulated Brillouin scattering," J. Opt. Soc. Am. B **32**, 1968–1978 (2015).

[215] Y.-R. Chien, "Design of GPS anti-jamming systems using adaptive notch filters," IEEE Syst. J. **9**, 451–460 (2015).

[216] E. Chan and R. Minasian, "Widely tunable, high-FSR, coherence-free microwave photonic notch filter," J. Lightwave Technol. **26**, 922–927 (2008).

[217] W. Li, N. H. Zhu, and L. X. Wang, "Continuously tunable microwave photonic notch filter with a complex coefficient," IEEE Photon. J. **3**, 462–467 (2011).

[218] X. Wang, J. Yang, E. Chan, X. Feng, and B. Guan, "All-optical continuously tunable flat-passband microwave photonic notch filter," IEEE Photon. J. **7**, 1–11 (2015).

[219] D. Zhang, X. Feng, X. Li, K. Cui, F. Liu, and Y. Huang, "Tunable and reconfigurable bandstop microwave photonic filter based on integrated microrings and Mach-Zehnder interferometer," J. Lightwave Technol. **31**, 3668–3675 (2013).

[220] J. Ge, H. Feng, G. Scott, and M. P. Fok, "High-speed tunable microwave photonic notch filter based on phase modulator incorporated Lyot filter," Opt. Lett. **40**, 48–51 (2015).

[221] W. Bogaerts, P. De Heyn, T. Van Vaerenbergh, K. De Vos, S. Kumar Selvaraja, T. Claes, P. Dumon, P. Bienstman, D. Van Thourhout, and R. Baets, "Silicon microring resonators," Laser Photon. Rev. **6**, 47–73 (2012).

[222] D. Marpaung, B. Morrison, R. Pant, C. Roeloffzen, A. Leinse, M. Hoekman, R. Heideman, and B. J. Eggleton, "Si3N4 ring resonator-based microwave photonic notch filter with an ultra-high peak rejection," Opt. Express **21**, 23286–23294 (2013).

[223] Y. Long and J. Wang, "Ultra-high peak rejection notch microwave photonic filter using a single silicon microring resonator," Opt. Express **23**, 17739–17750 (2015).

[224] R. Tao, X. Feng, Y. Cao, Z. Li, and B.-O. Guan, "Tunable microwave photonic notch filter and bandpass filter based on high-birefringence fiber-bragg-grating-based fabry-perot cavity," IEEE Photon. Technol. Lett. **24**, 1805–1808 (2012).

[225] D. Marpaung, B. Morrison, M. Pagani, R. Pant, and B. J. Eggleton, "Ultra-high suppression microwave photonic bandstop filters," Chin. Sci. Bull. **59**, 2684–2692 (2014).

[226] M. Izutsu, S. Shikama, and T. Sueta, "Integrated optical SSB modulator/frequency shifter," IEEE J. Quantum Electron. **17**, 2225–2227 (1981).

[227] T. Tanemura, Y. Takushima, and K. Kikuchi, "Narrowband optical filter, with a variable transmission spectrum, using stimulated Brillouin scattering in optical fiber," Opt. Lett. **27**, 1552–1554 (2002).

[228] A. Villafranca, J. Lázaro, I. Salinas, and I. Garcés, "Stimulated Brillouin scattering gain profile characterization by interaction between two narrow-linewidth optical sources," Opt. Express **13**, 7336–7341 (2005).

[229] T. Kurashima, T. Horiguchi, and M. Tateda, "Thermal effects on the Brillouin frequency shift in jacketed optical silica fibers," Appl. Opt. **29**, 2219–2222 (1990).

[230] T. R. Parker, M. Farhadiroushan, V. A. Handerek, and A. J. Rogers, "Temperature and strain dependence of the power level and frequency of spontaneous Brillouin scattering in optical fibers," Opt. Lett. **22**, 787–789 (1997).

[231] M. Nikles, L. Thevenaz, and P. Robert, "Brillouin gain spectrum characterization in single-mode optical fibers," J. Lightwave Technol. **15**, 1842–1851 (1997).

[232] V. L. Iezzi, S. Loranger, M. Marois, and R. Kashyap, "High-sensitivity temperature sensing using higher-order stokes stimulated Brillouin scattering in optical fiber," Opt. Lett. **39**, 857–860 (2014).

[233] R. W. Boyd, K. Rzazewski, and P. Narum, "Noise initiation of stimulated Brillouin scattering," Phys. Rev. A **42**, 5514–5521 (1990).

[234] R. W. Tkach and A. R. Chraplyvy, "Fibre Brillouin amplifiers," Opt. Quant. Electron. **21**, S105–S112 (1989).

[235] M. F. Ferreira, J. F. Rocha, and J. L. Pinto, "Analysis of the gain and noise characteristics of fibre Brillouin amplifiers," Opt. Quant. Electron. **26**, 35–44 (1994).

[236] T. Snow, J. Lee, and W. Chappell, "Tunable high quality-factor absorptive bandstop filter design," in "Microwave Symposium Digest (MTT), 2012 IEEE MTT-S International," (2012), pp. 1–3.

[237] G. Li and P. Yu, "Optical intensity modulators for digital and analog applications," J. Lightwave Technol. **21**, 2010–2030 (2003).

[238] M. Roelens, S. Frisken, J. Bolger, D. Abakoumov, G. Baxter, S. Poole, and B. Eggleton, "Dispersion trimming in a reconfigurable wavelength selective switch," J. Lightwave Technol. **26**, 73–78 (2008).

[239] J. Yang, E. H. W. Chan, X. Wang, X. Feng, and B. Guan, "Broadband photonic microwave phase shifter based on controlling two RF modulation sidebands via a Fourier-domain optical processor," Opt. Express **23**, 12100–12110 (2015).

[240] R. J. Mailloux, *Phased array antenna handbook* (Artech House, 2005), 2nd ed.

[241] J. Adam, L. Davis, G. F. Dionne, E. Schloemann, and S. Stitzer, "Ferrite devices and materials," IEEE Trans. Microw. Theory Techn. **50**, 721–737 (2002).

[242] J. G. Yang and K. Yang, "Ka-band 5-bit MMIC phase shifter using InGaAs PIN switching diodes," IEEE Microw. Compon. Lett. **21**, 151–153 (2011).

[243] B. Acikel, T. R. Taylor, P. J. Hansen, J. S. Speck, and R. York, "A new high performance phase shifter using Ba/sub x/Sr/sub 1-x/TiO3 thin films," IEEE Microw. Compon. Lett. **12**, 237–239 (2002).

[244] S. Winnall, A. Lindsay, and G. Knight, "A wide-band microwave photonic phase and frequency shifter," IEEE Trans. Microw. Theory Techn. **45**, 1003–1006 (1997).

[245] J. Shen, G. Wu, W. Zou, and J. Chen, "A photonic RF phase shifter based on a dual-parallel Mach-Zehnder modulator and an optical filter," Appl. Phys. Express **5**, 072502 (2012).

[246] S. Pan and Y. Zhang, "Tunable and wideband microwave photonic phase shifter based on a single-sideband polarization modulator and a polarizer," Opt. Lett. **37**, 4483–4485 (2012).

[247] W. Li, W. H. Sun, W. T. Wang, L. X. Wang, J. G. Liu, and N. H. Zhu, "Photonic-assisted microwave phase shifter using a DMZM and an optical bandpass filter," Opt. Express **22**, 5522–5527 (2014).

[248] W. Li, N. H. Zhu, and L. X. Wang, "Photonic phase shifter based on wavelength dependence of Brillouin frequency shift," IEEE Photon. Technol. Lett. **23**, 1013–1015 (2011).

[249] X. Sun, S. Fu, K. Xu, J. Zhou, P. Shum, J. Yin, X. Hong, J. Wu, and J. Lin, "Photonic RF phase shifter based on a vector-sum technique using stimulated Brillouin scattering in dispersion shifted fiber," IEEE Trans. Microw. Theory Techn. **58**, 3206–3212 (2010).

[250] Y. Dong, H. He, W. Hu, Z. Li, Q. Wang, W. Kuang, T. H. Cheng, Y. J. Wen, Y. Wang, and C. Lu, "Photonic microwave phase shifter/modulator based on a nonlinear optical loop mirror incorporating a Mach-Zehnder interferometer," Opt. Lett. **32**, 745–747 (2007).

[251] W. Xue, S. Sales, J. Capmany, and J. Mørk, "Wideband 360° microwave photonic phase shifter based on slow light in semiconductor optical amplifiers," Opt. Express **18**, 6156–6163 (2010).

[252] J. Sancho, J. Lloret, I. Gasulla, S. Sales, and J. Capmany, "Fully tunable 360° microwave photonic phase shifter based on a single semiconductor optical amplifier," Opt. Express **19**, 17421–17426 (2011).

[253] W. Li, W. Zhang, and J. Yao, "A wideband 360° photonic-assisted microwave phase shifter using a polarization modulator and a polarization-maintaining fiber Bragg grating," Opt. Express **20**, 29838–29843 (2012).

[254] H. Shahoei and J. Yao, "Tunable microwave photonic phase shifter based on slow and fast light effects in a tilted fiber Bragg grating," Opt. Express **20**, 14009–14014 (2012).

[255] W. Liu, W. Li, and J. Yao, "An ultra-wideband microwave photonic phase shifter with a full 360° phase tunable range," IEEE Photon. Technol. Lett. **25**, 1107–1110 (2013).

[256] W. Liu and J. Yao, "Ultra-wideband microwave photonic phase shifter with a 360° tunable phase shift based on an erbium-ytterbium co-doped linearly chirped FBG," Opt. Lett. **39**, 922–924 (2014).

[257] M. Pu, L. Liu, W. Xue, Y. Ding, H. Ou, K. Yvind, and J. M. Hvam, "Widely tunable microwave phase shifter based on silicon-on-insulator dual-microring resonator," Opt. Express **18**, 6172–6182 (2010).

[258] N. Ehteshami, W. Zhang, and J. Yao, "Optically tunable full 360° microwave photonic phase shifter using three cascaded silicon-on-insulator microring resonators," Opt. Commun. - In press (2015).

[259] M. Burla, L. R. Cortés, M. Li, X. Wang, L. Chrostowski, and J. Azaña, "Integrated waveguide Bragg gratings for microwave photonics signal processing," Opt. Express **21**, 25120–25147 (2013).

[260] M. Burla, L. R. Cortés, M. Li, X. Wang, L. Chrostowski, and J. Azaña, "On-chip programmable ultra-wideband microwave photonic phase shifter and true time delay unit," Opt. Lett. **39**, 6181–6184 (2014).

[261] J. Hervás, I. Suárez, J. Pérez, P. J. R. Cantó, R. Abargues, J. P. Martínez-Pastor, S. Sales, and J. Capmany, "MWP phase shifters integrated in PbS-SU8 waveguides," Opt. Express **23**, 14351–14359 (2015).

[262] J. Capmany, D. Domenech, and P. Muñoz, "Silicon graphene waveguide tunable broadband microwave photonics phase shifter," Opt. Express **22**, 8094–8100 (2014).

[263] J. E. Román, M. Y. Frankel, and R. D. Esman, "Spectral characterization of fiber gratings with high resolution," Opt. Lett. **23**, 939–941 (1998).

[264] A. Loayssa, D. Benito, and M. J. Garde, "Optical carrier Brillouin processing of microwave photonic signals," Opt. Lett. **25**, 1234–1236 (2000).

[265] M. Kumar, R. Menna, and H.-C. Huang, "Broad-band active phase shifter using dual-gate MESFET," IEEE Trans. Microw. Theory Techn. **29**, 1098–1102 (1981).

[266] L. Bui, A. Mitchell, K. Ghorbani, and T.-H. Chio, "Wideband RF photonic vector sum phase-shifter," Electron. Lett. **39**, 536–537 (2003).

[267] L. Bui, A. Mitchell, K. Ghorbani, and T.-H. Chio, "Wide-band RF photonic second order vector sum phase-shifter," IEEE Microw. Compon. Lett **15**, 309–311 (2005).

[268] P. Qu, C. Liu, W. Dong, W. Chen, F. Li, H. Li, Z. Gong, S. Ruan, X. Zhang, and J. Zhou, "Design of a vector-sum integrated microwave photonic phase shifter in silicon-on-insulator waveguides," Appl. Opt. **50**, 2523–2530 (2011).

[269] A. Loayssa, D. Benito, and M. J. Garde, "Applications of optical carrier Brillouin processing to microwave photonics," Opt. Fiber Technol. **8**, 24–42 (2002).

[270] X. Liu, W. Pan, X. Zou, D. Zheng, L. Yan, B. Luo, and B. Lu, "Photonic generation of triangular-shaped microwave pulses using SBS-based optical carrier processing," J. Lightwave Technol. **32**, 3797–3802 (2014).

[271] M. Pagani, E. Chan, and R. Minasian, "A study of the linearity performance of a stimulated Brillouin scattering-based microwave photonic bandpass filter," J. Lightw. Technol. **32**, 999–1005 (2014).

[272] A. Zadok, E. Zilka, A. Eyal, L. Thévenaz, and M. Tur, "Vector analysis of stimulated Brillouin scattering amplification in standard single-mode fibers," Opt. Express **16**, 21692–21707 (2008).

[273] D. L. Adamy, *Introduction to electronic warfare modeling and simulation* (SciTech Publishing, 2006), chap. 5, 1st ed.

[274] R. Mackay, "Instantaneous frequency measurement," Medical electronics and biological engineering **1**, 109–111 (1963).

[275] J. B. Y. Tsui, "Instantaneous frequency measurement system," Nov. 9, 1976. U.S. patent 3,992,365 .

[276] A. Graham, *Communications, Radar and electronic warfare* (Wiley, 2011), chap. 6, 1st ed.

[277] MEURO, *Instantaneous Frequency Measurement Receiver* (2015).

[278] Wide Band Systems, Inc., *Instantaneous Frequency Measurement Receiver Systems (IFM)* (2015).

[279] W. Wang, R. Davis, T. Jung, R. Lodenkamper, L. Lembo, J. Brock, and M. Wu, "Characterization of a coherent optical RF channelizer based on a diffraction grating," IEEE Trans. Microw. Theory Techn. **49**, 1996–2001 (2001).

[280] S. Winnall, A. Lindsay, M. Austin, J. Canning, and A. Mitchell, "A microwave channelizer and spectroscope based on an integrated optical Bragg-grating Fabry-Perot and integrated hybrid fresnel lens system," IEEE Trans. Microw. Theory Techn. **54**, 868–872 (2006).

[281] H. Guo, G. Xiao, N. Mrad, and J. Yao, "Measurement of microwave frequency using a monolithically integrated scannable Echelle diffractive grating," IEEE Photon. Technol. Lett. **21**, 45–47 (2009).

[282] X. Zou, W. Li, W. Pan, L. Yan, and J. Yao, "Photonic-assisted microwave channelizer with improved channel characteristics based on spectrum-controlled stimulated Brillouin scattering," IEEE Trans. Microw. Theory Techn. **61**, 3470–3478 (2013).

[283] S. Winnall and A. Lindsay, "A fabry-perot scanning receiver for microwave signal processing," IEEE Trans. Microw. Theory Techn. **47**, 1385–1390 (1999).

[284] P. Rugeland, Z. Yu, C. Sterner, O. Tarasenko, G. Tengstrand, and W. Margulis, "Photonic scanning receiver using an electrically tuned fiber Bragg grating," Opt. Lett. **34**, 3794–3796 (2009).

[285] S. Zheng, S. Ge, X. Zhang, H. Chi, and X. Jin, "High-resolution multiple microwave frequency measurement based on stimulated Brillouin scattering," IEEE Photon. Technol. Lett. **24**, 1115–1117 (2012).

[286] C. Ye, H. Fu, K. Zhu, and S. He, "All-optical approach to microwave frequency measurement with large spectral range and high accuracy," IEEE Photon. Technol. Lett. **24**, 614–616 (2012).

[287] L. Nguyen, "Microwave photonic technique for frequency measurement of simultaneous signals," IEEE Photon. Technol. Lett. **21**, 642–644 (2009).

[288] T. Nguyen, E. Chan, and R. Minasian, "Photonic multiple frequency measurement using a frequency shifting recirculating delay line structure," J. Lightw. Technol. **32**, 3831–3838 (2014).

[289] T. A. Nguyen, E. H. W. Chan, and R. A. Minasian, "Instantaneous high-resolution multiple-frequency measurement system based on frequency-to-time mapping technique," Opt. Lett. **39**, 2419–2422 (2014).

[290] L. Nguyen and D. Hunter, "A photonic technique for microwave frequency measurement," IEEE Photon. Technol. Lett. **18**, 1188–1190 (2006).

[291] H. Chi, X. Zou, and J. Yao, "An approach to the measurement of microwave frequency based on optical power monitoring," IEEE Photon. Technol. Lett. **20**, 1249–1251 (2008).

[292] M. V. Drummond, P. Monteiro, and R. N. Nogueira, "Photonic RF instantaneous frequency measurement system by means of a polarization-domain interferometer," Opt. Express **17**, 5433–5438 (2009).

[293] J. Zhou, S. Aditya, P. Shum, and J. Yao, "Instantaneous microwave frequency measurement using a photonic microwave filter with an infinite impulse response," IEEE Photon. Technol. Lett. **22**, 682–684 (2010).

[294] Z. Li, C. Wang, M. Li, H. Chi, X. Zhang, and J. Yao, "Instantaneous microwave frequency measurement using a special fiber Bragg grating," IEEE Microw. Compon. Lett. **21**, 52–54 (2011).

[295] B. Vidal, "Photonic-based instantaneous microwave frequency measurement with extended range," Opt. Commun. **284**, 3996–3999 (2011).

[296] Y. Wang, J. Ni, H. Chi, X. Zhang, S. Zheng, and X. Jin, "Photonic instantaneous microwave frequency measurement based on two different phase modulation to intensity modulation conversions," Opt. Commun. **284**, 3928–3932 (2011).

[297] X. Zou, W. Pan, B. Luo, L. Yan, and Y. Jiang, "Photonic approach to microwave frequency measurement with digital circular-code results," Opt. Express **19**, 20580–20585 (2011).

[298] W. Li, N. H. Zhu, and L. X. Wang, "Brillouin-assisted microwave frequency measurement with adjustable measurement range and resolution," Opt. Lett. **37**, 166–168 (2012).

[299] J. S. Fandiño and P. Muñoz, "Analysis of system imperfections in a photonics-assisted instantaneous frequency measurement receiver based on a dual-sideband suppressed-carrier modulation," J. Lightwave Technol. **33**, 293–303 (2015).

[300] H. Emami, N. Sarkhosh, L. A. Bui, and A. Mitchell, "Amplitude independent RF instantaneous frequency measurement system using photonic Hilbert transform," Opt. Express **16**, 13707–13712 (2008).

[301] N. Sarkhosh, H. Emami, L. Bui, and A. Mitchell, "Reduced cost photonic instantaneous frequency measurement system," IEEE Photon. Technol. Lett. **20**, 1521–1523 (2008).

[302] J. Dai, K. Xu, R. Duan, X. Zhang, D. Wang, J. Wu, and J. Lin, "Instantaneous frequency measurement based on complementary microwave photonic filters with a shared Mach-Zehnder interferometer," Opt. Commun. **284**, 5738–5741 (2011).

[303] S. Fu, M. Tang, and P. Shum, "Instantaneous microwave frequency measurement using optical carrier suppression based DC power monitoring," Opt. Express **19**, 24712–24717 (2011).

[304] H. Emami, N. Sarkhosh, and M. Ashourian, "Reconfigurable photonic radar warning receiver based on cascaded grating," Opt. Express **21**, 7734–7739 (2013).

[305] D. Marpaung, "On-chip photonic-assisted instantaneous microwave frequency measurement system," IEEE Photon. Technol. Lett. **25**, 837–840 (2013).

[306] L. Liu, F. Jiang, S. Yan, S. Min, M. He, D. Gao, and J. Dong, "Photonic measurement of microwave frequency using a silicon microdisk resonator," Opt. Commun. **335**, 266–270 (2015).

[307] M. Burla, X. Wang, M. Li, L. Chrostowski, and J. Azaña, "On-chip instantaneous microwave frequency measurement system based on a waveguide bragg grating on silicon," in "CLEO: 2015," (Optical Society of America, 2015), p. STh4F.7.

[308] K. Dolgaleva, W. C. Ng, L. Qian, and J. S. Aitchison, "Compact highly-nonlinear AlGaAs waveguides for efficient wavelength conversion," Opt. Express **19**, 12440–12455 (2011).

[309] M. A. Foster, A. C. Turner, R. Salem, M. Lipson, and A. L. Gaeta, "Broad-band continuous-wave parametric wavelength conversion in silicon nanowaveguides," Opt. Express **15**, 12949–12958 (2007).

[310] K.-Y. Wang and A. C. Foster, "Ultralow power continuous-wave frequency conversion in hydrogenated amorphous silicon waveguides," Opt. Lett. **37**, 1331–1333 (2012).

[311] K. K. Lee, D. R. Lim, L. C. Kimerling, J. Shin, and F. Cerrina, "Fabrication of ultralow-loss Si/SiO_2 waveguides by roughness reduction," Opt. Lett. **26**, 1888–1890 (2001).

[312] T. Murphy, J. Todd Hastings, and H. I. Smith, "Fabrication and characterization of narrow-band Bragg-reflection filters in silicon-on-insulator ridge waveguides," J. Lightw. Technol. **19**, 1938–1942 (2001).

[313] V. Ta'eed, D. Moss, B. Eggleton, D. Freeman, S. Madden, M. Samoc, B. Luther-Davies, S. Janz, and D. Xu, "Higher order mode conversion via focused ion beam milled Bragg gratings in silicon-on-insulator waveguides," Opt. Express **12**, 5274–5284 (2004).

[314] D. Moss, L. Fu, I. Littler, and B. Eggleton, "Ultrafast all-optical modulation via two-photon absorption in silicon-on-insulator waveguides," Electron. Lett. **41**, 320–321 (2005).

[315] A. Biberman, M. J. Shaw, E. Timurdogan, J. B. Wright, and M. R. Watts, "Ultralow-loss silicon ring resonators," Opt. Lett. **37**, 4236–4238 (2012).

[316] M. Cherchi, S. Ylinen, M. Harjanne, M. Kapulainen, and T. Aalto, "Dramatic size reduction of waveguide bends on a micron-scale silicon photonic platform," Opt. Express **21**, 17814–17823 (2013).

[317] R. A. Soref, J. Schmidtchen, and K. Petermann, "Large single-mode rib waveguides in GeSi-Si and Si-on-SiO_2," IEEE J. Quantum Electron. **27**, 1971–1974 (1991).

[318] S. Pogossian, L. Vescan, and A. Vonsovici, "The single-mode condition for semiconductor rib waveguides with large cross section," J. Lightw. Technol. **16**, 1851–1853 (1998).

[319] O. Boyraz, T. Indukuri, and B. Jalali, "Self-phase-modulation induced spectral broadening in silicon waveguides," Opt. Express **12**, 829–834 (2004).

[320] N. Lindenmann, G. Balthasar, D. Hillerkuss, R. Schmogrow, M. Jordan, J. Leuthold, W. Freude, and C. Koos, "Photonic wire bonding: a novel concept for chip-scale interconnects," Opt. Express **20**, 17667–17677 (2012).

[321] T. Aalto, M. Cherchi, M. Harjanne, S. Ylinen, M. Kapulainen, and T. Vehmas, "Launching of multi-project wafer runs in ePIXfab with micron-scale silicon rib waveguide technology," in "Proc. SPIE," (2014), pp. 899003–1–11.

[322] N.-N. Feng, P. Dong, D. Zheng, S. Liao, H. Liang, R. Shafiiha, D. Feng, G. Li, J. E. Cunningham, A. V. Krishnamoorthy, and M. Asghari, "Vertical p-i-n germanium photodetector with high external responsivity integrated with large core Si waveguides," Opt. Express **18**, 96–101 (2010).

[323] M. Cherchi, S. Ylinen, M. Harjanne, M. Kapulainen, T. Vehmas, T. Aalto, G. T. Kanellos, D. Fitsios, and N. Pleros, "Fabrication-tolerant optical filters for dense integration on a micron-scale SOI platform," in "Proc. SPIE," (2014), pp. 89900F–7.

[324] X. Xiao, H. Xu, X. Li, Z. Li, T. Chu, Y. Yu, and J. Yu, "High-speed, low-loss silicon mach-zehnder modulators with doping optimization," Opt. Express **21**, 4116–4125 (2013).

[325] S. Pathak, M. Vanslembrouck, P. Dumon, D. Van Thourhout, P. Verheyen, G. Lepage, P. Absil, and W. Bogaerts, "Effect of mask discretization on performance of silicon arrayed waveguide gratings," IEEE Photon. Technol. Lett. **26**, 718–721 (2014).

[326] L. Alloatti, R. Palmer, S. Diebold, K. P. Pahl, B. Chen, R. Dinu, M. Fournier, J.-M. Fedeli, T. Zwick, W. Freude, C. Koos, and J. Leuthold, "100 GHz silicon-organic hybrid modulator," Light Sci. Appl. **3**, e173 (2014).

[327] M. LaGasse and S. Thaniyavaru, "Bias-free high-dynamic-range phase-modulated fiber-optic link," IEEE Photon. Technol. Lett. **9**, 681–683 (1997).

[328] Y. Li, R. Wang, G. Ding, J. Klamkin, L. Johansson, P. Herczfeld, and J. Bowers, "Novel phase modulator linearity measurement," IEEE Photon. Technol. Lett. **21**, 1405–1407 (2009).

[329] R. Rudnick, A. Tolmachev, D. Sinefeld, O. Golani, S. Ben-Ezra, M. Nazarathy, and D. Marom, "Sub-banded/single-sub-carrier drop-demux and flexible spectral shaping with a fine resolution photonic processor," in "European Conference on Optical Communication," (2014), pp. 1–3.

[330] D. Pérez, I. Gasulla, and J. Capmany, "Software-defined reconfigurable microwave photonics processor," Opt. Express **23**, 14640–14654 (2015).

[331] D. Liang and J. E. Bowers, "Recent progress in lasers on silicon," Nat. Photon. **4**, 511–517 (2010).

[332] S. Tanaka, S.-H. Jeong, S. Sekiguchi, T. Kurahashi, Y. Tanaka, and K. Morito, "High-output-power, single-wavelength silicon hybrid laser using precise flip-chip bonding technology," Opt. Express **20**, 28057–28069 (2012).

[333] Y. Qiu, "Tunable, narrow line-width silicon micro-ring laser source for coherent optical communications," in "CLEO: 2015," (Optical Society of America, 2015), p. JTh2A.57.

[334] C. Zhang, D. Liang, G. Kurczveil, J. Bowers, and R. Beausoleil, "Thermal management of hybrid silicon ring lasers for high temperature operation," IEEE J. Sel. Topics Quantum Electron. **21**, 1–7 (2015).

[335] D. Feng, W. Qian, H. Liang, C.-C. Kung, Z. Zhou, Z. Li, J. Levy, R. Shafiiha, J. Fong, B. Luff, and M. Asghari, "High-speed GeSi electroabsorption modulator on the SOI waveguide platform," IEEE J. Sel. Topics Quantum Electron. **19**, 64–73 (2013).

[336] S. Miller, Y. H. D. Lee, J. Cardenas, A. L. Gaeta, and M. Lipson, "Electro-optic effect in silicon nitride," in "CLEO: 2015," (Optical Society of America, 2015), p. SF1G.4.

[337] C. T. Phare, Y.-H. D. Lee, J. Cardenas, and M. Lipson, "Graphene electro-optic modulator with 30 ghz bandwidth," Nat. Photon. **9**, 511–515 (2015).

[338] J. Capmany, D. Domenech, and P. Munoz, "Graphene integrated microwave photonics," J. Lightwave Technol. **32**, 3785–3796 (2014).

[339] S. Grillanda, M. Carminati, F. Morichetti, P. Ciccarella, A. Annoni, G. Ferrari, M. Strain, M. Sorel, M. Sampietro, and A. Melloni, "Non-invasive monitoring and control in silicon photonics using CMOS integrated electronics," Optica **1**, 129–136 (2014).